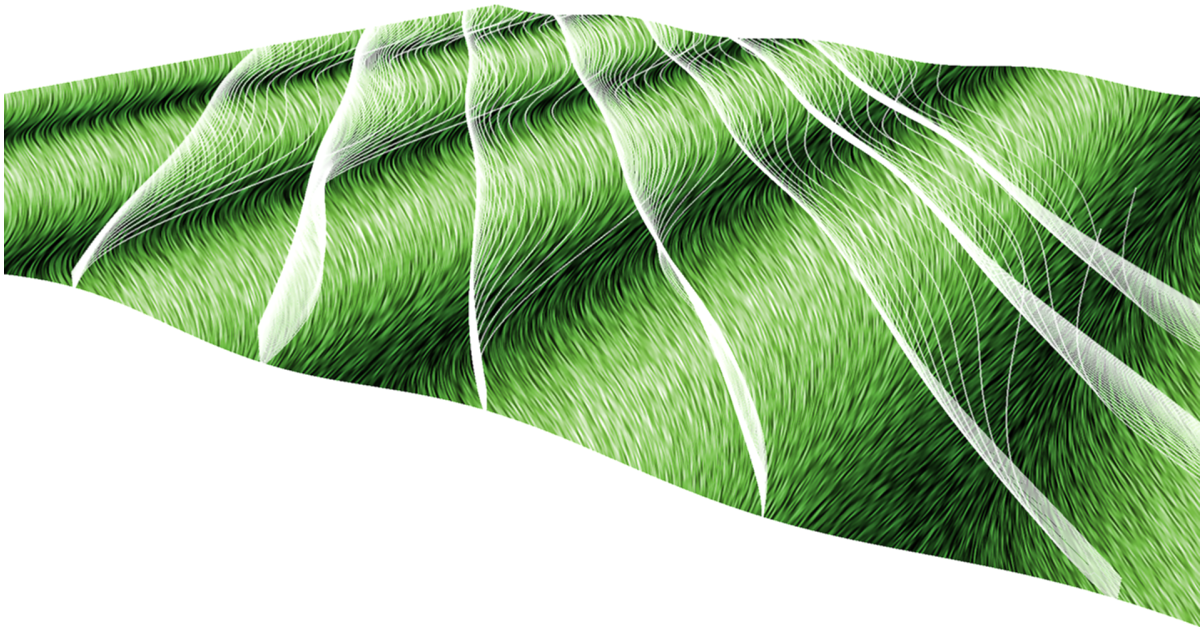
TURBULENT DRAG REDUCTION BY OBLIQUE WAVY WALL UNDULATIONS

Imperial College London

Department of Aeronautics
Faculty of Engineering

Turbulent drag reduction by oblique wavy wall undulations



by

Sacha D. Ghebali

A dissertation submitted for the degree of Doctor of Philosophy

and the Diploma of Imperial College

August 2018

Illustration on the title page

Visualisation of mean streamlines and streaklines in the lower half of a turbulent wavy channel, calculated from a DNS of the flow.

Copyright declaration

The copyright of this thesis rests with the author and is made available under a Creative Commons Attribution Non-Commercial No Derivatives licence. Researchers are free to copy, distribute or transmit the thesis on the condition that they attribute it, that they do not use it for commercial purposes and that they do not alter, transform or build upon it. For any reuse or redistribution, researchers must make clear to others the licence terms of this work.

Colophon

Text and figures are set in Times at 11pt, sans-serif elements are set in Helvetica

Typeset by the author in LaTeX 2ε with the KOMA-Script bundle

Source written in TeXstudio and compiled with LuaLaTeX

Illustrations generated with ParaView, Inkscape and MATLAB

Pagination follows the requirements of theses for Imperial College research degrees

Other style considerations intend to follow as much as possible the recommendations of the *Oxford Guide to Style* by R. M. Ritter (2002)

To the memory of my grandmother Sarah

To my sister

Γνῶθι σεαυτόν

Μηδὲν ἄγαν

Abstract

The turbulent flow past a horizontal wavy wall, positioned at an angle to the main flow direction, is investigated by means of Direct Numerical Simulations with the purpose of reducing the drag.

The concept aims to emulate the active control by spanwise wall oscillations—known for its high drag-reducing effectiveness—by use of a passive device. The latter takes advantage of the large characteristic spatial wavelength of the active method, which is a crucial aspect for the potential practical implementation on commercial aircraft.

Imparting wall oscillations in the form of a standing wave $w_w = A_{\mathrm{SSL}} \sin\left(\frac{2\pi}{\lambda_x} x\right)$ gives rise to a so-called Spatial Stokes Layer (SSL), resulting in a shear-strain layer, which induces a strong suppression of the near-wall turbulence, thereby leading to drag reduction. A skewed wavy wall described by $h_w = A_w \sin\left(\frac{2\pi}{\lambda_x} x + \frac{2\pi}{\lambda_z} z\right)$ is considered, so as to produce a shear-strain layer that is similar to that of the SSL in featuring the same streamwise wavelength λ_x. The main points of resemblance between the wavy wall and SSL are investigated, and then contrasted through the identification of significant differences.

A reduced-order model is formulated to aid the DNS exploration of the parameter space (wave height, flow angle and wavelength) in the search for the optimal flow configuration. The validity of the assumptions made in the model, as well as its ability to predict the main flow properties, are examined by comparison to the DNS results.

Arising from a DNS exploration of the 3D parameter space, a configuration yielding approximately 1% drag reduction is identified. The response of the flow properties and the drag to variations in the wave height, flow angle and wavelength on the flow properties is reported and analysed. Major emphasis is placed on quantifying the influence of numerical accuracy on the predicted drag-reduction margin and on the computational efforts required to achieve this margin.

Acknowledgements

First and foremost, I would like to express my deepest gratitude to my supervisors Prof. Sergei I. Chernyshenko and Prof. Michael A. Leschziner, for their relentless guidance, for their kind support and encouragement throughout my time at Imperial College, for always caring about my welfare and interests, for always letting the door open for discussions—be they scientific or not, and most importantly, for making this journey an incredibly empowering and fulfilling experience.

Funding for this work was provided by Innovate UK (Technology Strategy Board) and Airbus as part of the ALFET project (reference number 113022), and I would like to thank Stephen Rolston and Richard Ashworth from Airbus for their support and interest.

The computational work presented would not have been possible without access to Imperial College High Performance Computing Service, doi: 10.14469/hpc/2232, with a special mention to Simon Burbidge for his commitment and the quality of his technical support. The UK Turbulence Consortium (UKTC) is also gratefully acknowledged for providing two large resource allocations on the national supercomputing facility ARCHER under the EPSRC grant number EP/L000261/1.

Pierre Lanoisellé is acknowledged for his work related to the analysis presented in chapter 4.

I am thankful to Emile Touber and Nicolas Alferez for the numerous extended conversations we had over the beginning of my PhD, and for having always been welcomed to their group meetings. Many thanks also go to Lionel Agostini, Yongyun Hwang and Sylvain Laizet for helpful discussions.

I am indebted to Davide Gatti, Éric Lamballais, Paolo Luchini, Maurizio Quadrio and Pierre Ricco for interesting discussions during visits at Imperial College London and/or at conferences.

At various occasions, I was fortunate to benefit from enthralling conversations over the course of collaborations with Mihailo R. Jovanović and Armin Zare during their visit at Imperial College, as well as with Thomas Bewley and Shahrouz Alimohammadi. I would also like to thank Javier Jiménez

and Eusebio Valero for giving me the opportunity to take part in the third Multiflow summer school at Universidad Politécnica de Madrid, in collaboration with Jesús Garicano-Mena and Esteban Ferrer. It was a wonderful experience where I immensely appreciated the sometimes philosophical discussions with Ricardo García-Mayoral, Petros Ioannou and Peter J. Schmid. A special mention goes to the nights at 'El Chapandaz' and to all the participants of the summer school, including Adrián, Akshath, Carlos, Davide, Garazi, Jane, Ricardo and Rodolfo, to name a few.

In addition to the scientific interest, the conferences that I have attended would not have been as enjoyable without the extraordinary people I have met. Particular thanks go to Nicolas Renard for our Italian adventures, Carlos Sanmiguel Vila, the KTH team, and Ricardo García-Mayoral and his students.

Back to the origin of this adventure are the team at Safran Aircraft Engines in Villaroche, Damien Biau, Paola Cinnella, Éric Ducasse, Jérôme Hoepffner, Tamas Regert, Jean-Christophe Robinet and Jeroen van Beeck who, by their enthusiasm and excellent teaching/supervision, nurtured my desire to pursue a PhD.

Ultimately, the uniqueness of this experience was permitted by the priceless time spent with outstanding fellow PhD students. I will always cherish the countless memories of lunches and dinners together, the foosball matches, the barbecues, the cooking, the jamming, the operas, the salsa, the Japanese karaoke, the birthday surprises, the occasionally hazardous squash sessions, the tennis, the bouldering, the football, the house crawls, and all the good times we have had around the world. A special mention goes to Imperial College Lawn Tennis Club and to the following Imperial students/affiliated (including homonyms): Adam, Alejo, Alfonso, Andrea, André, Anna, Audrey, Chi, 'Coma', Dolo, Dom, Elinor, Felipe, Francesco, Giorgio, Giovanni, Hannes, Ifan, James, Jérémy, Jingjing, Jorge, Laurent, Lorenza, Marc, Marco, Marius, Nathan, Niki, Paige, Patrick, Raph, Ricardo, Richard, Rikka, Rob, Ruben, Salvatore, Selim, Simon, Sylvain, Tai, Tatsuya, Vasilis, Yoshi, Yacine, and all those I am bound to have regrettably forgotten in this list.

Beyond academic life, I would like to thank the community of Chelsea A. S. for their kind and warm welcome, as well as all the French alumni (FGEUK) and in particular the group of Arts et Métiers Grande-Bretagne and Karine. Special mentions include 'The Crying Carrot', the Galettes des Rois organised by Mathilde, many sport sessions and pints with Gabriel, and conferences/events with Laurent P. and Geordy. I will also miss my Spanish 'Iberdrolan' family, all the badminton, squash, and running with Lorena, Estefanía's tortilla, Ramón, and all the good times with Adri, Claira, Juanjo,

Koco, Lara, Maria, Noel, Sylvain, and everyone else in the group.

The path of my life has been strewn with incredible encounters, and I would like to warmly thank Laurent Debenedetti and his family for their support, benevolence, and for endless fascinating discussions.

Finally, I would like to wholeheartedly thank my family for their unconditional love and encouragement.

Declaration of originality

I hereby confirm that I am the sole author of the present work unless otherwise acknowledged and that all the work presented was undertaken over the course of my PhD at Imperial College London.

No portion of this work has been submitted in support of an application for another degree or qualification. Parts of this work have been presented at several international conferences; in particular, parts of chapter 4 are related to the content published in Ghebali et al. (2017b). Moreover, some parts of this thesis were published in Ghebali et al. (2017a) and Ghebali et al. (2017c), or will appear in the ERCOFTAC Series *Direct and Large-Eddy Simulation XI* under the title 'Turbulent-drag reduction by oblique wavy wall undulations'.

Contents

Abstract 7

Acknowledgements 9

Declaration of originality 13

List of tables 19

List of figures 21

Nomenclature 27

1 Introduction 33

1.1 Friction drag reduction – rationale and principal methodologies 33

1.2 Present research in the context of the subject 35

1.3 Literature review specific to the research 37

1.4 Research objectives 42

1.5 Outline of the thesis 43

2 Numerical framework 45

2.1 DNS code 45

2.2 Mesh generation 50

2.2.1 Plane channel 50

2.2.2 Wavy channel 51

2.3 Control of flow rate 52

2.4 Skewed-flow implementation . . . 54
2.4.1 Orientation of the wavy wall . . . 54
2.4.2 Oblique forcing of the flow . . . 56
2.5 Statistical averaging . . . 56
2.5.1 Pre-processing . . . 56
2.5.2 Post-processing . . . 58
2.6 Drag contributions and friction velocity . . . 59
2.6.1 Drag contributions . . . 59
2.6.2 Friction velocity . . . 64
2.7 Uncertainty quantification . . . 64
2.7.1 Spatial discretisation . . . 64
2.7.2 Finite number of statistical samples . . . 65
2.7.3 Quantification of the drag-reduction time-averaging error . . . 66

3 Verification and validation 67

3.1 Method of Manufactured Solutions . . . 68
3.1.1 Introduction . . . 68
3.1.2 Methodology . . . 69
3.1.3 Application 1 – Plane channel . . . 73
3.1.4 Application 2 – Wavy channel . . . 76
3.2 Taylor–Green vortex . . . 79
3.2.1 Problem definition . . . 80
3.2.2 Results . . . 81
3.3 Fully turbulent flows . . . 82
3.3.1 Turbulent plane channel at $Re_\tau \approx 180$ . . . 82
3.3.2 Channel-bump DNS . . . 87
3.3.3 In-plane wall motions . . . 93
3.4 Momentum compatibility condition . . . 94
3.5 Conclusions . . . 96

4 Semi-empirical modelling 97

4.1 Summary of Chernyshenko (2013) . . . 98

4.2 Linearised channel flow incorporating an eddy viscosity 100
4.2.1 Derivation of the linear model 100
4.2.2 Validation with DNS (laminar flow) 103
4.2.3 Comparison with DNS (turbulent flow) 106
4.3 Semi-empirical model for the drag contributions 107
4.3.1 Introduction 107
4.3.2 Model 1: changes in dissipation 111
4.3.3 Model 2: pressure and friction drag 115
4.4 Conclusions 122

5 Numerical simulations **125**

5.1 Overall strategy 125
5.2 Numerical set-up 126
5.2.1 Grid properties 126
5.2.2 Flow configurations 127
5.3 Overall physical characteristics 129
5.3.1 General description of the flow 129
5.3.2 Secondary flow 132
5.3.3 Influence of the upper wall 136
5.4 Drag behaviour and grid convergence 138
5.4.1 Net drag reduction and grid convergence 138
5.4.2 Friction-drag reduction and pressure-drag increase 142
5.4.3 Influence of the spanwise wavelength 143
5.5 Turbulence characteristics 148
5.5.1 Overview 148
5.5.2 PDFs of the velocity fluctuations 148
5.5.3 Anisotropy of the turbulence field 154
5.5.4 Energy budgets 156
5.6 Conclusions 159

6 Wavy walls and Stokes layers **161**

6.1 General observations 162

6.1.1 Transverse shear strain 162

6.1.2 Near-wall streaks 164

6.1.3 Streamwise velocity and Reynolds stresses 165

6.2 Focus on simulation G6W1A2 167

6.2.1 Transverse shear strain 167

6.2.2 Friction reduction 167

6.2.3 Streamwise velocity and Reynolds stress 168

6.2.4 Turbulence-energy budgets 169

6.2.5 Detrimental effects of the wavy wall 172

6.2.6 Effect of the streamwise forcing 175

6.3 Reynolds-number effect 176

6.4 Conclusions 180

7 Conclusions and outlook **183**

Bibliography **187**

List of tables

3.1 List of simulations performed and error in the peak of enstrophy relative to the spectral solution ($\varepsilon_{\mathcal{E}}$). 81

3.2 Turbulent plane-channel-flow simulations at $Re_\tau \approx 180$. 85

3.3 Turbulent plane-channel-flow simulations with in-plane wall forcing at $Re_\tau \approx 200$, with $A^+ = 6$ and $\lambda_x^+ \approx 1250$ in the baseline wall units. 94

5.1 Properties of the grid configurations on which almost all the simulations presented are based. 128

5.2 Flow configurations simulated. 130

5.3 Drag coefficients at both upper and lower walls, comparing a wavy–wavy channel (G2W1) to its wavy–flat counterpart (G2W1f). 137

5.4 Grid refinement study for wavy calculations, all at $\theta = 70°$. The coarsest grid is G2, and the finest is G6. Abbreviations are consistent with those of table 5.2. 139

5.5 Flow configurations extracted from table 5.2, all for $\lambda_x^+ \approx 2700$, and symbols used in figures 5.14 to 5.16. 144

6.1 Flow configurations for friction Reynolds numbers ranging from 180 to 1000. 176

List of figures

1.1 Schematic of the spanwise wall oscillations giving rise to the TSL. 38
1.2 Schematic of the steady in-plane wall motions giving rise to the SSL. 39
1.3 Emulation of the in-plane wall motions with a wavy wall. 42

2.1 Definition of the grid nodes and centroids for the collocated storage of the solution variables. 47
2.2 Multi-block domain decomposition and halo-data exchanges on a 2D model problem divided into four blocks numbered from 0 to 3, with periodic boundary conditions in the horizontal direction, and a wall at each vertical end. 49
2.3 Strong scaling on CX2-Helen and ARCHER. 50
2.4 Sketch of the generic plane-channel-flow configuration. 51
2.5 Generation of a wavy-channel mesh from a plane-channel mesh. 52
2.6 Adjustment of the bulk velocity versus number of time-steps for an initial field not satisfying the bulk-velocity condition. 54
2.7 Flow domain of wavy-wall channel: the wavy wall is tilted so that the computational z-direction is homogeneous. 55
2.8 Sketch of the configuration of the skewed-flow DNS, with flow-oriented coordinates $\check{x}$ and $\check{z}$, relative to domain coordinates x and z. 55
2.9 Time-evolution of the error in the bulk velocity $1 - \check{U}_b = 1 - \|\boldsymbol{U_b}\|$. 57
2.10 Alternative decompositions of the mean fields for the spanwise velocity $\overline{w}$. 59
2.11 Local tangential and wall-normal coordinate system for the integration of the frictional drag along a z-homogeneous wave. 61

3.1 Isosurfaces of the velocity components and pressure from the analytical expression of the manufactured solution equations (3.5) and (3.6). 74
3.2 Norms of the error for various levels of refinement (plane channel case). 75
3.3 Computational domain for the wavy-channel application on a multi-block partition comprising 8 blocks, shown for a coarse mesh with $N = 16$. 76
3.4 Isosurfaces of the resulting velocity components and pressure from the analytical expression of the manufactured solution derived from equations (3.9), (3.11) and (3.12). . 78
3.5 L^2- and L^∞-norms of the error for various levels of refinement (wavy-channel case). . . 79
3.6 Isocontours of the instantaneous z-vorticity coloured by vorticity magnitude at various time instants for the coarsest and finest 2nd-order simulations. 83
3.7 Temporal evolution of the kinetic energy compared to the spectral solution on a 512^3 grid. 84
3.8 Temporal evolution of the dissipation rate computed from the decay of $\mathcal{K}$. 84
3.9 Temporal evolution of the enstrophy computed explicitly from the velocity field. 84
3.10 Comparison of the wall-scaled streamwise velocity and Reynolds stresses of the simulations presented in table 3.2 with the spectral DNS of Moser et al. (1999), consisting of a plane-channel flow at $Re_\tau \approx 180$. 86
3.11 Contributions to the turbulence-energy budgets in wall units. Same legend as in figure 3.10. 87
3.12 Sketch of the reference simulation domain, comprising four waves, adapted from Maaß and Schumann (1996), with different notations consistent with the simulations presented herein. 88
3.13 Velocity profiles at various phase locations normalized by U_b. 89
3.14 Normal Reynolds stresses normalized by U_b^2 at various phase locations. 90
3.15 Reynolds shear stress $\overline{u'v'}$ normalized by U_b^2 at various phase locations. 91
3.16 Velocity gradient $\partial\overline{u}/\partial y$ normalised by U_b/h at various phase locations. 91
3.17 Pressure gradient $\partial\overline{p}/\partial y$ normalised by U_b^2/h at various phase locations. 92
3.18 Gradient of the variance of the pressure fluctuations $\partial\overline{p'^2}/\partial y$ normalised by U_b^4/h at various phase locations. 92
3.19 Comparison of the spanwise profiles with the results of Viotti et al. (2009a). 94
3.20 Verification of the compatibility condition (3.23) at the cells closest to the walls. 95

4.1 Sketch of the configuration for the linear analysis. 101

4.2 Comparison of the modelled base flow with DNS, the coefficients for the eddy viscosity are $c_1 = 29$ and $c_2 = 0.46$. 104
4.3 Validation of the linear solver for a laminar channel with both walls wavy. 105
4.4 Same as figure 4.3 but for a larger amplitude $\alpha = 0.1$. 106
4.5 Validation of the linear solver for a laminar channel. The lower wall is wavy, whereas the upper wall is flat. 107
4.6 Comparison between the linear solution and DNS for $A_w = 0.05h$, $\theta = 70°$, and $\lambda^+ \approx 920$, at $Re_\tau \approx 360$. 108
4.7 Comparison of the linear solution with DNS for the same configuration as figure 4.6. . 109
4.8 Comparison of the transverse shear-strain for the same configuration as figure 4.6. . . . 110
4.9 Power saved as a function of the wavelength and forcing amplitude. 113
4.10 Power required for SSL as a function of the wavelength and forcing amplitude. 113
4.11 Ratio r for fixed λ_x and varying wave angle θ. 115
4.12 **(a)** Prediction of the drag reduction from the semi-empirical model 1 at $Re_\tau = 200$, **(b)** minimum ratio r for fixed λ_x (dashed line, left axis) and corresponding flow angle θ_{opt} (continuous line, right axis). 116
4.13 Friction-drag reduction obtained in a SSL as a function of the streamwise actuation wavelength λ_x^+, for a forcing amplitude of $A^+_{\text{SSL}} = 1$, at $Re_\tau \approx 200$. 117
4.14 Level of pressure drag relative to the baseline drag for a wave at an angle $\theta = 70°$, at $Re_\tau \approx 360$. 119
4.15 Contours of α_{eq} (similar to A_w/h) corresponding to $A^+_{\text{SSL}} = 1$, obtained by minimising the L^2-norm-distance between the transverse shear-strains of the wavy wall and the SSL, defined in equation (4.32). 121
4.16 Minimum distance l_{min} between the transverse shear-strains of the wavy wall and the SSL. 121
4.17 Prediction of the total drag reduction for Model 2, as a function of the wavelength λ^+ and angle of the wave θ. 122

5.1 Sketch of the geometrical configurations: **(a)** wavy–wavy channel and **(b)** wavy–flat channel. 127
5.2 Ratios between grid spacings and the Kolmogorov length scale across the wall-normal direction for a plane channel, and for the grid configuration G6. 128

5.3 Phase variations of the velocity and pressure fields for G6W1A2 ($A_w^+ = 18$, $\theta = 70°$ and $\lambda^+ = 918$, cf. table 5.2), normalised with the actual friction velocity. Contour levels are equispaced, symmetric around zero, and the range of the scale on each plot corresponds to that of the data shown. Solid lines correspond to positive levels, whereas dashed lines correspond to negative levels. The quantity shown is labelled in the grey area corresponding to the wave shape. 132

5.4 Reynolds stresses normalised by the mean friction velocity u_τ^2 for G6W1A2. Same legend as figure 5.3. 133

5.5 Phase-wise variation of the wall friction. 134

5.6 Phase-wise variation of the total-drag stress at the wall (upper curves) and contribution from the pressure-drag stress (lower curves). 134

5.7 Mean streaming motion $W(y)$ for increasing wave slopes. 135

5.8 Contributions to the maximum (under the L^∞-norm) spanwise velocity: dependence of the maxima of the phase-integrated ($W_{\max}^+$), and phase-varying ($\widetilde{w}_{\max}^+$) spanwise velocities upon the wave slope $2A_w/\lambda$. 136

5.9 Comparison of the spanwise velocity for the wavy–wavy (G2W1) and wavy–flat (G2W1f) cases. 137

5.10 Total-drag reduction for $A_w^+ = 18$, $\theta = 70°$, and $\lambda^+ = 918$, for grids G2, G3, G6, and G7. 141

5.11 Comparison of the streamwise velocity and Reynolds stresses for the flow configuration ($A_w^+ = 18$, $\theta = 70°$, $\lambda^+ = 918$). 142

5.12 Comparison of the transverse-strain profiles for the flow configuration ($A_w^+ = 18$, $\theta = 70°$, $\lambda^+ = 918$). 143

5.13 Levels of friction-drag reduction (FDR) and pressure-drag increase (PD) relative to the baseline. 144

5.14 Reduction in skin-friction drag relative to the baseline drag level versus wave slope or projected slope. 145

5.15 Pressure-drag penalty relative to the baseline drag level. Same legend as figure 5.14. . 145

5.16 Net drag reduction relative to the baseline drag level. Same legend as figure 5.14. . . . 145

5.17 Reduction in skin-friction drag relative to the baseline drag level versus maximum spanwise velocity $\overline{w}_{\max}^+$ or maximum phase-varying velocity $\widetilde{w}_{\max}^+$, expressed in actual wall units. 146

5.18 Pressure-drag penalty relative to the baseline drag level. Same legend as figure 5.17. . 146
5.19 Net drag reduction relative to the baseline drag level. Same legend as figure 5.17. . . . 146
5.20 Joint PDFs at $y^+ \approx 14$ of the velocity fluctuations for G6W1A2 and the baseline. . . . 150
5.21 Joint u'–v' PDFs at fixed phase locations. Same legend as figure 5.20. 151
5.22 Joint v'–w' PDFs at fixed phase locations. Same legend as figure 5.20. 152
5.23 Joint w'–v' PDFs at fixed phase locations. Same legend as figure 5.20. 153
5.24 Lumley triangle for the baseline G6P1 (black dash-dotted lines), G6W1A2 (blue solid line) and G6W1A4 (red dashed line). 155
5.25 Lumley triangle at various phase locations. Same legend as figure 5.24. 155
5.26 Phase-integrated contributions to the turbulence-energy budgets in outer units as a function of the wall-normal coordinate multiplied by the *baseline* friction Reynolds number Re_τ^0. 157
5.27 Phase-integrated contributions to the turbulence-energy budgets in wall units, calculated with the actual friction velocity. 158

6.1 Total shear strain $(\partial\overline{w}^+/\partial y^+ + \partial\overline{v}^+/\partial z^+)/2$ (black line) and contribution of $(\partial\overline{w}^+/\partial y^+)/2$ (blue dashed line) for G6W1A2. 162
6.2 Comparison of $\partial\overline{w}^+/\partial y^+$ scaled by the streamwise-projected wave slope A_w/λ_x for various flow configurations. 163
6.3 Turbulent fluctuations of the streamwise velocity u'^+ for G6W1A4 ($A_w^+ = 32$, $\theta = 70°$, $\lambda^+ = 918$), normalised by the local mean friction velocity at the particular phase location $\sqrt{\nu(\partial\overline{u}/\partial y)|_w}$ in a wavy horizontal slice located at constant y/h, around $y^+ \approx 10$. 164
6.4 Comparison of **(a)** the mean streamwise velocity $U^+ = \langle\overline{u}\rangle_{x,z}/u_\tau$ and **(b)** Reynolds stresses $\langle\overline{u_i'u_j'}\rangle_{x,z}/u_\tau^2$ for wavy walls with wave slopes of $2A_w/\lambda \in \{0.05, 0.07\}$ (corresponding to labels *A3 and *A4) and wavelengths of $\lambda^+ \in \{612, 918\}$ (corresponding to labels *W2* and *W1*), and the baseline plane channel (G6P1) (scaled using the actual friction velocity). 166
6.5 Comparison of the transverse strain non-dimensionalised by the actual friction velocity, for the SSL (green dashed lines) and the wavy-wall flow configuration G6W1A2 ($A_w^+ = 18$, $\theta = 70°$ and $\lambda_x^+ = 2684$; blue solid lines). The SSL flow is for a wavelength of $\lambda_x^+ = 2679$ and forcing amplitude $A_{\mathrm{SSL}}^+ = 1.23$ based on the unactuated friction velocity. 168

6.6 Black dash-dotted line: baseline flow G6P1; green dashed line: SSL; blue solid line: wavy wall G6W1A2. Wall units are calculated with the actual friction velocity. **(a)** Log-law region of the streamwise velocity profile, **(b)** phase-integrated Reynolds stresses. . 169

6.7 Phase-integrated contributions to the turbulence-energy budgets in outer units as a function of the wall-normal coordinate multiplied by the *baseline* friction Reynolds number Re_τ^0. 170

6.8 Phase-integrated contributions to the turbulence-energy budgets in wall units, calculated with the actual friction velocity. 171

6.9 Phase-wise variation of the turbulent skin friction. 173

6.10 Change in the production $\widehat{\Pi}_k$ and dissipation $\widehat{\epsilon}_k$ from the baseline for G6W1A2 ($A_w^+ = 18$, $\theta = 70°$, $\lambda^+ = 918$). 174

6.11 Change in the streamwise Reynolds-stress component with respect to the baseline. Contours of $\widehat{u'^2}/u_{\tau,0}^2$ for G6W1A2 ($A_w^+ = 18$, $\theta = 70°$, $\lambda^+ = 918$). 175

6.12 Profiles of the phase-varying longitudinal and transverse shear strains in actual wall units. 177

6.13 Change in the streamwise energy relative to the baseline value $\widehat{u'^2}/U_b^2$. 178

6.14 Comparison of the streamwise velocity profiles and Reynolds stresses with the baseline at $Re_\tau \approx 1000$ for the flow configuration G5W1 ($A_w^+ = 20$, $\theta = 70°$, $\lambda^+ = 900$). 179

6.15 Comparison of the shear strain $\partial\overline{w}^+/\partial y^+$ for the same configuration at various Reynolds numbers. $A_w^+ \approx 20$, $\lambda^+ \approx 900$, $\theta = 70°$ (cf. table 6.1). 180

Nomenclature

The Einstein summation convention is adopted so that repeated indices imply summation over the three spatial directions.

Roman

A	Amplitude
Ai	Airy function of the first kind
b	Traceless anisotropy tensor
c_1, c_2	Parameters defining the eddy-viscosity profile
C_f	Friction coefficient
$D_\star$	Drag coefficient associated with the contribution of $\star$
D_k	Viscous diffusion
$\boldsymbol{e}_{x_i}$	Unit vector associated with the x_i-direction
$\mathcal{E}$	Enstrophy
$\boldsymbol{f}$	Momentum body force
F	Force
h	Channel half-height
H	Total height of the channel
h_w	Wall shape
$\Im$	Imaginary part
II	Second invariant of the anisotropy tensor
III	Third invariant of the anisotropy tensor

k	Wave number *or* order of accuracy *or* turbulence energy
$\mathcal{K}$	Kinetic energy
l	L^2-norm distance
L_{x_i}	Size of the computational domain in the x_i-direction
N_{x_i}	Number of cells in the x_i-direction
$\boldsymbol{n}$ *or* $\boldsymbol{n_w}$	Wall-normal unit vector
p	Pressure
P	Pressure *or* power
$\mathcal{P}_k$	Turbulence production
P_{x_i}	Driving pressure gradient in the x_i-direction
Q, q	Generic quantity
r	Penalising factor in section 4.3.3
$\mathfrak{R}$	Real part
Re	Reynolds number
$\boldsymbol{S}$	Source term (for the MMS)
$\mathcal{S}$	Surface
t	Time instant
T	Time period
T_k	Turbulent diffusion
$\boldsymbol{t_w}$	Wall-tangential unit vector
u, v, w	Velocity components
$\mathcal{V}$	Volume
x, y, z	Spatial coordinates

Greek

α	Amplitude of the shape perturbation in the linear analysis
α, β	Grid-stretching parameters
δ	Kronecker delta
Δ	Cell distance or time-step duration
ϵ	Dissipation

ϵ_k	Turbulence dissipation
ϵ_P	Mass-residual threshold for the convergence of the pressure solver
ε	Error measure
ξ, η, ζ	Transformed coordinates
η	Kolmogorov length scale
θ	Angle of the wave relative to the flow
θ_f	Angle of the flow relative to the mesh
κ *or* λ	Spatial wavelength
λ_{x_i}	Spatial wavelength projected onto the x_i-direction
μ	Dynamic viscosity of the fluid
ν	Kinematic viscosity of the fluid
ν_t	Turbulent viscosity normalised by ν
ξ, η, ζ	Transformed coordinates
Π_k	Pressure diffusion
ρ	Fluid density
σ	Standard deviation of the time-averaging error
$\sigma_1, \ldots, \sigma_7$	Time-advancement coefficients of the Gear-like scheme
τ	Wall stress
τ_l, τ_u	Phase shifts relative to a sinusoidal wave, at the lower and upper walls respectively
Φ_k	Pressure strain
ψ	Stream function
ω	Vorticity *or* angular frequency

Abbreviations

ADI	Alternate Direction Implicit
B.C.	Boundary Condition
CFR	Constant Flow Rate
CPG	Constant Pressure Gradient
DNS	Direct Numerical Simulation
DR	Drag Reduction

FDR	Friction-Drag Reduction
GSL	Generalised Stokes Layer
HPC	High-Performance Computing
LES	Large-Eddy Simulation
MMS	Method of Manufactured Solutions
MPI	Message Passing Interface
NS	Navier–Stokes
PD	Pressure Drag
PDF	Probability Density Function
RANS	Reynolds-Averaged Navier–Stokes
SLOR	Successive Line Over Relaxation
SSL	Spatial Stokes Layer
TDR	Total-Drag Reduction
TSL	Temporal Stokes Layer
WW	Wavy Wall

Subscripts

0	Initial condition *or* pertaining to the baseline case
b	Bulk
f	Flow *or* friction
lw	Lower wall
m	Manufactured
net	Net
p	Pressure
req	Required
sav	Saved
sh	Shear
t *or* tot.	Total
th.	Theoretical
uw	Upper wall

w	Wall
ww	Pertaining to the wavy-wall case

Superscripts

$*$	Intermediate velocity field in the fractional step
$+$	Expressed in wall units
0	Initial condition *or* pertaining to the baseline case
n	Time-step number n
ww	Pertaining to the wavy-wall case

Other notation

$\langle\cdot\rangle_\star$	Averaged with respect to $\star$
$\widetilde{(\cdot)}$	Phase-varying field
$\widehat{(\cdot)}$	Change from the baseline case
$\overline{(\cdot)}$	Time average
$\check{(\cdot)}$	Expressed in the flow-aligned coordinates
$(\cdot)'$	Turbulent fluctuation *or* derivative (when function of a single variable)
$\|\| \cdot \|\|$	Norm

Chapter 1

Introduction

Contents

1.1 Friction drag reduction – rationale and principal methodologies 33
1.2 Present research in the context of the subject 35
1.3 Literature review specific to the research 37
1.4 Research objectives 42
1.5 Outline of the thesis 43

1.1 Friction drag reduction – rationale and principal methodologies

Transportation systems, requiring the displacement either of objects in a fluid or of the fluid itself (e.g. oil pipelines), are ubiquitous and necessitate large expenditures of energy. As is the case in the aeronautical industry, the energy used to this end is generated from fossil-fuels, which causes the emission of harmful gases that are released into the atmosphere. In particular, CO_2 emissions are known to enhance the greenhouse effect and to contribute to global warming. In this context, improvements in fuel-efficiency result directly in reductions in costs and greenhouse-related emissions. In order to improve fuel-efficiency, one way is to reduce the turbulent friction drag on surfaces, friction drag representing a large proportion of the overall aerodynamic drag in cruise-speed conditions. The present research is intended to contribute to this aim via passive flow control (cf. Gad-el Hak (2000) for an extensive review on flow-control methods).

Turbulent-drag reduction can be achieved by applying some form of control to the turbulent flow that results in a reduction in the energy being dissipated by the turbulence activity, which in turn results in a reduction in drag. In order to focus on fundamental turbulence processes and their manipulation, the

general problem is simplified to that of a canonical flow consisting of a fully developed plane-channel flow, i.e. a flow confined between two infinite plates separated by a constant distance H. The turbulent flow can be manipulated by various means: the surface geometry may be changed, some polymer chains may be inserted into the flow, or some jets/actuators/electromagnetic fields may be used to modify the flow properties. All these strategies fall into either one of two categories: passive and active control. In the former, the control device does not require any power input, and the net energy gain corresponds directly to the reduction in drag. In the latter, the control strategy involves an external source of energy—e.g. to power an actuator; in this case, a reduction in drag is not equivalent to a net energy gain. In fact, in adverse circumstances, the power required by the actuator may be greater than the power saved by the drag reduction.

In principle, active mechanisms allow for larger effects on the flow than passive control, but are much more complex to implement, in addition to which the efficiency of the mechanical-energy conversion also comes into play. Active control methods may rely upon sensors located in the flow, or simply operate in an open-loop manner. An example of such methods is opposition control via blowing and suction (Kim, 2011; Choi et al., 1994; Lee and Kim, 1997). At any time instant, the blowing/suction at the wall opposes the wall-normal motion detected in a plane parallel to the wall located at $y = y_d$, resulting in a wall-normal velocity $v(x,0,z,t) = -A\,v(x,y_d,z,t)$, where A is the control amplitude. The influence on the flow properties of the amplitude and the location of the detection plane was studied numerically by Chung and Talha (2011) who showed that significant drag reduction could be achieved.

In order to have the greatest reduction of turbulence, control strategies have built upon the fundamental understanding of the physical mechanisms underpinning the increased turbulent friction level relative to the laminar state (Lumley and Blossey, 1998; Kim, 2011), which was shown to be the theoretical energy-saving limit by Bewley (2009). Recent experiments by Kühnen et al. (2018) in pipe flows—which, unlike channel flows, are linearly stable for all Reynolds numbers—for Reynolds numbers ranging from 3000 to 100,000, indicated that complete suppression of turbulence was achievable by initially intensifying the turbulence level, thereby obtaining net energy savings of 31%, with *all* actuation losses taken into account.

Conversely, passive devices, in the form of a change in the surface geometry, are simpler to implement but suffer from maintenance and manufacturing constraints. For practical applications, other constraints may also be posed, such as the acoustic and visual perception of the device by the passengers, or the ability for the aircraft manufacturer to display painted information on the fuselage.

1.2 Present research in the context of the subject

The existence of non-smooth surfaces, *riblets*, that experience lower drag levels than their flat counterpart was first demonstrated by Walsh and Weinstein in 1979. The riblets consist of longitudinal ribs, and their effectiveness (up to about 10% drag reduction) was confirmed by numerous studies, including numerical simulations (Choi et al., 1993), experiments on canonical flows (Bechert et al., 1992, 1997), and flight tests (Szodruch, 1991; Abrams and Hanratty, 1984). From a Darwinian perspective, Bechert et al. (1985) and Bechert and Bartenwerfer (1989) argued that the riblets resembled the placoid scales observed on the skin of specific species, among fast-swimming sharks. Wen et al. (2014) obtained a drag-reduction level of 8.7% with 3D-printed synthetic shark skin made from a pattern of a 3D-scanned denticle taken from a male shortfin mako shark. However, the effectiveness of such synthetic shark skins was questioned by Boomsma and Sotiropoulos (2016) whose direct numerical simulations rather indicated an increase in drag for the synthetic denticle patterns.

The riblet performance depends upon multiple factors, including the height and spacing of the ribs, as well as the shape of the cross-section of the ribs. All these parameters can be optimised to maximise the drag-reduction rate, but this maximum appears to lie around the 10% mark (Bechert et al., 1997). As the size of the riblets is increased, the emergence of spanwise rollers, observed in simulations by García-Mayoral and Jiménez (2011a,b) and shown to scale in wall units with Reynolds number (García-Mayoral and Jiménez, 2012), degrades the drag-reduction performance, and the riblets enter a k-roughness regime for large spacings.

Practical applications of drag-reducing riblets have been attempted, e.g. with plastic films developed by the 3M Company (McLean et al., 1987; Viswanath, 2002), but due to constraints posed by manufacturing and maintenance, current technologies have not yet been successful at making riblets practical.

In addition to sharks, some birds are known to have high flying efficiencies (i.e. they require a low metabolic power input for flight). A close examination of bird feathers led Chen et al. (2014) to consider riblets that are skewed with respect to the main flow direction, arranged in an alternating pattern. Various herringbone patterns were investigated by Chen et al. (2014) for a range of riblet angle and a maximum drag-reduction rate of 21% was reported for an angle of 60°, which corresponds to alternating flow-to-rib angles of ±30°. However, this performance cannot be explained by the skewness of the grooves, as riblets' performance was shown to decrease when misaligned with respect to the flow direction: for misalignments of about 30°, even no drag reduction is observed (García-Mayoral and Jiménez, 2011a; Bannier, 2016), and in some cases there is an increase in drag (a drag increase of

3.7% was reported in Benschop and Breugem (2017) for a misalignment of 20°). Chen et al. (2014) suggested that the drag reduction observed originated from the generation of spanwise vortices via a reduction of the bursting events, but the broad parametric DNS exploration of Benschop and Breugem (2017) contradicted their results. In Benschop and Breugem (2017), it was shown, for a wide range of flow configurations studied by DNS, that the herringbone riblets had an adverse effect on turbulence. The maximum drag reduction observed was of about 2% but most cases featured a drag increase. Thus, the experimental results of Chen et al. (2014) remain to be reproduced, and there is a strong body of evidence that herringbone riblets are significantly outperformed by conventional straight riblets. As to the question of the origin of birds' aerodynamic prowesses, other mechanisms may be more influential—e.g. in the delay of the transition to turbulence (Lentink and de Kat, 2014).

Other bio-inspired configurations were considered for drag reduction (Bushnell and Moore, 1991), and other marine animals with high swimming efficiencies were investigated. The release of slime by some species was compared in Bushnell and Moore (1991) to the action of elongated polymers, known to dramatically reduce the turbulent drag (Virk, 1975). Furthermore, the swimming efficiency of dolphins was also closely examined. In 1936, Gray estimated the drag acting on a swimming dolphin and compared it to the energy that the dolphin's muscles were able to generate. Gray (1936) observed that the estimated drag was considerably larger than the work the dolphin's muscles could produce, which prompted Gray to postulate that dolphins were equipped with some physical characteristics able to reduce drag. This observation became known as 'Gray's paradox', and many researchers attempted to identify the mechanisms by which dolphins may be able to reduce drag. One attempt to resolve this paradox followed the observation of oblique skin undulations on the skin of a swimming dolphin: Fujii et al. (2011) performed numerical simulations of an oblique wavy wall, seeking to show that the solid undulations would result in a significant drag reduction. However, the results were negative, and only drag increase was observed. Other attempts to solve Gray's paradox included the study of compliant surfaces for turbulent drag reduction, but Gad-el-Hak (2002) argued that, as far as the compliance of the dolphin skin was concerned, a delay in the transition to turbulence was a more plausible explanation.

Compliant surfaces aside, wherein the skin would simply comply with the flow stresses, several active mechanisms were considered, such as travelling wavy undulations generated by the muscles beneath the skin of swimming bodies. Shen et al. (2003) showed by DNS that net gains were achievable in the case of a wavy wall travelling at a constant speed in the streamwise direction, and an experimental confirmation of the drag reduction was undertaken at high Reynolds number by Yao et al. (2010).

While modelling efforts targeting the turbulent flow past a moving boundary had already been undertaken decades before (McLean, 1983; Sengupta and Lekoudis, 1984), progress in computing power brought new insights and allowed for a more accurate estimation of the drag level. In a turbulent channel at low Reynolds number, Nakanishi et al. (2012) showed that the stabilising effect of the moving wavy boundary could even lead to a relaminarisation of the flow. Whilst most of the research on travelling wall undulations focused on deformations travelling in the streamwise direction, Tomiyama and Fukagata (2013) and Koh et al. (2015) showed that spanwise-moving surfaces could also reduce the drag level. An intermediate scenario that is particularly relevant to the present research is that of a rigid and moving oblique wavy surface, modelled by Lekoudis and Sengupta (1986), where it was indicated that the pressure force could produce thrust under specific actuation conditions.

The use of rigid wavy walls for drag-reduction purposes was also investigated at NASA in the 1980s. Cary et al. (1980) observed experimentally that a wavy wall with the crests and troughs perpendicular to the main flow direction could yield significant friction reductions. Some numerical models were developed at NASA Langley to optimise the geometry in order to minimise the overall drag (Cary et al., 1980; Balasubramanian, 1980; Balasubramanian and Orszag, 1981). It transpired that the pressure-drag increase was much larger than the friction reduction for sinusoidal waves perpendicular to the main flow direction, which encouraged research efforts on finding a non-sinusoidal shape that would reduce the pressure drag. It was shown in Lin et al. (1983) that this was indeed achievable with some asymmetric waves. Yet, the levels of drag reduction achieved remained only marginal, which led Wilkinson et al. (1988) to eventually report longitudinal and transverse wavinesses under the section title ‘Approaches which evidently do not work’.

The present research is concerned with the use of an oblique wavy wall as a passive device that would emulate the effect of imparting a velocity at the wall in order to control the flow. The rationale is that the solid wavy wall, positioned obliquely to the main flow direction, induces a spanwise motion that is absent from the cases reported in Wilkinson et al. (1988).

1.3 Literature review specific to the research

As mentioned above, active techniques are, from a practical standpoint, more difficult to implement than passive techniques, but they often allow for more sophisticated control strategies, which yield greater effects. Despite the practical limitations, the study of active control methods brings insight into

the mechanisms by which turbulence can be reduced, and the greater effects entailed facilitate such an understanding. It was observed by Jung et al. (1992) that transverse wall oscillations, numerically imposed as a wall boundary condition of the form $w_w = A_{\mathrm{TSL}} \sin\left(\frac{2\pi}{T}t\right)$, as shown in figure 1.1, could yield up to about 40% drag reduction for an actuation period of $T^+ = T\,u_\tau^2/\nu = 100$, where u_τ is the friction velocity $u_\tau = \sqrt{\nu \left.\frac{\mathrm{d}U}{\mathrm{d}y}\right|_w}$. There exist numerous computational and experimental confirmations of this result, in channels (Baron and Quadrio, 1996; Quadrio and Ricco, 2004; Touber and Leschziner, 2012; Choi et al., 1998), boundary layers (Ricco and Wu, 2004; Lardeau and Leschziner, 2013), and pipes (cf. Quadrio (2011) and Touber and Leschziner (2012) for reviews of the relevant literature). However, in the case of active control methods, the energy balance depends crucially on the energy expenditure required to actuate the system. In wall oscillations, the power input required corresponds to that necessary for the displacement of the wall. In numerical simulations, this can be quantified from the velocity field under the assumption of a perfect actuator. When the energy expenditure required to control the flow is taken into account, maximum net energy savings of 7.3% were reported in Quadrio and Ricco (2004) for a gross drag-reduction rate of about 17%. In order to improve the net energy savings, Vodop'yanov et al. (2013) considered an oscillating plate mounted with ribbed grooves, and their results indicated that the synergistic effect between the riblets and the wall oscillations could yield net energy savings up to about 13.6%. Moreover, non-sinusoidal temporal waveforms of the spanwise motion were investigated in Cimarelli et al. (2013), but none of the configurations tested surpassed the performance of the sinusoidal wave.

The purely temporal transverse wall motion can be augmented with a spatial dependence of the forcing, which gives rise to a travelling wave. Whilst the flow resulting from purely temporal oscillations is often referred to as 'temporal Stokes layer' (TSL), a forcing of the form $w_w = A_{\mathrm{GSL}} \sin(\kappa_x x - \omega t)$ was studied in Quadrio et al. (2009) and the associated flow was later named 'generalised Stokes layer'

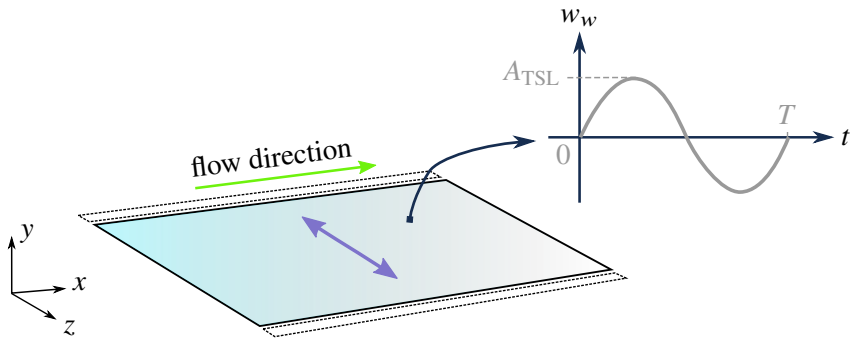


Figure 1.1: Schematic of the spanwise wall oscillations giving rise to the TSL.

(GSL) in Quadrio and Ricco (2010). This more general formulation of the forcing is more effective, both in terms of drag reduction and net energy gains, with net energy savings in excess of 26% (Quadrio et al., 2009) at a friction Reynolds number of $Re_\tau \approx 200$. Additional experimental confirmations of the drag reduction were undertaken in pipes (Auteri et al., 2010) and channels (Bird et al., 2015a,b). An intermediate scenario is the steady forcing examined in a plane channel by Viotti et al. (2009a) and in a boundary layer by Skote (2011). In this 'spatial Stokes layer' (SSL), the wall actuation is steady in time, but inhomogeneous in the streamwise direction: $w_w = A\sin(\kappa_x x) = A\sin\left(\frac{2\pi}{\lambda_x}x\right)$, as shown in figure 1.2. The SSL actuation, although more difficult to implement experimentally than the wall oscillations generating a TSL, yields maximum net energy savings that are greater than for the TSL (Viotti et al., 2009a).

The behaviour of the Stokes layer was mostly studied at relatively modest Reynolds numbers, due to computational and experimental limitations, and the behaviour at larger Reynolds numbers relevant to commercial-aviation applications remains unknown. However, DNS studies at moderate Reynolds numbers show that the drag-reduction performance degrades as the Reynolds number increases. This degradation is often attributed to the increasing influence of the large-scale structures onto which the control method has little effect (Hurst et al., 2014). In the case of the temporal wall oscillations, the results of Touber and Leschziner (2012) empirically indicated that the drag-reduction performance was declining, in optimal actuation conditions, approximately as $Re_\tau^{-0.2}$ based on simulations at friction Reynolds numbers in the range of $200 \leqslant Re_\tau \leqslant 1000$. Hurst et al. (2014) extended the results for the travelling wave in a broad range of actuation conditions up to $Re_\tau = 1600$. Hurst et al. (2014) not only showed that the optimal a control parameters depend on the Reynolds number, but also that the power decay of the drag-reduction rate depends on the actuation parameters. An alternative argument for the account of the Reynolds-number effect is that the drag reduction arises from a shift in the

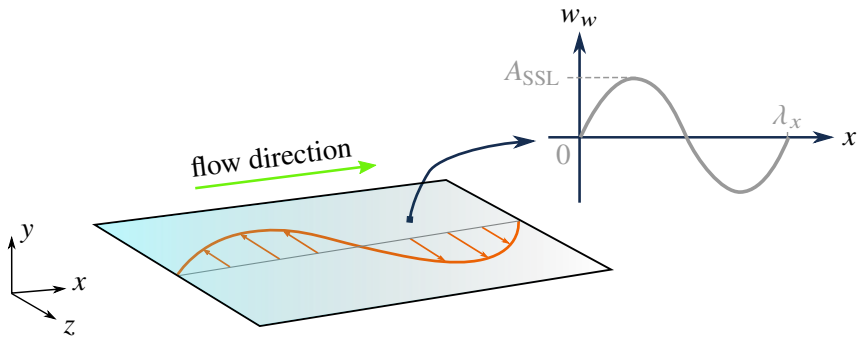


Figure 1.2: Schematic of the steady in-plane wall motions giving rise to the SSL.

universal log-law profile relative to the baseline and that this shift is Reynolds-number independent. This behaviour was supported for riblets in Luchini (1996) and tested for the travelling wave in Gatti and Quadrio (2016). The study of Gatti and Quadrio (2016), albeit for small domain sizes in most of the simulations, showed—consistently with Hurst et al. (2014)—that the exponent γ, in a power-law degradation of the drag-reduction margin of the form $Re_\tau^{-\gamma}$, was strongly dependent on the actuation parameters, whereas the shift in the log-law was approximately independent of the Reynolds number for $Re_\tau \geqslant 1000$, which allowed them to extrapolate the drag-reduction margins to flight Reynolds numbers. The resulting extrapolation yields a much more optimistic performance at large Reynolds numbers than the power-law relations inferred from low-Reynolds-number simulations (Touber and Leschziner, 2012; Hurst et al., 2014).

The wall oscillations, in optimal conditions, result in a strong suppression of near-wall turbulence. The mechanisms by which this is effected were studied in a pipe flow by Nikitin (2000) who suggested that the wall oscillations hamper the growth of longitudinal vortices. It was argued by Choi and Clayton (2001) that the main mechanism giving rise to the suppression of turbulence—and consequently to the drag reduction—was linked to the spanwise vorticity generated at the top of the viscous sublayer, which weakens the streamwise vortices and hence reduces the streamwise vorticity. In addition, Choi et al. (1998) experimentally observed a reorientation of the streamwise vortices with the wall oscillations. This was later confirmed by the DNS studies of Touber and Leschziner (2012) and it was shown that the near-wall velocity-streak orientation followed the shear-strain field, with the strong reduction in turbulence activity occurring during the reorientation phases. The effect of the Stokes strain on the turbulent flow was further examined for optimal and sub-optimal actuation in Agostini et al. (2014, 2015) and a significant hysteresis of the flow properties over the actuation cycle was identified. In addition, the underlying physical mechanisms pertaining to the behaviour of the oscillating flow were studied in light of the filtering properties of the linearised Navier–Stokes equations. The orientation of the near-wall streaks during the oscillation phases was successfully predicted in Blesbois et al. (2013) using a generalised-optimal-perturbation approach (Chernyshenko and Baig, 2005), and Duque-Daza et al. (2012) observed a correlation between the streak amplification calculated from the linearised Navier–Stokes equations and the drag-reduction rate calculated from DNS. Remarkably, quantitative predictions of the drag reduction were achieved by Moarref and Jovanović (2012) where the optimal actuation period was predicted using a model based on stochastically forced linearised Navier–Stokes equations.

From a practical perspective, the consequent net savings observed in DNS are of course unreachable. In effect, regardless of the maintenance and manufacturing aspects, some of the most energy-efficient actuator designs still require more energy input than the actual savings they yield (Gouder, 2011; Gatti et al., 2015). Nevertheless, the insight gained from the active wall-actuation technique may be exploited in the search of more practical devices designed to emulate the spanwise motion underpinning the friction reduction. Tay et al. (2015) and Van Nesselrooij et al. (2016) claimed drag reductions achieved by dimpled surfaces and proposed the spanwise forcing induced by the dimples as a major contributor to the drag reduction. Other methods were explored with the aim of improving the performance of riblets by inducing a spanwise motion. This gave rise to the consideration of sinusoidal riblets studied in Peet et al. (2008), Kramer et al. (2010) and Sasamori et al. (2014). Contrary to Peet et al. (2008) who reported improvements in the drag-reduction rate with the sinusoidal riblets, the results of Kramer et al. (2010), later supported by Bannier (2016), indicated that no significant gain could be achieved compared to conventional straight riblets.

Finally, Chernyshenko (2013) proposed to position a wavy wall obliquely relative to the flow direction in order to emulate a SSL. This approach is closely connected to the properties of the SSL and is based on the assumption that the friction-reduction capabilities of the SSL are exclusively linked to the transverse shear-strain rather than simply the forcing velocity. This is precisely what allows for a passive device, i.e. with the velocity vanishing at the wall by virtue of the no-slip condition, to potentially emulate the effect of in-plane wall motions, as illustrated in figure 1.3. Under specific assumptions regarding how this emulation could be achieved and translate in terms of energetic changes relative to the baseline, Chernyshenko (2013) showed, by means of linearised boundary layer equations, that drag-reduction levels of about 2% could be expected from a wavy wall at an angle of $\theta \approx 52^\circ$, with a streamwise wavelength $\lambda_x^+ \approx 1500$, so that it would emulate the effect of a SSL with a maximum wall velocity of $A_{\mathrm{SSL}}^+ = 2$. The configuration reported in Chernyshenko (2013) was analysed experimentally and numerically at NASA by Denison et al. (2015). Denison et al.'s simulations indicated a slight drag increase for a wave slope of 0.5%, whilst the experimental results were inconclusive within the repeatability tests undertaken.

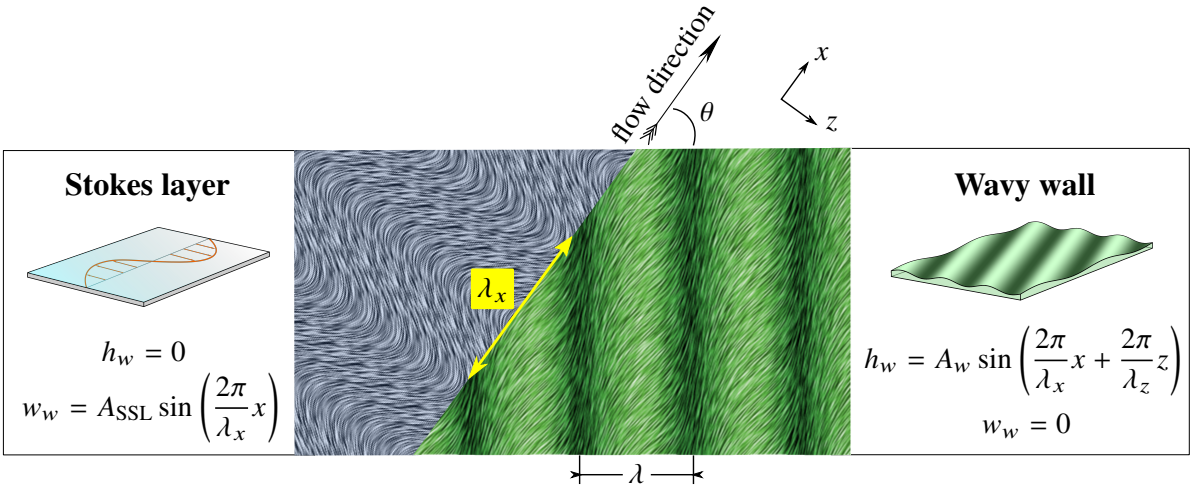


Figure 1.3: Emulation of the in-plane wall motions with a wavy wall. Visualisation of the mean streakline close to the wall for SSL (left) and wavy wall (right). The background is coloured by the norm of the velocity vector.

1.4 Research objectives

The primary aim of this research is to investigate the drag-reduction capabilities of solid oblique wall undulations. Although reduced-order models may be used to derive a preliminary estimate of the location of the minimum-drag state in the parameter space, an accurate evaluation of the drag level requires the resolution of all relevant scales of the turbulent flow, only possible by use of DNS.

The main objective is to find the wavy-channel flow configuration—given a Reynolds number, the wave height, wavelength and angle at which the wave is positioned relative to the flow—that minimises the overall drag. Unfortunately, the prohibitive cost of DNS does not allow for an extensive parametric exploration of all the possible configurations. Therefore, priority will be given to the understanding of the influence of each parameter on the drag and on the flow properties.

In addition to the search of a low-drag configuration, another fundamental aspect of the research is concerned with gaining insight into the mechanisms by which the drag is reduced. Because the skewing of the waves is motivated by the observations of the drag reduction induced by Stokes layers, the relationship between wavy walls and Stokes layers will also be examined.

More generally, the aim of the present research is to contribute to the body of knowledge on effective and efficient ways to reduce the turbulent drag, in a manner that is compatible with all operational constraints, thus addressing the pressing needs of the aeronautical industry for greener and more cost-efficient civil aviation.

1.5 Outline of the thesis

The remainder of the thesis is structured in five parts as follows:

- Chapter 2 presents the numerical methods employed. It includes the description of the grid properties and definition of the geometrical parameters describing the wave geometry, the control of the flow-rate inside the channel, the convention used for the angle of the flow based on the bulk velocity, the calculation of the drag contribution, as well as the method chosen for the quantification of the time-averaging uncertainty.
- Chapter 3 is concerned with the verification and validation of the numerical framework presented in chapter 2. It starts with the verification of the formal accuracy of the spatial discretisation via the method of manufactured solutions. An extensive range of tests and comparisons to independent simulations and experiments available in the literature is then presented. These include fully developed turbulent flows relevant to the configurations later simulated.
- In chapter 4, a RANS-based linear approximation of the wavy channel is presented and compared to DNS. The linear solution is then used jointly with DNS data from Viotti et al. (2009a) in order to generate semi-empirical models based on physical analogies between wavy walls and spatial Stokes layers. Indications on the region of the parameter space where the lowest drag level is most likely to be expected are derived from the semi-empirical models to guide the selection of the flow configurations investigated by DNS.
- Chapter 5 contains the DNS results. The flow characteristics are presented and analysed, and the adequacy of the grid properties chosen for the discretisation of the problem is discussed. The accuracy of the drag-reduction rate with respect to grid convergence is assessed by multiple simulations of a single flow configuration with varying cell distance and flow-to-mesh angle. The influence of the wave height, angle and wavelength on the drag contributions is studied and the changes in the turbulence properties, relative to the baseline plane channel, are investigated.
- Finally, chapter 6 provides a quantitative comparison between wavy walls and Stokes layers in order to gain insight into the mechanisms at the origin of the friction reduction, and whether a common ground can be found between the two scenarios. In addition, the Reynolds-number dependence, in terms of the spanwise motion, is considered with respect to the scaling of the wave dimensions.

Chapter 2

Numerical framework

Contents

2.1 DNS code 45
2.2 Mesh generation 50
2.2.1 Plane channel 50
2.2.2 Wavy channel 51
2.3 Control of flow rate 52
2.4 Skewed-flow implementation 54
2.4.1 Orientation of the wavy wall 54
2.4.2 Oblique forcing of the flow 56
2.5 Statistical averaging 56
2.5.1 Pre-processing 56
2.5.2 Post-processing 58
2.6 Drag contributions and friction velocity 59
2.6.1 Drag contributions 59
2.6.2 Friction velocity 64
2.7 Uncertainty quantification 64
2.7.1 Spatial discretisation 64
2.7.2 Finite number of statistical samples 65
2.7.3 Quantification of the drag-reduction time-averaging error 66

2.1 DNS code

The foundation of the present research is the computational implementation of the LES equations in the code STREAM-LES, originally developed by Lardat and Leschziner (1998). The code solves the

incompressible Navier–Stokes equations

$$\begin{cases} \dfrac{\partial u_i}{\partial t} + \dfrac{\partial u_i u_j}{\partial x_j} = -\dfrac{\partial p}{\partial x_i} + \nu \dfrac{\partial^2 u_i}{\partial x_j \partial x_j} + f_i, & (2.1) \\ \dfrac{\partial u_j}{\partial x_j} = 0, & (2.2) \end{cases}$$

where $\boldsymbol{u} = (u, v, w)^T$ is the velocity field, p is the pressure normalised by the fluid density ρ, and $\boldsymbol{f}$ is a forcing term. The numerical implementation makes use of a fractional-step method (Kim and Moin, 1985; Brown et al., 2001) in conjunction with a non-orthogonal hexahedral finite-volume discretisation. Each time-step comprises two substeps, as detailed below.

At time $t^{n+1} = \sum_{i=1}^{n+1} \Delta t^i$, the momentum equation (2.1) is written as:

$$\left.\frac{\partial u_i}{\partial t}\right|^{n+1} = -\left.\frac{\partial p}{\partial x_i}\right|^{n+1} + F_i^{n+1}, \tag{2.3}$$

where F_i contains the convective, diffusive and body-force terms:

$$F_i = -\frac{\partial u_i u_j}{\partial x_j} + \nu \frac{\partial^2 u_i}{\partial x_j \partial x_j} + f_i. \tag{2.4}$$

The time-advancement is performed by use of a third-order gear-like scheme,

$$\sigma_1\, u_i^{n+1} + \sigma_2\, u_i^n + \sigma_3\, u_i^{n-1} + \sigma_4\, u_i^{n-2} = -\left.\frac{\partial p}{\partial x_i}\right|^{n+1} + \sigma_5\, F_i^n + \sigma_6\, F_i^{n-1} + \sigma_7\, F_i^{n-2}, \tag{2.5}$$

where the coefficients $(\sigma_k)_{1 \leqslant k \leqslant 7}$ depend on the time-step and are calculated so that the scheme is third-order accurate, as described in Fishpool and Leschziner (2009).

The fractional step introduces the intermediate velocity field $\boldsymbol{u}^*$ as

$$\begin{aligned} &\sigma_1 \left(u_i^{n+1} - u_i^*\right) + \sigma_1\, u_i^* + \sigma_2\, u_i^n + \sigma_3\, u_i^{n-1} + \sigma_4\, u_i^{n-2} \\ &\qquad = -\left.\frac{\partial p}{\partial x_i}\right|^{n+1} + \sigma_5\, F_i^n + \sigma_6\, F_i^{n-1} + \sigma_7\, F_i^{n-2}, \end{aligned} \tag{2.6}$$

which is solved in two successive substeps:

$$\text{Substep 1:} \quad \sigma_1\, u_i^* + \sigma_2\, u_i^n + \sigma_3\, u_i^{n-1} + \sigma_4\, u_i^{n-2} = \sigma_5\, F_i^n + \sigma_6\, F_i^{n-1} + \sigma_7\, F_i^{n-2}, \tag{2.7}$$

$$\text{Substep 2:} \quad \sigma_1 \left(u_i^{n+1} - u_i^*\right) = -\left.\frac{\partial p}{\partial x_i}\right|^{n+1} \qquad \text{(projection step)}. \tag{2.8}$$

First, the intermediate velocity $\boldsymbol{u}^*$ is calculated *explicitly* from equation (2.7). The variable storage

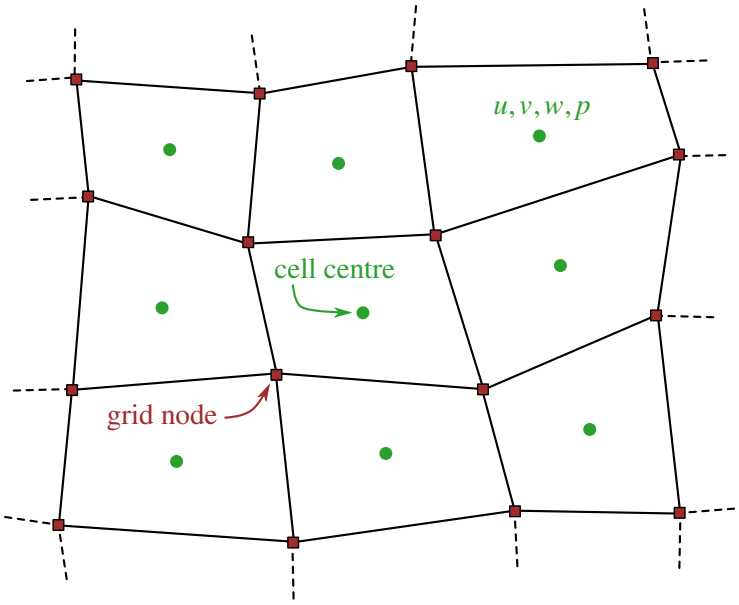


Figure 2.1: Definition of the grid nodes and centroids for the collocated storage of the solution variables.

is collocated, as shown in figure 2.1, with second-order spatial approximations implemented within the non-orthogonal finite-volume framework. A fourth-order-accurate representation of the convective and diffusive fluxes was implemented by Touber and Leschziner (2012) under the assumption of a Cartesian mesh. Most of the simulations presented make use of the second-order version, although the fourth-order scheme was preferred in some cases featuring Cartesian grids.

Second, the non-solenoidal intermediate velocity field $\boldsymbol{u}^*$ is projected onto the solenoidal subspace by solving an *implicit* pressure–Poisson equation, obtained by applying the divergence operator to equation (2.8):

$$\nabla^2 p^{n+1} = -\sigma_1 \, \boldsymbol{\nabla} \cdot \left(\boldsymbol{u}_j^{n+1} - \boldsymbol{u}_j^* \right) , \tag{2.9}$$

and use of the continuity equation (2.2) implying $\boldsymbol{\nabla} \cdot \boldsymbol{u}^{n+1} = 0$. This yields the pressure–Poisson equation

$$\nabla^2 p^{n+1} = \sigma_1 \, \boldsymbol{\nabla} \cdot \boldsymbol{u}_j^* . \tag{2.10}$$

This is a linear equation, the solution of which requires a significant proportion of the total computational effort when advancing the solution fields. The 3D Poisson solver applies the Alternate Direction Implicit (ADI) relaxation method (Peaceman and H. H. Rachford, 1955), with sweeps effected by use of the Successive Line Over-Relaxation (SLOR) method (Hirsch, 2007, p. 510). The rate of convergence to the exact solution of the projection step is accelerated by a multigrid algorithm consisting of

V-cycles, as described in Lien and Leschziner (1993). The multigrid iterations within any time-step are terminated when a convergence criterion, based on the L^2-norm of the mass residuals, made non-dimensional with the mass-flow rate, is met. A typical value used for this criterion in the simulations presented below is $\epsilon_P = 10^{-10}$. Stable velocity–pressure coupling is ensured by use of the Rhie-and-Chow interpolation (Rhie and Chow, 1983), preventing odd-even oscillations that may arise from the collocated storage of the solution variables.

In the context of parallel processing, the solution domain is partitioned using the Message Passing Interface (MPI). The computational domain is subdivided into blocks, and each of them is assigned to a single processor. Boundary conditions and inter-block communications are handled by use of halo cells, as illustrated in figure 2.2. Data transfer is handled via the creation of a set of MPI communicators at the beginning of the simulation.

On increasing the number of blocks, the number of cells per block diminishes accordingly, but the total number of cells present in the halo regions increases. Therefore, the computation time per processor reduces, in contrast to the overall communication time, since there is more data to be exchanged. When running simulations on a large number of processors, it is important, therefore, to ensure that the overall CPU time, i.e. the number of processors multiplied by the execution time, remains reasonably close to the serial execution time (on one single core), implying linear scaling.

The measure of this loss of efficiency was investigated via a strong-scaling study, the outcome of which is shown in figure 2.3. The study was performed on two different HPC clusters, namely the local facility at Imperial College London (CX2-Helen) and the national HPC (ARCHER). In both cases, the code was run for a number of iterations without performing any data output. The problem size (number of cells) was kept constant and the number of blocks was gradually increased. Figure 2.2 demonstrates that the scaling efficiency is acceptable both for small (7M cells) and large problem (0.5B cells) sizes.

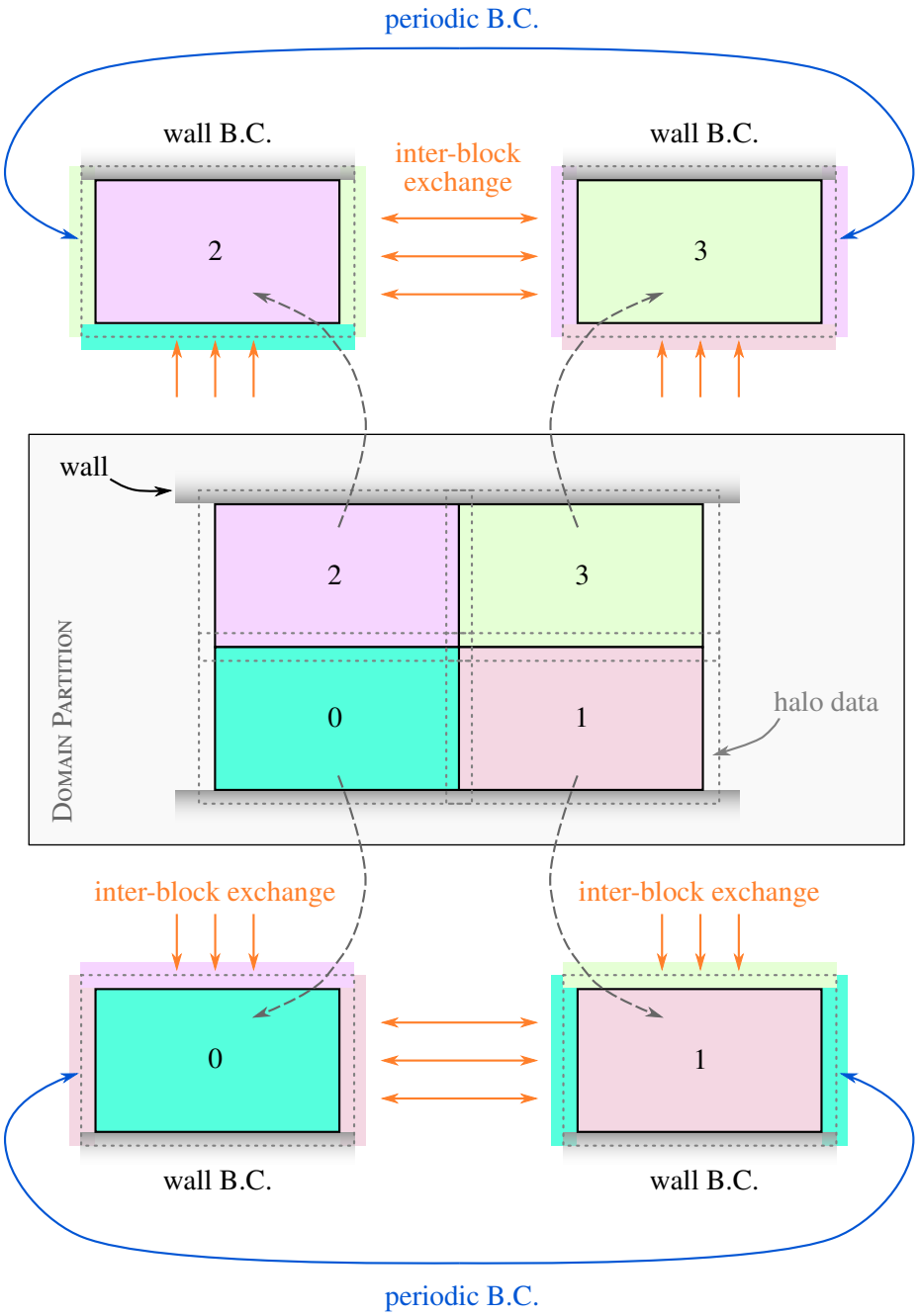


Figure 2.2: Multi-block domain decomposition and halo-data exchanges on a 2D model problem divided into four blocks numbered from 0 to 3, with periodic boundary conditions in the horizontal direction, and a wall at each vertical end.

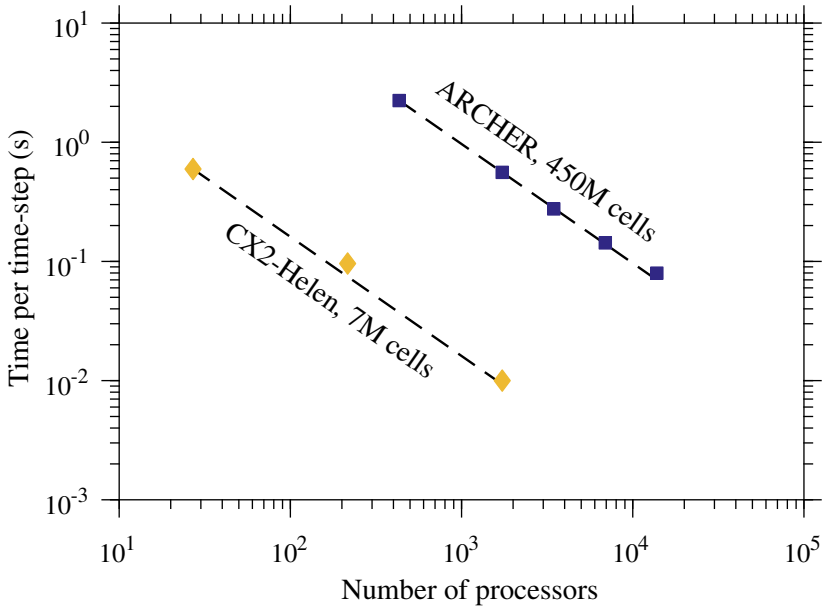


Figure 2.3: Strong scaling on CX2-Helen and ARCHER, dashed lines: ideal scaling based on the execution time on the smallest partition.

2.2 Mesh generation

2.2.1 Plane channel

The basic plane-channel-flow configuration, a schematic of which is given in figure 2.4, comprises two flat walls, separated by a fixed distance of $2h$, and located at $y = \pm h$. Unless stated otherwise, the domain extends from $z = -L_z/2$ to $z = L_z/2$ in the spanwise direction, and from $x = 0$ to $x = L_x$ in the streamwise direction. The number of cells in each direction is denoted N_x, N_y and N_z, respectively. The flow is driven by imposing of a body force $\boldsymbol{f}$ in the momentum equation (2.1), as will be described in section 2.3, so that only the periodic part of the pressure field is computed as part of the local solution. A pressure reference value is fixed by setting the pressure to zero at one corner of the domain. No-slip boundary conditions are used at the two solid walls, and periodic boundary conditions are applied at both streamwise and spanwise ends of the finite domain.

In order secure adequate resolution near the walls, the mesh is refined in the wall-normal direction by stretching the grid. With the location of Cartesian grid nodes denoted by $(\xi,\eta,\zeta)_{i,j,k}$, the wall-parallel coordinates are left unchanged $(\xi,\zeta) = (x,z)$, but the vertical nodal coordinates are transformed via

$$y_{i,j,k} = \frac{1}{\alpha}\tanh\left(\beta\,\eta_{i,j,k}\right) \qquad \text{with} \qquad \beta = \frac{1}{2}\ln\left(\frac{1+\alpha}{1-\alpha}\right), \tag{2.11}$$

where the parameter α can be adjusted to control the concentration of cells close to the walls. The value

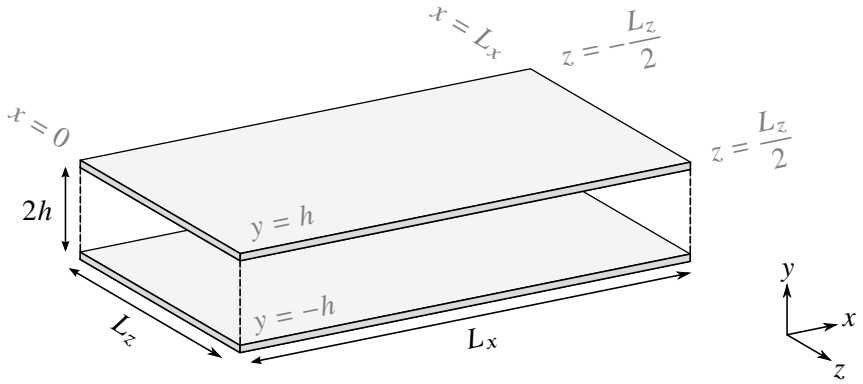


Figure 2.4: Sketch of the generic plane-channel-flow configuration.

of this parameter is set by prescribing the size of the cell closest to the wall $\Delta y^+|_w = \Delta y|_w Re_\tau^{\text{target}}$, where Re_τ^{target} is the target friction Reynolds number. For DNS applications, it is generally agreed that a value lower than unity is required to yield sufficient accuracy. In all the simulations presented, the practice adopted is $\Delta y^+|_w \leqslant 0.7$.

2.2.2 Wavy channel

A simple transfinite mesh generator was devised to account for the mild wall distortions of a wavy geometry. In the simulations presented, sinusoidal undulations are prescribed, but there is no particular limitation placed on the mesh-generation process. However, although any analytical formula is allowed for the mesh distortion, it should remain smooth enough for the numerical accuracy of the scheme to be retained.

The mesh generation was performed by adding an increment $h_w(x, y, z)$ to the y-coordinate of each and every node of the original Cartesian plane-channel mesh, as shown in figure 2.5. Thus, different shapes can be obtained at the lower and upper walls by interpolating the increment h_w between the two desired geometries, denoted $h_{lw}(x, z)$ and $h_{uw}(x, z)$, respectively. In the case of the two boundaries being different, a linear interpolation is chosen as

$$h_w = \frac{h - y}{2h} h_{lw} + \frac{h + y}{2h} h_{uw}. \tag{2.12}$$

The increment h_w must satisfy L_x- and L_z-periodicity in the x- and z-directions respectively in order to be consistent with the periodic boundary conditions imposed at the edges of the wall-parallel directions. Consequently, a constraint on the domain length is that it must be an integer multiple of the wavelength in the corresponding direction, so to satisfy the periodic boundary conditions. This

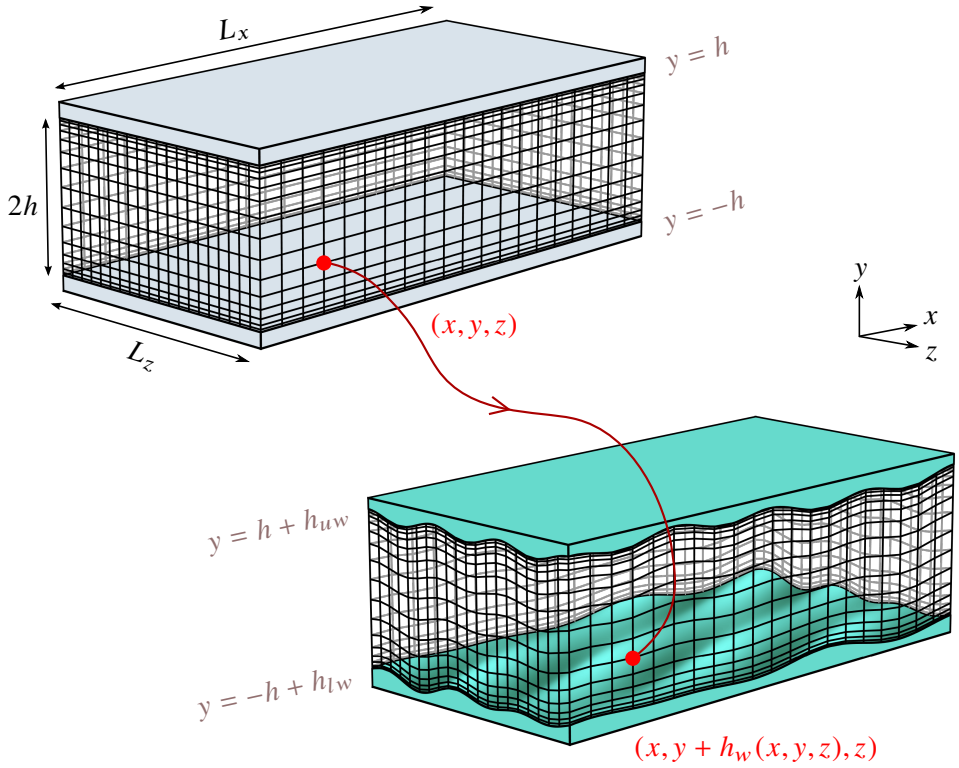


Figure 2.5: Generation of a wavy-channel mesh from a plane-channel mesh.

constraint has major resource implications when the wavelength is large, as at least 2–3 waves need to be included in the solution domain.

2.3 Control of flow rate

In the present incompressible flow, maintaining a constant flow rate (CFR) is equivalent to maintaining a target Reynolds number $Re_b = U_b\, h/\nu$, based on the bulk velocity U_b. This can be done by iteratively adjusting a spatially homogeneous pressure gradient. Alternatively, a temporally constant pressure gradient (CPG) can be prescribed to maintain a constant shear stress. In that case, the Reynolds number is not exactly the one initially targeted, but should be close if the pressure gradient is estimated from available data for channel flow. In both cases, the body force $\boldsymbol{f} = f_i\, \boldsymbol{e_i}$ takes the form of a spatially homogeneous pressure gradient.

The above two strategies were implemented and tested on laminar and turbulent channel flows. In the laminar case, the two strategies are equivalent, since the solution is steady, and it can be shown that the parabolic Poiseuille solution is $u(y) = 3/2\left(1 - y^2\right)$, with a body force $f_x = 3/Re_b$ maintaining a

unit bulk velocity. Very good agreement with the analytical expression was obtained when refining the mesh in the wall-normal direction.

The CFR strategy is computationally advantageous, as it requires a shorter transient time following the start of the solution. In the CPG case, the two strategies can be used successively, the former being employed for the initial part of the simulation, so as to swiftly bring the flow to a statistically stationary state and yield a reasonable estimate for the driving force. In any case, the results obtained with both strategies are very similar, as shown in Quadrio et al. (2016).

The enforcement of a constant flow rate requires the update of the time-dependent body force $\boldsymbol{f}(t)$. In the case of a plane channel, this can be achieved by adding a corrective profile increment to the velocity to satisfy the flow-rate condition exactly, as explained in Quadrio et al. (2016). However, the strategy adopted herein, applicable to non-planar and variable-time-step channel-flow simulations, is different, the flow-rate condition being only approximately satisfied.

First, a body force of the form $\boldsymbol{f} = -P_x \boldsymbol{e_x}$ is considered. The objective is to find an explicit estimate of the pressure gradient P_x to be applied at the following time-step t^{n+1} using information taken at the two previous ones. The target bulk velocity is denoted U_{target}, while at time $t^n = \sum_{i=1}^{n} \Delta t^i$, the actual bulk velocity, is

$$U_b^n = \frac{1}{\mathcal{V}} \iiint_{\mathcal{V}} \rho\, u^n \, \mathrm{d}V, \tag{2.13}$$

where $\mathcal{V}$ is the total volume of the domain. The driving pressure gradient applied at the following time-step is then estimated explicitly from:

$$P_x^{n+1} = \alpha\, \sigma_1 \left(U_b^n - U_{\text{target}} \right) + (1-\alpha)\, P_x^{n-1}, \tag{2.14}$$

where $\alpha \in [0,1]$, and σ_1 is inversely proportional to the time-step Δt^n.

Next, this formulation can be extended to a body force $\boldsymbol{f} = -P_x\, \boldsymbol{e_x} - P_z\, \boldsymbol{e_z}$, thereby driving the bulk velocity in the z-direction

$$W_b^n = \frac{1}{\mathcal{V}} \iiint_{\mathcal{V}} \rho\, w^n \, \mathrm{d}V \tag{2.15}$$

to the desired value W_{target} via the addition of a driving pressure gradient in the z-direction, analogous to equation (2.14):

$$P_z^{n+1} = \alpha\, \sigma_1 \left(W_b^n - W_{\text{target}} \right) + (1-\alpha)\, P_z^{n-1}, \tag{2.16}$$

so that the target vectorial bulk velocity is $\boldsymbol{U}_{\text{target}} = [U_{\text{target}}, W_{\text{target}}]^T = [1,0]^T$.

For finite mesh spacing and domain size, and in the case of a flow aligned with the x-direction, this is not exactly equivalent to the former method ($\boldsymbol{f} = -P_x \boldsymbol{e_x}$), as there is a residual spanwise driving pressure gradient $P_z \neq 0$, small though it may be, enforcing $W_b \approx 0$. However, no noticeable difference was found between the two forcing strategies, the one implemented via equations (2.13) to (2.16) having the advantage of precisely prescribing the main flow direction. The effectiveness of the numerical implementation, demonstrated in figure 2.6, shows that the solution quickly adapts to satisfy the unit-bulk-velocity constraint.

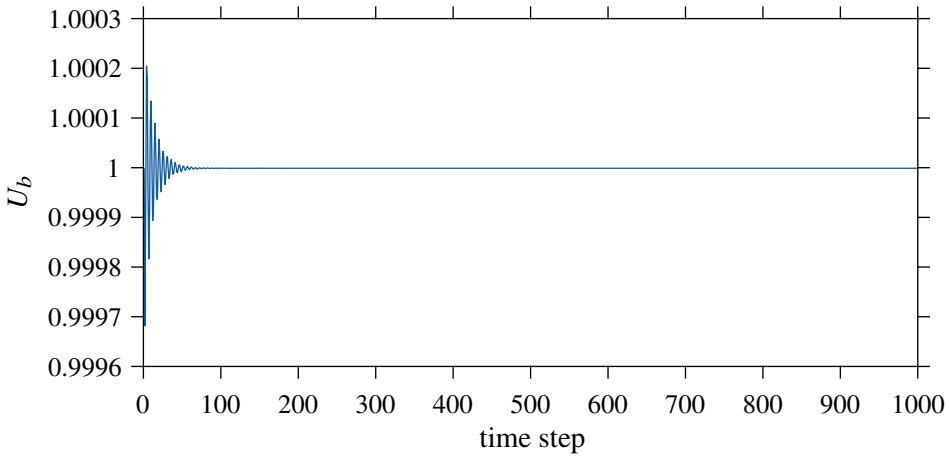


Figure 2.6: Adjustment of the bulk velocity versus number of time-steps for an initial field not satisfying the bulk-velocity condition.

2.4 Skewed-flow implementation

The imposition of the time-dependent, spatially homogeneous body force $\boldsymbol{f}(t)$, as defined in section 2.3, allows the flow to be driven at an angle θ_f to the mesh. As will transpire, this choice of driving the flow at an angle to the mesh was motivated by the multiple numerical and data-processing constraints that are inherent in the type of flows studied.

2.4.1 Orientation of the wavy wall

The skewed wavy channel can be simulated in two ways: the grid can be aligned with the wave or with the main flow direction. Although the two are physically equivalent, keeping the wavy boundary aligned with the numerical box and skewing the flow at an angle to the grid allows greater flexibility. The two equivalent configurations are shown in figure 2.7. Specifically, the main advantages of the latter approach are as follows:

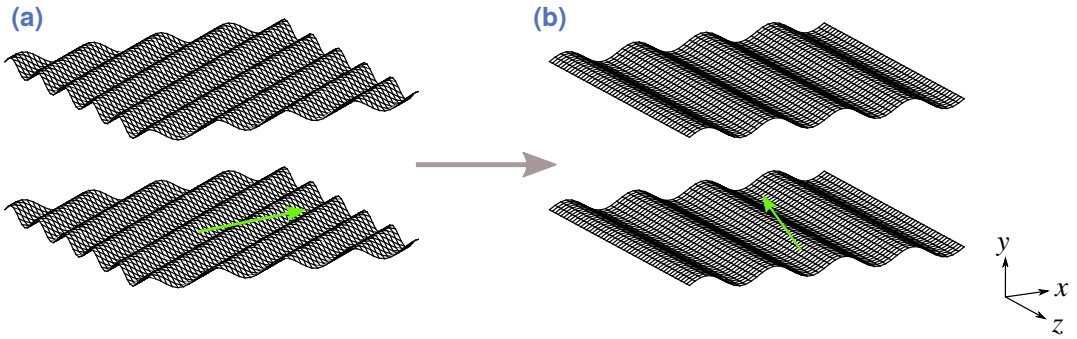


Figure 2.7: Flow domain of wavy-wall channel: the wavy wall is tilted so that the computational z-direction is homogeneous. The green arrow indicates the direction of the flow. **(a)** main flow direction aligned with the x-direction, **(b)** equivalent configuration with the flow at an angle to the mesh.

(1) if the crests are aligned with the z-direction, this direction becomes statistically homogeneous;

(2) the post-processing is significantly eased; and

(3) this option allows continuous variations of the domain extent in the z-direction without affecting the periodicity boundary conditions applied to the z-direction boundaries.

However, a disadvantage of this option is that it increases the problem size, since there is no longer an alignment between the x–z coordinates and the streamwise and spanwise directions, respectively (cf. figure 2.8), necessitating both the domain size and resolution to be increased in the two wall-parallel (x–z) directions. This is in contrast to the usual practice of increasing the spanwise resolution whilst decreasing the spanwise domain width.

An approximately constant flow rate is maintained across the channel by iteratively updating the two orthogonal pressure gradients, P_x and P_z, implemented as explicit body forces in the momentum

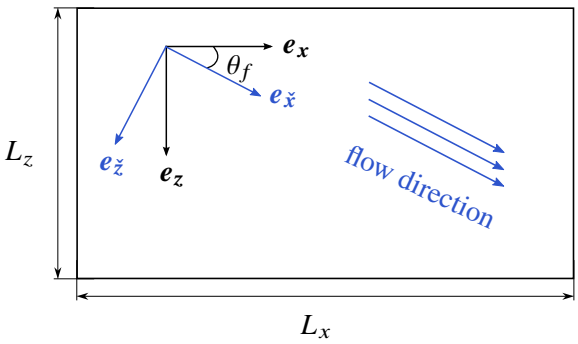


Figure 2.8: Sketch of the configuration of the skewed-flow DNS, with flow-oriented coordinates $\check{x}$ and $\check{z}$, relative to domain coordinates x and z.

equations, as described in section 2.3, so that the bulk velocity is close to unity in the streamwise ($\check{x}$) direction and zero in the spanwise ($\check{z}$) direction.

In the following description, quantities expressed in the frame of reference of the flow will be denoted with an overlaying inverted circumflex accent ($\check{}$), as in figure 2.8, although this notation will be omitted later when the meaning is obvious. Unless stated otherwise, all physical interpretations are given in the frame of reference aligned with the flow.

2.4.2 Oblique forcing of the flow

The flow is forced obliquely at a particular angle θ_f relative to the coordinates of the domain by prescribing two orthogonal bulk-velocity components different from unity. A schematic of the flow-direction rotation is shown in figure 2.8. With the coordinate system aligned with the flow ($\boldsymbol{e_{\check{x}}}, \boldsymbol{e_{\check{y}}}, \boldsymbol{e_{\check{z}}}$), the bulk velocity must remain at the unity value in the streamwise direction in order to secure the correct Reynolds number. The latter is $\boldsymbol{U_b} = \check{U}_b \, \boldsymbol{e_{\check{x}}}$ where $\check{U}_b = 1$. Thus, expressed in terms of the frame of reference of the computational domain, the bulk velocity is:

$$\begin{aligned} \boldsymbol{U_b} &= \check{U}_b \, \boldsymbol{e_{\check{x}}} && (2.17)\\ &= \check{U}_b \left(\cos\theta_f \; \boldsymbol{e_x} + \sin\theta_f \; \boldsymbol{e_z} \right) && (2.18)\\ &= U_b \, \boldsymbol{e_x} + W_b \, \boldsymbol{e_z}, && (2.19) \end{aligned}$$

so that the components to be prescribed are

$$\begin{cases} U_b &= \check{U}_b \, \cos\theta_f, \\ W_b &= \check{U}_b \, \sin\theta_f. \end{cases} \tag{2.20}$$

As shown in figure 2.9, the target streamwise bulk velocity is satisfied within an error lower than 0.001%.

2.5 Statistical averaging

2.5.1 Pre-processing

Sample accumulation at runtime

When a homogeneous direction is available, all quantities are integrated at runtime in order to significantly reduce the amount of data to be saved to disk. Furthermore, samples are gathered every 10

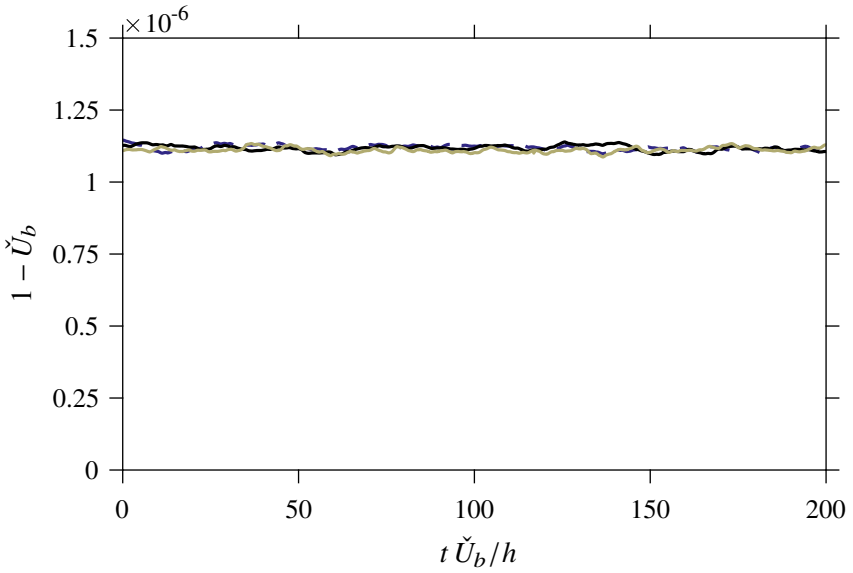


Figure 2.9: Time-evolution of the error in the bulk velocity $1-\check{U}_b = 1-\|\boldsymbol{U_b}\|$. Black line: plane-channel flow aligned with the mesh, green line: plane-channel flow at $\theta_f = 70°$, blue dashed-line: wavy channel at $\theta_f = 70°$.

iterations and integrated in time over a fixed number of samples. Once the desired number of samples is reached, a set of files is written to disk, and this is repeated throughout the entire simulation. This procedure allows for the final averaging time range, composed of the contiguous integral over the windows available after the end of the transient period, to be adjusted a posteriori without any prior knowledge of the time evolution of the solution, thus reducing the amount of statistically stationary data discarded for transient-removal purposes.

Rotation prior to the accumulation of statistics

The statistical quantities (first- to third-order statistics) are calculated in the frame of reference aligned with the main flow direction $(\check{u},\check{v},\check{w})$. This is performed by applying the following transformations before the accumulation of the statistics:

$$\begin{cases} \check{u} &= \cos\theta_f\ u &+ \sin\theta_f\ w, \\ \check{w} &= -\sin\theta_f\ u &+ \cos\theta_f\ w, \\ \check{v} &= v, \end{cases} \tag{2.21}$$

where the regular notations correspond to the quantities in the computational domain—that is, the solution in the coordinate system $(\boldsymbol{e_x},\boldsymbol{e_y},\boldsymbol{e_z})$, with the x-direction perpendicular to the crests and troughs of the waves and the z-direction homogeneous along the crests and troughs as in figure 2.7b.

The terms required for the turbulence-kinetic-energy budget involving spatial derivatives are not rotated and remain in the computational frame of reference. The rotation is then implemented in the post-processing routine and will be validated in sections 3.3.1 and 3.4. For a problem that is z-homogeneous, the flow-orientated derivatives become simply:

$$\begin{cases} \dfrac{\partial}{\partial \check{x}} &= \cos\theta_f \dfrac{\partial}{\partial x}, \\ \dfrac{\partial}{\partial \check{z}} &= -\sin\theta_f \dfrac{\partial}{\partial x}. \end{cases} \tag{2.22}$$

2.5.2 Post-processing

All statistical quantities can be averaged in the homogeneous direction parallel to the wave crests and troughs. This groove-wise-averaging procedure is significantly eased by the choice made in section 2.4 of forcing the flow at an angle θ_f to the numerical grid, and it is already performed at runtime, as previously described, in order to reduce the volume of the data output. Phase-averaging is also performed when multiple waves are included within the domain of solution. Furthermore, in the case of a wavy channel with constant wall separation, both boundaries are statistically equivalent, which allows for a doubling of the data included in the phase-averaging by shifting one of the walls by half a period and then taking advantage of the symmetry to average over both walls. Thus, any time- and phase-averaged quantity $\overline{\boldsymbol{q}}$ only depends upon the phase location x/λ and the wall-normal location y, reducing the dependence to $\overline{\boldsymbol{q}}(x/\lambda, y)$.

Depending on the objective of the analysis, two types of statistical decomposition of the mean turbulence properties can be considered. The first decomposition is relevant to studying how the flow properties vary in phase:

$$\overline{\boldsymbol{q}} = \boldsymbol{Q} + \widetilde{\boldsymbol{q}}, \tag{2.23}$$

where $\overline{\boldsymbol{q}}$ is any time- and phase-averaged quantity, $\widetilde{\boldsymbol{q}}$ is the phase-varying part of the mean field, and

$$\boldsymbol{Q}(y) = \int_0^1 \overline{\boldsymbol{q}}\left(\frac{x}{\lambda}, y + y_w\right) \mathrm{d}\left(\frac{x}{\lambda}\right), \tag{2.24}$$

where $y_w = A_w \sin(2\pi\, x/\lambda)$ is the wall-normal location of the wall.

The second approach lays emphasis on the action of the wavy boundaries relative to the plane-channel flow:

$$\overline{\boldsymbol{q}} = \boldsymbol{Q_0} + \widehat{\boldsymbol{q}} \tag{2.25}$$

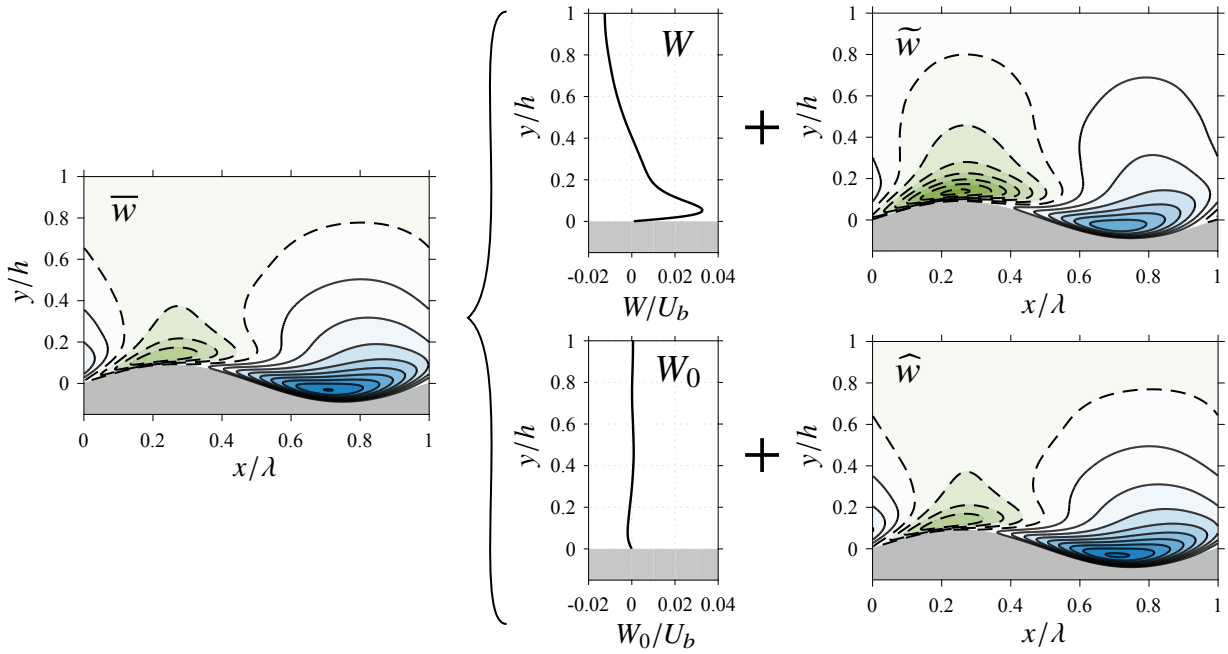


Figure 2.10: Alternative decompositions of the mean fields for the spanwise velocity $\overline{w}$, upper plots correspond to equation (2.23), and lower plots to equation (2.25).

where $\boldsymbol{Q_0}$ is the baseline plane-channel-flow value, and $\widehat{\boldsymbol{q}}$ is the difference to the plane-channel-flow solution. These decompositions, exemplified in figure 2.10 by reference to the spanwise velocity, will be referred to as 'phase-integrated' ($\boldsymbol{Q}$), 'phase-varying' ($\widetilde{\boldsymbol{q}}$), and 'difference' ($\widehat{\boldsymbol{q}}$).

2.6 Drag contributions and friction velocity

2.6.1 Drag contributions

A drag coefficient is defined for each contribution to the drag as:

$$D_\star = \frac{\bar{F}_\star}{\frac{1}{2}\rho\, L_x\, L_z\, \|\boldsymbol{U_b}\|^2}, \tag{2.26}$$

where '$\star$' identifies the contribution (e.g. 'f' for friction), $\bar{F}_\star$ is the mean force exerted on the walls opposing the flow direction, and $\boldsymbol{U_b}$ the bulk velocity.

For the wavy channel, the total drag force is composed of two contributions: friction and pressure drag so that the total-drag stress at the wall is:

$$\tau_t = \tau_f + \tau_p, \tag{2.27}$$

where τ_f and τ_p are respectively the frictional and pressure contributions to the total stress, later referred

to as 'friction-drag stress' and 'pressure-drag stress'.

Friction drag

The calculation of the friction drag was performed from the gradient of the mean velocity field averaged along the grooves. In this case, the flow direction is not aligned with the wave, so the integration must be done carefully to account for the misalignment of the surface normal. The frame of reference considered is that attached to the wave, so that the z-direction is homogeneous, as shown in figure 2.11. However, u and w are no longer the streamwise and spanwise velocity components, and they can be of the same order of magnitude. The wall is located at $f_w(x,y,z) = 0$ where $f_w = y - y_w$, with $y_w = \pm h + h_w(x)$. The surface normal $\boldsymbol{n_w}$ of unit length pointing outwards from the integration volume can be expressed as the gradient of f_w so that $\boldsymbol{n_w} = \left(1 + h_w'^2\right)^{-1/2} [h_w', -1, 0]^T$. The local force arising from the shear stress on a surface element $\mathrm{d}S$ is then,

$$\boldsymbol{F_{sh}} = \mu \left(\nabla \boldsymbol{u} + \nabla \boldsymbol{u}^T\right)\Big|_w \boldsymbol{n_w}\, \mathrm{d}S, \tag{2.28}$$

and the resulting drag force is its projection onto the flow opposite direction, that is,

$$F_f = \boldsymbol{F_{sh}} \cdot (-\boldsymbol{e_{\check{x}}})\,, \tag{2.29}$$

where $\boldsymbol{e_{\check{x}}}$ is the direction of the flow (cf. figure 2.8), i.e. $\boldsymbol{e_{\check{x}}} = [\cos\theta_f, 0, \sin\theta_f]^T$. The local frictional stress can thus be calculated as:

$$\tau_f = \frac{F_f}{\mathrm{d}S} = \frac{-\mu}{\sqrt{1 + h_w'^2}} \left(\left[\begin{array}{ccc} 2\dfrac{\partial u}{\partial x} & \dfrac{\partial v}{\partial x} + \dfrac{\partial u}{\partial y} & \dfrac{\partial w}{\partial x} \\ \dfrac{\partial v}{\partial x} + \dfrac{\partial u}{\partial y} & 2\dfrac{\partial v}{\partial y} & \dfrac{\partial w}{\partial y} \\ \dfrac{\partial w}{\partial x} & \dfrac{\partial w}{\partial y} & 0 \end{array} \right] \left[\begin{array}{c} h_w' \\ -1 \\ 0 \end{array} \right] \right)\Bigg|_w \cdot \left[\begin{array}{c} \cos\theta_f \\ 0 \\ \sin\theta_f \end{array} \right], \tag{2.30}$$

by using the fact that homogeneity in the z-direction implies $\partial \cdot / \partial z = 0$. Equation (2.30) can then be expanded as:

$$\begin{aligned} \tau_f = \frac{-\mu}{\sqrt{1 + h_w'^2}} \Bigg(& h_w' \left.\frac{\partial u}{\partial x}\right|_w \cos\theta_f + h_w' \left.\frac{\partial u}{\partial x}\right|_w \cos\theta_f - \left.\frac{\partial u}{\partial y}\right|_w \cos\theta_f \\ & - \left.\frac{\partial v}{\partial x}\right|_w \cos\theta_f + h_w' \left.\frac{\partial w}{\partial x}\right|_w \sin\theta_f - \left.\frac{\partial w}{\partial y}\right|_w \sin\theta_f \Bigg). \end{aligned} \tag{2.31}$$

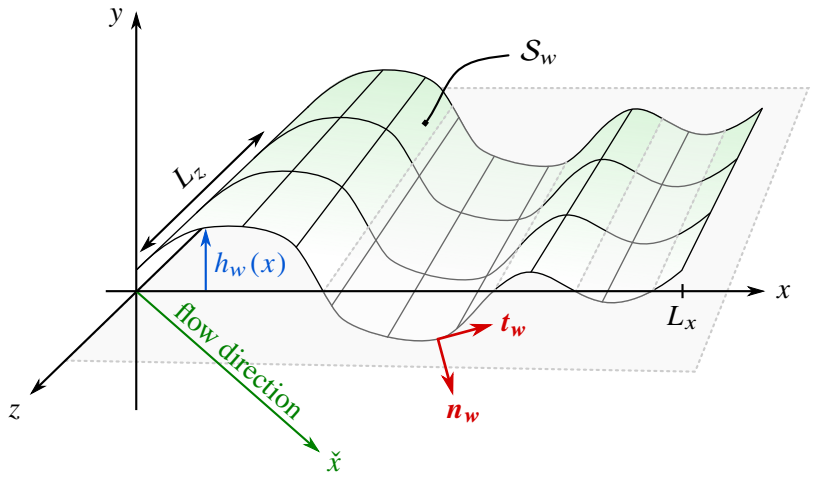


Figure 2.11: Local tangential and wall-normal coordinate system for the integration of the frictional drag along a z-homogeneous wave.

As the streamwise velocity is $\check{u} = u\cos\theta_f + w\sin\theta_f$, this friction stress reduces to

$$\tau_f = \frac{-\mu}{\sqrt{1+h_w'^2}}\left[-\left.\frac{\partial\check{u}}{\partial y}\right|_w + h_w'\left.\frac{\partial\check{u}}{\partial x}\right|_w + \cos\theta_f\left(h_w'\left.\frac{\partial u}{\partial x}\right|_w - \left.\frac{\partial v}{\partial x}\right|_w\right)\right]. \tag{2.32}$$

Next, a practice similar to that adopted by Peet and Sagaut (2009) was used to simplify equation (2.32) by considering the coordinate system $(\boldsymbol{t_w},\boldsymbol{n_w})$, shown in figure 2.11, which are wall tangent and normal vectors, respectively. The gradient of the velocity component u_i at the wall is:

$$\boldsymbol{\nabla} u_i|_w = \left.\frac{\partial u_i}{\partial t_w}\right|_w \boldsymbol{t_w} + \left.\frac{\partial u_i}{\partial n_w}\right|_w \boldsymbol{n_w}, \tag{2.33}$$

but at the solid wall, owing to the no-slip boundary condition, the tangential gradients must satisfy $(\partial u_i/\partial t_w)|_w = 0$, so that

$$\boldsymbol{\nabla} u_i|_w = \left.\frac{\partial u_i}{\partial n_w}\right|_w \boldsymbol{n_w}. \tag{2.34}$$

The local derivatives of the velocity at the wall $(\partial u_i/\partial x_j)|_w$ are by definition

$$\boldsymbol{\nabla} u_i|_w \cdot \boldsymbol{e_j} = \left.\frac{\partial u_i}{\partial n_w}\right|_w \boldsymbol{n_w}\cdot\boldsymbol{e_j}, \tag{2.35}$$

which yields:

$$\begin{cases} \left.\dfrac{\partial u_i}{\partial x}\right|_w = \dfrac{h_w'}{\sqrt{1+h_w'^2}}\left.\dfrac{\partial u_i}{\partial n_w}\right|_w, \\ \left.\dfrac{\partial u_i}{\partial y}\right|_w = \dfrac{-1}{\sqrt{1+h_w'^2}}\left.\dfrac{\partial u_i}{\partial n_w}\right|_w. \end{cases} \tag{2.36}$$

As a consequence of equation (2.36), the previous formula in equation (2.32) becomes

$$\tau_f = -\mu \left.\frac{\partial \check{u}}{\partial n_w}\right|_w + \mu \cos\theta_f \frac{h'_w}{1+h'^2_w}\left(-h'_w \left.\frac{\partial u}{\partial n_w}\right|_w + \left.\frac{\partial v}{\partial n_w}\right|_w\right), \tag{2.37}$$

and the continuity equation implies

$$\left.\frac{\partial u}{\partial x}\right|_w + \left.\frac{\partial v}{\partial y}\right|_w = -h'_w \left.\frac{\partial u}{\partial n_w}\right|_w + \left.\frac{\partial v}{\partial n_w}\right|_w = 0, \tag{2.38}$$

which, when inserted into equation (2.37), simplifies the expression of the frictional stress to

$$\tau_f = -\mu \left.\frac{\partial \check{u}}{\partial n_w}\right|_w, \tag{2.39}$$

so that, using equation (2.36), the final expression of the local frictional stress is

$$\tau_f = \mu \sqrt{1+h'^2_w} \left.\frac{\partial \check{u}}{\partial y}\right|_w. \tag{2.40}$$

The force F_f is then integrated on the wall surface $\mathcal{S}_w$ as:

$$\bar{F}_f = \iint_{\mathcal{S}_w} \tau_f \, \mathrm{d}S \tag{2.41}$$

$$= \int_{-L_z/2}^{L_z/2} \int_0^{L_x} \tau_f \, \mathrm{d}l \, \mathrm{d}z, \tag{2.42}$$

where l is the curvilinear abscissa. It follows that,

$$\bar{F}_f = L_z \int_0^{L_x} \tau_f \, \mathrm{d}l \tag{2.43}$$

$$= L_z \int_0^{L_x} \tau_f \sqrt{1+h'^2_w(x)} \, \mathrm{d}x, \tag{2.44}$$

so that the final expression for the mean friction-drag force is:

$$\bar{F}_f = L_z \int_0^{L_x} \left(1+h'^2_w\right) \mu \left.\frac{\partial \check{u}}{\partial y}\right|_w \mathrm{d}x. \tag{2.45}$$

Pressure drag

The calculation of the pressure drag is obtained in a similar fashion by integrating the pressure at the wall multiplied by the projection of the local surface normal onto the flow opposite direction. The

pressure-drag stress at the wall is that arising from the isotropic stresses at the wall:

$$\tau_p = -(p_w \, \mathbb{1} \cdot \boldsymbol{n_w}) \cdot \boldsymbol{e_{\check{x}}}, \tag{2.46}$$

where $\mathbb{1}$ is the identity tensor and p_w is the wall pressure. Since the near-wall cell dimension is small in DNS, the pressure at the wall is well approximated by simply taking the value at the centroid closest to the wall. The final expression for the pressure stress at the wall is

$$\tau_p = -\frac{p_w \, h'_w \, \cos\theta_f}{\sqrt{1 + h'^2_w}}, \tag{2.47}$$

and the resulting pressure-drag force

$$\bar{F}_p = L_z \int_0^{L_x} \tau_p \, \sqrt{1 + h'^2_w} \, \mathrm{d}x \tag{2.48}$$

can be integrated after inserting the expression for the wall stress in equation (2.47):

$$\bar{F}_p = -L_z \, \cos\theta_f \int_0^{L_x} p_w \, h'_w \, \mathrm{d}x. \tag{2.49}$$

Total drag

As mentioned in section 2.4, in all the cases presented, the flow is driven at approximately constant flow rate, so that $\|\boldsymbol{U_b}\| \approx 1$, via the imposition of a spatially homogeneous (vectorial) pressure gradient in order to balance the total drag force $\bar{F}_t$. The resulting pressure force driving the flow is:

$$\bar{F}_t = -\left(P_{\check{x}} \, L_x\right) 2h \, L_z, \tag{2.50}$$

where $P_{\check{x}}$ is the projection of the pressure gradient onto the flow direction:

$$P_{\check{x}} = P_x \, \cos\theta_f + P_z \, \sin\theta_f. \tag{2.51}$$

The friction and pressure forces were integrated according to the above formulae in equations (2.45) and (2.49) on the upper and lower surfaces in order to calculate the respective drag coefficients D_f and D_p from equation (2.26). Moreover, since only pressure and friction forces act on the walls, the total drag is:

$$D_t = D_p + D_f. \tag{2.52}$$

This provides, via equation (2.50), a direct relation between the driving pressure gradient and the total-

drag coefficient. By way of global verification, the imbalance between the value of D_t, evaluated from the friction- and pressure-drag contributions, and that arising from the calculation of $P_{\check{x}}$, is observed to be lower than 0.05% of the total drag in most cases. This is an entirely acceptable margin in comparison with previous studies. For example, the force imbalance in Wang et al. (2006) was about 3–4%.

2.6.2 Friction velocity

The friction velocity is defined relative to the frictional stresses as

$$u_\tau = \sqrt{\frac{\bar{\tau}_f}{\rho}}, \tag{2.53}$$

where the mean frictional wall stress $\bar{\tau}_f$ is always positive. This choice is similar to that used in Zilker et al. (1977) and Thorsness et al. (1978), but differs from that of Buckles et al. (1984) or Napoli et al. (2008), who used the total stress instead, i.e. with the pressure drag taken into account. Alternatively, Frederick and Hanratty (1988) based their friction velocity on the baseline friction. In the present research, the main underlying justification for the definition of the friction velocity in equation (2.53) is that the consideration of only the shear-stress contribution presents the advantage of facilitating the focus on the frictional effects in order to compare the results for wavy walls to the those of Stokes layers.

2.7 Uncertainty quantification

The major two sources of error in the numerical solution and its statistical averages are the spatial-discretisation error and the time-averaging error (also sometimes referred to as sampling error). Given the small drag-reduction margins of about 2%, predicted for the wavy wall in Chernyshenko (2013), it is essential to identify and quantify the confidence interval associated with the drag-reduction margin as accurately as possible.

2.7.1 Spatial discretisation

Although strong evidence will be given in section 3.1 that the spatial-discretisation error decreases, in the asymptotic range, in a manner consistent with the 2nd-order discretisation of the fluxes, the provision of a precise confidence interval would require a model of the error for each and every quantity of interest. A detailed analysis of the discretisation error for a plane-channel flow at $Re_\tau \approx 180$ is given

in Oliver et al. (2014), using Bayesian Richardson extrapolations. Satisfactory results were obtained by the model for various quantities such as the centreline velocity and the skin-friction drag. However, it was shown that not all quantities were converging monotonically to the exact value, implying that the model used was not always appropriate—in particular, for the streamwise-velocity variance.

In the context of the present wavy-wall simulations, there is a greater number of degrees of freedom for the discretisation error, arising from the flow skewness and the non-Cartesian deformation of the mesh. Therefore, no general model of the error will be given. Rather, the degree of grid-convergence will be evaluated later in greater detail for some specific cases, with reference to a large pool of selected simulations, and for various relevant quantities.

2.7.2 Finite number of statistical samples

In order to satisfy the stability constraints (Courant–Friedrichs–Lewy condition) of the numerical scheme employed (cf. Hirsch, 2007), the time-stepping interval in the simulations presented is often extremely small ($\Delta t^+ < 0.05$) as a consequence of the spatial spacing being small, thus requiring a larger number of iterations to obtain statistical convergence.

By virtue of the central-limit theorem, the standard deviation of the stochastic fluctuations around the deterministic limit decreases with the inverse of the square-root of the number of independent and identically distributed samples. It is possible to increase the number of independent samples via three main routes:

(1) increasing the duration of the time integration;

(2) ensemble-averaging over multiple independent simulations; or

(3) increasing the domain size.

Nevertheless, it should be noted that the third option may influence the discretisation error which may be sensitive to changes in the former if confinement effects are significant. In terms of the simulation cost and other computational constraints of each route,

(1) the cost of integrating in time is dependent on the time scheme employed;

(2) performing independent simulations requires the use of different initial conditions and hence replicates the number of transient phases;

(3) increasing the domain size prolongs the transient phase by increasing the duration of one flow-through time, and increases the memory and power requirements by enlarging the problem size.

Under the hypothesis of ergodicity, any of the above-mentioned options can be used interchangeably. Nevertheless, it is common practice, for the type of simulations relevant to this work, to select the domain size as small as possible, in the limits allowed by the error associated with finite periodic domain, in order to keep the problem size and the duration of the transient phase to minima.

2.7.3 Quantification of the drag-reduction time-averaging error

The standard deviation of the time-averaging error is estimated using the method of batch means and batch correlations (Russo and Luchini, 2017) applied to the statistically stationary part—i.e. after discarding the transient—of the time history of the total-drag coefficient, defined in equation (2.52), and computed from the value of the instantaneous driving pressure gradient (cf. equation (2.50)). Using the algorithm of Russo and Luchini (2017), estimates for the standard deviation σ and expected value of the drag coefficient D_t are obtained. In the case of the drag-reduction level, both the baseline and the wavy-channel drag levels are affected by a different sampling uncertainty. The drag-reduction rate DR is defined as

$$\mathrm{DR}\left(D_t^0, D_t^{\mathrm{ww}}\right) = \frac{D_t^{\mathrm{ww}}}{D_t^0} - 1, \tag{2.54}$$

where D_t^{ww} and D_t^0 are the expected values of the drag coefficients for the wavy and baseline configurations, respectively. On the assumption that the baseline drag and the wavy-wall drag are independent random variables of respective standard deviations σ_0 and σ_{ww}, the variance of the drag-reduction rate can be calculated from the propagation

$$\sigma_{\mathrm{DR}}^2 = \left(\frac{\partial \mathrm{DR}}{\partial D_t^0}\,\sigma_0\right)^2 + \left(\frac{\partial \mathrm{DR}}{\partial D_t^{\mathrm{ww}}}\,\sigma_{\mathrm{ww}}\right)^2 \tag{2.55a}$$

$$= \left(\frac{D_t^{\mathrm{ww}}}{D_t^0}\frac{\sigma_0}{D_t^0}\right)^2 + \left(\frac{\sigma_{\mathrm{ww}}}{D_t^0}\right)^2 \tag{2.55b}$$

$$= \left(\frac{D_t^{\mathrm{ww}}}{D_t^0}\right)^2 \left[\left(\frac{\sigma_0}{D_t^0}\right)^2 + \left(\frac{\sigma_{\mathrm{ww}}}{D_t^{\mathrm{ww}}}\right)^2\right], \tag{2.55c}$$

where gradients are evaluated from equation (2.26). This yields the expression of the standard deviation of the drag-reduction rate:

$$\sigma_{\mathrm{DR}} = \frac{D_t^{\mathrm{ww}}}{D_t^0}\sqrt{\left(\frac{\sigma_0}{D_t^0}\right)^2 + \left(\frac{\sigma_{\mathrm{ww}}}{D_t^{\mathrm{ww}}}\right)^2}. \tag{2.56}$$

Chapter 3

Verification and validation

Contents

3.1 Method of Manufactured Solutions 68
3.1.1 Introduction 68
3.1.2 Methodology 69
3.1.3 Application 1 – Plane channel 73
3.1.4 Application 2 – Wavy channel 76
3.2 Taylor–Green vortex 79
3.2.1 Problem definition 80
3.2.2 Results 81
3.3 Fully turbulent flows 82
3.3.1 Turbulent plane channel at $Re_\tau \approx 180$ 82
3.3.2 Channel-bump DNS 87
3.3.3 In-plane wall motions 93
3.4 Momentum compatibility condition 94
3.5 Conclusions 96

The purpose of this chapter is to present investigations and tests that demonstrate the validity and formal accuracy of the code. As such, it combines elements of verification and validation. Both are crucially important in the context of predicting solutions for which there are experimental data or independent numerical solution that can be regarded as secure to evaluate the sanity of the numerical implementation.

Verification is a set of tests, some synthetic, that are designed to demonstrate that the basic functionality of the code is correct, with the aim of ensuring that the code is free of influential errors. This is mostly pursued here by the method of manufactured solution.

Validation is more concerned with identifying the predictive performance of the code for geometries akin to those eventually predicted, but with reference to other well-regarded data or analytical solutions.

In this chapter, the series of validation and verification tests employed was carefully selected in preparation for the simulation of turbulent wavy channels, and is comprised of the following elements:

- Method of manufactured solutions in section 3.1
- Three-dimensional Taylor–Green vortex in section 3.2
- Fully turbulent plane-channel flow in section 3.3.1
- Turbulent wavy-wall flow in section 3.3.2
- Turbulent Spatial Stokes Layer in section 3.3.3
- Momentum compatibility condition in section 3.4

3.1 Method of Manufactured Solutions

3.1.1 Introduction

The Method of Manufactured Solution (MMS) is a purely mathematical exercise designed to verify the validity of a numerical implementation within a computational Navier–Stokes solver. The motivation for using this kind of verification method is rooted in the rationale that the verification of the expected numerical validity and accuracy of a code—for example, in terms of convergence—is very sensitive to even subtle coding errors in practical computations of physically realistic flows (Roache, 1997; Salari and Knupp, 2000). The MMS thus offers a powerful tool to verify a numerical code, provided its implementation is undertaken with care.

The MMS consists of an, essentially, arbitrary choice of velocity and pressure fields, which, upon being inserted into the Navier–Stokes equations (in their differential form), result in (non-physical) residuals that are treated as 'source terms'. In effect, these artificial source terms allow the manufactured solution to satisfy the source-term-augmented Navier–Stokes equations. The method thus allows a much greater breadth of flow conditions than physical ones to be examined. When the source terms are inserted into the computational code, the verification entails a comparison of the numerical solution with the manufactured solution that gave rise to source terms. Thus, the code can be tested with complex velocity and pressure fields with no need for physical realism, or even for satisfying physical boundary conditions in some cases (cf. Salari and Knupp, 2000; Roache, 1997, 2002; Roy et al., 2004).

After presenting the procedure used for the derivation of the manufactured solution and associated source terms in section 3.1.2, this method will be applied to two cases. The first, presented in section 3.1.3, was implemented in a plane-channel geometry, while the second, in section 3.1.4, was implemented in a more complex contracting/expanding channel covered by a non-orthogonal irregular mesh.

3.1.2 Methodology

Derivation of the manufactured source term

In the context of realistic simulations, the equations being solved are the Navier–Stokes and mass-conservation equations. With the MMS, a source term $\boldsymbol{S}$ is added to the momentum equation, so that the system to be solved numerically becomes

$$\begin{cases} \dfrac{\partial \boldsymbol{u}}{\partial t} + (\boldsymbol{u}\cdot\boldsymbol{\nabla})\boldsymbol{u} = -\boldsymbol{\nabla}p + \dfrac{1}{Re}\boldsymbol{\nabla}^2\boldsymbol{u} + \boldsymbol{S}, & \text{(3.1a)} \\ \boldsymbol{\nabla}\cdot\boldsymbol{u} = 0, & \text{(3.1b)} \\ \boldsymbol{u}(t=0) = \boldsymbol{u_0}(x,y,z) \qquad \text{plus B.C.'s} & \text{(3.1c)} \end{cases}$$

The boundary conditions are deliberately chosen to reflect subsequent simulations, namely, periodicity in the streamwise and spanwise directions and no-slip conditions at both walls.

Let $\boldsymbol{u_m}$ and p_m be the manufactured velocity and pressure fields, respectively. These satisfy equations (3.1b) and (3.1c), but not the standard Navier–Stokes momentum equation (i.e. equation (3.1a) with $\boldsymbol{S} = \boldsymbol{0}$). In order for the manufactured solution to satisfy the equations solved numerically, it is required that the manufactured source term $\boldsymbol{S} = \boldsymbol{S_m}$ be derived from:

$$\boldsymbol{S_m} = \frac{\partial \boldsymbol{u_m}}{\partial t} + (\boldsymbol{u_m}\cdot\boldsymbol{\nabla})\boldsymbol{u_m} + \boldsymbol{\nabla}p_m - \frac{1}{Re}\boldsymbol{\nabla}^2\boldsymbol{u_m}. \tag{3.2}$$

It follows that $(\boldsymbol{u_m}, p_m, \boldsymbol{S_m})$ is made to be the solution of equation (3.1a). This analytically defined source term is then introduced into the numerical solver, and the test is whether the source-augmented solver yields numerical solutions for the velocity and pressure that are close to $\boldsymbol{u_m}$ and p_m.

While any choice of $\boldsymbol{u_m} = \boldsymbol{f}(x,y,z,t)$ and $p_m = g(x,y,z,t)$ is permissible, in principle, the fields most sensibly chosen, in practice, satisfy the boundary conditions that are most pertinent to later applications. Despite the resulting additional analytical constraint imposed on the manufactured solution, it presents the advantage of not requiring any modification of the implementation of the boundary condi-

tions in the code. Moreover, in incompressible conditions, another important constraint retained is that the velocity field has to satisfy continuity. Although it is possible to add a source term in equation (3.1b) to accommodate for a non-solenoidal manufactured velocity field, only divergence-free fields were considered here. The initial conditions are deduced by simply evaluating the manufactured solution at $t = 0$.

Once an analytical solution satisfying equations (3.1b) and (3.1c) has been selected, the corresponding source terms are calculated analytically from equation (3.1a). Depending on the expression chosen for the manufactured solution, the analytical formulae for the source terms may become lengthy, thus requiring great care in their derivation and numerical implementation in the code. In order to minimise the scope for errors, both the derivation of the source terms and their FORTRAN coding were performed automatically, taking advantage of computer algebra, as pioneered by Steinberg and Roache (1985).

Order of accuracy

In order to evaluate the order of accuracy of the numerical scheme in the code, a suitable norm of the difference between the analytical manufactured solution and the numerical solution is recorded as the grid is refined, or as the time step is diminished in a temporal framework. The error is thus defined as $\varepsilon = \|q - q_m\|$ with $\|\cdot\|$ being a norm, q the numerical solution and q_m the analytical manufactured solution. Here, only the space-discretisation error is considered so that the norm is taken over the 3D volume of the domain, and only L^2- and L^∞-norms are considered: $\|\cdot\| \in \{\|\cdot\|_2, \|\cdot\|_\infty\}$ and $q \in \{u, v, w, p\}$. By decreasing the spacing Δ, if the numerical scheme is consistent and of theoretical order k, then the error asymptotically decreases as $\varepsilon \underset{\Delta \to 0}{\sim} C\,\Delta^k$, where $C > 0$.

The verification criterion for the manufactured solution consists of verifying that the observed order of convergence is consistent with the theoretical order of the numerical scheme employed. The observed order of accuracy k can be calculated as

$$k = \frac{\ln\left(\dfrac{\varepsilon_{\text{coarse}}}{\varepsilon_{\text{fine}}}\right)}{\ln\left(\dfrac{\Delta_{\text{coarse}}}{\Delta_{\text{fine}}}\right)}, \tag{3.3}$$

and this is then compared with the theoretical order. In the present verification, the version of the code use is second order so that the theoretical order for the spatial discretisation is $k_{\text{th.}} = 2$.

Grid refinement

The computational domain contains N cells in each direction (i.e. $(N+1)^3$ mesh points). In the uniform directions, the grid spacing is thus L_i/N. A mapping is applied in the vertical direction so as to refine the grid near the walls, and if the wall-to-wall distance varies with streamwise distance, the wall-normal grid is stretched accordingly. This treatment is very similar to the grid-generation procedure described in sections 2.2.1 and 2.2.2. However, one difference is that the size of the cell closest to the wall is obviously not held constant and has to be refined together with the rest of the mesh. Accordingly, the value of the stretching parameter α in equation (2.11) is set once and kept constant throughout the study.

The pressure solution

The divergence of equation (3.1a), in combination with equation (3.1b), yields a Poisson equation for the pressure:

$$\nabla^2 p = \boldsymbol{\nabla} \cdot [-(\boldsymbol{u} \cdot \boldsymbol{\nabla})\boldsymbol{u} + \boldsymbol{S}] \tag{3.4}$$

in which the divergence of the source term appears. However, it should be noted that the pressure–Poisson equation (2.10) solved during the projection step is distinct in that the contribution of the source terms is already included in the calculation of the non-physical intermediate velocity. As long as the solution velocity field is solenoidal, or that the divergence of the end-of-time-step velocity $\boldsymbol{\nabla} \cdot \boldsymbol{u}^{n+1}$ is negligible in equation (2.9), the manufacturing of the desired test solution $(\boldsymbol{u_m}, p_m)$ does not require any addition of a source term in the pressure solver.

Also, the use of multiple norms provides information about the locality of the error. More specifically, in the context of fractional-step methods, the use of the L^∞-norm is of prime importance for the pressure error, as shown in Brown et al. (2001) and Shirokoff and Rosales (2011). When inadequate boundary conditions are used for the pressure, high error-concentration levels may occur at the no-slip walls. In addition, since the cell volume is small at the wall, such errors would bear a small weight in the L^2-norm. Although the imposition of homogeneous Neumann boundary conditions adopted in STREAM-LES for the pressure field is a standard practice, it should be noted that it is fundamentally approximate (Shirokoff and Rosales, 2011; Chorin, 1969; Ferziger, 1987; Orszag, 1986).

It was observed in Meneghello (2013) that, especially for stationary solutions and anisotropic meshes, homogeneous Neumann boundary conditions resulted in 'unrealistically thick boundary layers where mass is generated or destroyed'. The homogeneous Neumann boundary conditions used in the present

code were described in Temmerman (2004) and follow the recommendations of Bernard and Kapitza (1992) for the determination of the pressure in the halo cells within the solid boundaries. Although the pressure storage is collocated, so that there is no centroid lying exactly on the boundary, the approach includes the imposition of homogeneous Neumann boundary conditions in the Laplace operator and it was observed that the phenomenon described in Meneghello (2013) could indeed occur in some specific cases, with mass residuals being generated in the vicinity of the wall and giving rise to a low-wave-number error in the pressure solution.

When the convergence test of the pressure–Poisson equation was too lax, it was observed that such mass residuals could be maintained and persist until the end of the projection step. When only SLOR sweeps were performed without triggering the multigrid acceleration, these mass residuals were observed to be propagated inside the domain and bounce back and forth from the walls in time, travelling from the upper to the lower solid boundaries and vice versa. The low-wave-number error would then be allowed to subsist and would whether be slowly damped, or more problematically grow until the multigrid cycles were triggered again, thereby resulting in time-discontinuous changes in the pressure solution. This was observed for particular stationary laminar cases of wavy channels and was solved by enforcing a minimum of one multigrid cycle per time-step.

The reason why this problem is particularly sensitive in the case of stationary solutions is that little correction of the pressure solution is required from one time-step to the following, so that the large—but localised—error arising after the SLOR sweeps is not sufficient to make the L^2-norm of the mass residuals overcome the threshold ϵ_P. As far as anisotropic meshes are concerned, the same reasoning leads to the under-representation of the localised mass-conservation violation in the smallest cells which bear a lower weight in the L^2-norm. In a turbulent simulation with sufficiently large time-step[1], the changes in pressure are usually so important that multiple multigrid cycles are required within each time-step, thus effectively preventing such an effect to occur. Therefore, this numerical instability is sensitive to the choices made relative to the number of V-cycles, line relaxations performed at each step of the V-cycles, the number of levels present in the V-cycle and the value chosen for ϵ_P. Possible mitigations include the evaluation of ϵ_P based on the L^∞-norm rather than the L^2-norm, or the improvement of the accuracy of the pressure boundary conditions, but may obviously come at a significant computational cost. In the present research, this phenomenon was never observed when a minimum of one V-cycle per iteration was enforced, with a depth of at least 3 levels in the multigrid V-cycles and $\epsilon_P \leqslant 10^{-9}$.

[1] For small time-steps, another concern that may come into play is the lack of convergence of the classical Rhie-and-Chow interpolation (Shen et al., 2001; Kolmogorov et al., 2015).

3.1.3 Application 1 – Plane channel

Problem definition

The domain under consideration is a plane channel, of half-height h, with periodic streamwise and spanwise directions. All distances are made non-dimensional using the half-height of the channel $h = 1$, so that the streamwise and spanwise lengths are respectively $L_x = 2$ and $L_z = 2$. The walls are located at $y = \pm 1$.

The construction of a manufactured solution is begun by requiring the pressure field to be

$$p_m = A_p \left(1 - y^2\right)^2 \cos\left(\frac{2\pi}{L_x} x\right) \cos\left(\frac{2\pi}{L_z} z\right), \tag{3.5}$$

where the coefficient A_p is set to unity. This pressure field satisfies homogeneous Neumann boundary conditions at the walls and periodicity in the streamwise and spanwise directions.

Next, a solenoidal velocity field $\boldsymbol{u_m} = (u_m, v_m, w_m)^T$ satisfying the boundary conditions is sought. A simple way of satisfying mass conservation is to first choose (u_m, v_m) and then deduce w_m explicitly. Here again, the velocity field has to satisfy periodicity in the longitudinal and transverse directions. The velocity components chosen are:

$$\begin{cases} u_m &= A_u \left(1 - y^2\right) \cos\left(\frac{2\pi}{L_x} x\right) \cos\left(\frac{2\pi}{L_z} z\right), \\ v_m &= A_v \left(1 - y^2\right)^2 \cos\left(\frac{2\pi}{L_x} x\right) \cos\left(\frac{2\pi}{L_z} z\right), \\ w_m &= -\frac{\partial u_m}{\partial x} - \frac{\partial v_m}{\partial y}, \end{cases} \tag{3.6}$$

with the amplitude coefficients all set equal to unity: $A_u = A_v = 1$. The resulting transverse velocity is then explicitly calculated from the other two components:

$$w_m = \frac{L_z \left(1 - y^2\right)}{\pi L_x} \sin\left(\frac{2\pi}{L_z} z\right) \left[\pi A_u \sin\left(\frac{2\pi}{L_x} x\right) + 2 A_v L_x y \cos\left(\frac{2\pi}{L_x} x\right)\right]. \tag{3.7}$$

The final manufactured solution is shown in figure 3.1, demonstrating that the fields chosen for the wall-normal and longitudinal velocities lead to the presence of tilted rolls for the transverse velocity.

Next, the source terms are calculated according to equation (3.2) and their analytical formulae are written automatically into a FORTRAN subroutine. The correctness of the conversion to FORTRAN was manually tested on a particular case by comparing the values given by the compiled code and the evaluation of the analytical formula in Mathematica at a few space locations. The results were found to

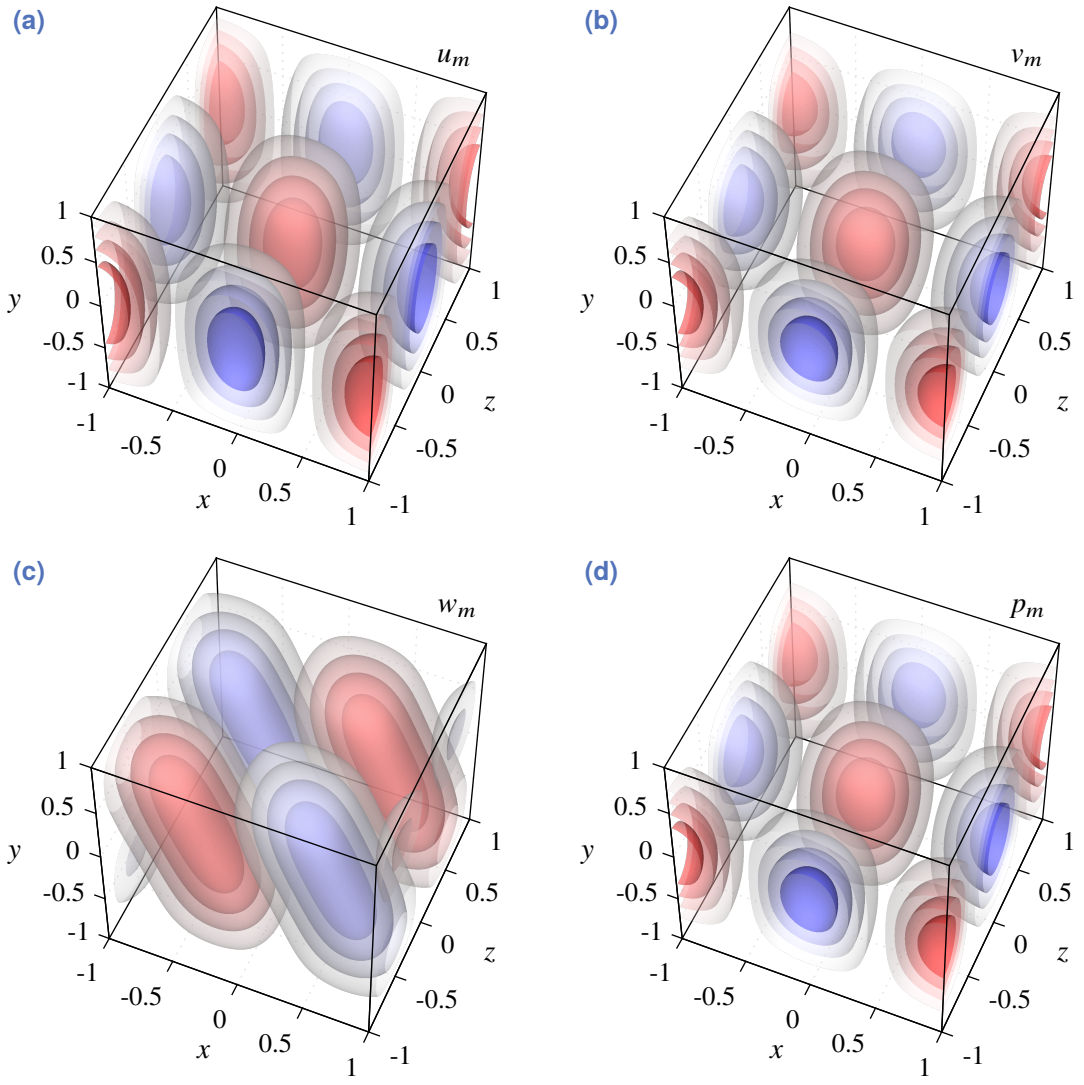


Figure 3.1: Isosurfaces of the velocity components and pressure from the analytical expression of the manufactured solution equations (3.5) and (3.6). The contour values are $\{\pm 0.2, \pm 0.4, \pm, 0.6, \pm 0.8\}$ for **(a)** longitudinal velocity u_m, **(b)** wall-normal velocity v_m, **(c)** transverse velocity w_m, and **(d)** pressure p_m.

match within round-off error.

Results

The numerical solution was calculated by time-advancement starting from the analytical initial condition and marched to convergence. Note that the numerical domain is partitioned into 8 sub-domains (cf. figure 2.2) in order to concurrently exercise the parallel implementation.

The outcome of the study is shown in figure 3.2. The results convey the fact that, as the mesh is refined, the error norms decay in very good accordance with the second-order accuracy of the numerical scheme. It is appropriate to qualify, however, that securing this consistent behaviour necessitated considerable care being taken in respect of the convergence of the pressure-Poisson equation, within any time step, to a level that ensured a very low level of mass residual at the end of the in-step iteration, prior to the next time step being taken. In typical (physical) channel-flow simulations, the L^2-norm of the mass residuals, is set at $\epsilon_P = 10^{-10}$, but this was reduced to 10^{-15} in the present case in order to significantly reduce the time needed for the solution to converge.

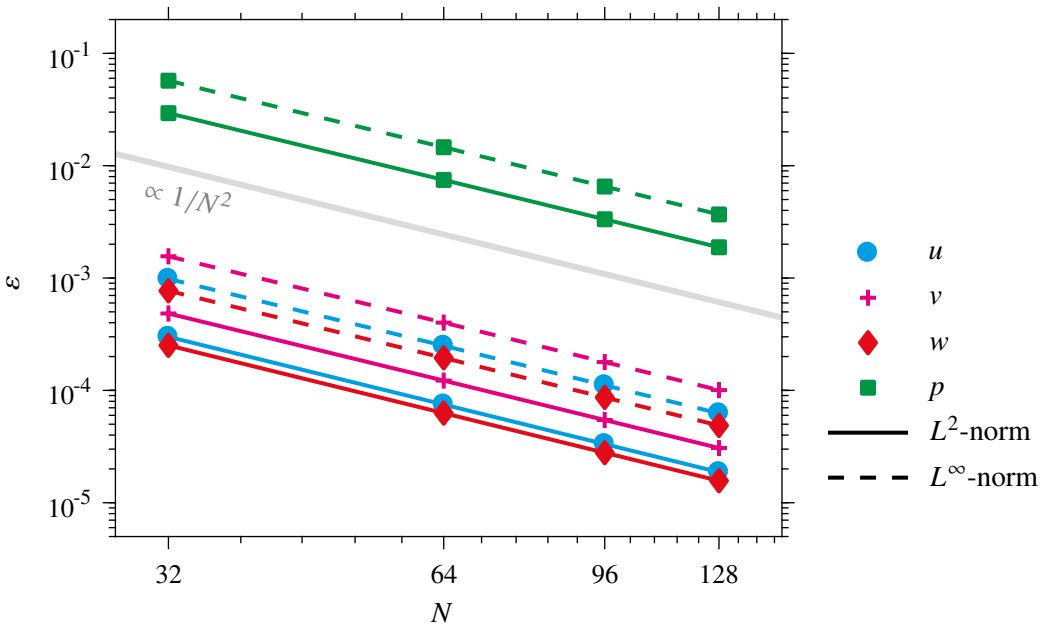


Figure 3.2: Norms of the error for various levels of refinement (plane channel case). There are two lines per quantity, the upper one (dashed) corresponds to the L^∞-norm and the lower (continuous) to the L^2-norm.

3.1.4 Application 2 – Wavy channel

Problem description

The above study is here extended to a wavy channel with a geometry similar to that considered by Maaß and Schumann (1996) in their DNS study. This will test the reliability of the code in the case of non-orthogonal grids.

The domain of solution is shown in figure 3.3. The mean height is $L_y = 2h = 2$, and the streamwise and spanwise directions are periodic of length $L_x = L_z = 2$, with $x_i \in [-L_i/2, L_i/2]$. The upper wall is located at $y_{uw} = 1$ and the lower wall at $y_{lw} = -1 + h_w(x)$ where:

$$h_w(x) = \frac{1}{10}\cos\left(\frac{2\pi}{L_x}x\right). \tag{3.8}$$

The pressure field is chosen to be

$$p_m = (y - y_{lw})^2(y - y_{uw})^2 \cos\left(\frac{2\pi}{L_x}x + \frac{2\pi}{L_z}z\right), \tag{3.9}$$

so that it approximately satisfies homogeneous Neumann boundary conditions at both walls.

Next, a non-trivial velocity field is sought. Unfortunately, the procedure used for the plane channel is not as straightforward in the wavy case owing to the more complex geometry of the wavy boundary. However, a particular solenoidal solution satisfying the boundary conditions was found using two three-

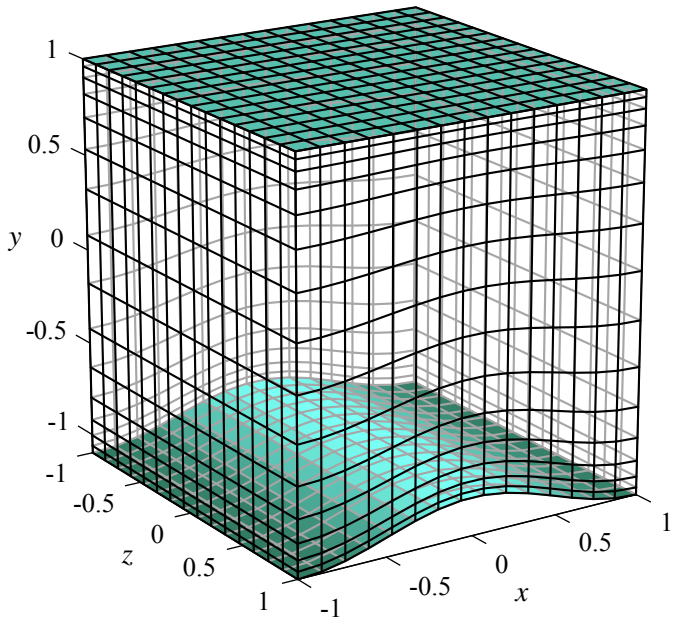


Figure 3.3: Computational domain for the wavy-channel application on a multi-block partition comprising 8 blocks, shown for a coarse mesh with $N = 16$.

dimensional stream functions ψ_1 and ψ_2 (Greywall, 1991; Warsi, 1999). A streamline results from the intersection of two stream surfaces defined by ψ_1 = constant and ψ_2 = constant. Given two stream functions ψ_1 and ψ_2, a three-dimensional velocity field can then be derived from:

$$\boldsymbol{u_m} = (\boldsymbol{\nabla}\psi_1) \times (\boldsymbol{\nabla}\psi_2). \tag{3.10}$$

A pair of stream functions that result in the boundary conditions and mass conservation being satisfied are:

$$\begin{cases} \psi_1 &= \sin(y - y_{lw}) \sin(y - y_{uw}) \cos\left(\dfrac{2\pi}{L_x}x + \dfrac{2\pi}{L_z}z\right), \\ \psi_2 &= (y - y_{lw})(y - y_{uw}) \cos\left(\dfrac{2\pi}{L_x}x + \dfrac{2\pi}{L_z}z\right). \end{cases} \tag{3.11}$$

Once the two stream functions have been chosen, the velocity field is deduced from equation (3.10) in Cartesian coordinates:

$$\begin{cases} u_m &= \dfrac{\partial\psi_1}{\partial y}\dfrac{\partial\psi_2}{\partial z} - \dfrac{\partial\psi_1}{\partial z}\dfrac{\partial\psi_2}{\partial y}, \\ v_m &= \dfrac{\partial\psi_1}{\partial z}\dfrac{\partial\psi_2}{\partial x} - \dfrac{\partial\psi_1}{\partial x}\dfrac{\partial\psi_2}{\partial z}, \\ w_m &= \dfrac{\partial\psi_1}{\partial x}\dfrac{\partial\psi_2}{\partial y} - \dfrac{\partial\psi_1}{\partial y}\dfrac{\partial\psi_2}{\partial x}. \end{cases} \tag{3.12}$$

Isosurfaces of the resulting manufactured solution fields are presented in figure 3.4. The plots show the distortion of the rolls accommodating for the no-slip boundary condition at the wavy surface, and visually display more complexity than the plane-channel manufactured solution in figure 3.1.

Eventually, the same procedure described in section 3.1.3 was repeated: the manufactured fields equations (3.9) and (3.11) were inserted into equation (3.2), a FORTRAN subroutine containing the manufactured solution and the source terms was written, and the numerical fields were derived by a time-marching solution. In this case, the automatic generation of the FORTRAN subroutine by the symbolic computation program is essential since the resulting manufactured fields and source terms contain a large number of terms.

Results

The results for this more complex case are similar to those previously obtained for the plane channel. Figure 3.5 shows the norm of the error for four levels of grid refinement with the total number of cells ranging from 32^3 to 128^3. As in the previous plane-channel-flow case, second-order accuracy is recovered. For example, applying equation (3.3) to the coarsest and finest simulations for the error in

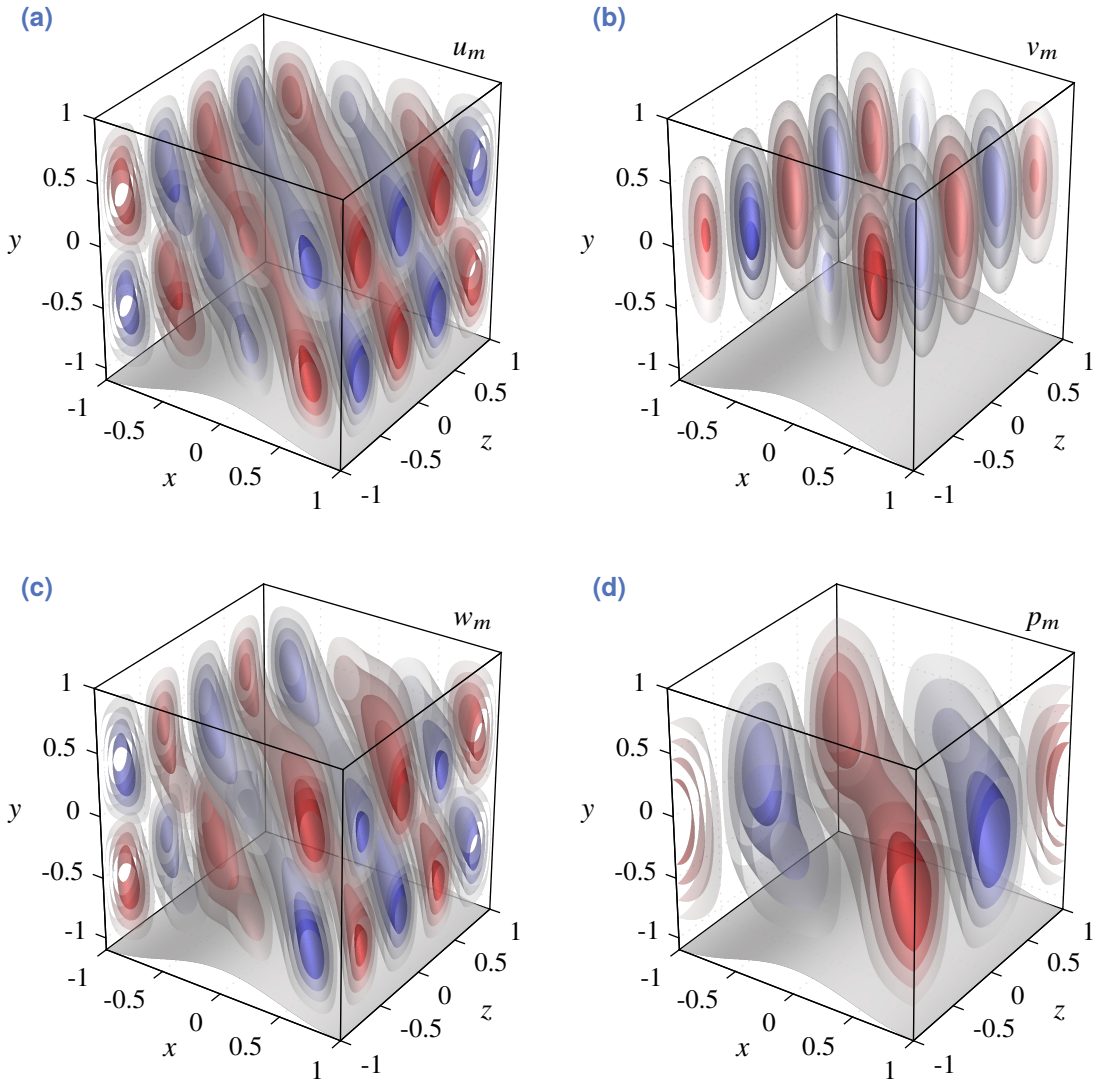


Figure 3.4: Isosurfaces of the resulting velocity components and pressure from the analytical expression of the manufactured solution derived from equations (3.9), (3.11) and (3.12). The contours correspond to $\{\pm 0.2, \pm 0.4, \pm, 0.6, \pm 0.8\}$ times the L^∞-norm of **(a)** longitudinal velocity u_m, **(b)** wall-normal velocity v_m, **(c)** transverse velocity w_m, and **(d)** pressure p_m.

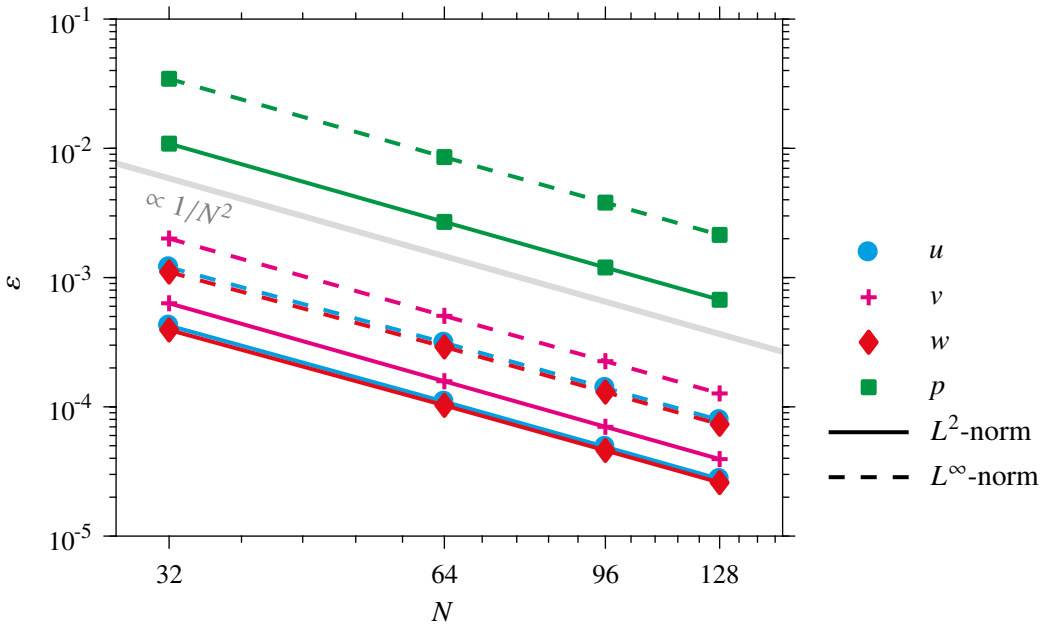


Figure 3.5: L^2- and L^∞-norms of the error for various levels of refinement (wavy-channel case).

pressure under the L^∞-norm yields an observed order of 1.98 which is in very good agreement with the expected second-order accuracy.

3.2 Taylor–Green vortex

The three-dimensional incompressible Taylor–Green vortex was originally studied in the seminal paper of Taylor and Green (1937). It is a very simple configuration in which a set of large vortices form an initial field that is allowed to evolve into turbulence that eventually decays by dissipation. The test criteria are then the evolution of turbulence energy, enstrophy, and dissipation rate. The initial velocity field is described by:

$$\begin{cases} u(t=0) &= A\cos(ax)\sin(by)\sin(cz), \\ v(t=0) &= B\sin(ax)\cos(by)\sin(cz), \\ w(t=0) &= C\sin(ax)\sin(by)\cos(cz), \end{cases} \tag{3.13}$$

where A, a, B, b, C, c must satisfy some constraints ensuring that the velocity field is consistent with the Navier–Stokes equations, and the initial pressure field is calculated analytically from the pressure–Poisson equation. An equivalent formulation of this flow was then studied by Brachet et al. (1983) who used a change of reference in order to simplify the Fourier representation used in the numerical

solution. This yields the following expression for the initial condition:

$$\begin{cases} u(t=0) &= \sin x \cos y \cos z, \\ v(t=0) &= -\cos x \sin y \cos z, \\ v(t=0) &= 0, \end{cases} \tag{3.14}$$

which is the formulation chosen in this section.

Beyond the fundamental interest of the properties of the Taylor–Green vortex for understanding turbulence, it also serves as a sensitive test-case for validation purposes. Thus, there is a plethora of available studies comparing numerical simulations of the exact same problem spanning a wide range of discretisation strategies (e.g. Wang et al., 2013; Bull and Jameson, 2015; Jacobs et al., 2017; Vermeire et al., 2017).

3.2.1 Problem definition

The simulations were performed in a triply periodic cubic box of size $2\pi L$, each direction spanning $[-\pi L, \pi L]$ and discretised over N cells. Unlike in periodic channels, there is no driving force powering the system, so there is no momentum body force: $\boldsymbol{f} = \boldsymbol{0}$. The initial flow solution, at a given Reynolds number of $Re = V_0\, L/\nu = 1600$, was taken to be:

$$\begin{cases} u^0 &= V_0 \sin\left(\dfrac{x}{L}\right) \cos\left(\dfrac{y}{L}\right) \cos\left(\dfrac{z}{L}\right), \\ v^0 &= -V_0 \cos\left(\dfrac{x}{L}\right) \sin\left(\dfrac{y}{L}\right) \cos\left(\dfrac{z}{L}\right), \\ w^0 &= 0, \\ p^0 &= p_0 + \dfrac{\rho V_0}{16}\left[\cos\left(\dfrac{2x}{L}\right) + \cos\left(\dfrac{2y}{L}\right)\right]\left[\cos\left(\dfrac{2z}{L}\right) + 2\right], \end{cases} \tag{3.15}$$

and was then advanced in time until the non-dimensional time $tV_0/L = 20$ was reached.

Although there is no spanwise velocity at $t = 0$, the initial vortex lines are twisted, and all the components of the corresponding initial vorticity field $\boldsymbol{\omega}^0$ are non-zero, resulting in three-dimensional vortex stretching, which in turn produces small-scale eddies. More precisely, the initial vorticity field is more intense in the transverse direction, as shown by calculating the components of $\boldsymbol{\omega}^0 = \boldsymbol{\nabla} \times \boldsymbol{u}^0$

arising from equation (3.15):

$$\begin{cases} \omega_x^0 &= -\dfrac{V_0}{L}\cos\left(\dfrac{x}{L}\right)\sin\left(\dfrac{y}{L}\right)\sin\left(\dfrac{z}{L}\right), \\ \omega_y^0 &= \dfrac{V_0}{L}\sin\left(\dfrac{x}{L}\right)\cos\left(\dfrac{y}{L}\right)\sin\left(\dfrac{z}{L}\right), \\ \omega_z^0 &= 2\dfrac{V_0}{L}\sin\left(\dfrac{x}{L}\right)\sin\left(\dfrac{y}{L}\right)\cos\left(\dfrac{z}{L}\right). \end{cases} \tag{3.16}$$

3.2.2 Results

The simulations are run with a variable time step, which is adjusted to maintain the convective CFL number below 0.25 and the diffusive one below 0.1. Since the mesh is Cartesian, both the 4th- and 2nd-order versions of the code may be used, allowing for the two to be compared. At each time step, the kinetic energy in integrated in the solution volume $\mathcal{V}$ as

$$\mathcal{K} = \frac{1}{\mathcal{V}}\iiint_{\mathcal{V}} \frac{1}{2}u_i u_i \,\mathrm{d}V, \tag{3.17}$$

together with the enstrophy

$$\mathcal{E} = \frac{1}{\mathcal{V}}\iiint_{\mathcal{V}} \frac{1}{2}\omega_i \omega_i \,\mathrm{d}V \tag{3.18}$$

which is also computed.

The simulations performed are presented in table 3.1, along with a measure of the error in the amplitude of the peak of enstrophy relative to the spectral simulation

$$\varepsilon_{\mathcal{E}} = \frac{\left|\mathcal{E}_{\max} - \mathcal{E}_{\max}^{\text{spectral}}\right|}{\mathcal{E}_{\max}^{\text{spectral}}}. \tag{3.19}$$

The generation of small eddies is illustrated by means of isosurfaces of the instantaneous z-vorticity at several time instants in figure 3.6 for the 2nd-order results, at the coarsest and finest resolutions,

Table 3.1: List of simulations performed and error in the peak of enstrophy relative to the spectral solution ($\varepsilon_{\mathcal{E}}$).

Order	N	Number of time steps	$\varepsilon_{\mathcal{E}}$ (%)
2	64	620	52
2	128	1283	17
2	256	2783	10
4	64	655	37
4	128	1340	11
4	256	2773	1

namely for $N = 64$ and $N = 256$ cases, respectively. Although at time $tV_0/L \approx 5$ the isosurfaces are qualitatively similar in figure 3.6(c,d), the lack of spatial resolution is clearly noticeable in figure 3.6c.

The time evolutions of $\mathcal{K}$ and $\mathcal{E}$ are shown in figures 3.7 to 3.9 in comparison with a spectral DNS solution. As expected, the 4th-order solution is closer to the spectral DNS and both versions seem to converge to the same profile as the spectral solution.

For an incompressible flow, there exists an exact correspondence between the energy dissipation rate and the enstrophy $-\mathrm{d}\mathcal{K}/\mathrm{d}t = 2\nu\mathcal{E}$. Therefore, figure 3.8 and figure 3.9 are physically the same by a scale factor of 2ν. The agreement between the present solutions and the spectral solution for the dissipation rate, shown in figure 3.8, is better than that achieved for the enstrophy. Thus, the increase and decay of the enstrophy is significantly more sensitive to the grid resolution than the energy dissipation rate, when calculated from the kinetic energy.

The data show, as expected, that when a 4th-order discretisation is employed in lieu of a 2nd-order discretisation, the error is smaller and decreases at a faster rate. Additionally, the decay of the error in the peak enstrophy as the mesh spacing is decreased, deductible from table 3.1, leads to the conclusion that the convergence rate is slower for the latter quantity than that of the solution variables (i.e. 2nd- or 4th-order).

3.3 Fully turbulent flows

3.3.1 Turbulent plane channel at $Re_\tau \approx 180$

Detailed statistical fields from DNS of plane-channel flows at $Re_\tau \approx 180$ are well documented in the literature (e.g. Moser et al., 1999; Hoyas and Jiménez, 2008) hence this particular value of the friction Reynolds number was used as part of the validation and verification of the code and the associated post-processing routines. As the channel flow is invariant to changes in flow angle θ_f, it may also serve as a verification of the implementation of the flow-skewness methodology (cf. section 2.4). Thus, three cases are considered in table 3.2: the first is not skewed, made of a standard box size slightly larger than $4\pi h \times 2\pi h$, with a resolution twice as fine in the spanwise direction as in the streamwise direction. In contrast, in the other two cases, the main flow direction makes an angle of $\theta_f \in \{52°, 70°\}$ with the grid, and the x- and z-wise resolutions and periodic lengths are identical in the wall-parallel directions. The reason for selecting angles different from $\pi/4$ is to ensure that $\cos\theta_f \neq \sin\theta_f$, in order to prevent possible exact cancellations of the skewness effects, which could potentially mask

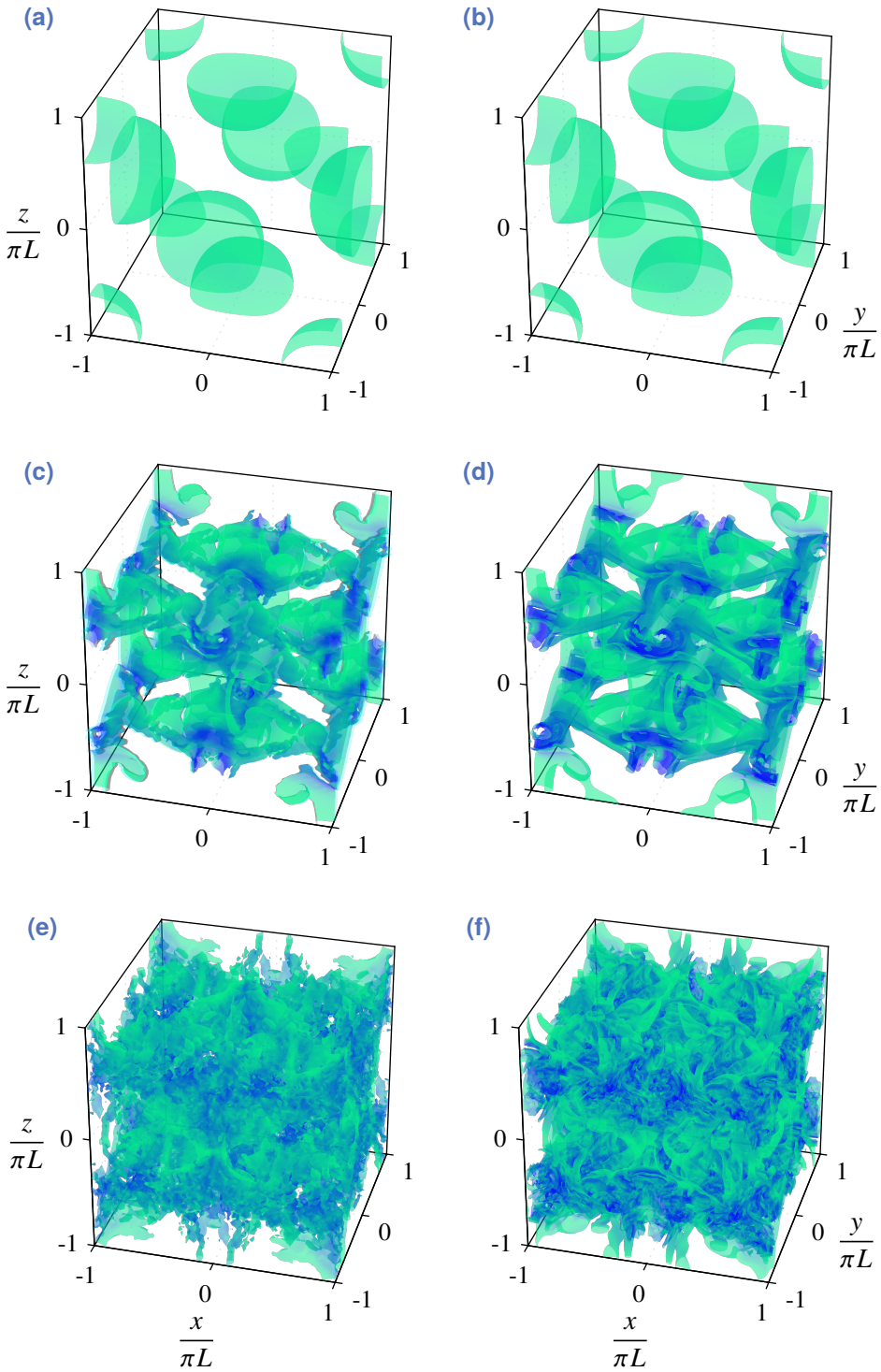


Figure 3.6: Isocontours of the instantaneous z-vorticity coloured by vorticity magnitude at various time instants for the coarsest and finest 2nd-order simulations. Columns: **(a,c,e)** 64^3-cell grid, **(b,d,f)** 256^3-cell grid; rows: **(a,b)** at $tV_0/L \approx 0.1$, **(c,d)** $tV_0/L \approx 5$, **(e,f)** $tV_0/L \approx 10$.

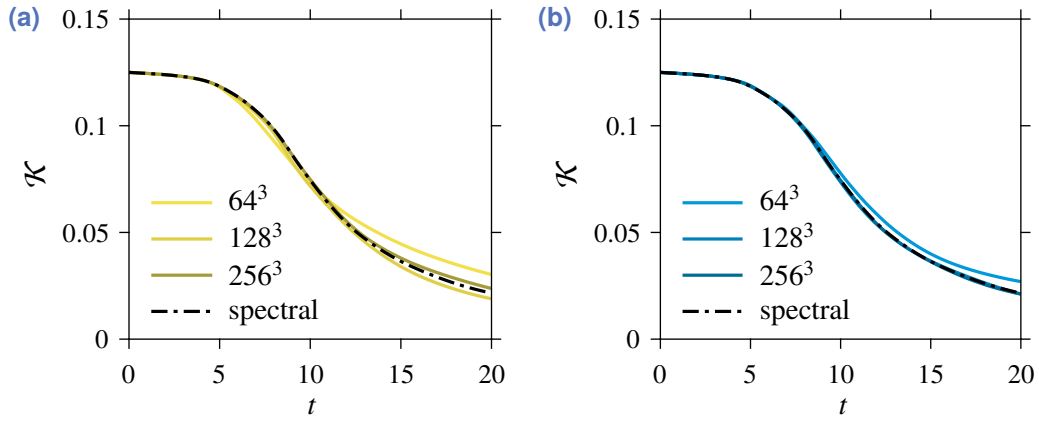


Figure 3.7: Temporal evolution of the kinetic energy compared to the spectral solution on a 512^3 grid. All quantities are made non-dimensional using V_0 and L. **(a)** 2nd-order code, **(b)** 4th-order code.

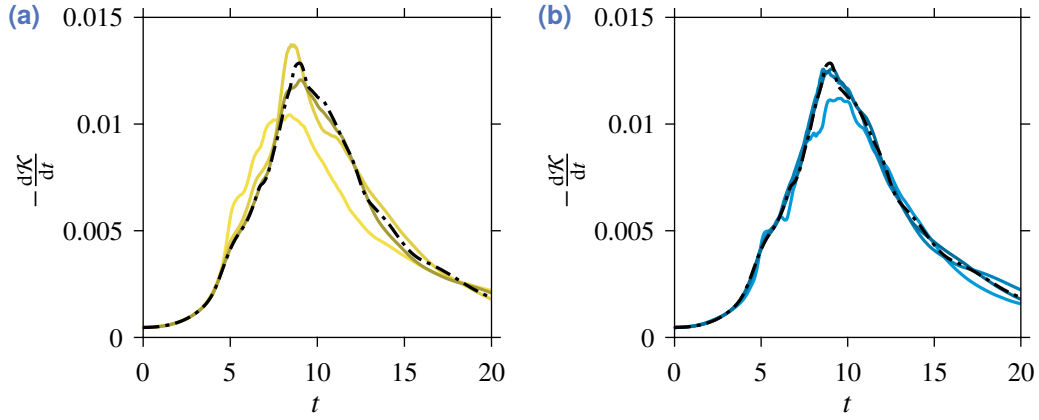


Figure 3.8: Temporal evolution of the dissipation rate computed from the decay of $\mathcal{K}$. Same legend as figure 3.7. **(a)** 2nd-order code, **(b)** 4th-order code.

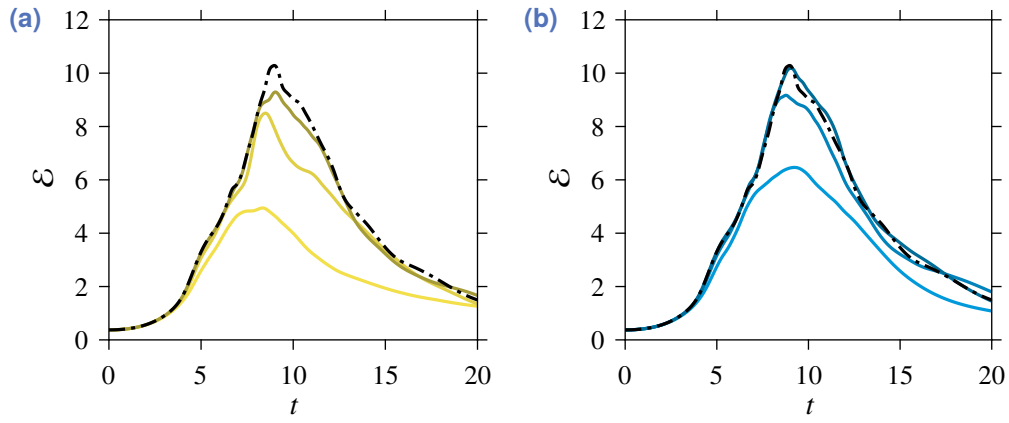


Figure 3.9: Temporal evolution of the enstrophy computed explicitly from the velocity field. Same legend as figure 3.7. **(a)** 2nd-order code, **(b).** 4th-order code

Table 3.2: Turbulent plane-channel-flow simulations at $Re_\tau \approx 180$.

	Re_b	Re_τ	Δx^+	Δy^+	Δz^+	L_x/h	L_z/h	$N_x \times N_y \times N_z$
$\theta_f = 0°$	2925	185.0	3.2	0.5 – 3.3	1.8	15	7.5	$864 \times 192 \times 768$
$\theta_f = 52°$	2820	179.4	2.4	0.7 – 2.9	2.4	10.2	10.2	$768 \times 192 \times 768$
$\theta_f = 70°$	2820	179.4	1.2	0.6 – 3.1	1.2	10.2	15.3	$1536 \times 192 \times 2304$

implementation errors in the post-processing, especially in the calculation of spatial partial derivatives.

First, the streamwise-velocity and Reynolds-stress profiles are compared with the spectral simulation of Moser et al. (1999) in figure 3.10. The agreement with the reference data is very satisfactory for all flow angles, thus validating the implementation of the rotation for first- and second-order statistics described in section 2.5.1.

Second, the contributions to the transport of turbulence energy are also compared with the reference data as follows:

$$\text{Production:} \quad \mathcal{P}_k = -\overline{u_i' u_j'} \frac{\partial \overline{u}_i}{x_j}, \tag{3.20a}$$

$$\text{Dissipation:} \quad \epsilon_k = \nu \overline{\frac{\partial u_i'}{\partial x_j} \frac{\partial u_i'}{\partial x_j}}, \tag{3.20b}$$

$$\text{Pressure diffusion:} \quad \Pi_k = -\frac{\partial \overline{p' u_i'}}{\partial x_i}, \tag{3.20c}$$

$$\text{Turbulent diffusion:} \quad T_k = -\frac{1}{2} \frac{\partial \overline{u_i' u_j' u_j'}}{\partial x_j}, \tag{3.20d}$$

$$\text{Viscous diffusion:} \quad D_k = \frac{\nu}{2} \frac{\partial^2 \overline{u_i' u_i'}}{\partial x_j \partial x_j}, \tag{3.20e}$$

$$\text{Pressure strain:} \quad \Phi_k = \overline{p' \frac{\partial u_i'}{\partial x_i}} = 0, \tag{3.20f}$$

where the pressure strain is zero as a consequence of the incompressibility condition. The balance for the turbulence energy becomes:

$$\frac{\bar{D}k}{Dt} = \mathcal{P}_k - \epsilon_k + \Pi_k + T_k + D_k. \tag{3.21}$$

All quantities are calculated in the frame of reference of the flow, but the notation '$\breve{\cdot}$' is omitted for simplicity. For cases where the main flow direction is at an angle to the mesh, since the statistics

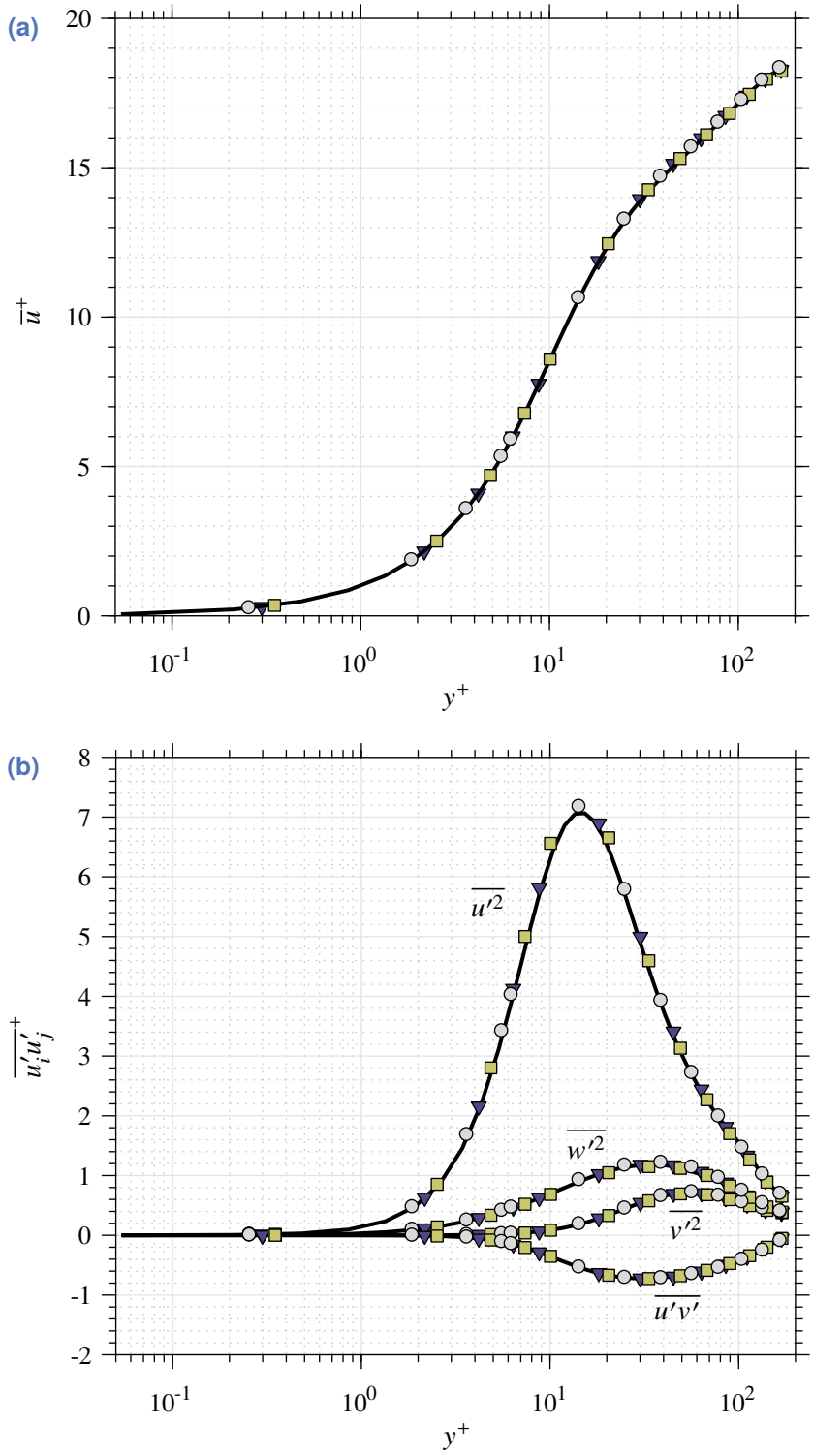


Figure 3.10: Comparison of the wall-scaled streamwise velocity and Reynolds stresses of the simulations presented in table 3.2 with the spectral DNS of Moser et al. (1999), consisting of a plane-channel flow at $Re_\tau \approx 180$, **(a)** streamwise velocity $\overline{u}^+$, **(b)** Reynolds stresses $\overline{u_i' u_j'}^+$. The black line is the reference simulation Moser et al. (1999), circles are for a flow aligned with the grid at $\theta_f = 0°$, squares at $\theta_f = 52°$, and inverted triangles at $\theta_f = 70°$.

are accumulated in an x–y plane, special care was required in the calculation of the flow-orientated derivatives.

Figure 3.11 demonstrates that the present simulations agree very well with the reference spectral DNS regardless of the angle of the flow. Attention is drawn, in particular, to the values of the dissipation and viscous diffusion at the cell closest to the wall, where the two match, as required. This agreement was found to be particularly sensitive to the way in which the second derivatives are computed at the wall in the post-processing.

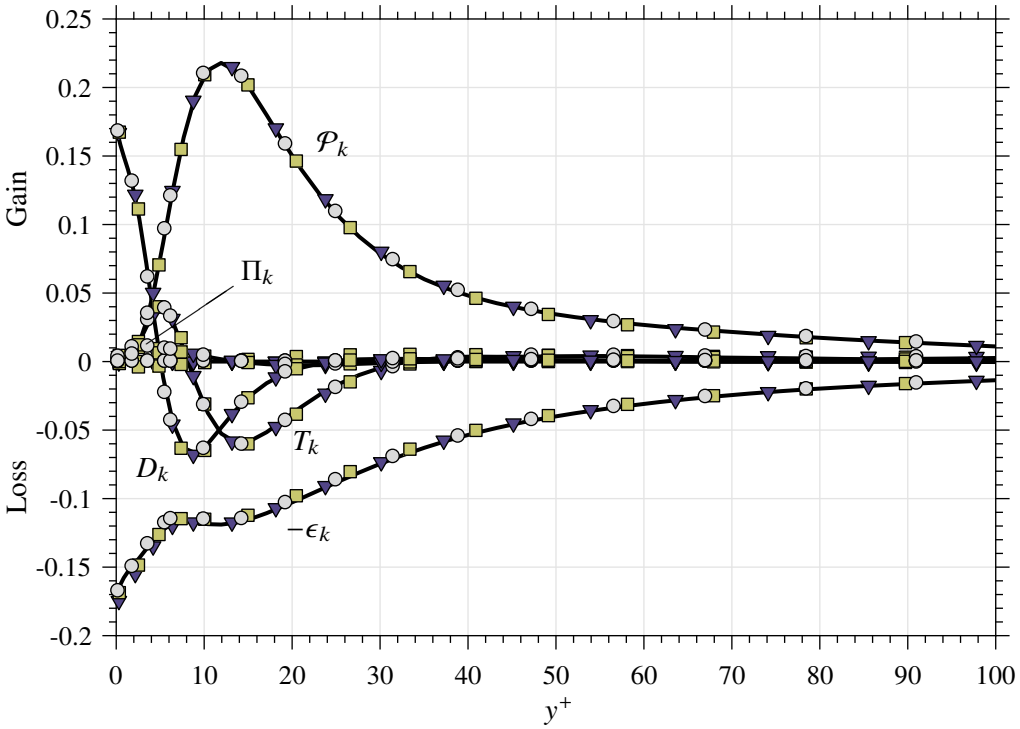


Figure 3.11: Contributions to the turbulence-energy budgets in wall units. Same legend as in figure 3.10.

3.3.2 Channel-bump DNS

Presentation of the numerical experiment

Several studies of flows over sinusoidally shaped walls, either experimental or analytical, can be found in the literature (Zilker et al., 1977; Abrams and Hanratty, 1985; Hudson et al., 1996; De Angelis et al., 1997; Calhoun and Street, 2001; Knotek and Jícha, 2014). Efforts were mainly devoted to understanding and modelling the turbulent flow properties, which are pertinent to geophysical applications such as sediment transport or flow coupling between ocean and atmosphere (cf. Calhoun and Street, 2001;

De Angelis et al., 1997; Cherukat et al., 1998). Various degrees of wave steepness (the ratio between wave height and length) were explored, from the linear response over small-amplitude waves (Zilker et al., 1977; Abrams and Hanratty, 1985), to higher amplitudes leading to flow-separation and exhibiting high adverse pressure gradients (Hudson et al., 1996; Maaß and Schumann, 1996). Although separation is outside the scope of the principal research effort pursued here, separated flows are rich and complex cases, which present high sensitivity in the spatial location of the separation and reattachment points. For this reason, the DNS of a separated flow over a wavy terrain, presented along with experimental data in Maaß and Schumann (1996), and shown in figure 3.12, was selected as a validation case. Since the experimental data reported in Maaß and Schumann (1996) was in good agreement with their DNS, only the DNS results are shown in the present comparison.

DNS results

Figures 3.13 to 3.18 show comparisons with the data provided by Maaß and Schumann in the ERCOFTAC Classic Database (case 77). Only the lower half of the domain is presented for brevity, focusing on the separated region of the flow. The computational domain, covered with a body-fitted mesh, consists of an upper plane wall and a lower cosinusoidal wall, accommodating two full wavelengths. The statistics presented are phase averaged over both waves.

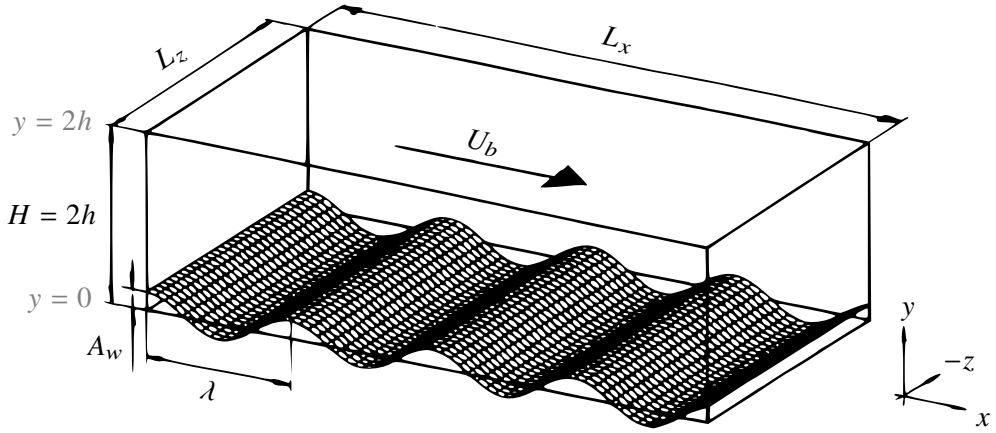


Figure 3.12: Sketch of the reference simulation domain, comprising four waves, adapted from Maaß and Schumann (1996), with different notations consistent with the simulations presented herein. The parameters of the flow configuration are $A_w/\lambda = 0.1$, $\lambda = H$, and $Re_H = U_b H/\nu = 6760$. [Adapted by permission from Springer eBook: Springer Nature, *Notes on Numerical Fluid Mechanics*, 'Direct numerical simulation of separated turbulent flow over a wavy boundary', Maaß, C. and Schumann, U. (1996), doi:10.1007/978-3-322-89849-4_17, license number 4315941022427.]

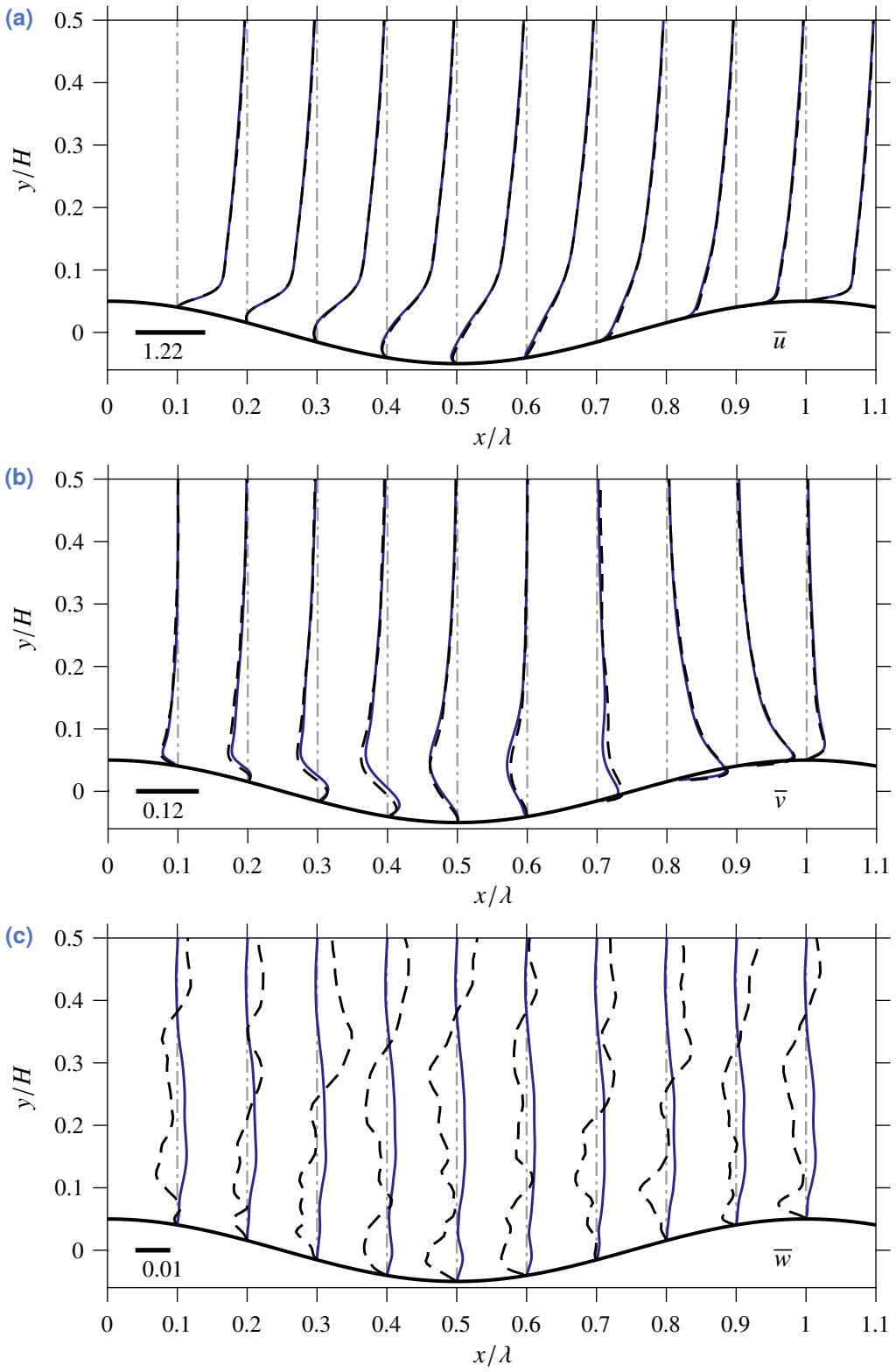


Figure 3.13: Velocity profiles at various phase locations normalized by U_b. The scale is indicated in the bottom left corner. The grey dot-dashed line represents the zero line. Dashed lines: data of Maaß and Schumann (1996), continuous blue lines: present DNS. **(a)** streamwise velocity $\overline{u}$, **(b)** vertical velocity $\overline{v}$, and **(c)** spanwise velocity $\overline{w}$.

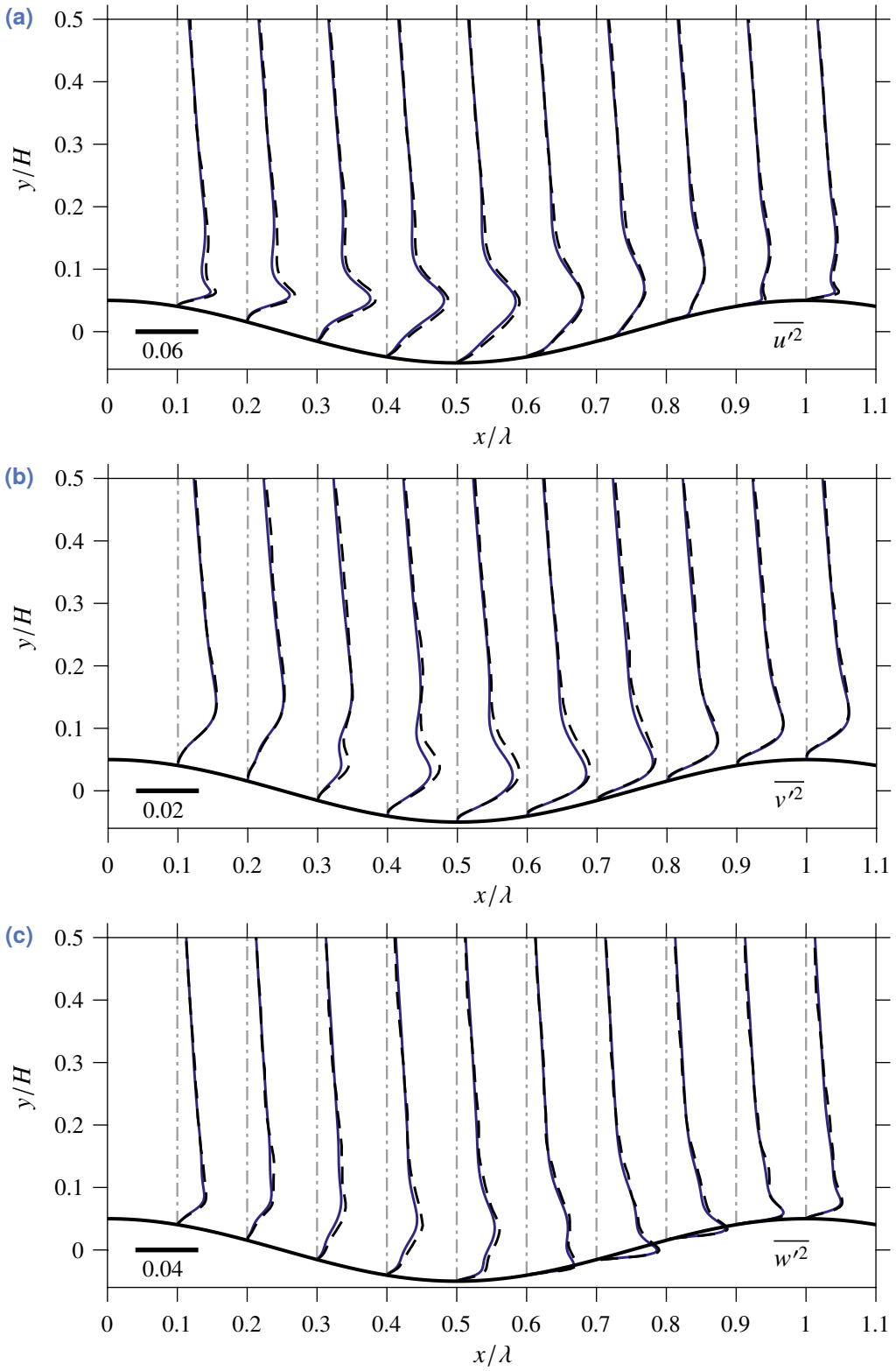


Figure 3.14: Normal Reynolds stresses normalized by U_b^2 at various phase locations; **(a)** longitudinal stresses $\overline{u'^2}$, **(b)** vertical stresses $\overline{v'^2}$, and **(c)** transverse stresses $\overline{w'^2}$; same legend as figure 3.13.

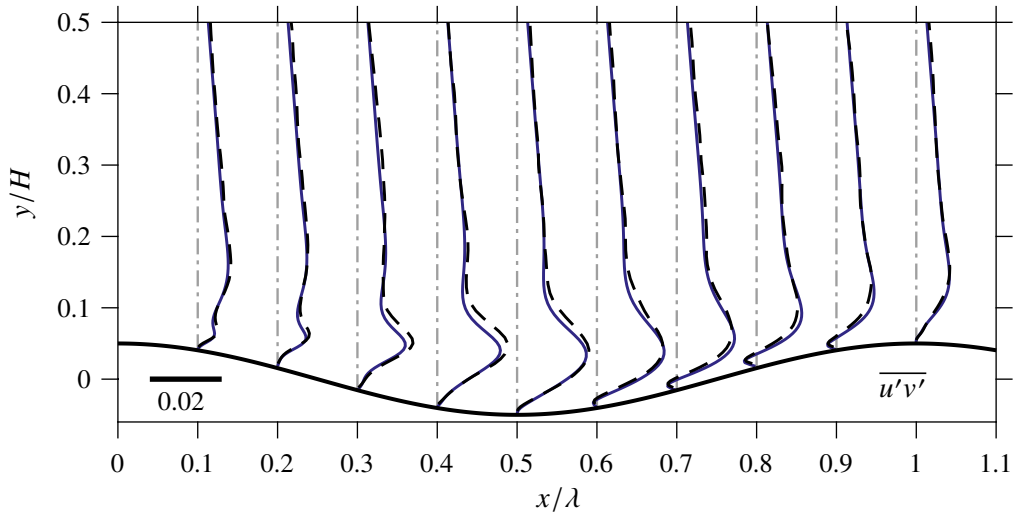


Figure 3.15: Reynolds shear stress $\overline{u'v'}$ normalized by U_b^2 at various phase locations; same legend as figure 3.13.

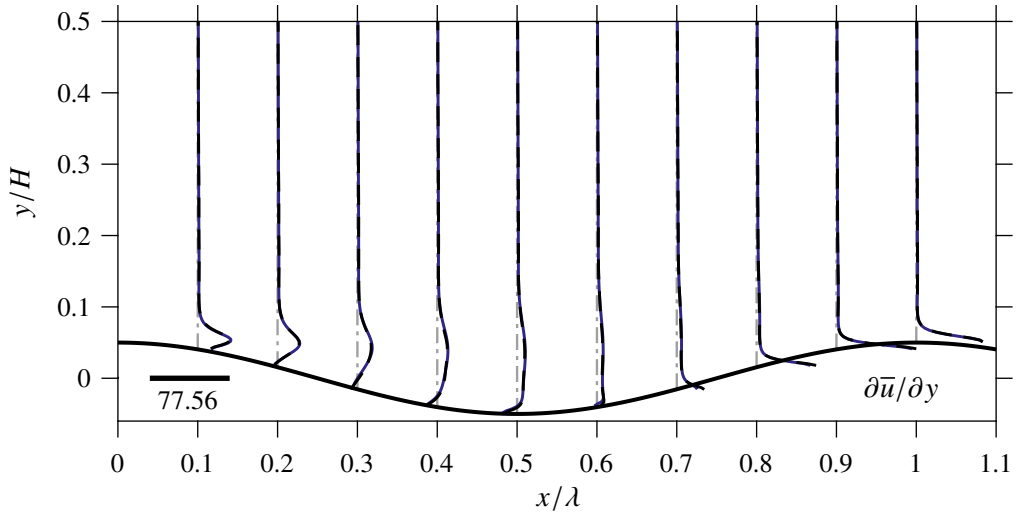


Figure 3.16: Velocity gradient $\partial\overline{u}/\partial y$ normalised by U_b/h at various phase locations; same legend as figure 3.13.

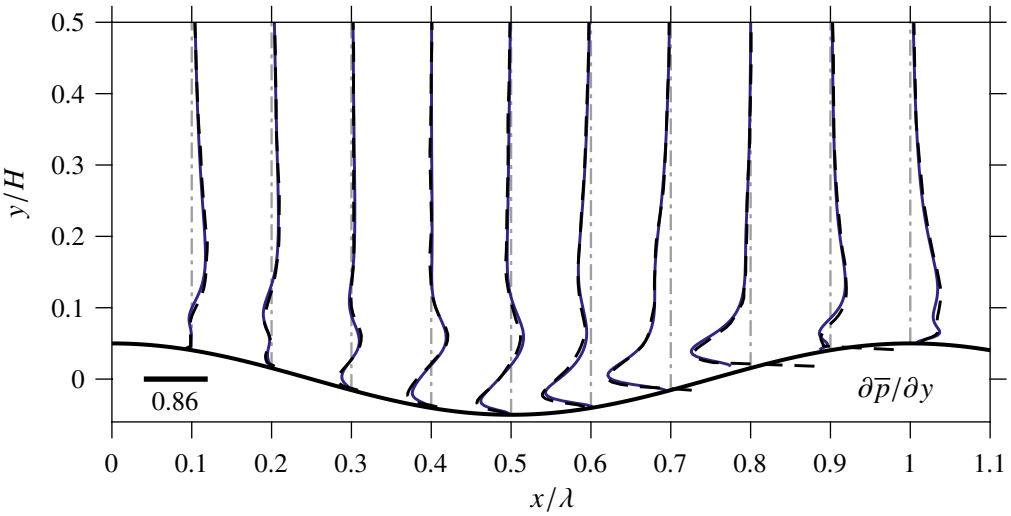


Figure 3.17: Pressure gradient $\partial\overline{p}/\partial y$ normalised by U_b^2/h at various phase locations; same legend as figure 3.13.

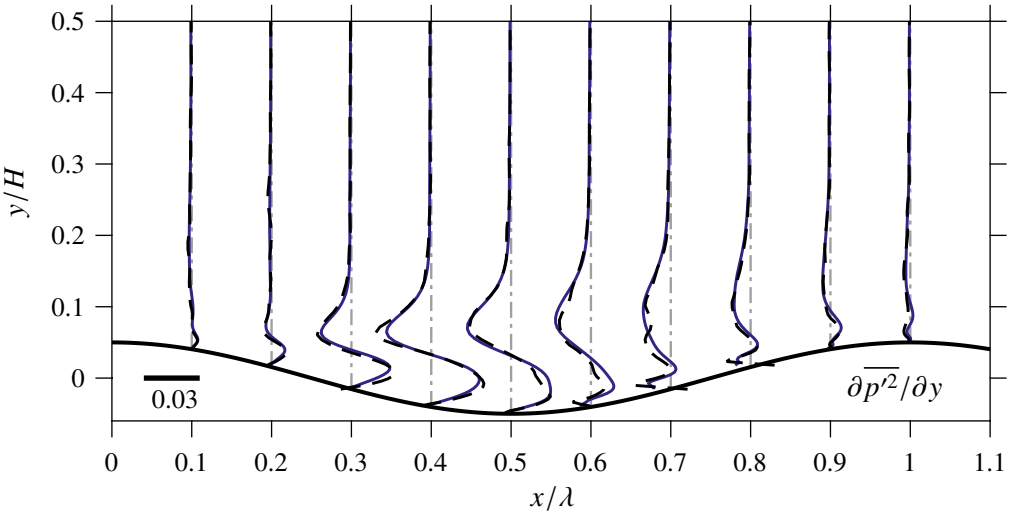


Figure 3.18: Gradient of the variance of the pressure fluctuations $\partial\overline{p'^2}/\partial y$ normalised by U_b^4/h at various phase locations; same legend as figure 3.13.

The present DNS is in good agreement with all the quantities provided in the database from Maaß and Schumann. Modest discrepancies are observed in the separated region—in particular, close to the separation and reattachment locations, i.e. where the complexity of the flow is higher. The flow separates at approximately $x/\lambda = 0.15$ and reattaches at $x/\lambda = 0.62$. Thus, the separated region is slightly larger than in Maaß and Schumann (1996) ($x/\lambda \in [0.15, 0.59]$). The vertical pressure gradient of the reference case, corresponding to the dashed line in figure 3.17, was calculated from the pressure profiles provided in the database by central differencing and single-sided differences at the walls. This may account for the abnormal values very close to the wall around the position $x/\lambda \approx 0.8$.

The spanwise velocity profiles are compared in figure 3.13c. Although they are not physically meaningful—the spanwise direction being homogeneous, their comparison provides a good indication of the convergence of the statistics and shows that the longer integration time of the present DNS compared to that in Maaß and Schumann (1996) results in a lower spanwise velocity.

3.3.3 In-plane wall motions

Key simulations of turbulent channel flows undergoing streamwise-modulated spanwise in-plane wall actuation will be presented in chapter 6. In view of the importance of simulating this type of flow with high accuracy for this analysis, the implementation of the forcing boundary conditions is validated by reproducing one of the simulations presented in Viotti et al. (2009a). Since the mesh is Cartesian, these simulations are performed using the 4th-order formulation of the code. First, a regular unactuated plane-channel flow is simulated, yielding the value of the baseline drag coefficient. Second, the wall-actuated case is run, with the following wall motion imparted at both walls:

$$w_w = A \sin\left(\frac{2\pi}{\lambda_x} x\right). \tag{3.22}$$

The configuration chosen from the set simulated in Viotti et al. (2009a) features a forcing amplitude of $A^+ = 6$ and a streamwise wavelength $\lambda_x^+ \approx 1250$, based on the baseline wall units. Table 3.3 shows that, for a numerical box similar to that of Viotti et al. (2009a), the drag-reduction levels compare favourably.

As the drag-reduction level is an integrated measure that may mask some degree of error cancellation, an additional comparison of the spanwise-velocity profiles is given in figure 3.19. Figure 3.19a is a partial reproduction of FIG. 3 in Viotti et al. (2009a), and figure 3.19b shows the same plot with the present DNS data, demonstrating a very good agreement with the present simulation.

Table 3.3: Turbulent plane-channel-flow simulations with in-plane wall forcing at $Re_\tau \approx 200$, with $A^+ = 6$ and $\lambda_x^+ \approx 1250$ in the baseline wall units. The value of the drag-reduction level in Viotti et al. (2009a) was read from the plot shown in figure 5 of Viotti et al. (2009b).

	Δx^+	Δy^+	Δz^+	L_x/h	L_z/h	$N_x \times N_y \times N_z$	DR
Viotti et al. (2009a)	11.8	N/A	5.9	6π	3π	$320 \times 160 \times 320$	32.4%
Present DNS	9.8	0.6 – 3.5	4.9	18.85	9.42	$384 \times 192 \times 384$	32.5%

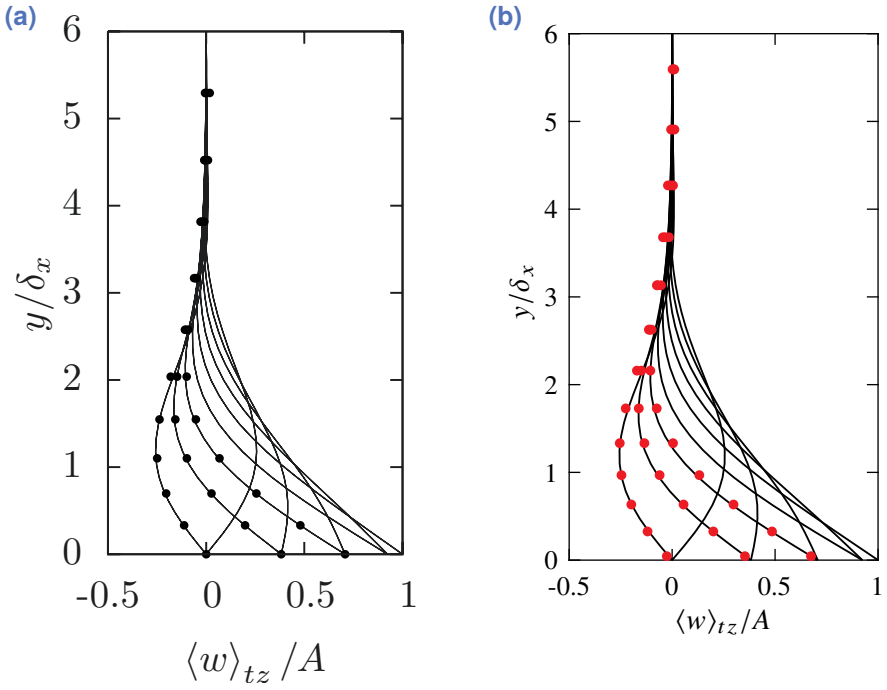


Figure 3.19: Comparison of the spanwise profiles with the results of Viotti et al. (2009a); lines: laminar solution, dots: DNS of the turbulent case; **(a)** extracted from Viotti et al. (2009a), **(b)** present DNS. [Reprinted with the permission of AIP Publishing from *Physics of Fluids*, 'Streamwise oscillation of spanwise velocity at the wall of a channel for turbulent drag reduction', Viotti, C., Quadrio, M. and Luchini, P. (2009), doi:10.1063/1.3266945, license number 4315970826741.]

3.4 Momentum compatibility condition

Once the correctness of the solution fields has been assessed, it is also important to perform the post-processing in a manner that is consistent with the numerical discretisation. To this aim, the consistency between the post-processed data and the numerical scheme employed in the solution of the Navier–Stokes equations is examined in the case of a wavy channel by verifying the conservation of mean spanwise-momentum at the wall.

As a consequence of the no-slip boundary condition, for smooth undulations, a condition that needs

to be satisfied at the wall is:

$$\nu \frac{\partial^2 w}{\partial y^2}\bigg|_{y=y_w} \approx \frac{\partial p}{\partial z}\bigg|_{y=y_w}, \tag{3.23}$$

where all quantities are the total physical quantities in the frame of reference aligned with the flow, i.e. including any pressure-driving term. This provides a relationship between the spanwise diffusion term and the spanwise pressure gradient that can be verified numerically.

Since equation (3.23) is satisfied at any time instant, it is also satisfied by the phase-averaged fields. Thus, the satisfaction of equation (3.23) can be examined based on the first-order flow statistics of a turbulent simulation. The configuration considered, at a friction Reynolds number of $Re_\tau \approx 360$, is a wavy wall of height $A_w/h = 0.03$ and wavelength $\lambda/h = 2.55$, making an angle with the main flow direction $\theta = 70°$. The mesh is generated using the increment $h_w = A_w \sin(2\pi/\lambda\, x)$ and the flow is driven at an angle of $\theta_f = \theta$, following the procedure explained in section 2.4. Next, the spanwise velocity (relative to the flow orientation) $\overline{\breve{w}}$ is calculated from the x-wise and z-wise velocity components $\overline{u}$ and $\overline{w}$, and the two derivatives in equation (3.23) are calculated and evaluated at the cell closest to the wall.

The results shown in figure 3.20 demonstrate an excellent agreement between the spanwise momentum diffusion term and the spanwise pressure gradient at both walls. The main outcome is the validation of the calculation of the flow-oriented derivatives from the reduced statistical database and the calculation of the second derivatives at the wall in the post-processing. Moreover, for the small streamwise

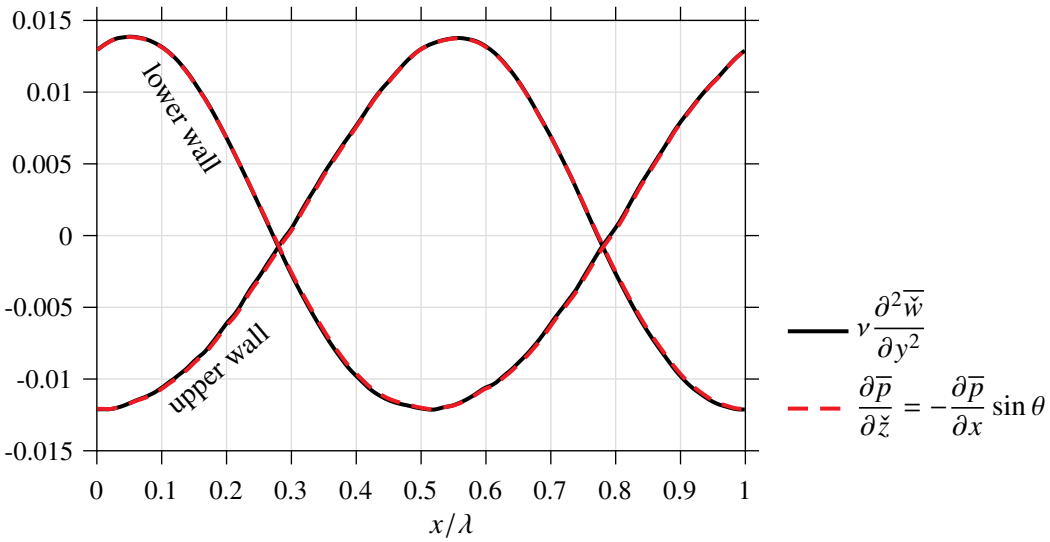


Figure 3.20: Verification of the compatibility condition (3.23) at the cells closest to the walls, for a wavy channel at $Re_\tau \approx 360$, $A_w/h = 0.03$, $\lambda/h = 2.55$, and $\theta = 70°$.

wave slope considered $A_w/\lambda_x \approx 0.004$, this can be regarded as a sensitive test as the quantities contained in this verification are all relatively small.

3.5 Conclusions

A broad range of verification and validation cases were studied to demonstrate the ability of the code to deliver sensible results.

The MMS is a powerful tool to hunt for inconsistencies in a code. It cannot be used to validate a code with respect to its ability to reproduce the physics involved, but it is effective at verifying that the discretised equations are being solved with the expected order of accuracy. Moreover, testing can be performed with sophisticated velocity and pressure fields which are more demanding than physical solutions, thus effectively exercising the numerical procedure. However, the primarily binary nature of the answer given by the method, i.e. 'yes' the theoretical order of accuracy is consistent with the order observed, or 'no' it is not, is merely mostly able to identify the presence of inconsistencies. It can thus indicate the need for further debugging, but may only provide rather enigmatic clues about the origin of the mismatch.

The current version of STREAM-LES displays a second-order accuracy in both velocities and pressure, as expected. Although the manufactured solution used was steady in order to be able to neglect the time-discretisation error, this test needs to be appreciated as a complement to the validation cases that followed. Additionally, this method only exhibits *the lowest* order present in the code. This is a well-known limitation of the MMS (Roache, 1998). It entails that testing the fourth-order version of the code is not straightforward.

Although the MMS study does not prove that the entirety of the code is absolutely correct as the MMS can understandably be blind to subtle coding errors, it does procure a strong level of confidence in the results, which feature a non-orthogonal body-fitted mesh with similar set-up to the ones considered in this study.

Finally, a set of reference numerical solutions of the Navier–Stokes equations were successfully reproduced, both for non-statistically stationary and statistically stationary flows. In addition to testing the validity of the solution fields, more advanced statistics requiring supplementary post-processing, such as the contributions to the turbulence-kinetic-energy budget, were validated against reference data for a turbulent plane-channel flow, and for multiple flow-to-mesh angles.

Chapter 4

Semi-empirical modelling

Contents

4.1 Summary of Chernyshenko (2013) 98
4.2 Linearised channel flow incorporating an eddy viscosity 100
4.2.1 Derivation of the linear model 100
4.2.2 Validation with DNS (laminar flow) 103
4.2.3 Comparison with DNS (turbulent flow) 106
4.3 Semi-empirical model for the drag contributions 107
4.3.1 Introduction 107
4.3.2 Model 1: changes in dissipation 111
4.3.3 Model 2: pressure and friction drag 115
4.4 Conclusions 122

Prior to engaging into costly simulations of the flow in a wavy channel, some computationally inexpensive models were formulated in an effort to aid the exploration of the parameter space. Many attempts in the past, of varying degrees of complexity, have been successful at reproducing the main features of the flow past a wavy wall with the crests perpendicular to the main flow direction, corresponding to the configuration $\theta = 0$ (e.g. Zilker et al., 1977). However, the prediction of the skin-friction distribution is often more demanding than that of the pressure field (Abrams and Hanratty, 1984; Balasubramanian and Orszag, 1981; Sengupta and Lekoudis, 1984). Therefore, the present analysis does not aim to predict the friction level in a direct manner. Rather, the performance of the wavy wall was estimated by means of a semi-empirical model based upon a presupposed analogous behaviour with spatial Stokes layers, by exploiting the DNS data of the SSL configurations given in Viotti et al. (2009a). The major goals of this analysis are to obtain an estimate of the velocity and pressure perturbations, and thus

yield insight into the main characteristics of skewed wavy channels for a broad range of flow configurations, as well as to identify trends in the predicted drag level in order to guide the DNS exploration of the parameter space.

4.1 Summary of Chernyshenko (2013)

In Chernyshenko (2013), a proxy for the objective function was used, based upon the assumption that some equivalence can be found between the flow distortions provoked by the wavy wall and those induced by the spatially varying steady wall actuation. The major ingredients and results of this approach are briefly summarised.

The boundary-layer equations are linearised around a linear profile for the mean streamwise velocity. This results in ordinary differential equations for the perturbation fields (u, v, w, p), expressed in wall units. The latter are solved both for the SSL (as in Viotti et al. (2009a)) and the wavy wall.

- In the SSL case, the streamwise and wall-normal momentum equations decouple from the spanwise direction, so that the streamwise velocity is unchanged, and only distortions of the spanwise component are present. The spanwise-velocity perturbation satisfies the Airy equation, the solution of which is given by

$$w_{\mathrm{SSL}} = \frac{A_{\mathrm{SSL}}}{Ai(0)} \, \Re \left[\mathrm{e}^{\mathrm{i}k_x x} \, Ai\left(-\mathrm{i}\, \tilde{y}\, \mathrm{e}^{-\mathrm{i}4\pi/3} \right) \right], \tag{4.1}$$

  where $\Re$ denotes the real part, $\tilde{y} = k_x^{1/3} y$, and Ai is the Airy function of the first kind.

- In the wavy-wall case, however, there are also perturbations in the streamwise velocity, arising from a combined effect of the wall-normal velocity induced by the spanwise inhomogeneity of the spanwise velocity and the longitudinal pressure gradient induced by the wall. Assuming a perturbation of the form $(u, v, w, p) = (\hat{u}(y), \hat{v}(y), \hat{w}(y), \hat{p})\, \mathrm{e}^{\mathrm{i}(k_x x + k_z z)}$, the linearised boundary-layer equations become

$$\begin{cases} \mathrm{i}k_x y \hat{u} + \hat{v} = -\mathrm{i}k_x \hat{p} + \dfrac{\mathrm{d}^2 \hat{u}}{\mathrm{d}y^2}, \\ \mathrm{i}k_x y \hat{w} = -\mathrm{i}k_z \hat{p} + \dfrac{\mathrm{d}^2 \hat{w}}{\mathrm{d}y^2}, \\ \mathrm{i}k_x \hat{u} + \dfrac{\mathrm{d}\hat{v}}{\mathrm{d}y} + \mathrm{i}k_z \hat{w} = 0. \end{cases} \tag{4.2}$$

  Equations (4.2) are then transformed into ordinary differential equations, which are solved numerically.

The L^2-norm of the difference in the spanwise shear-strain profiles between a SSL of given forcing amplitude, A_{SSL} (denoted $\hat{W}$ in Chernyshenko (2013)), and the wavy wall, is minimised over $\hat{p}$, resulting in the ratio of $\hat{p}$ to A_{SSL} yielding close shear strain profiles. However, owing to the nature of the analysis, no explicit formula was obtained for the correspondent height of the wavy wall A_w.

Next, it is assumed that the generation of a similar spanwise shear-strain layer causes the same level of weakening of the near-wall turbulence as in the wall-actuated case. In both cases, the net energy savings are decomposed as $P_{\mathrm{net}} = P_{\mathrm{sav}} + P_{\mathrm{req}}$, where P_{sav} is the power saved from the turbulence weakening, and P_{req} is the power required to do so.

- Given the above-mentioned condition on the wave-induced pressure gradient, the value of P_{sav} is taken from a polynomial interpolation of the DNS results of Viotti et al. (2009a) for the SSL at various forcing amplitudes and wavelengths.

- In the SSL case, the power required P_{req} is evaluated from the dissipation arising from the mean-velocity gradient induced by the control effects

$$P_{\mathrm{req}}^{\mathrm{SSL}} = -\sqrt{\frac{C_f}{2}}\left[k_x^+(1-P_{\mathrm{sav}})\right]^{1/3}\int_0^\infty \frac{1}{2}\left|\frac{\mathrm{d}w_{\mathrm{SSL}}}{\mathrm{d}\tilde{y}}\right|^2 \mathrm{d}\tilde{y}, \tag{4.3}$$

  where the value of the friction coefficient is evaluated from the empirical relation given by Pope (2000): $C_f = 0.0336 Re_\tau^{-0.273}$. Thus, in the case of a wavy wall, additional dissipation arises not only from the generation of the spanwise shear strain, but also from the streamwise perturbation of the velocity. For a given wavelength λ_x and spanwise pressure gradient (i.e. fixed A_{SSL}), this effect can be minimised by varying the angle of the wave through λ_z, and the calculation of Chernyshenko (2013) yields an optimal angle $\theta_{\mathrm{opt}} \approx 52°$. At $\theta = \theta_{\mathrm{opt}}$, the ratio

$$r = \frac{\displaystyle\int_0^\infty \left(\left|\frac{\mathrm{d}\hat{u}}{\mathrm{d}\tilde{y}}\right|^2 + \left|\frac{\mathrm{d}\hat{w}}{\mathrm{d}\tilde{y}}\right|^2\right)\mathrm{d}\tilde{y}}{\displaystyle\int_0^\infty \left|\frac{\mathrm{d}\hat{w}}{\mathrm{d}\tilde{y}}\right|^2 \mathrm{d}\tilde{y}} \tag{4.4}$$

  between the total additional dissipation and that due to the generation of the spanwise motion is $r_{\mathrm{min}} \approx 5.8$, implying that the energy dissipation arising from the streamwise-velocity perturbation is almost 5 times as large as that associated with the generation of the spanwise shear strain.

Finally, at the optimal angle $\theta_{\mathrm{opt}} \approx 52°$, the power required for the wavy wall to generate the spanwise motion is evaluated as $P_{\mathrm{req}} = r_{\mathrm{min}}\, P_{\mathrm{req}}^{\mathrm{SSL}}$, i.e. that of the equivalent SSL $P_{\mathrm{req}}^{\mathrm{SSL}}$ multiplied by the optimal

ratio $r_{\min}$ accounting for the additional streamwise distortion. The resulting net energy saving $P_{\text{net}} = P_{\text{sav}} + r_{\min} P_{\text{req}}^{\text{SSL}}$ is then maximised with respect to the forcing amplitude of the equivalent SSL and the associated wavelength, yielding $A^+_{\text{SSL,opt}} = 2$ and $\lambda^+_{x,\text{opt}} = 1520$.

The importance of the streamwise phase-varying velocity, relative to that of the induced spanwise velocity, was confirmed by the DNS results. Indeed, a simulation was carried out at $Re_\tau \approx 180$, for $\lambda_x^+ \approx 1510$, $\theta = 52°$, and $A_w^+ \approx 20$, resulting in a ratio

$$r_{\text{DNS}} = \frac{\displaystyle\int_{-h}^{h}\int_{0}^{\lambda}\left(\left|\frac{\partial\widetilde{u}}{\partial y}\right|^2 + \left|\frac{\partial\widetilde{w}}{\partial y}\right|^2\right)\mathrm{d}x\,\mathrm{d}y}{\displaystyle\int_{-h}^{h}\int_{0}^{\lambda}\left|\frac{\partial\widetilde{w}}{\partial y}\right|^2\mathrm{d}x\,\mathrm{d}y} = 5.4, \tag{4.5}$$

which is close to the estimate given in the analysis of Chernyshenko (2013) of $r_{\min} \approx 5.8$.

4.2 Linearised channel flow incorporating an eddy viscosity

4.2.1 Derivation of the linear model

A simplified model of the wavy-channel flow was formulated with the assumption of a gentle sinusoidal perturbation of a plane channel. The system of equations to be linearised was derived from a Reynolds-averaged framework. The RANS equations are:

$$\begin{cases} \dfrac{\partial}{\partial x_j}\left[\overline{u}_i^+\overline{u}_j^+ + \overline{p}^+\,\delta_{ij} - \dfrac{1}{Re_\tau}\left(\dfrac{\partial\overline{u}_i^+}{\partial x_j} + \dfrac{\partial\overline{u}_j^+}{\partial x_i}\right) + \overline{u_i'u_j'}^+\right] = 0, & \text{(4.6a)} \\[2ex] \dfrac{\partial\overline{u}_i^+}{\partial x_i} = 0, & \text{(4.6b)} \end{cases}$$

where over-bars denote time averaging. For simplicity, the + superscript will be omitted in the remainder of this chapter, but all velocities, pressure and stresses remain expressed in wall units, unless stated otherwise. Moreover, all distances are expressed in outer units, i.e. non-dimensionalised by $h = 1$.

The Reynolds stresses are modelled using a eddy viscosity ν_t, so that the modelled momentum equation becomes

$$\frac{\partial}{\partial x_j}\left[\overline{u}_i\overline{u}_j + \overline{p}\,\delta_{ij} - \frac{1+\nu_t}{Re_\tau}\left(\frac{\partial\overline{u}_i}{\partial x_j} + \frac{\partial\overline{u}_j}{\partial x_i}\right)\right] = 0. \tag{4.7}$$

Equation (4.7) is then expanded, and the wall-parallel variations of the eddy viscosity neglected, so that

the final RANS equations are:

$$\begin{cases} \dfrac{\partial \overline{u}_i \overline{u}_j}{\partial x_j} + \dfrac{\partial \overline{p}}{\partial x_i} - \dfrac{1}{Re_\tau}\left[(1+\nu_t)\dfrac{\partial^2 \overline{u}_i}{\partial x_j \partial x_j} + \dfrac{\partial \nu_t}{\partial y}\left(\dfrac{\partial \overline{v}}{\partial x_i} + \dfrac{\partial \overline{u}_i}{\partial y}\right)\right] = 0, & \text{(4.8a)} \\ \dfrac{\partial \overline{u}_i}{\partial x_i} = 0. & \text{(4.8b)} \end{cases}$$

A sketch of the wavy wall is given in figure 4.1, together with the geometrical parameters defining the wall shape $h_w = h\sin(2\pi/\lambda_x\, x + 2\pi/\lambda_z\, z)$. In the context of this analysis, the base flow consists of a plane channel of half-height h, and the shape of the plane walls, located at $y = \pm h$, is perturbed by adding a small-amplitude waviness of the form:

$$y_w = \pm h + \alpha\, h_w(x, y, z), \tag{4.9}$$

where α is the amplitude of the perturbation and h_w is the shape perturbation. In the numerical simulations, α is simply A_w/h, but the Greek notation was preferred here as a reminder of the linear approximation of the present derivation.

In order to facilitate the implementation of the boundary conditions in the discretised RANS equations, a non-orthogonal mapping is performed between the physical coordinates $\boldsymbol{x} = [x, y, z]^T$ and the Cartesian coordinates $\boldsymbol{\xi} = [\xi, \eta, \zeta]^T$ via the relation:

$$x_i = \xi_i + \alpha\, h_w\, \delta_{i2}. \tag{4.10}$$

Thus, as per equation (4.9), the walls are located at constant values of η, at $\eta_w/h = \pm 1$.

In order to obtain the wavy geometry, a sinusoidal perturbation of the geometry is considered, as

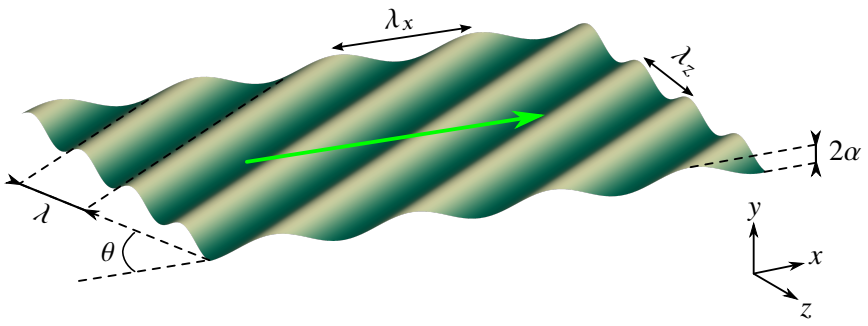


Figure 4.1: Configuration for the linear analysis. The green arrow indicates the main flow direction, and the wavy surface illustrates a shape perturbation h_w of amplitude α.

shown in figure 4.1, the latter being defined as:

$$h_w = \Re\left[\hat{h}_w(\eta)\ \exp(\mathrm{i}\boldsymbol{k}\cdot\boldsymbol{\xi})\right], \tag{4.11}$$

where $\boldsymbol{k}$ is the vector wave number $[k_x, 0, k_z]^T$, and $\hat{h}_w$ was introduced as a means of shifting the walls relative to one another, or of accommodating a flat wall at one of the boundaries. The phase shifts at the lower and upper walls are denoted τ_l and τ_u, respectively, and are defined in $[0, 2\pi)$. An expression of $\hat{h}_w$ achieving this purpose is:

$$\hat{h}_w(\eta) = \frac{\eta+1}{2}\left(e^{\mathrm{i}\tau_u} - e^{\mathrm{i}\tau_l}\right) + e^{\mathrm{i}\tau_l}. \tag{4.12}$$

This same formulation can also be employed in order to impose a flat wall at one of the boundaries by considering an infinite imaginary phase shift at the corresponding boundary.

Next, the differential operators are expressed in the physical domain:

$$\frac{\partial}{\partial x_i} = \frac{\partial}{\partial \xi_i} + \alpha\,\frac{\partial h_w}{\partial x_i}\frac{\partial}{\partial \eta}, \tag{4.13}$$

to be later inserted in equation (4.8). Before doing so, the base flow is augmented by a linear perturbation:

$$\boldsymbol{q}(\boldsymbol{\xi}) = \boldsymbol{Q}(\xi,\eta) + \alpha\,\Re\left[\hat{\boldsymbol{q}}(\eta)\ \exp(\mathrm{i}\boldsymbol{k}\cdot\boldsymbol{\xi})\right], \tag{4.14}$$

where $\boldsymbol{q} = [u, v, w, p]^T$, $\boldsymbol{Q} = [U(\eta), 0, 0, -P_x\,\xi]^T$ and $\hat{\boldsymbol{q}} = [\hat{u}, \hat{v}, \hat{w}, \hat{p}]^T$. The driving pressure gradient in the channel is u_τ^2, which, expressed in wall units, yields $P_x = 1$. Equations (4.13) and (4.14) are then inserted into the RANS equations (4.8), and only the terms up to first order in α are retained. The equation containing only $O(1)$ terms provides as a solution $U(\eta)$, whilst the first-order equations lead to a linear system for $\hat{\boldsymbol{q}}$.

With derivatives with respect to η denoted with primes, the equation for U—i.e. retaining only $O(1)$ terms—becomes

$$Re_\tau + U'(\eta)\,\nu_t'(\eta) + (1+\nu_t(\eta))\,U''(\eta) = 0, \tag{4.15}$$

which integrates over $\eta \in [-1, 0]$ and $\eta \in [0, 1]$—i.e. between the wall and the centre of the channel—to give

$$\eta + \frac{1+\nu_t(\eta)}{Re_\tau}\,U'(\eta) = 0, \tag{4.16}$$

under the assumption that the derivative of the velocity U' vanishes at $\eta = 0$.

The eddy viscosity chosen, similar to that of Reynolds and Tiederman (1967), is normalised by the flow kinematic viscosity, and shifted in order to follow the wavy boundary. The assumption is made that the eddy viscosity remains unchanged in the controlled case, which may be seen as a strong simplification. Nevertheless, the eddy viscosity used in this analysis is

$$\nu_t = \frac{1}{2}\left(\sqrt{1 + \left\{ \frac{c_2}{3} Re_\tau \ [1-\eta^2] \ [1+2\eta^2] \left[1 - \exp\left(-Re_\tau \frac{1-|\eta|}{c_1} \right) \right] \right\}^2} - 1 \right). \tag{4.17}$$

Equation (4.16) is solved numerically, and the coefficients of the model are set to match the velocity profile of a turbulent plane-channel flow calculated from DNS. Good agreement between the two is demonstrated in figure 4.2.

Lastly, the first-order equations, obtained from the perturbed RANS equations, were derived. In order to make the notation more compact, the operator M is introduced as:

$$M := \mathrm{i}\, k_x\, U - \frac{1+\nu_t}{Re_\tau} \left[\left(\frac{\mathrm{d}^2}{\mathrm{d}\eta^2} - \|\boldsymbol{k}\|^2 \right) + \frac{\nu_t'}{1+\nu_t} \frac{\mathrm{d}}{\mathrm{d}\eta} \right], \tag{4.18}$$

and the linear system, written in matrix form, is:

$$\begin{bmatrix} \mathrm{i}\, k_x & \dfrac{\mathrm{d}}{\mathrm{d}\eta} & \mathrm{i}\, k_z & 0 \\ M & U' - \mathrm{i}\, k_x \dfrac{\nu_t'}{Re_\tau} & 0 & \mathrm{i}\, k_x \\ 0 & M & 0 & \dfrac{\mathrm{d}}{\mathrm{d}\eta} \\ 0 & -\mathrm{i}\, k_z \dfrac{\nu_t'}{Re_\tau} & M & \mathrm{i}\, k_z \end{bmatrix} \begin{bmatrix} \hat{u} \\ \hat{v} \\ \hat{w} \\ \hat{p} \end{bmatrix} = \begin{bmatrix} \mathrm{i}\, k_x\, \hat{h}_w\, U' \\ U'\, M\left(\hat{h}_w\right) - 2\, \dfrac{1+\nu_t}{Re_\tau}\, \hat{h}_w'\, U'' \\ 0 \\ 0 \end{bmatrix}, \tag{4.19}$$

where the first line relates to continuity, and the last three lines to the momentum equations. The above equations were discretised with centred second-order finite differences on a collocated grid. Homogeneous Dirichlet boundary conditions are imposed at the boundaries ($\eta = \pm 1$) for the velocity components, and free boundary conditions for the pressure. The resulting system is solved numerically by direct inversion of the linear system, and the physical fields are calculated according to equation (4.14).

4.2.2 Validation with DNS (laminar flow)

The numerical implementation of the linear solver was validated by comparing the results to DNS for small-amplitude waves. In the case of a laminar flow, there is no eddy viscosity $\nu_t = 0$ and the base flow is a parabolic profile. Thus, the modelling error is suppressed and only remain errors arising from

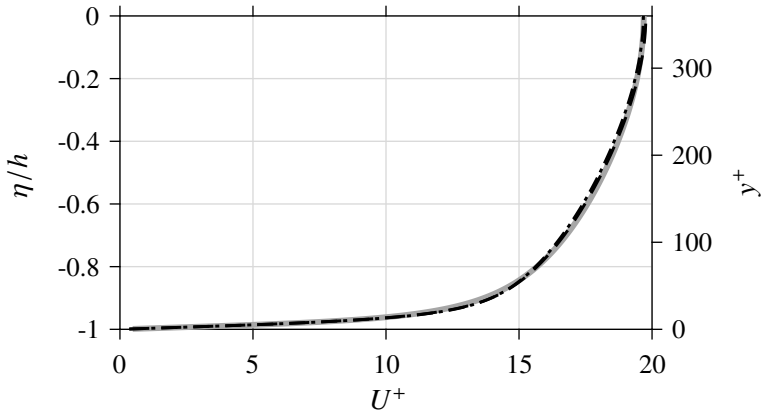


Figure 4.2: Comparison of the modelled base flow with DNS, the coefficients for the eddy viscosity are $c_1 = 29$ and $c_2 = 0.46$. The grey line corresponds to $U(\eta)$ from the model, the dash-dotted and dashed lines correspond, respectively, to the simulations at $\theta_f = 52°$ and $70°$ in table 3.2.

the numerical discretisation and the linearisation of the Navier–Stokes equations.

Channel with both walls wavy

A laminar wavy channel with both walls wavy and separated by a distance $2h$ was investigated at a low Reynolds number of $Re_b = 100$. The wave is of height $\alpha = A_w/h = 0.02$, of wavelength $\lambda/h = 5.1$, and it makes an angle of $\theta = 52°$ to the main flow direction, which translates to the wavenumbers $k_x = 0.76h^{-1}$ and $k_z = -0.97h^{-1}$. The resulting friction velocity calculated from DNS is $Re_\tau \approx 17$. Figure 4.3 demonstrates that an excellent agreement is obtained between the linear solution and the phase-varying fields of the DNS solution, for all solution variables.

As the amplitude of the wave is increased, unlike the fields calculated in the full non-linear DNS, the linear solution $\hat{\boldsymbol{q}}$ remains unchanged, and discrepancies naturally begin to appear between the two, as shown for a wave slope five times as large ($A_w/h = 0.1$) in figure 4.4.

Channel with lower wavy and upper flat walls

For the solution to exercise as many of the various components of the code as possible, a case with a lower wavy wall and an upper flat wall was also investigated. The amplitude of the wave is $\alpha = A_w/h = 0.02$, the wave numbers are $k_x = 0.76h^{-1}$ and $k_z = -1.0h^{-1}$, and the Reynolds number is $Re_b = 500$ which corresponds to $Re_\tau \approx 39$. Figure 4.5 shows that the DNS results also compare favourably with the linear solution for this different case.

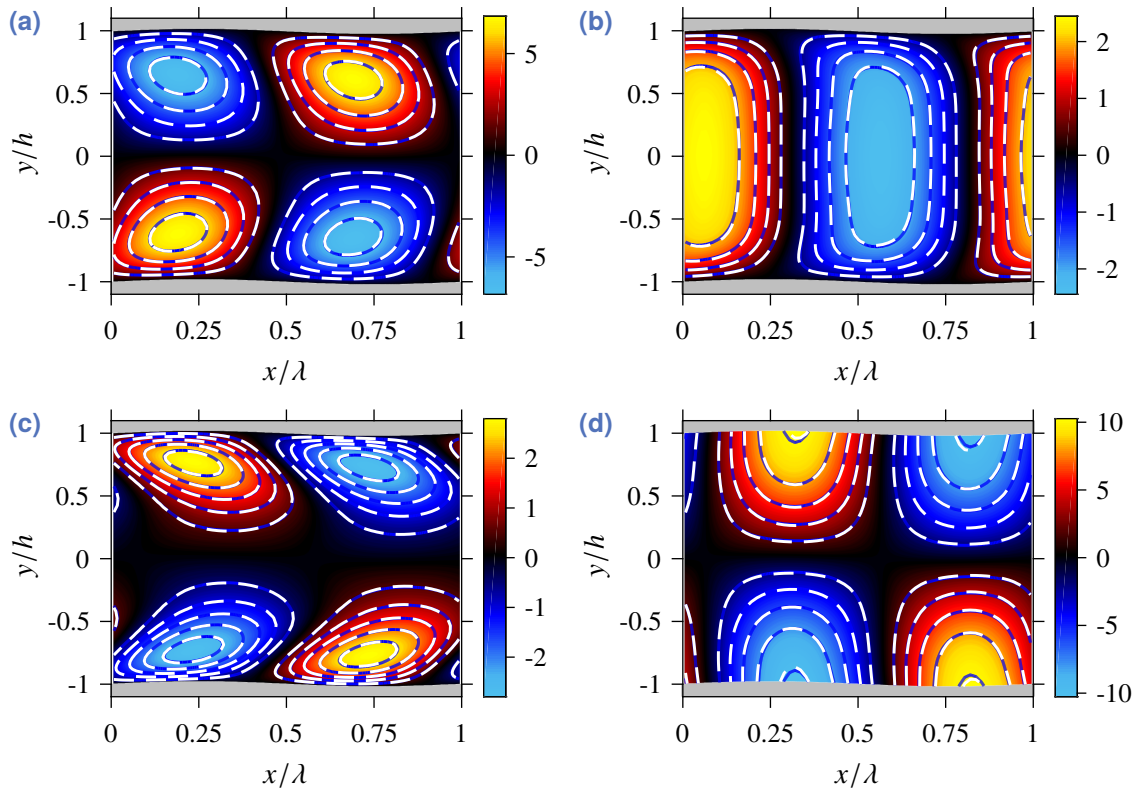


Figure 4.3: Validation of the linear solver for a laminar channel with both walls wavy (shown in grey), and parameters $\alpha = 0.02$, $k_x = 0.76h^{-1}$, $k_z = -0.97h^{-1}$, at $Re_b = 100$. The background coloured contours correspond to the components of the linear solution. Blue solid contours: linear solution $\Re\left[\hat{\boldsymbol{q}} \exp(\mathrm{i}\boldsymbol{k}\cdot\boldsymbol{\xi})\right]$, white dashed contours: DNS data $\widetilde{\boldsymbol{q}}^{+}/\alpha$. **(a)** u with contour levels $\pm 1.5, \pm 3, \pm 4.5$ and ± 6; **(b)** v with contour levels $\pm 0.5, \pm 1, \pm 1.5$ and ± 2; **(c)** w with contour levels $\pm 0.5, \pm 1, \pm 1.5, \pm 2$ and ± 2.5; **(d)** p with contour levels $\pm 2, \pm 4, \pm 6, \pm 8$ and ± 10.

Summary (laminar flow)

The numerical implementation of the linear system of equations was validated in the case of laminar flows wherein no closure model is involved. For small amplitudes, the linear solution is virtually indistinguishable from the numerical solution of the full Navier–Stokes equations, and even though non-linear effects are not negligible for larger wave slopes, the response remains well-approximated by the linear solution.

Since these results are merely based on analytical derivations and are entirely independent from the DNS code, they also provide additional support to the results of chapter 3 in showing the consistency of the DNS results presented.

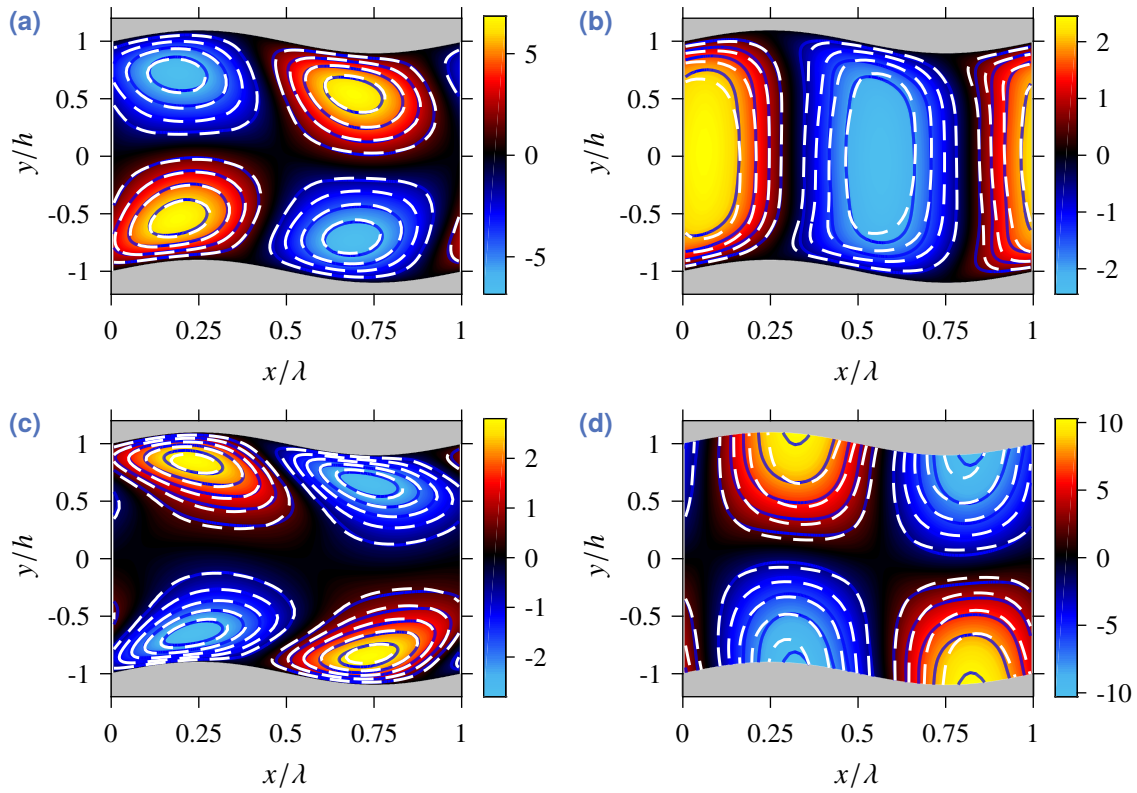


Figure 4.4: Same as figure 4.3 but for a larger amplitude $\alpha = 0.1$. The blue solid contours correspond to the linear solution, and the dashed white contours to the DNS results for a wave height $A_w/h = \alpha$.

4.2.3 Comparison with DNS (turbulent flow)

In the case of a turbulent flow, an eddy viscosity is used in order to close the RANS equations, as described in section 4.2.1. The friction Reynolds number considered in the remainder of this chapter is—unless stated otherwise—$Re_\tau = 360$ and the parameters required in the definition of the eddy viscosity are set to $c_1 = 29$ and $c_2 = 0.46$ so that the baseline profile corresponds to that calculated from DNS, as was shown in figure 4.2.

The contours of the velocity components and pressure field in figure 4.6 show that the DNS data agree qualitatively very well with the linear analysis. However, in quantitative terms, there is a significant underestimation of the phase variations of the streamwise velocity, as shown in greater detail in figure 4.7. As for the spanwise velocity, its phase variations are well predicted in the viscous sublayer, but in common with the streamwise component, they are under-estimated in the buffer layer, where it peaks. The extrema of the phase-varying spanwise velocity slightly precede the crest and trough, and this phase location is in good quantitative agreement with the linear model. The effect of the non-linearity can be observed in the different heights at which the minimum and maximum values are located. In the linear

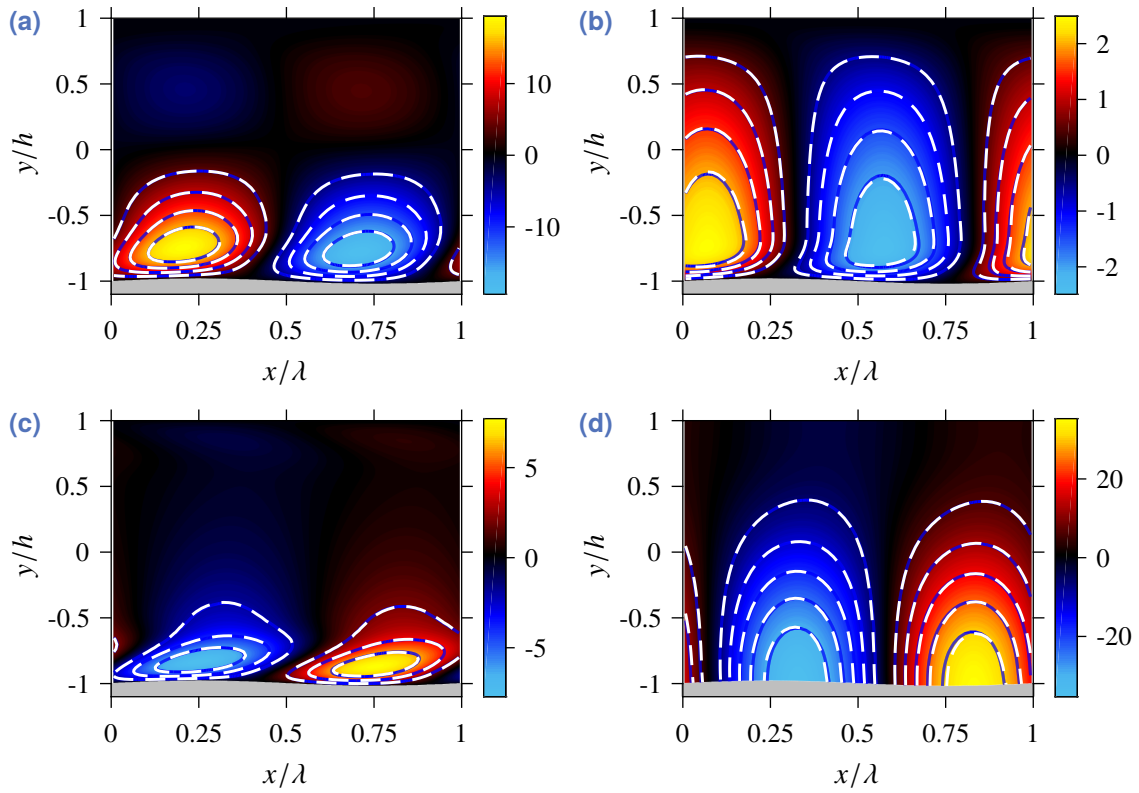


Figure 4.5: Validation of the linear solver for a laminar channel. The lower wall is wavy (shown in grey), whereas the upper wall is flat, and the parameters are $\alpha = 0.02$, $k_x = 0.76h^{-1}$, $k_z = -1.0h^{-1}$, and $Re_b = 500$. The legend is similar to figure 4.3. **(a)** u with contour levels at $\pm4, \pm8, \pm12$ and ±16; **(b)** v with contour levels $\pm0.5, \pm1, \pm1.5$ and ±2; **(c)** w with contour levels $\pm2, \pm4$ and ±6; **(d)** p with contour levels $\pm6, \pm12, \pm18, \pm24$ and ±30.

model, both are located at a wall-distance (based on the baseline friction) of about $y^+ \approx 13$, whereas in the DNS, these occur at $y^+ \approx 15$ and $y^+ \approx 18$ for the minimum and maximum values of $\widetilde{w}^+$, respectively. Yet, despite the underestimation of the spanwise velocity away from the wall, it is sufficiently accurate very close to the wall so that the prediction of the phase-varying transverse shear-strain be significantly better, as shown in figure 4.8.

4.3 Semi-empirical model for the drag contributions

4.3.1 Introduction

The linear model described above in section 4.2 is able to provide estimates of the perturbation fields for any flow configuration (A_w, λ, θ), but this perturbation does not contribute to the friction owing to the linear form chosen for the velocity field which integrates to zero. Nevertheless, rather than evaluating the change in friction directly from the linearised RANS equations, the present approach relies on the

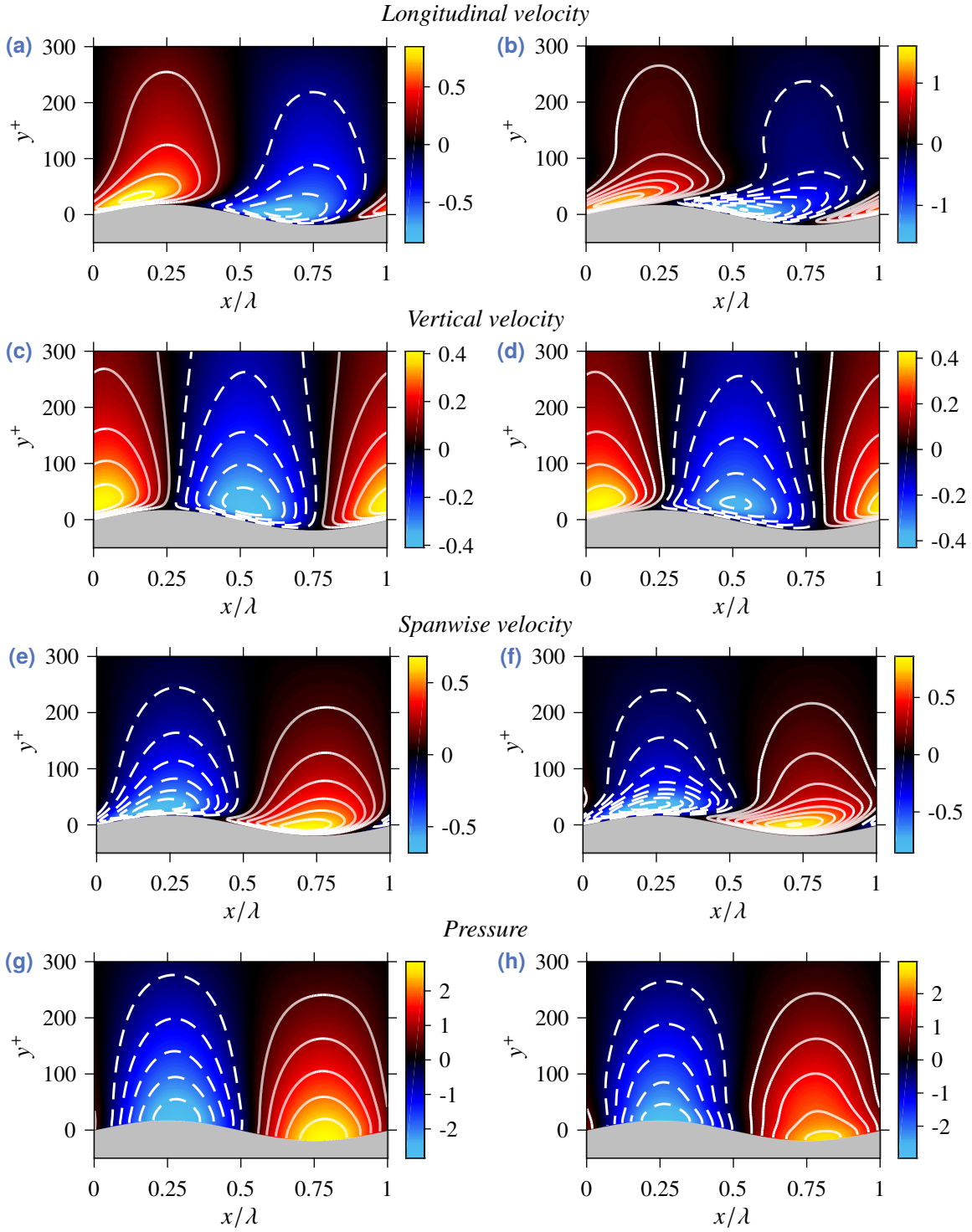


Figure 4.6: Comparison between the linear solution (left column) and DNS (right column) for $A_w = 0.05h$, $\theta = 70°$, and $\lambda^+ \approx 920$, at $Re_\tau \approx 360$. The data extracted from the DNS are the phase variations $\widetilde{\boldsymbol{q}}$ of the velocity and pressure, normalised using the friction velocity. Dashed white contours indicate negative values, and continuous contours positive ones, with a constant spacing of **(a,b)** 0.2 **(c,d)** 0.08 **(e,f)** 0.1 **(g,h)** 0.5.

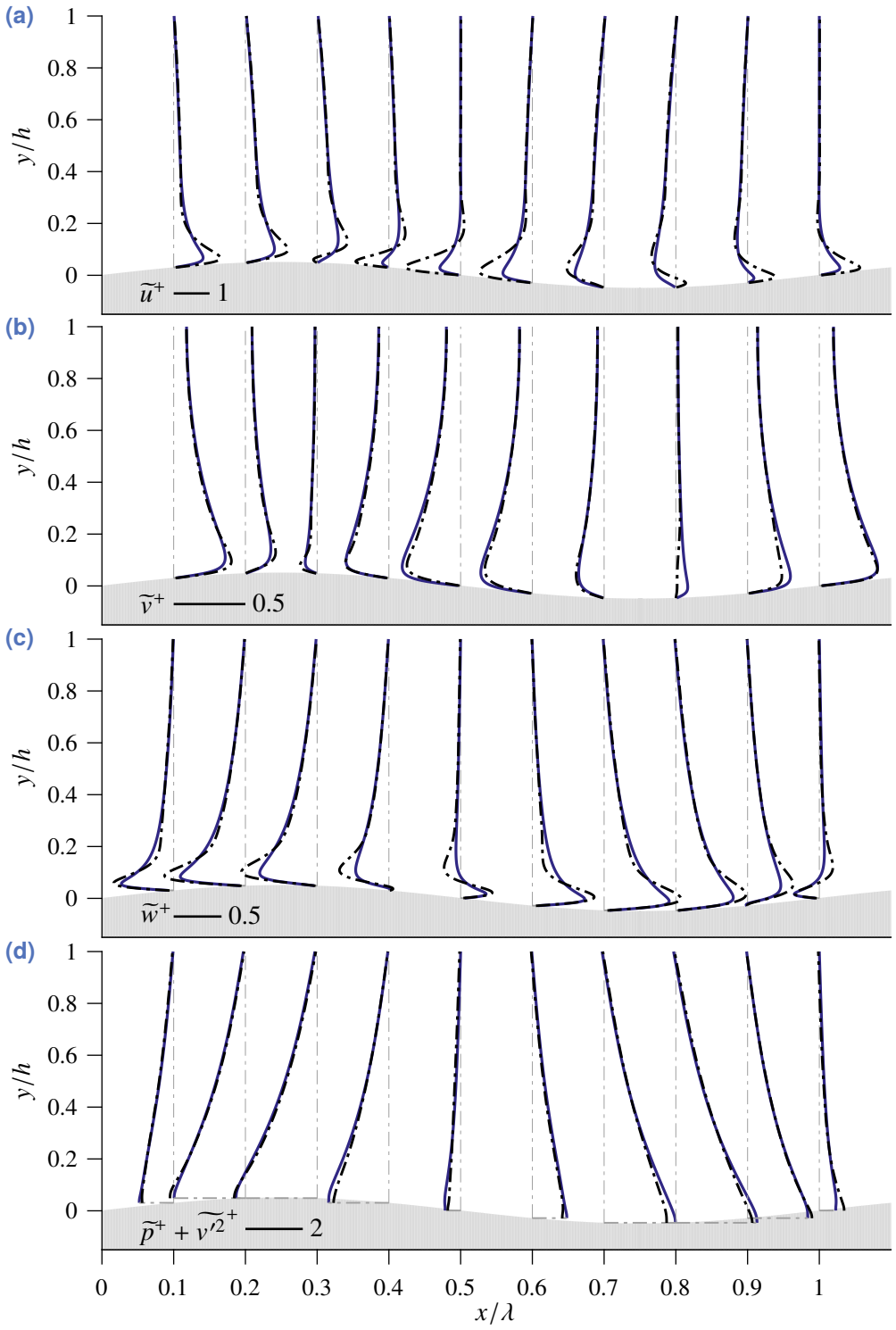


Figure 4.7: Comparison of the linear solution with DNS for the same configuration as figure 4.6. Black dashed-dotted lines: DNS, blue lines: linear model.

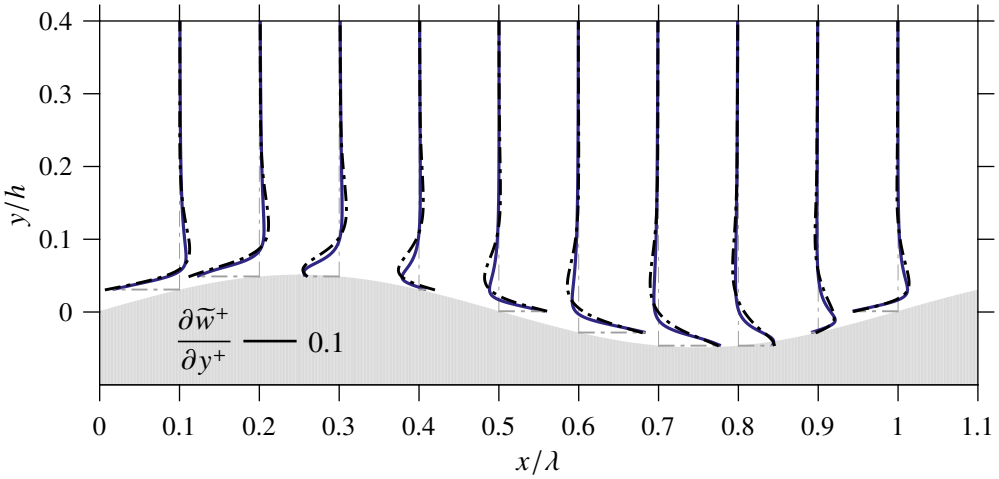


Figure 4.8: Comparison of the transverse shear-strain for the same configuration as figure 4.6. Black dashed-dotted lines: DNS, blue lines: linear model.

assumption of an approximate equivalence between the wavy wall and a corresponding Spatial Stokes Layer at same λ_x, and empirical data consisting of the DNS results of Viotti et al. (2009a) are thus used to predict the performance of the wavy wall. Various hypotheses are considered—following and augmenting the study of Chernyshenko (2013)—as for how the two different flows may quantitatively relate to each other, and implications on the location of the optimal configuration in the parameter space are drawn.

The objective of finding the wall shape h_w (defined in figure 4.1) that maximises the drag reduction can be formulated as an optimisation problem, wherein the quantity to be minimised is the total drag, and the parameter space is three-dimensional, composed of the wave amplitude, wavelength, and flow-to-crest angle θ. A proxy for the objective function is used, based on different assumptions relating the flow distortions provoked by the wavy wall and those induced by the spatially varying steady wall actuation (SSL). The two core components necessary to build the semi-empirical models later constructed are:

(1) an estimation of the desired effect of the control method, which can be a reduction in friction, or a measure of the weakening of turbulence achieved, relative to the baseline; and

(2) a measure of the expense of enforcing the control, that is the cost of creating of a local pressure gradient driving in part the transverse motion, or the additional dissipation arising from the changes in mean-velocity gradients.

The latter effects are quantified in two different conceptual frameworks. The first extends the results

of Chernyshenko (2013) by replacing the linearised boundary-layer equations with the model derived in section 4.2, whereas the second relies on an estimation of the total drag force acting on the wavy surface, split into frictional and pressure contributions.

Thus, in both cases, the model can be seen as a way of evaluating the net power benefits P_{net}, computed as the sum of the power saved by applying the passive control P_{sav}, plus a term corresponding to the additional power expenditure required to enforce the control P_{req}:

$$P_{\text{net}} = P_{\text{sav}} + P_{\text{req}}. \tag{4.20}$$

Note that this convention implies that the power required be a negative quantity in the present context, i.e. an energy sink.

4.3.2 Model 1: changes in dissipation

In this section, the linear model previously described in section 4.2 is used at the same Reynolds number as in the study of Chernyshenko (2013), i.e. at $Re_\tau = 200$, and the empirical relation given in Pope (2000) is used to estimate the friction coefficient $C_f = 0.0335 Re_\tau^{-0.273}$. The bulk Reynolds number is calculated from $Re_b = Re_\tau \sqrt{\frac{2}{C_f}}$, which can be derived from the definition of C_f, and the corresponding Reynolds number is $Re_b \approx 3226$.

Power saved

The assumptions made for the power saved follow those of Chernyshenko (2013), i.e. that the spanwise shear-strain profiles for a wavy wall at given λ_x can be made reasonably close to those of a SSL with a forcing amplitude A_{SSL} and same forcing wavelength λ_x, by adjusting the amplitude of the pressure gradient driving the spanwise flow, which relates to the amplitude of the wave. Thus, the dependence of the power saved upon the angle of the wave is circumvented by considering that A_w was chosen to generate the same transverse shear-strain as in the SSL case. As a consequence, the power saved for a given equivalent forcing amplitude A_{SSL} is estimated as $P_{\text{sav}}(\lambda_x, A_{\text{SSL}}) = P_{\text{sav}}^{\text{SSL}}(\lambda_x, A_{\text{SSL}})$, regardless of whether there exists a height A_w able to achieve such a forcing amplitude.

The power saved $P_{\text{sav}}^{\text{SSL}}$ is evaluated from the polynomial interpolations given in equations (4) to (7) in Chernyshenko (2013). The latter interpolations express $P_{\text{sav}}^{\text{SSL}}$, at fixed forcing amplitude for $A_{\text{SSL}}^+ \in \{1, 2, 6, 12\}$, and were obtained from the DNS data of Viotti et al. (2009a). Additional linear interpolations were performed between the various forcing amplitudes, and the resulting curves for P_{sav}

are shown in figure 4.9.

Power required

The power required in the SSL case $P_{\text{req}}^{\text{SSL}}$ is evaluated exactly as in Chernyshenko (2013), and depends on the power saved to account for the change in friction that occurs in the constant-bulk DNS, unlike the present model which is at constant pressure gradient $P_x^+ = 1$. The approximate expression given in Chernyshenko (2013) for the power required is:

$$P_{\text{req}}^{\text{SSL}} = -0.3157 A_{\text{SSL}}^{+2} \sqrt{\frac{C_f}{2}} \left[\frac{2\pi(1 - P_{\text{sav}}^{\text{SSL}})}{\lambda_x^+} \right]^{1/3}. \tag{4.21}$$

The resulting power required is shown in figure 4.10.

Unlike in the SSL case where the moving wall imparts a velocity solely in the spanwise direction, the oblique wavy wall induces longitudinal and transverse pressure gradients. This implies that in order to generate the same spanwise shear strain as in the SSL, the wavy wall also provokes some dissipation of energy in the longitudinal direction, which reduces its efficiency relative to the SSL. The reduced effectiveness $P_{\text{req}} < P_{\text{req}}^{\text{SSL}}$ is taken into account by multiplying $P_{\text{req}}^{\text{SSL}}$ by a penalising factor r, defined in Chernyshenko (2013) as the ratio between the energy dissipation arising from the mean velocity in the longitudinal and transverse directions, relative to that serving the emulation of the forcing in the the spanwise direction. In the present case, with the additional turbulent viscosity, the ratio r is calculated as:

$$r = \frac{\left\| \nu_{\text{tot.}} \left(\frac{\mathrm{d}\hat{u}}{\mathrm{d}\eta} \right)^2 \right\| + \left\| \nu_{\text{tot.}} \left(\frac{\mathrm{d}\hat{w}}{\mathrm{d}\eta} \right)^2 \right\|}{\left\| \nu_{\text{tot.}} \left(\frac{\mathrm{d}\hat{w}}{\mathrm{d}\eta} \right)^2 \right\|}, \tag{4.22}$$

where the double bars represent the L^2-norm $\|\cdot\|^2 : q \mapsto \int_{-1}^{1} |q|^2 \mathrm{d}\eta$, and the total viscosity is $\nu_{\text{tot.}} = \nu(1 + \nu_t)$. The turbulent viscosity used is the one defined in equation (4.17) and the values for the parameters at $Re_\tau = 200$ are taken to approximately match the baseline DNS data, which resulted in $c_1 = 25.7$ and $c_2 = 0.5$ with similar fidelity to that shown in figure 4.2 at $Re_\tau = 360$.

Although the ratio r does not depend on the amplitude of the wave in the linear context of this study, it is dependent on the wavelength of the wave λ, unlike in Chernyshenko (2013) where r only depends on the ratio k_x/k_z. For fixed streamwise wavelengths, the effect on r of changing the spanwise wavelength, or equivalently, of changing the angle of the grooves, is shown in figure 4.11. The linear model indicates that the longer the streamwise wavelength, the lower the cost of driving the spanwise

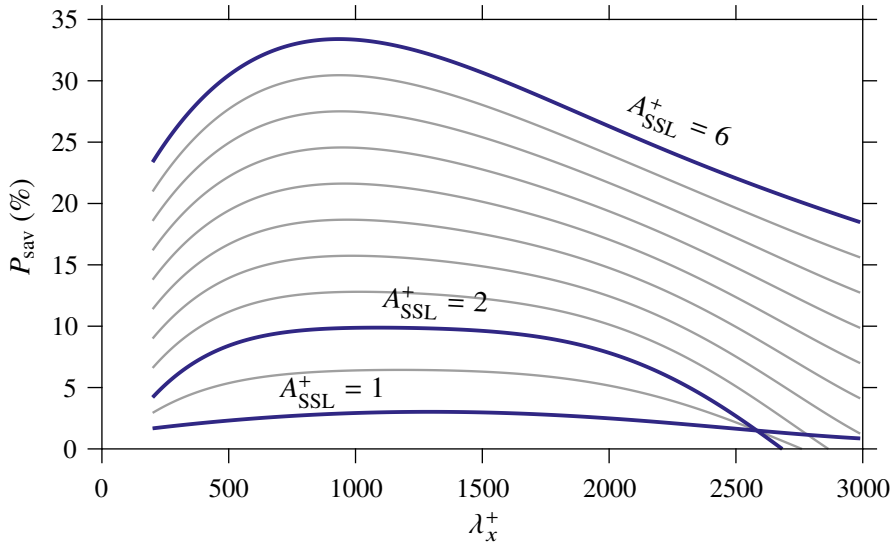


Figure 4.9: Power saved as a function of the wavelength and forcing amplitude. Thick blue lines correspond to the polynomial interpolations given in Chernyshenko (2013), thin grey lines correspond to additional linear interpolations performed in the present analysis.

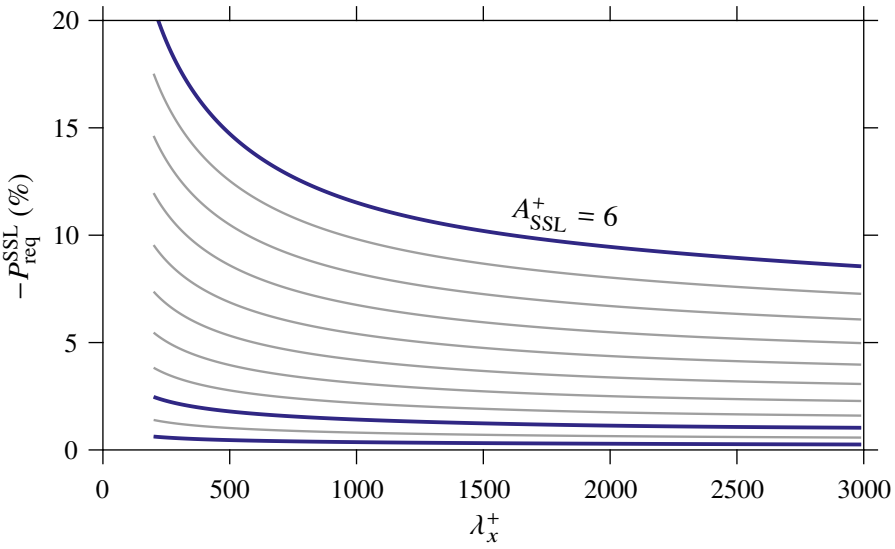


Figure 4.10: Power required for SSL as a function of the wavelength and forcing amplitude. Same legend as figure 4.9 regarding the value of the forcing amplitude.

flow. Therefore, the results indicate that large wavelengths are preferable, and that for such large wavelengths, the angle of the wave minimising the ratio r lies somewhere between $\theta = 55°$ and $\theta = 75°$. However, the streamwise wavelength is important with respect to the transverse shear-strain and the physical wavelength associated with the weakening of near-wall turbulence, so there is a trade-off to be found between increasing the wavelength to reduce the additional dissipation in the longitudinal direction and keeping a dimension adequate with the mechanism of drag reduction occurring in the SSL scenario, so as to retain a significant P_{sav}. This trade-off is precisely the purpose of the section to follow.

Drag-reduction prediction

The prediction of P_{net} for the wavy wall can be summarised as:

$$P_{\text{net}}(\lambda_x, \theta, A_{\text{SSL}}) = P_{\text{sav}}^{\text{SSL}}(\lambda_x, A_{\text{SSL}}) + r(\lambda_x, \theta)\, P_{\text{req}}^{\text{SSL}}(\lambda_x, A_{\text{SSL}}), \tag{4.23}$$

where all the terms were shown in figures 4.9 to 4.11.

In order to maximise P_{net}, the angle of the wave is chosen so as to minimise r. Given a streamwise wave length λ_x, the optimal groove angle θ_{opt} is chosen to minimise the ratio r. The latter optimal angle can be easily identified on figure 4.11 as the minimum of each curve. For this optimal angle, $r(\lambda_x, \theta_{\text{opt}}) = r_{\text{min}}(\lambda_x)$ and the prediction for P_{net} becomes

$$P_{\text{net}} = P_{\text{sav}}^{\text{SSL}} + r_{\text{min}}\, P_{\text{req}}^{\text{SSL}}. \tag{4.24}$$

The net power benefit is shown in figure 4.12a, whilst the corresponding ratio r_{min} is shown in figure 4.12b. The optimum found is for a wavelength $\lambda_x^+ = 1530$, at an angle of $\theta = 60°$, so that the wavy wall emulates the effect of a SSL with a forcing amplitude of $A_{\text{SSL}}^+ = 2.9$, predicting net energy savings of about 6.6%.

Compared to the results of Chernyshenko (2013), who found about 2.4% net savings for the configuration $\lambda_x^+ = 1520$, $\theta = 52.5°$ and $A_{\text{SSL}}^+ = 2$, the prediction of the drag reduction is much higher in the new model owing to the ratio r being reduced, which allowed the forcing amplitude to be increased. Unfortunately, as will appear later, the forcing amplitudes achievable with the wavy wall for small wave slopes, before other effects become predominant, are much lower than the optimal value of $A_{\text{SSL}}^+ = 2.9$ found in this study. Nevertheless, two major observations can be drawn from the present model:

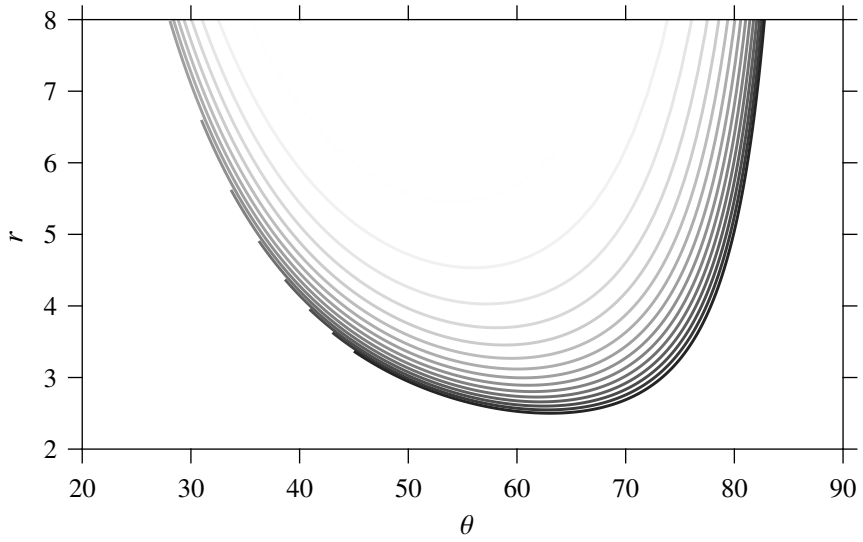


Figure 4.11: Ratio r for fixed λ_x and varying wave angle θ, light grey: small λ_x, dark grey: large λ_x. $Re_\tau = 200$, $\nu \approx 1/3180$, $c_1 = 25.7$, $c_2 = 0.5$.

- long wavelengths may be favourable as they decrease the ratio r; and
- the optimal angle minimising the ratio r at fixed λ_x is approximately located between $\theta = 55°$ and $\theta = 75°$ for most of the wavelengths considered.

4.3.3 Model 2: pressure and friction drag

In contrast to Model 1, the focus of Model 2 is the decomposition of the drag reduction into a friction reduction and a pressure-drag penalty. It is assumed that the emulation of the SSL shear-strain layer of forcing amplitude A_{SSL} results in the same level of friction reduction along the wavy wall as over the actuated wall. The power required to generate the spanwise motion is then estimated from the level of pressure drag exerted on the wavy wall. The total drag-reduction rate is accordingly evaluated as

$$\mathrm{TDR} = \mathrm{FDR} - \mathrm{PD}, \tag{4.25}$$

where TDR and FDR respectively stand for Total and Friction Drag Reduction, and PD stands for Pressure Drag.

Friction drag

The friction drag is estimated by assuming that the SSL is perfectly emulated and that this results in the friction being reduced by exactly the same amount as for the SSL with a forcing amplitude A_{SSL},

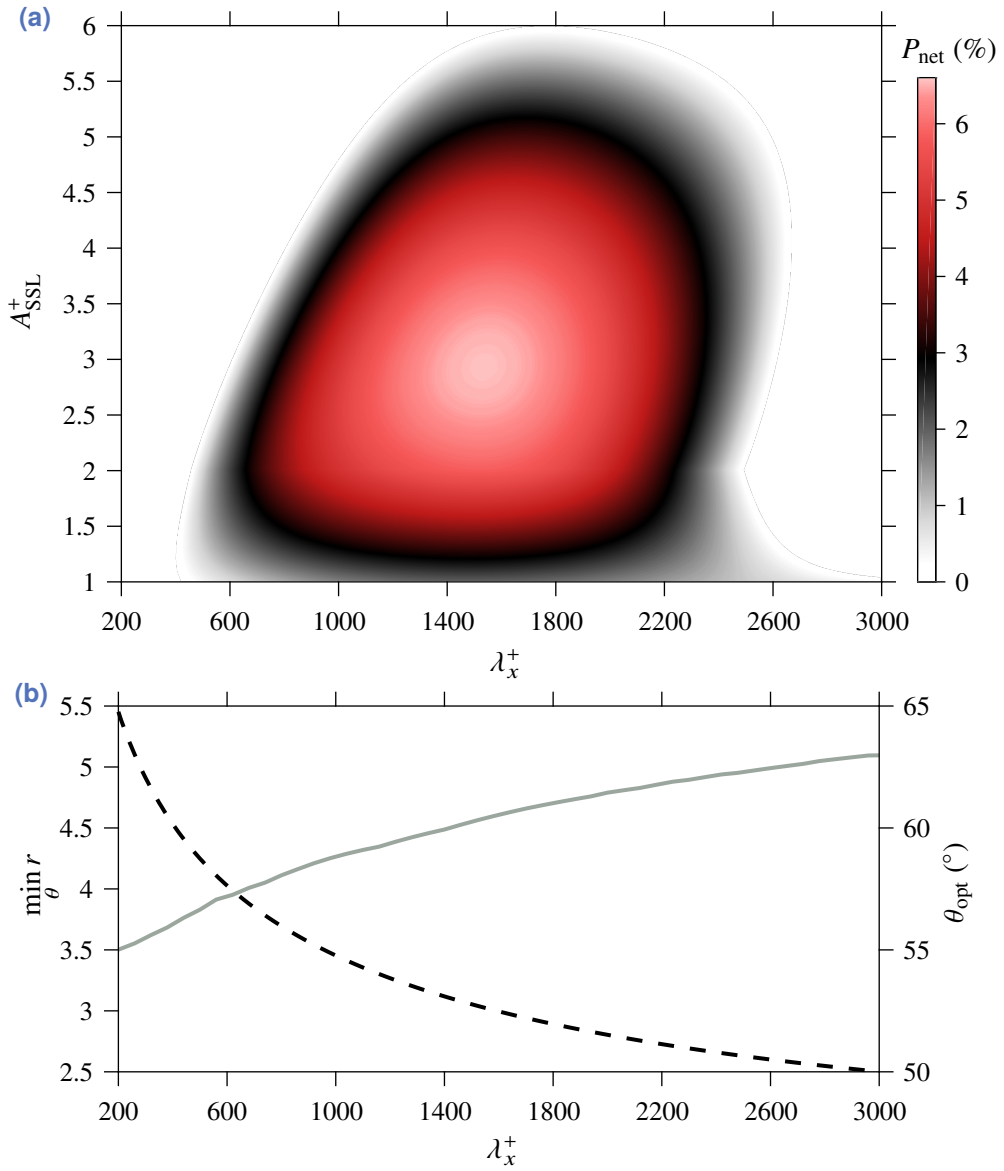


Figure 4.12: (a) Prediction of the drag reduction from the semi-empirical model 1 at $Re_\tau = 200$, **(b)** minimum ratio r for fixed λ_x (dashed line, left axis) and corresponding flow angle θ_{opt} (continuous line, right axis).

and wavelength λ_x. Since the estimation of the friction reduction relies on the DNS data given in Viotti et al. (2009a), the study is performed at constant forcing amplitude A_{SSL}. Moreover, it was observed in figure 4.6 that the spanwise motion generated by the wavy wall was relatively weak which undermines the capacity of the wavy wall of emulating large forcing amplitudes. Consequently, the present study is performed at the smallest forcing amplitude present in Viotti et al.'s database, namely $A^+_{\text{SSL}} = 1$. Also, in order to obtain a smooth drag-reduction curve for the SSL data, a spline was fitted to the DNS data as shown in figure 4.13.

Upon increasing the height of the wavy wall in order to reach larger forcing amplitudes, the ratio

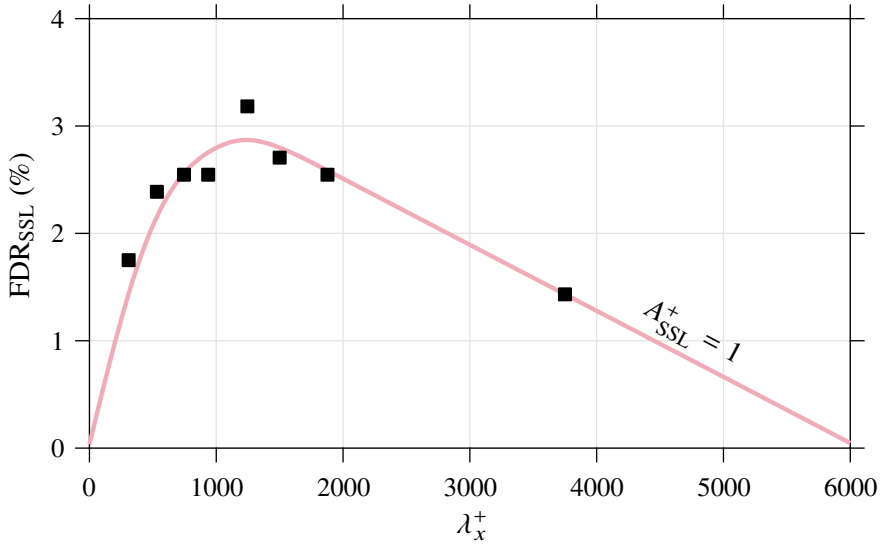


Figure 4.13: Friction-drag reduction obtained in a SSL as a function of the streamwise actuation wavelength λ_x^+, for a forcing amplitude of $A_{SSL}^+ = 1$, at $Re_\tau \approx 200$. Symbols: DNS data extracted from Viotti et al. (2009b), solid line: fit of the data used in the present study.

between the wave height and the channel height becomes critical and should remain small in order to avoid interferences between the lower and upper boundaries. Since for small Reynolds numbers a low sensitivity to the Reynolds number may be expected when the configuration parameters are scaled in wall units, given a fixed wave amplitude A_w^+, a possible way of diminishing the ratio A_w^+/h^+ is to increase h^+ or, equivalently, to increase the Reynolds number. For this reason, the Reynolds number was increased from Viotti et al.'s $Re_\tau \approx 200$ to $Re_\tau \approx 360$ in order to avoid ratios A_w/h greater than 15%. However, it is known that there is some dependence of the SSL drag-reduction level on the Reynolds number, and that the optimal actuation parameters tend to decrease in period or wavelength at higher Reynolds numbers (Gatti and Quadrio, 2013). Yet, Hurst et al. (2014) showed that this effect on the optimal actuation parameter was rather small between $Re_\tau \approx 200$ and $Re_\tau \approx 400$. For the very small Reynolds numbers considered, this sensitivity may thus be jettisoned as a first estimate in view of the target of identifying trends to guide the DNS exploration. It is nevertheless possible to partially account for the performance loss by degrading the friction-drag reduction with the assumption of a power-law decay of the efficiency of the control method with Reynolds number (Touber and Leschziner, 2012). Thus, the final expression for the friction-drag-reduction estimate is obtained by penalising the value at $Re_\tau \approx 200$ by a factor $(Re_\tau/200)^{-0.2}$:

$$\mathrm{FDR} = \mathrm{FDR}_{\mathrm{SSL}}(\lambda_x^+, A_{\mathrm{SSL}}^+ = 1)\left(\frac{Re_\tau}{200}\right)^{-0.2}. \tag{4.26}$$

Pressure drag

The pressure drag can be calculated directly from the linear solution $\hat{p}$ by integration over one wavelength. In the case where the two wavy boundaries are of same amplitude, wavelength and angle, by equivalence of the upper and lower walls, the pressure-drag force is twice the force exerted on the lower wall:

$$\frac{\bar{F}_p}{u_\tau^2} = -2 \iint_{S_w} p|_w \, n_x \, \mathrm{d}S \tag{4.27}$$

where $\boldsymbol{n} = (n_x, n_y, n_z)^T$ is the unit surface normal pointing outward of the fluid volume, and $p|_w$ the pressure at the lower wall, i.e. at $\eta = -1$. The factor u_τ^2 is a consequence of p being expressed in wall units. From the definition equation (4.14) and $n_x = -\alpha \, k_x \, \cos(k_x x + k_z z) + O(\alpha^2)$, the first-order estimate of the pressure-drag force becomes:

$$\frac{\bar{F}_p}{u_\tau^2} = -2 \int_{x=0}^{\lambda_x} \int_{z=0}^{\lambda_z} \alpha \, \Re \left[\hat{p}(-1)\right] \cos^2(k_x x + k_z z)(-k_x \alpha) \, \mathrm{d}x \, \mathrm{d}z, \tag{4.28}$$

which, after simplification, reduces to

$$\frac{\bar{F}_p}{u_\tau^2} = \pi \, \Re \left[\hat{p}(-1)\right] \; \lambda_z \, \alpha^2, \tag{4.29}$$

so that the pressure-drag coefficient becomes

$$D_p = \frac{\pi \, \Re \left[\hat{p}(-1)\right] \; \lambda_z \, \alpha^2}{\frac{1}{2} \, \lambda_x \, \lambda_z} \, u_\tau^2. \tag{4.30}$$

Since the total baseline-drag coefficient is $D_0 = 2u_\tau^2$, the relative increase in drag due to the pressure drag D_p/D_0 is

$$\mathrm{PD} = \frac{D_p}{D_0} = \frac{\pi}{\lambda_x} \, \Re \left[\hat{p}(-1)\right] \; \alpha^2, \tag{4.31}$$

which depends quadratically on the wave amplitude. Note that this behaviour is similar to P_{req} in Model 1 which was also quadratic in A_{SSL}^2. However, the height required to get the right spanwise motion is not known at this point, its quantification will be the purpose of section 4.3.3.

The formula given in equation (4.31) was validated with laminar simulations (not shown), and later with the turbulent DNS results presented in chapter 5. As shown in figure 4.14 for turbulent configurations, the resulting estimation of the pressure drag is good for small wave slopes, but underestimates the DNS value at large wave slopes for which the linear approximation loses accuracy. However, since the pressure-drag level is small compared to the much larger baseline-drag level, the linear model pro-

vides an estimate of the pressure-drag relative contribution PD within 0.25% of the DNS value for wave slopes $2A_w/\lambda$ up to 0.05, which yet corresponds to a relative error in pressure drag of about 12%.

For the wave slopes considered, the quadratic behaviour of the pressure drag is also consistent with previous studies, e.g. Henn and Sykes (1999), who observed a quadratic behaviour up to $2A_w/\lambda \approx 0.1$ in the case of a non-skewed wavy wall. Moreover, the DNS data shown in figure 4.14 indicate little change in pressure drag upon a change in wavelength at $\theta = 70°$.

Forcing amplitude and wave height

The last—and not least—missing piece of the puzzle is the determination of the wave height required to emulate the effect of the SSL. Whereas it was possible to circumvent this step in section 4.3.2 by only reasoning on the SSL forcing amplitude, the evaluation of the pressure drag absolutely requires prior knowledge of the equivalent height $A_w/h = \alpha_{\text{eq}}$ for which the transverse shear strain resembles that of a SSL with forcing amplitude $A^+_{\text{SSL}} = 1$. Had the shear-strain fields been identical in the SSL and wavy-wall cases for some wave height, the relationship between A_{SSL} and α_{eq} would have been less equivocal, but because the SSL's transverse shear-strain is only approximately mimicked, the value of the required height could be determined with differing assumptions regarding the quantification of an equivalent forcing amplitude. One of the most natural ways to define the equivalent height is by minimising the L^2-norm of the difference in transverse shear-strain between the SSL and the wavy

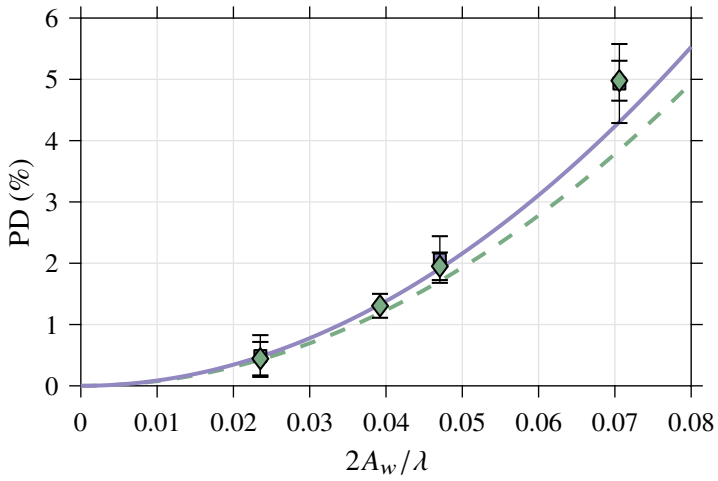


Figure 4.14: Level of pressure drag relative to the baseline drag for a wave at an angle $\theta = 70°$, at $Re_\tau \approx 360$. Green lozenges: DNS data at $\lambda^+ = 918$, blue squares: DNS data at $\lambda^+ = 612$, green dashed line: linear solution for $A_w/h = \alpha$ and $\lambda^+ = 918$, blue solid line: linear solution for $A_w/h = \alpha$ and $\lambda^+ = 612$. The error-bars show the 90%-confidence interval for the total drag of each simulation relative to the baseline drag σ_{ww}/D^0_t (cf. section 2.7.3).

wall, in order to make the wavy-wall and SSL solutions as close as possible. For the wavy wall, the transverse shear-strain is calculated from the linear solution as in figure 4.8. For the SSL, although no DNS data are available for the turbulent profiles, it is often the case that the spanwise profiles, scaled in wall units, are similar to the laminar profiles as shown in figure 3.19 (as well as in Viotti et al., 2009a; Quadrio and Ricco, 2010; Touber and Leschziner, 2012). Although the latter statement is not necessarily true at sub-optimal actuation, it is one of the most reasonable ways of estimating such information. The distance between the two solutions for the optimal value of α_{eq} is:

$$l_{\min} = \min_{\alpha_{\mathrm{eq}}} \left\| \frac{\alpha_{\mathrm{eq}}}{Re_\tau} \Re \left[\frac{\mathrm{d}\hat{w}}{\mathrm{d}\eta} \exp(\mathrm{i}\boldsymbol{k}\cdot\boldsymbol{\xi}) \right] - \frac{\partial w^+_{\mathrm{SSL}}}{\partial \eta^+} \right\|, \tag{4.32}$$

where $\|\cdot\|$ denotes the L^2-norm, $w_{\mathrm{SSL}}(\xi,\eta)$ is the laminar SSL spanwise velocity, and $\hat{w}$ is taken from the solution of equation (4.19).

The values of α_{eq} and its corresponding $l_{\min}$ are shown in figures 4.15 and 4.16, respectively. Figure 4.15 shows that for larger wavelengths the wave height has to be significantly increased in order to generate the same shear-strain level as in the SSL case. This indicates that a more representative quantity with respect to the level of transverse shear-strain may be the wave slope, something that will be tested in chapter 6. Moreover, figure 4.16 shows that the L^2-norm distance between the wavy-wall shear strain and that of the SSL decreases with the wavelength.

Drag reduction

The value of the wave height $\alpha_{\mathrm{eq}}(\lambda_x,\theta,A_{\mathrm{SSL}})$ corresponding to the desired SSL is evaluated using the method described in section 4.3.3, which allows to determine the associated pressure drag, and eventually to the total drag reduction, evaluated as:

$$\mathrm{TDR}|_{A^+_{\mathrm{SSL}}=1} = \mathrm{FDR}(\lambda_x) - \mathrm{PD}(\lambda_x,\theta,\alpha_{\mathrm{eq}}). \tag{4.33}$$

The corresponding map, shown in figure 4.17, does not present any optimum in the region consisting of gentle large-scale wavy undulations, but indicates that larger angles may be preferable, together with smaller wavelengths λ. This does not contradict the observation of section 4.3.2 since the *streamwise* wavelength remains large at these high angles. Indeed, the orientation of the drag-reduction contours for vanishing wavelength and angle tending to 90° approximately follows the line of constant streamwise wavelength $\lambda^+_x \approx 1300$, which roughly corresponds to the maximum of $\mathrm{FDR}_{\mathrm{SSL}}$ (cf. figure 4.13).

However, small values of λ coincide with the region of the parameter space were the distance $l_{\min}$ is

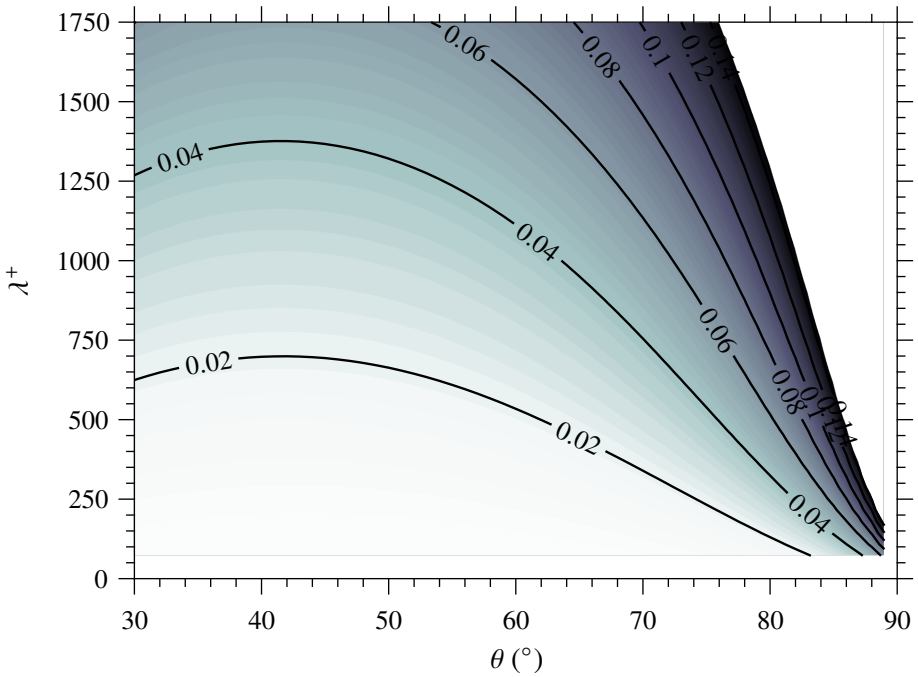


Figure 4.15: Contours of α_{eq} (similar to A_w/h) corresponding to $A^+_{\text{SSL}} = 1$, obtained by minimising the L^2-norm-distance between the transverse shear-strains of the wavy wall and the SSL, defined in equation (4.32). The data shown are in the region where α_{eq} is lower than 15%.

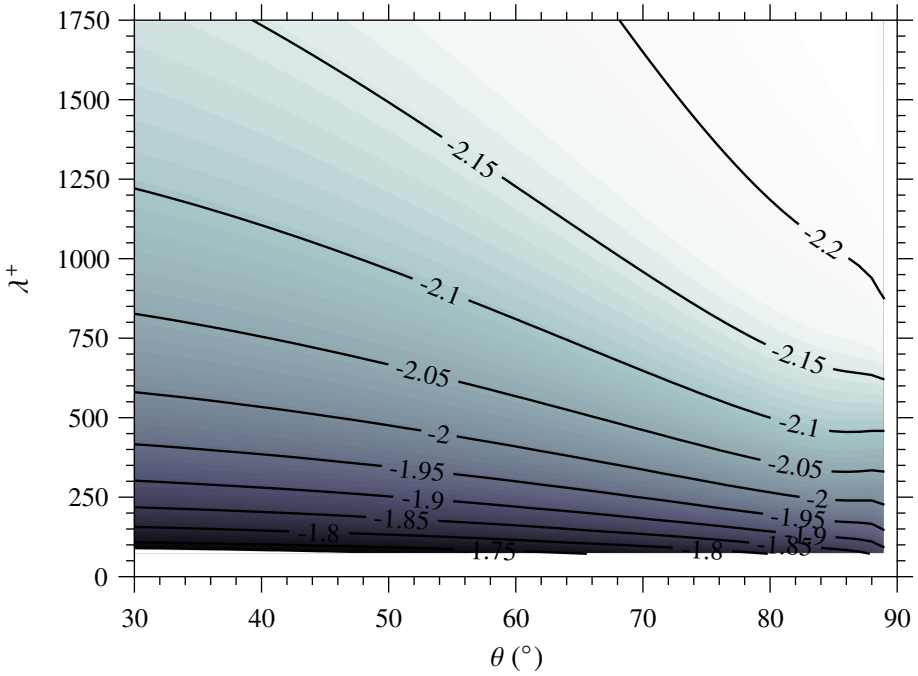


Figure 4.16: Minimum distance l_{min} between the transverse shear-strains of the wavy wall and the SSL. The isocontour labels show the value of $\log_{10}(l_{\text{min}})$.

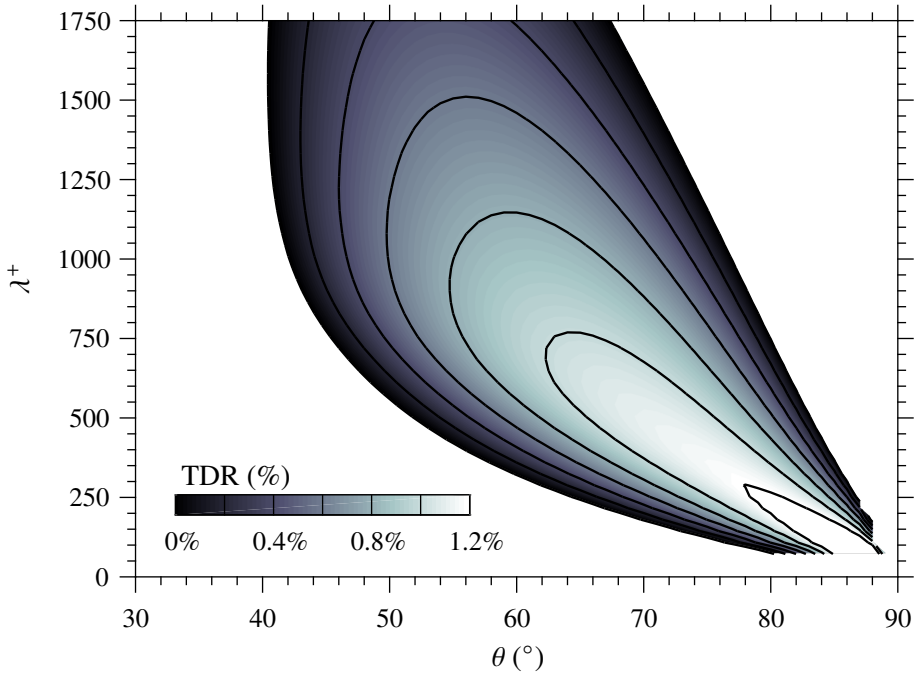


Figure 4.17: Prediction of the total drag reduction for Model 2, as a function of the wavelength λ^+ and angle of the wave θ. The contours are equispaced between 0 and 1.2% and correspond to the ticks present on the legend colour-bar.

larger (cf. figure 4.16), i.e. where the emulation of the shear-strain is less truthful, so that the prediction of the friction reduction is unlikely to be accurate. This behaviour may stem from the fact that the pressure drag decreases as the angle of the wave is increased. Although this region is outside of the scope of the present research, an interesting coincidence is that for vanishing values of λ and at an angle tending to $\theta = 90°$, the geometry consists of small grooves aligned with the flow direction, i.e. riblets.

4.4 Conclusions

A linear solution to the RANS equations was presented and compared to laminar and turbulent non-linear solutions of the full Navier–Stokes equations. Given a set of parameters describing the wave geometry and orientation of the flow, the linear solution provides an estimate of the flow distortions provoked by the wavy wall. The latter were then used in conjunction with the DNS data of Viotti et al. (2009a) and two semi-empirical models were formulated in order to infer trends on the most likely location of the optimal wavy-wall configuration in the parameter space.

Model 1 indicates that longer streamwise wavelengths may be beneficial as they mitigate the additional longitudinal energy dissipation, and that the optimal angle of the grooves may be located between

$\theta = 55^\circ$ and $\theta = 75^\circ$.

Model 2 assumes that a similarity in the transverse shear-strain results in the same level of friction reduction, which is militated against by the pressure drag evaluated from the linear solution. Results from Model 2 were shown only for small forcing amplitudes $A^+_{\mathrm{SSL}} = 1$ where the analogy is most likely to hold, and the linear approximation most likely to be accurate. The study indicated that larger angles where favourable as they decrease the pressure drag, and that longer undulations yielded a transverse shear-strain closer to that of the SSL. Unfortunately, the intensity of the transverse shear-strain generated by the wavy wall remains weak relative to the forcing amplitudes considered in the literature on Stokes layers. This is not entirely surprising though, as the velocity imparted at the wall is often greater than a third of the centreline velocity, and this limitation is somewhat reminiscent of the difficulty faced when attempting to efficiently impart spanwise wall oscillations in a laboratory using electro-actuators, as in the work of Gatti et al. (2015).

Chapter 5

Numerical simulations

Contents

5.1 Overall strategy 125
5.2 Numerical set-up 126
5.2.1 Grid properties 126
5.2.2 Flow configurations 127
5.3 Overall physical characteristics 129
5.3.1 General description of the flow 129
5.3.2 Secondary flow 132
5.3.3 Influence of the upper wall 136
5.4 Drag behaviour and grid convergence 138
5.4.1 Net drag reduction and grid convergence 138
5.4.2 Friction-drag reduction and pressure-drag increase 142
5.4.3 Influence of the spanwise wavelength 143
5.5 Turbulence characteristics 148
5.5.1 Overview 148
5.5.2 PDFs of the velocity fluctuations 148
5.5.3 Anisotropy of the turbulence field 154
5.5.4 Energy budgets 156
5.6 Conclusions 159

5.1 Overall strategy

An obvious problem is posed by the absence of any guidance on which combination of geometric parameters offers the promise of maximum drag reduction. An exploration of the three-dimensional

parameter space (wave height, wavelength, and flow angle) by a 'carpet-bombing' strategy, or classical formal optimisation strategy, is not tenable on cost grounds, especially because of the tight resolution requirements needed for an accurate prediction of the drag increase/decrease margin, as will transpire in this chapter. For this reason, a preliminary low-order study was undertaken in chapter 4 to narrow down the exploration range within which the drag reduction might be maximised. Moreover, the semi-empirical models presented in chapter 4 cast light on the potential benefit of having longer streamwise wavelengths, and identified a promising range of angles to explore.

The present strategy was initiated with the configuration given in Chernyshenko (2013), but the subsequent exploration made use of the observations reported in chapter 4. The study undertaken by Chernyshenko found an estimate for the streamwise-projected wavelength of $\lambda_x^+ \approx 1500$, and the flow angle $\theta \approx 52°$, but it did not provide an estimate for the height of the wave. Rather, a condition was given for the wave height, subject to the amplitude of the forcing of the emulated spatial Stokes layer $A_{\mathrm{SSL}}^+ = 2$. The wave height was chosen in order to approximately satisfy the condition on the pressure gradient given in Chernyshenko's analysis, using the linear model presented in section 4.2, with considerations on the equivalent height akin to those of section 4.3.3. Other configurations, a selection of which will be presented below, were later simulated, and the exploration was essentially undertaken by trial an error, with the aim of incorporating the results of chapter 4 in the search direction, whilst seeking an understanding of the influence of each parameter on the drag levels and flow properties.

5.2 Numerical set-up

5.2.1 Grid properties

The simulations were performed with surface-conformal meshing, as detailed in section 2.2. Two types of wavy geometries are considered in this chapter: one with both walls wavy and the other with one wall flat, as shown in figure 5.1. In the former, shown in figure 5.1a, both walls are spatially in phase, i.e. yielding a constant passage height of $2h$ along the entire channel. In the latter, shown in figure 5.1b, the local height varies from $2h - A_w$ to $2h + A_w$, where $2h$ is the mean channel height, and A_w the amplitude of the sinusoidal wall undulations.

A number of grid configurations have been simulated, at constant flow rate (cf. section 2.3), with the characteristics of the plane-channel mesh listed in table 5.1, where all quantities are scaled by reference to the target friction Reynolds number. The labels G1 to G11 will be used later to identify these cases.

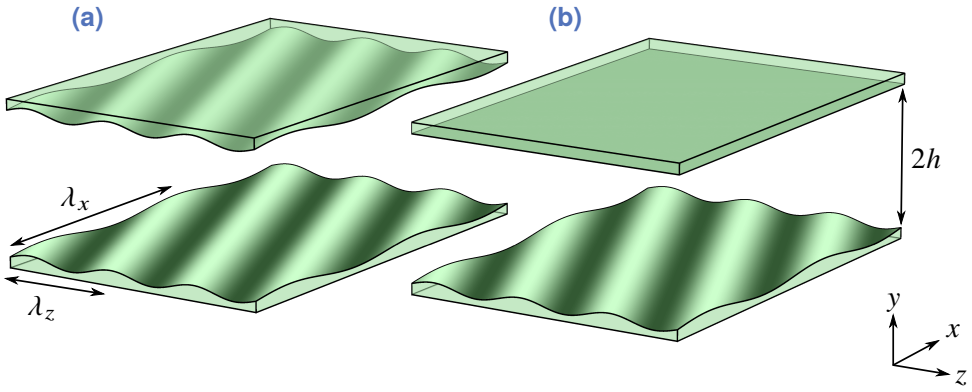


Figure 5.1: Sketch of the geometrical configurations: **(a)** wavy–wavy channel and **(b)** wavy–flat channel. Here, the main flow direction is along the x-coordinate.

As will transpire, the changes in drag relative to the plane channel are small, pushing the requirements for the spatial resolution to much more stringent levels than those for regular DNS. Therefore, particular emphasis is placed on a few simulations performed at the highest tractable resolution within the resources available. These key simulations correspond to the finest grid G6, at a bulk Reynolds number of $Re_b = 6200$ (corresponding to $Re_\tau \approx 360$). Quantitative evidence for the level of refinement is given in figure 5.2, by grid dimensions scaled with the Kolmogorov length scale in a plane-channel DNS for the mesh G6. This shows that the ratio Δ/η, where $\Delta = \sqrt[3]{\Delta x \Delta y \Delta z}$, remains lower than unity throughout the channel.

5.2.2 Flow configurations

Most simulations were performed at $Re_\tau \approx 360$ for various configurations, grid resolutions, and domain sizes. This Reynolds number was chosen so that the total cost of the simulations remained tractable. The ratio between the height of the wave and the channel height A_w/h was kept relatively modest. The corresponding parameters are given in table 5.2, along with the drag levels calculated as explained in section 2.6. The standard deviation of the total drag calculated from the driving pressure gradient is also shown, and this was calculated as described in section 2.7. The net drag variation can be evaluated in two ways: from the imposed pressure gradient and from the sum of the surface-integrated pressure force and friction-drag force. As expressed by equation (2.52), the two should be identical. However, they differ very slightly in the simulations, but in all cases, the imbalance of the forces is regarded as negligible so only the surface integrals are reported in table 5.2. One exception is the set of simulations whose labels are shown in italic typeface: unlike other simulations where this imbalance was lower

Table 5.1: Properties of the grid configurations on which almost all the simulations presented are based. Viscous units are based on the target value of Re_τ for the plane channel. (Note that the angle of the flow may vary, e.g. for an angle of $\pi/2$, the roles of x and z are reversed.)

Label	Re_τ	N_x	N_y	N_z	Δx^+	Δy^+	Δz^+	Δt^+	L_x/h	L_z/h
G1	180	768	192	768	2.4	0.7 – 2.9	2.4	0.04	10.2	10.2
G2	360	768	192	768	4.8	0.7 – 7.3	4.8	0.05	10.2	10.2
G3	360	2208	192	2208	2.5	0.4 – 8.5	2.5	0.02	15	15
G4	360	1104	192	1104	2.5	0.4 – 8.5	2.5	0.02	7.5	7.5
G5	1000	1024	768	1152	7.1	0.5 – 5.0	8.7	0.03	7.2	10
G6	360	1104	288	2208	1.7	0.6 – 4.5	1.7	0.02	5.1	10.2
G7	360	1104	288	2208	1.7	0.6 – 4.5	2.5	0.02	5.43	14.91
G8	360	1104	288	2208	1.9	0.6 – 4.5	1.6	0.02	5.8	10
G9	360	1152	288	2304	1.8	0.6 – 4.4	1.8	0.02	5.8	12
G10	360	1104	288	2208	1.9	0.6 – 4.5	1.6	0.02	5.8	10
G11	360	2208	288	1104	2.5	0.6 – 4.5	2.5	0.03	15	7.5

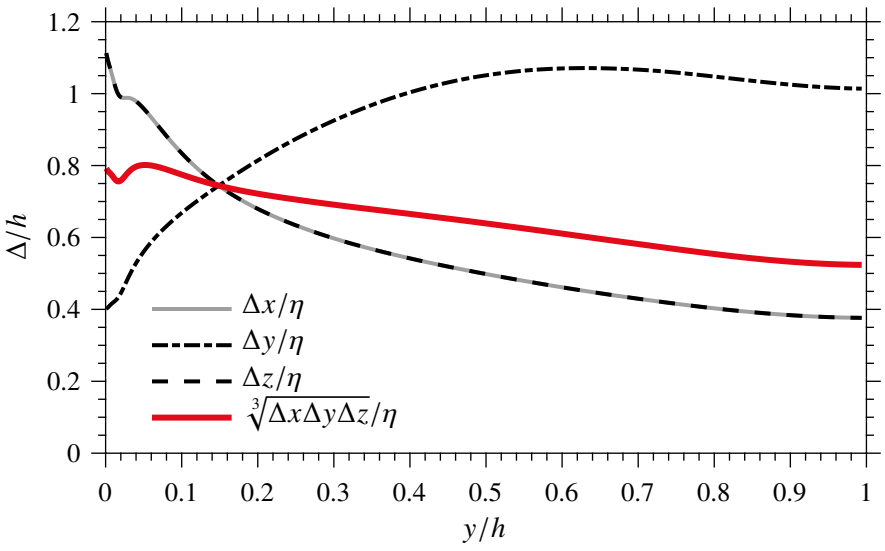


Figure 5.2: Ratios between grid spacings and the Kolmogorov length scale across the wall-normal direction for a plane channel, and for the grid configuration G6.

than 0.05% of the total drag, the simulations in question here suffered from an insufficient number of grid levels (only two) in the V-cycles of the multigrid algorithm used to accelerate the convergence of the pressure solution (cf. discussion in section 3.1.2). Although some caution is called for when interpreting the results of these simulations, the effect on the drag levels was observed to be insignificant upon further investigation: the number of cells was changed in order to be able to increase the number of levels in the V-cycles of the multigrid algorithm, and so *G8W1A3* and G10W1A3 became equivalent configurations (cf. grids G8 and G10 in table 5.1). The drag levels calculated from the surface integrals in *G8W1A2* and G10W1A2 are identical within the time-averaging error. By way of contrast with previous DNS studies reporting this value, the force imbalance in Wang et al. (2006) was of about 3–4%, compared to a maximum of 0.2% in the problematic simulations identified in italics.

5.3 Overall physical characteristics

5.3.1 General description of the flow

As the flow progresses past the skewed wavy wall, the most obvious and accessible quantity is the wall-normal velocity: a positive slope of the boundary will deviate the flow upwards, thus inducing positive values for $\widetilde{v}$. Conversely, a negative slope induces negative values of $\widetilde{v}$, as can be observed in figure 5.3b.

Upon climbing the windward side of the wave, the fluid accelerates, which results in a low-pressure region above the crest, and high-pressure region in the trough (cf. figure 5.3d). The pressure minimum is located approximately above the crest, whereas the pressure maximum is located in the trough, slightly downstream of the lowest point. This asymmetry results from non-linear (convective) effects, which become more and more pronounced as the height of the wave is increased, and which cause the pressure maximum to move even further downstream, thus accentuating the triangular shape of the pressure contours. These changes in pressure are associated with positive values of $\widetilde{u}$ on the windward side and negative values on the leeward side of the wave (cf. figure 5.3a). This goes hand-in-hand with a thinning of the near-wall layer uphill and thickening downhill, leading to an increase and decrease in friction, respectively, as will be shown in figure 5.5. The wall friction reaches its maximum (for this particular flow configuration G6W1A2) around $x/\lambda = 0.04$, and its minimum at $x/\lambda = 0.5$, so that there is a noticeable shift in phase of the maximum friction. As the wave amplitude increases, the friction extrema get closer to each other, the maximum shifting uphill, whilst the minimum regresses

Table 5.2: See top of facing page for caption.

Simulation label	Flow configuration				Drag coefficients and UQ ($\times 10^6$)			Relative drag variation		
	A_w^+	θ_f (°)	λ^+	λ_x^+	$\sigma_{\text{tot.}}$	D_p	D_f	TDR	PD	FDR
Key simulations										
G6P1	0	70	–	–	11	0	6677			
G6W1A1	11	70	918	2684	11	30	6628	0.3%	0.45%	0.74%
G6W1A2	18	70	918	2684	8	87	6544	0.7%	1.30%	1.99%
G6W1A3	22	70	918	2684	9	130	6507	0.6%	1.95%	2.55%
G6W1A4	32	70	918	2684	13	332	6394	-0.7%	4.97%	4.24%
G6W2A1	7	70	612	1789	14	32	6637	0.1%	0.48%	0.60%
G6W2A3	14	70	612	1789	15	138	6539	0.0%	2.07%	2.07%
G6W2A4	22	70	612	1789	26	329	6450	-1.5%	4.92%	3.40%
Influence of the spanwise wavelength										
G8W1A1	11	75	695	2685	9	26	6626	0.2%	0.39%	0.6%
G8W1A3	22	75	695	2685	6	112	6501	0.8%	1.68%	2.48%
G8W1A4	32	75	695	2685	12	277	6423	-0.5%	4.16%	3.65%
G9W1A1	11	80	468	2685	8	22	6624	0.3%	0.33%	0.64%
G9W1A3	22	80	468	2685	11	89	6576	0.0%	1.33%	1.35%
G9W1A4	32	80	468	2685	14	195	6569	-1.5%	2.92%	1.46%
G10P1	0	75	–	–	11	0	6666			
G10W1A3	22	75	695	2685	9	113	6495	0.9%	1.70%	2.57%
G11P1	0	0	–	–	9	0	6642			
G11W1	18	0	2700	2700	7	91	6636	-1.3%	1.37%	0.10%
Other simulations										
G3P1	0	0	–	–	11	0	6639			
G3P2	0	45	–	–	14	0	6688			
G3W1	18	70	918	2684	10	87	6533	1.1%	1.29%	2.41%
G4P1	0	0	–	–	17	0	6640			
G4P2	0	45	–	–	16	0	6691			
G2P1	0	52	–	–	4	0	6809			
G2P2	0	70	–	–	4	0	6755			
G2W1	18	52	918	1491	4	544	6479	-3.0%	7.99%	4.85%
G2W1f	18	52	918	1491	6	271	6641	-1.5%	3.98%	2.47%
G2W1bis	18	70	918	2684	4	87	6560	1.6%	1.29%	2.89%
G2W2	14	70	612	1789	8	138	6503	1.7%	2.04%	3.73%
G6W3	7	70	306	895	15	125	6647	-1.4%	1.88%	0.45%
G6W4	36	70	1836	5368	8	51	6646	-0.3%	0.76%	0.46%
G6W1bis	14	60	918	1836	9	171	6548	-0.6%	2.56%	1.94%
G7P1	0	90	–	–	15	0	6656			
G7W1A2[a]	18	90	918	2684	8	(D_t = 6613)		0.7%	N/A	N/A

[a]For this particular case, $\theta \neq \theta_f$ since the mesh is wavy in both directions. The angle of the wave is $\theta = 70°$.

Table 5.2: Configurations simulated, all at $Re_\tau \approx 360$. Each simulation is designated by a label consisting of a set of letters plus identifiers, meant to convey as much information as possible in a compact manner, and identifying each calculation uniquely. 'G' stands for 'Grid' and refers to the grid configurations detailed in table 5.1, 'W' stands for 'Wavy', 'P' for 'Plane', and 'A' for 'Amplitude'. The figure following the letter 'A' identifies a particular value of the wave slope A_w/λ_x. The suffix 'f' indicates the presence of a flat upper wall instead of two in-phase wavy walls, and 'bis' reflects the fact that the wavelength of 'G2W1bis' is equal to that of 'G2W1', but the flow angle θ_f is different. TDR, PD and FDR respectively stand for Total-Drag Reduction, Pressure Drag and Friction-Drag Reduction.

towards the crest. The extrema of the streamwise phase variations are located above the windward and leeward sides of the walls—that is, where the absolute value of the local slope is a maximum. A similar behaviour is observed for the extrema of the wall-normal velocity component.

Most of the effects described so far are qualitatively similar to those described in Maaß and Schumann (1996) and Henn and Sykes (1999) for a wavy wall with its crests perpendicular to the flow direction. Despite the presence of flow separation in the latter study, strong resemblance is observed with the present results for the streamwise- and wall-normal-related statistics. In particular, the variation of the phase-varying stresses in a dual layer, as shown in figure 5.4b, changing sign going further away in the wall-normal direction, was already evidenced in Henn and Sykes (1999). A drastically different statistical feature of the skewed wavy wall is, however, the presence of a non-zero spanwise velocity, and the effect of the skewness will become clearer in the course of the comparison between skewed and orthogonal wavy walls given in section 6.2.6.

For an oblique wavy wall, the non-zero spanwise velocity is shown in figure 5.3c. Because the wave is at an angle to the main flow direction, the pressure phase variations give rise to a pressure gradient both in the streamwise and spanwise direction. The latter gradient generates a spanwise motion, shown in figure 5.3c, which is asymmetric in phase and penetrates into the log layer. The sign of the phase variations of the spanwise velocity can be explained by considering the local periodic mean pressure gradient, which is oriented at right angle to the crests of the grooves, and then adding the driving pressure gradient, which is aligned with the flow direction.

The extrema of the spanwise velocity are located above the crest and in the trough, which corresponds to the locations where the spanwise component of the pressure gradient changes sign. Attention is drawn to the fact that the sign of $\widetilde{w}$ is dependent upon the sign chosen for θ, although $+\theta$ and $-\theta$ configurations evidently remain exactly the same in terms of flow properties and overall drag.

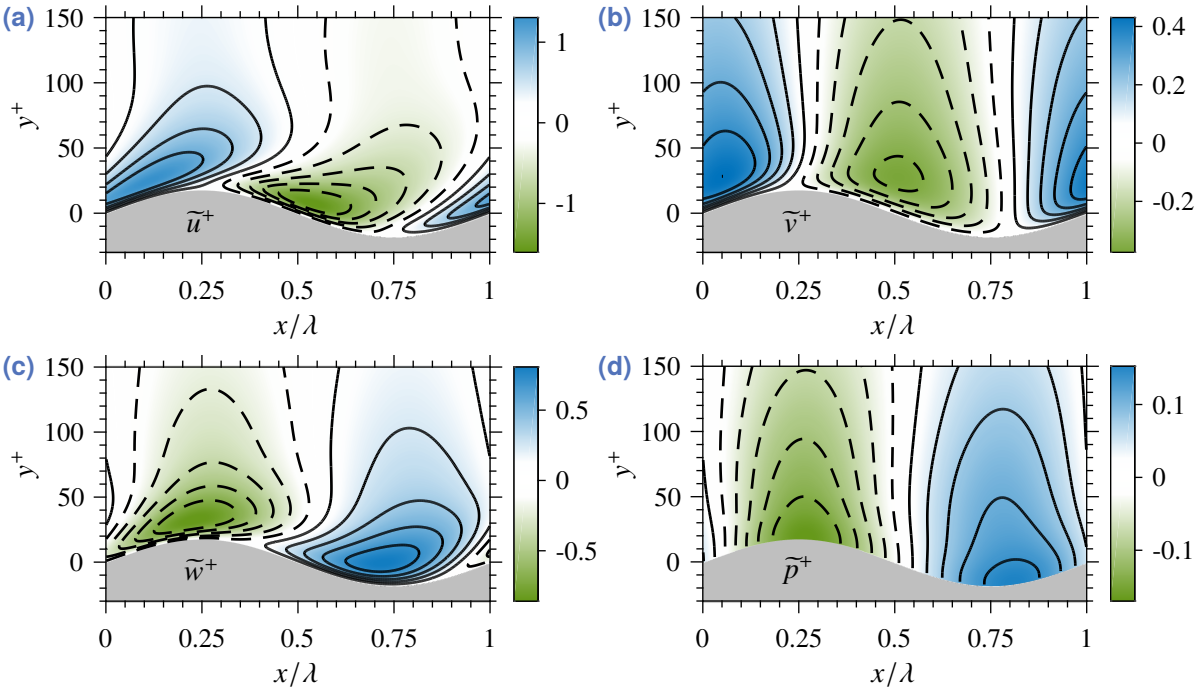


Figure 5.3: Phase variations of the velocity and pressure fields for G6W1A2 ($A_w^+ = 18$, $\theta = 70°$ and $\lambda^+ = 918$, cf. table 5.2), normalised with the actual friction velocity. Contour levels are equispaced, symmetric around zero, and the range of the scale on each plot corresponds to that of the data shown. Solid lines correspond to positive levels, whereas dashed lines correspond to negative levels. The quantity shown is labelled in the grey area corresponding to the wave shape.

The total-drag stress, defined in equation (2.27), is shown in figure 5.6 together with the contribution arising from pressure. The effect of the pressure drag is most significant slightly before the crests, where it has a favourable effect, and on the upward slope where it adds to the increased friction. While the friction reduction starts around the crest for all wave slopes and recovers the baseline level in the trough at a location slightly moving downstream with increasing wave slope, the increase in the total wall stress begins around $x/\lambda = 0.76$ for all wave slopes and recovers the baseline level slightly downstream the crest at a wave-slope-dependent location.

5.3.2 Secondary flow

An intuitive assumption is that the direction of the flow is locally modified and tends to follow the grooves when a flow is forced across skewed grooves. When the flow progresses towards a crest, it climbs uphill whilst being deviated sideways by the action of the local pressure gradient. Around this location, the scalar product between the surface normal and the velocity vector is negative. The flow

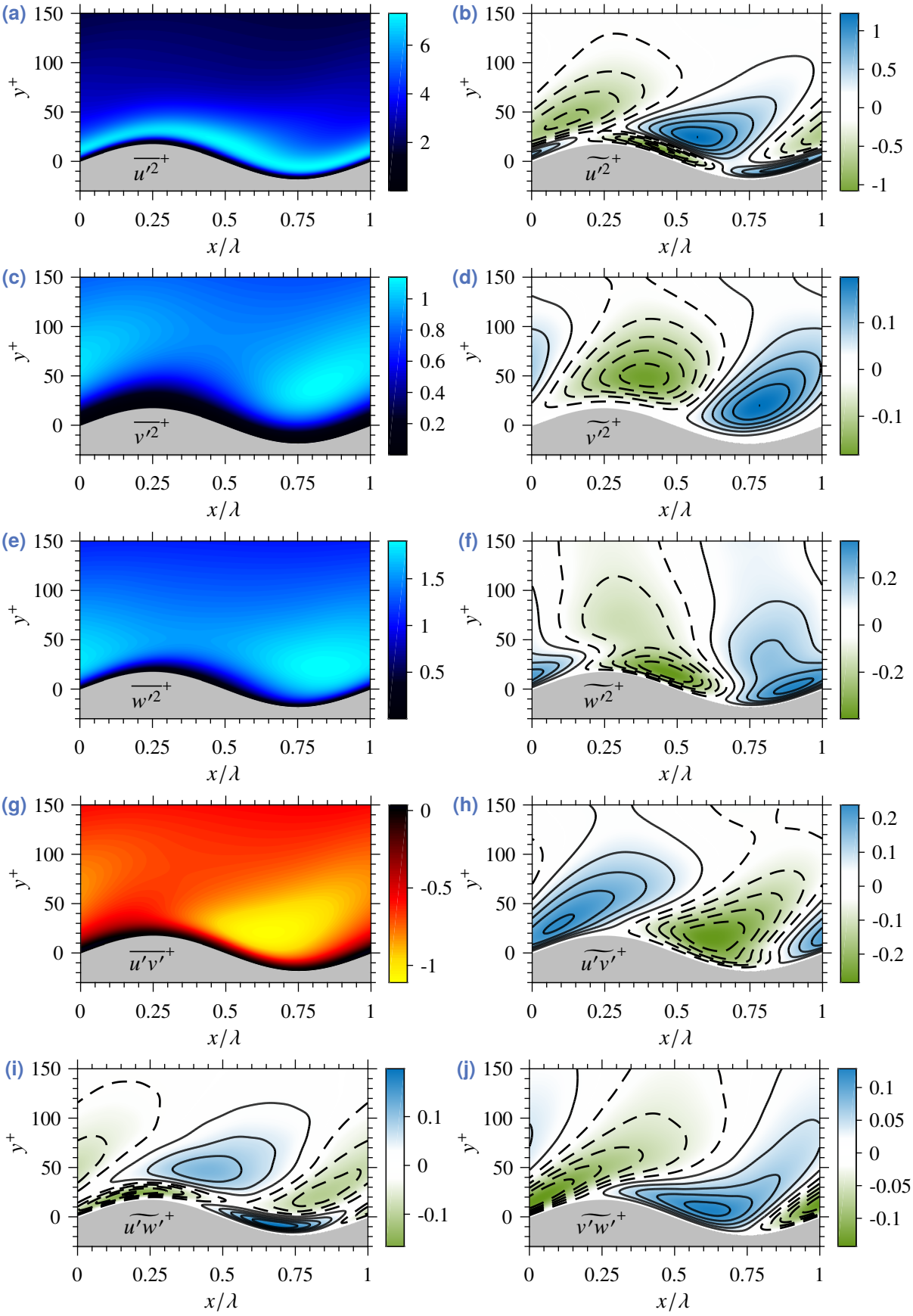


Figure 5.4: Reynolds stresses normalised by the mean friction velocity u_τ^2 for G6W1A2. Same legend as figure 5.3.

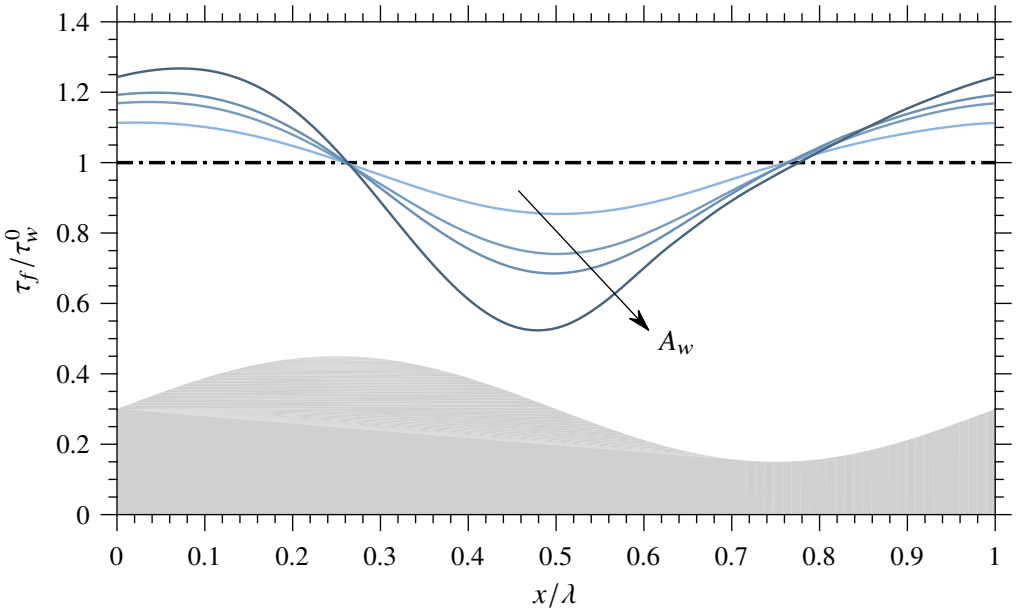


Figure 5.5: Phase-wise variation of the wall friction. The baseline friction is denoted τ_w^0. Black dash-dotted line: plane channel, solid lines: G6W1A*, i.e. for $\lambda^+ = 918$, $\theta = 70°$, and $A_w^+ \in \{11, 18, 22, 32\}$. The grey area shows the corresponding phase location on the wavy wall.

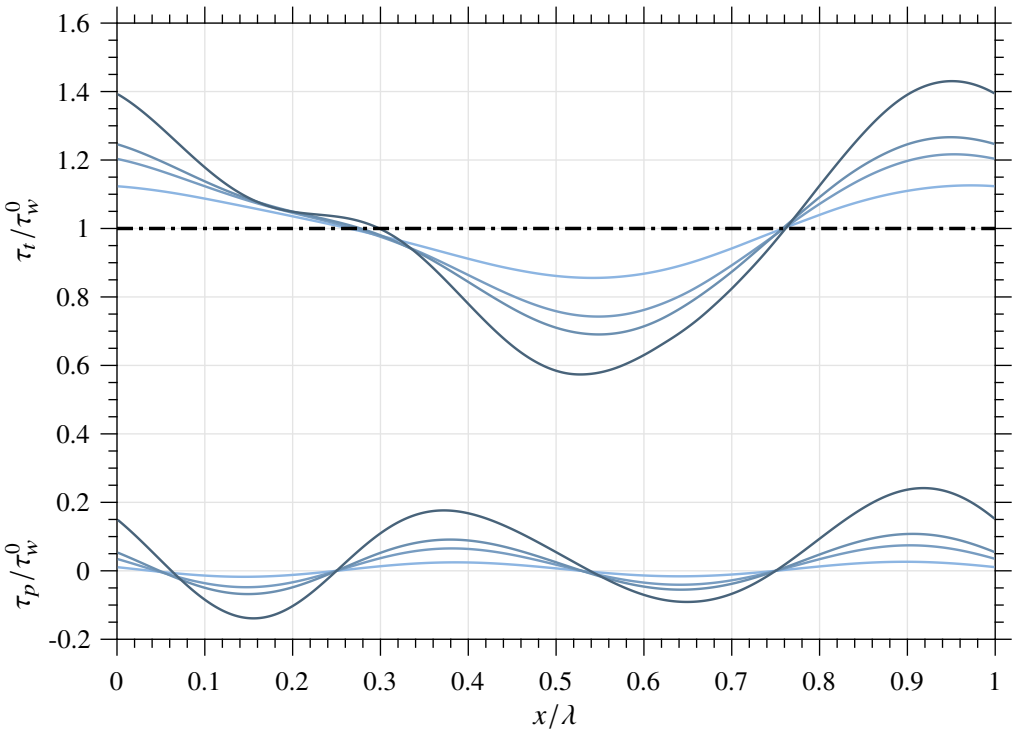


Figure 5.6: Phase-wise variation of the total-drag stress at the wall (upper curves) and contribution from the pressure-drag stress (lower curves). See definitions in equations (2.27) and (2.47). Same legend as figure 5.5.

then moves down the hill and is deviated to the other side, with the scalar product between the surface normal and the flow direction then being positive. Because of this change in the orientation of the surface normal, the deviation is more pronounced towards the trough, so that the sideways motion is not symmetric in phase. This gives rise to a mean drift that gently modulates the angle of the mean velocity vector in the wall-normal direction. For the amplitude of greatest interest, i.e. for A_w^+ of about 20, this angle variation remains lower than 1° throughout the cross-section. The method by which the driving procedure enforces an approximately constant flow rate in the streamwise and spanwise directions involves setting the spanwise component of the bulk velocity to approximately zero. This constraint results in a streaming motion (cf. figure 5.7) with a mean spanwise velocity along the centreline, of opposite sign to the mean motion close to the wall. Figure 5.7 also shows that the phase-integrated profiles are similar for given wave slopes but varying wavelengths. Naturally, the maximum phase-integrated spanwise velocity $W_{\max} = \max_y |W(y)|$ is expected to rise as the slope of the wave increases. Moreover, this effect is observed to be quadratic in figure 5.8, and remains much weaker than the phase-varying spanwise velocity $\widetilde{w}$ for the small amplitudes relevant to the drag-reduction properties of such geometries. In contrast to this quadratic variation, the maximum of the phase-varying spanwise velocity $\widetilde{w}_{\max}$ features a linear behaviour with increasing wave slope (cf. figure 5.8).

In chapter 4, the linear approximation was by construction only able to capture the phase variations, and the quadratic streaming effect was neglected. The present results show that such an approximation

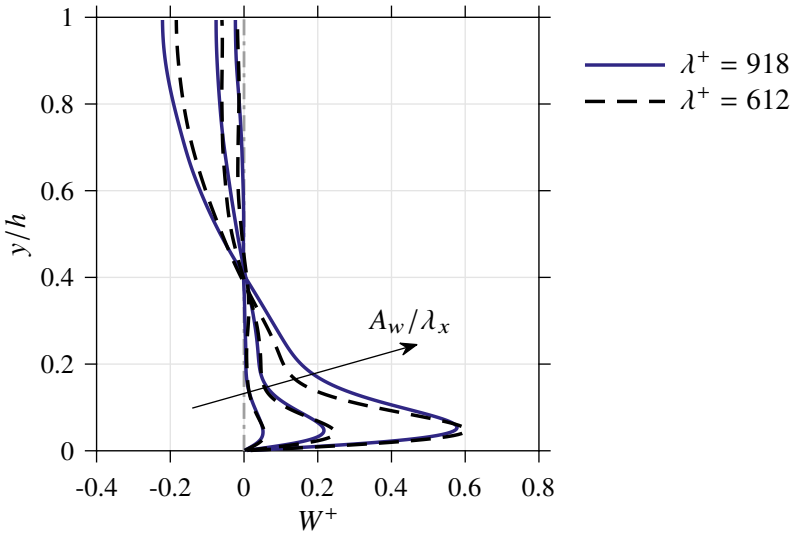


Figure 5.7: Mean streaming motion $W(y)$ for increasing wave slopes. Solid blue lines correspond to G6W1A1, G6W1A3, and G6W1A4, dashed black lines correspond to G6W2A1, G6W2A3, and G6W2A4.

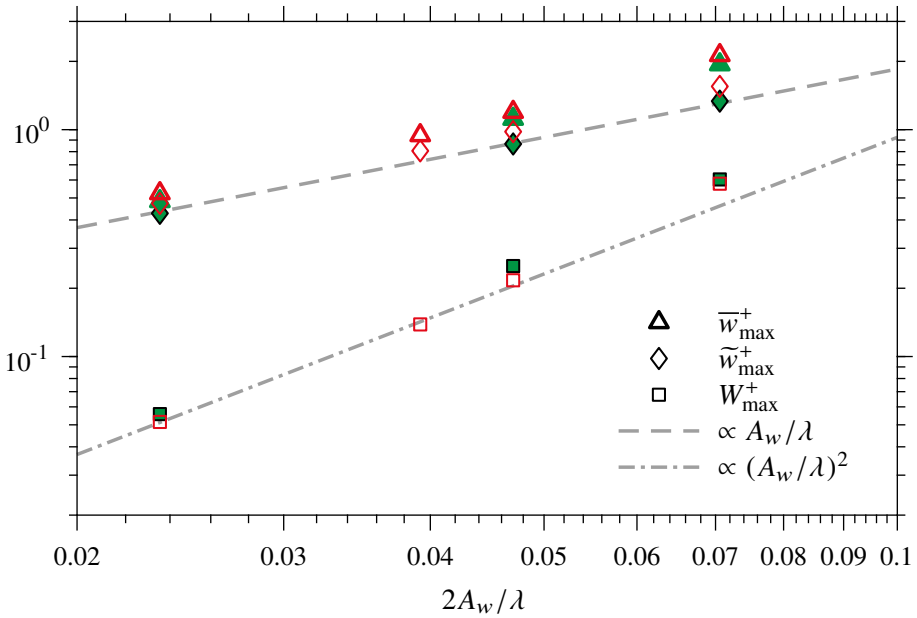


Figure 5.8: Contributions to the maximum (under the L^∞-norm) spanwise velocity: dependence of the maxima of the phase-integrated ($W^+_{\max}$), and phase-varying ($\widetilde{w}^+_{\max}$) spanwise velocities upon the wave slope $2A_w/\lambda$. Filled symbols: $\lambda^+ = 612$, open symbols: $\lambda^+ = 918$.

is reasonable for small wave slopes, but it also indicates that the streaming effect rapidly becomes more important for larger wave slopes, which limits the maximum wave slope that may be used.

5.3.3 Influence of the upper wall

Previous studies on wavy channels often had only a single wavy wall, or featured varicose wall undulations (Cherukat et al., 1998; Henn and Sykes, 1999; Yoon et al., 2009; Nakanishi et al., 2012; Mamori, 2012; Luchini, 2016). A distinct feature of the present configuration is that the passage height is constant at any phase location. Thus, comparing various wall configurations is interesting in order to ensure that the distance between the two walls is large enough, so that the upper wavy wall does not influence significantly the flow above the lower one. This was addressed by comparing simulations for channels with one or both walls wavy. The relevant entries in tables 5.2 and 5.3 are G2W1 and G2W1f, and the corresponding plane-channel baseline G2P1.

The results in table 5.3 show that the friction on the lower (wavy) boundary of G2W1f has a lower value than for G2W1, whilst the friction on the upper (flat) surface of G2W1f is slightly increased with respect to the baseline drag. The latter is a consequence of the control strategy of keeping the flow rate constant. The drag coefficients reported in table 5.3 show that the drag relative to the baseline level (in this case, drag increase) is about half of that of the case with both walls wavy: the drag increase per

wavy wall in G2W1 is 1.58%, compared to 1.54% for the wavy–flat case G2W1f. Since the difference between the two corresponds to a change in drag of about 3×10^{-6}, which is smaller than the standard deviation of the time-averaging error $\sigma_{\text{tot.}}$ reported in table 5.3, this strongly supports the assertion that the two configurations are close to each other in terms of the processes effective at each wavy wall separately.

Quantitative evidence of the closer correspondence between the two flows is given in figure 5.9. The phase-varying spanwise motion is almost identical near the wavy wall, as shown in figure 5.9b, which indicates that the ratio A_w/h is small enough for the near-wall statistics on the lower wall not to be significantly influenced by the upper boundary.

However, the streaming effect described in section 5.3.2 for a wavy channel with both walls wavy is expected to be different from that in which only one of the walls is wavy. This is also affected by

Table 5.3: Drag coefficients at both upper and lower walls, comparing a wavy–wavy channel (G2W1) to its wavy–flat counterpart (G2W1f).

Simulation label	$\sigma_{\text{tot.}}$ ($\times 10^6$)	D_f ($\times 10^6$)		D_p ($\times 10^6$)		TDR
		lower	upper	lower	upper	(total)
G2P1	4	3405	3402	0	0	–
G2W1	4	3242	3237	272	271	-3.16%
G2W1f	6	3220	3421	271	0	-1.54%

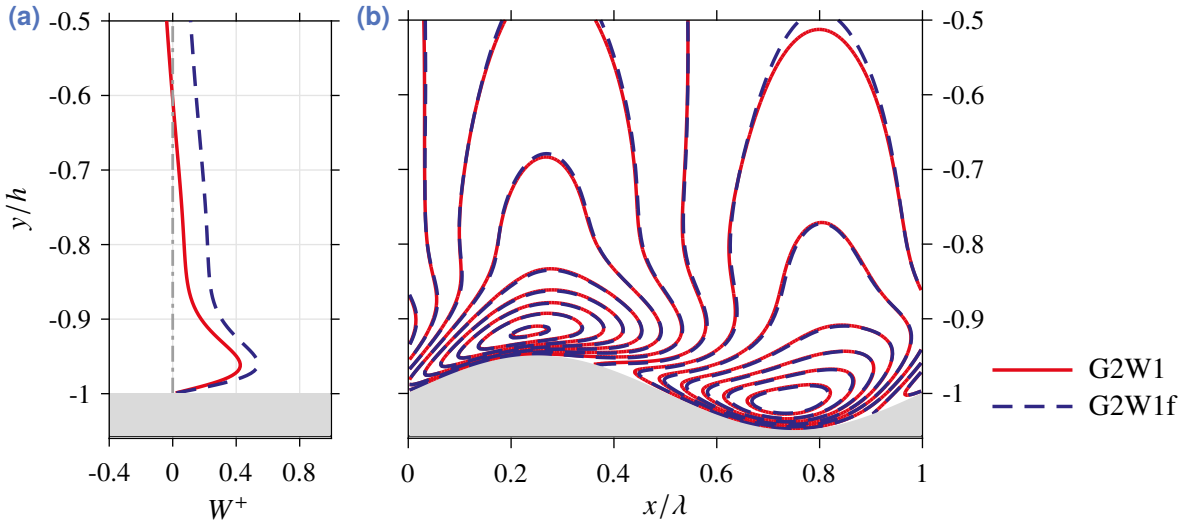


Figure 5.9: Comparison of the spanwise velocity for the wavy–wavy (G2W1) and wavy–flat (G2W1f) cases: **(a)** phase-integrated velocity W^+, **(b)** contours of the phase-varying velocity $\widetilde{w}^+$ spaced by from -1.4 to 1.2, evenly spaced by 0.2 increments. The reference friction velocity is that of the corresponding baseline flow.

the control strategy of maintaining the flow rate constant: since there ought to be no deviation of the flow in the vicinity of the flat wall, unlike when the upper boundary is wavy, the imposition of a zero spanwise bulk velocity affects this streaming effect which features a larger W^+ above the wavy wall in the wavy–flat case, as shown in figure 5.9a.

5.4 Drag behaviour and grid convergence

5.4.1 Net drag reduction and grid convergence

Baseline drag level

In table 5.2, TDR represents the drag relative to that of the plane channel. Physically, the latter is unique regardless of the angle between the flow an the mesh. However, this is not so computationally, owing to variations in solution domain and numerical errors, including the finite time of averaging, grid resolution, and the finite size and orientation of the periodic domain which does not allow very long structures to be captured. As the angle between the main flow direction and the grid varies, the length of the longest structure allowed to exist within the periodic boundaries changes. At the same time, the grid resolution is also altered in the flow-oriented directions. This results, in a plane channel, in a slight dependence of the drag on the flow direction. By way of example of the influence of the domain size on the drag, Ricco and Wu (2004) observed, for a flow aligned with the mesh at $Re_\tau = 200$, that changing the streamwise extent from $4\pi h$ to $21h$ whilst keeping roughly the same spatial resolution, resulted in a drag increase of 0.6%. This difference in drag is already large enough to be of the same order of magnitude as the variations of the total drag level in the cases considered herein. Therefore, a careful assessment of key computational parameters is required, as detailed below.

First, the influence of the domain size is considered for plane-channel flows. This was investigated by means of highly resolved simulations, with constant resolution, but varying domain sizes. For this purpose, grids G3 and G4 are chosen to have the same spatial resolution $\Delta x^+ = \Delta z^+ = 2.5$ and Δy^+ ranging from 0.4 at the wall up to 8.5 in the centre, but the domain size of G4 is one half of that of G3 in the x–z directions (cf. table 5.1). The largest domain considered is $L_x = L_z = 15h$, which represents about 5400 wall units, i.e. longer than the commonly chosen value of $8\pi h^+ = O(4500)$ at $Re_\tau = O(180)$. Table 5.2 shows that the relative difference in drag between the larger domain (grid G3) and the smaller (grid G4) is lower than 0.05%, both at an angle of 0° (G3P1 and G4P1) and 45° (G3P2 and G4P2).

Next, the impact of resolution is quantified, still for the case of a plane channel. To this end, simulations were run with the domain size kept constant, as in G3, but with a mesh coarser by a factor of 2 in the wall-parallel and wall-normal directions independently. Then, the drag levels for $\theta = 0°$ and $45°$ configurations were compared. As expected for a consistent discretisation, the difference between the two physically equivalent configurations ($\theta = 0°, 45°$) decreases as the resolution is increased. However, this difference remains significant at about 0.7% for grid G3, despite the mesh being fine with respect to usual DNS standards. An important observation is that increasing the number of cells in the wall-normal direction has little impact on the total drag, whereas increasing the resolution in the wall-parallel directions reduces significantly the difference in friction between $\theta = 0°$ and $\theta = 45°$. Drag differences with respect to the angle of the flow were observed to vary monotonically, the minimum drag coefficient being found at $\theta = 0°$, and the maximum at $\theta = 45°$.

Drag-reduction level

A possible approach to reducing the error in the predicted drag-reduction level is to evaluate it by reference to a plane-channel flow simulation at exactly the same spatial resolution, domain size, and flow angle. This is the approach preferred here, in light of the work of Gatti and Quadrio (2013, 2016) who observed some cancellation of the systematic bias associated with the domain size. Thus, for example, the baseline drag for G2W1 is G2P1 (both at $\theta = 52°$), whereas for G2W1bis ($\theta = 70°$), the baseline is taken to be G2P2 (also at $\theta = 70°$). However, even this elaborate approach may not suffice, in the face of the small drag-reduction margin, to remove uncertainties associated with the numerical aspects that contribute to the total error. A factor that may also be influential is the distortion of the cells fitted to the wavy boundary. As shown in table 5.4, changes in the total drag from grid G2 to the finest grid G6 are not independent of the wave geometry.

Table 5.4: Grid refinement study for wavy calculations, all at $\theta = 70°$. The coarsest grid is G2, and the finest is G6. Abbreviations are consistent with those of table 5.2.

Simulation label	Δx^+	Δz^+	FDR	PD	TDR
G2W1bis	4.8	4.8	3.0%	1.3%	1.7%
G3W1	2.5	2.5	2.4%	1.3%	1.1%
G6W1A2	1.7	1.7	2.0%	1.3%	0.7%
G2W2	4.8	4.8	3.8%	2.0%	1.8%
G6W2A3	1.7	1.7	2.1%	2.1%	0.0%

The variation of the total-drag reduction with grid refinement was studied in greater detail for the most promising simulation, namely G6W1A2: $(A_w^+, \theta, \lambda^+) = (18, 70°, 918)$. Since the drag was found to be mainly sensitive to the wall-parallel resolutions, only Δx and Δz are used as indicators of the grid refinement, as shown in figure 5.10a. More precisely, for such fine resolutions, and in light of the results shown for the plane channel, it is reasonable to assume the accuracy to be mostly sensitive to the spacing in the spanwise direction. Since the flow is not aligned with the grid, the measure of the grid spacing used for the spanwise direction is the spanwise-projected cell spacing, defined as $\Delta\check{z} = \min\{\Delta z/\cos\theta, \Delta x/\sin\theta\}$. The main outcome of the study, shown in figure 5.10b, is that the total-drag reduction predicted decreases as the mesh is refined, with a quadratic dependence on the wall-parallel mesh spacing, consistent with the order of accuracy of the spatial discretisation. The drag-reduction value appears to tend, asymptotically, to a positive value of about 0.6%.

Additionally, the ratios of the friction- and pressure-drag coefficients (D_f and D_p respectively), relative to the total $D_{\text{tot.}}$, remain constant for grids G2 and G6: thus, the value of D_p is 1.314% that of $D_{\text{tot.}}$ for the coarsest mesh G2W1A2, compared with 1.315% for the finest mesh G6W1A2. Therefore, whilst the share between the pressure and friction drag is grid-independent, the absolute value of the total drag is a very sensitive quantity that requires substantial computational efforts to be accurately predicted.

One additional simulation, physically equivalent to G6W1A2, was undertaken, but in a computational box aligned with the main flow direction, the waves being at an angle to the grid. Two wavelengths were included in the streamwise and spanwise directions, and the grid resolution is similar to that of the grid G6. The result, shown in figure 5.10 by the red cross, is in line with the simulations of the skewed configuration, with excellent agreement when considering the spanwise-projected spacing $\Delta\check{z}$ in figure 5.10b.

Velocity and Reynolds-stress profiles

Although figure 5.10 may give the impression that there is a large difference between the coarsest- and finest-grid simulations, it needs to be emphasised that the grid-dependence of the absolute drag level and other flow properties is very modest. To substantiate this claim, results for velocity and Reynolds stresses obtained with the coarsest and finest grids are compared in figures 5.11 and 5.12 for the same flow configuration already studied in figure 5.10 ($A_w^+ = 18$, $\theta = 70°$, $\lambda^+ = 918$). Figure 5.11a shows that the streamwise-velocity profiles are virtually indistinguishable. Differences in the phase-integrated

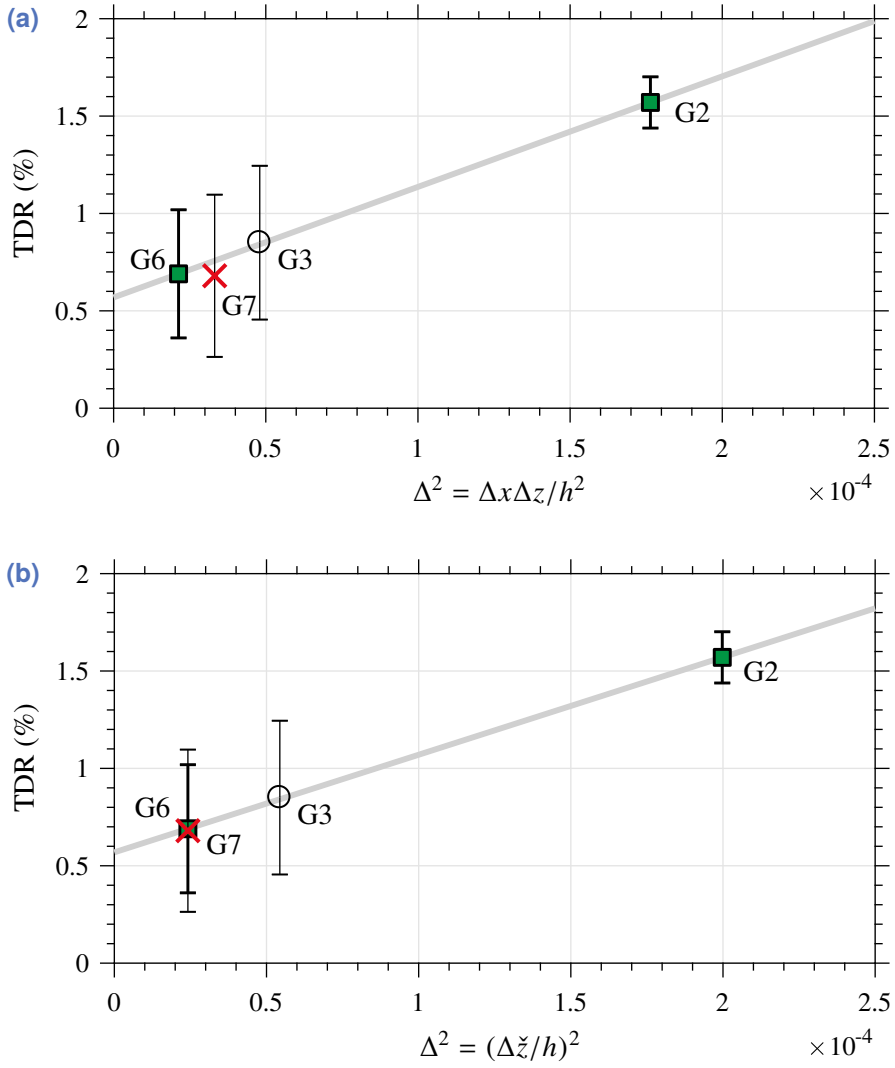


Figure 5.10: Total-drag reduction for $A_w^+ = 18$, $\theta = 70°$, and $\lambda^+ = 918$, for grids G2, G3, G6, and G7. Red x-cross: supplementary run with the wave at an angle and the flow aligned with the grid. The baseline drag level is taken at the same angle, except for G3 where the baseline drag is found by interpolation between $\theta_f = 0°$ and $\theta_f = 90°$ cases. Error bars: 90% confidence interval of the time-averaging error calculated using the method of batch means and batch correlations by Russo and Luchini (2017), and assuming that the baseline and controlled drag levels are independent variables, as derived in section 2.7. **(a)** As a function of the wall-parallel spacing; **(b)** as a function of the spanwise-projected spacing.

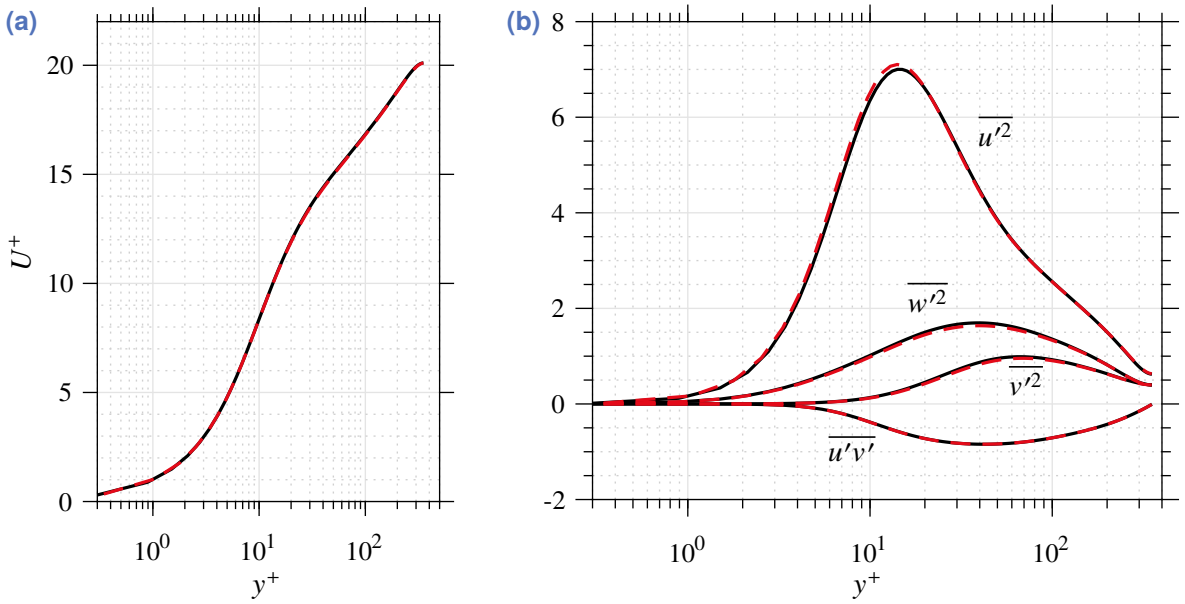


Figure 5.11: Comparison of the streamwise velocity and Reynolds stresses for the flow configuration ($A_w^+ = 18$, $\theta = 70°$, $\lambda^+ = 918$), the black solid lines correspond to the simulation G6W1A2, and the red dashed lines to the coarser mesh G2W1bis. **(a)** Streamwise velocity profile, **(b)** phase-integrated Reynolds stresses.

Reynolds stresses, shown in figure 5.11b, are slightly larger, but also very small. Finally, figure 5.12 demonstrates that the corresponding profiles of phase-averaged transverse (Stokes) strain are virtually indistinguishable.

5.4.2 Friction-drag reduction and pressure-drag increase

In view of the rationale behind the use of a skewed wavy wall for drag reduction—namely, the emulation of in-plane spanwise wall oscillations—a link between the level of skin-friction reduction and a measure of the intensity of the forcing generated by the spanwise pressure gradient arising from the wavy geometry may be expected. In Viotti et al. (2009a), the reduction in skin friction was observed to increase linearly with forcing amplitudes up to $A_{\mathrm{SSL}}^+ \approx 5$, and then to increase at a slower rate. Such an observation is not consistent with the expected symmetry of the problem around $A_{\mathrm{SSL}}^+ = 0$, which would imply a zero value of the first derivative of the drag reduction as a function of the amplitude. For the wavy wall, the dependence of the friction-drag reduction (FDR) on the wave slope, shown in figure 5.13a, is compatible with a symmetry condition, thus indicating that this is a local effect taking place below $2A_w/\lambda \approx 0.04$: for very small actuation amplitudes, the FDR profile is compatible with a quadratic behaviour around zero. Although more points would be required to precisely quantify the order for vanishing amplitudes, some additional support for a quadratic behaviour of the friction re-

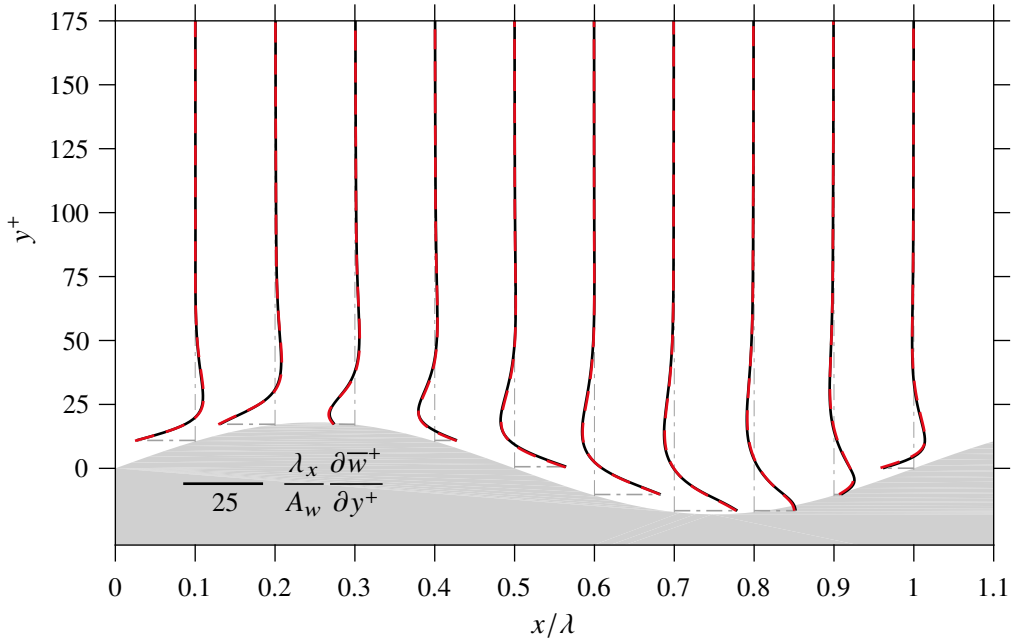


Figure 5.12: Comparison of the transverse-strain profiles for the flow configuration ($A_w^+ = 18$, $\theta = 70°$, $\lambda^+ = 918$). Same legend as in figure 5.11.

duction can be found in the case of wall oscillations at small actuation amplitudes in the perturbation analyses of Moarref and Jovanović (2012) and Zare et al. (2012). For larger wave slopes, the behaviour then becomes close to linear. As will be shown in chapter 6, the amplitude of the spanwise shear strain at $2A_w/\lambda \approx 0.04$ approximately corresponds to that of a SSL with a forcing amplitude of about $A_{SSL}^+ \approx 1.25$, thereby corroborating the observations of Viotti et al. (2009a), since the smallest amplitude they considered was $A_{SSL}^+ = 1$, which occurs at the intersection between the quadratic and linear behaviour for the present key simulations.

The decrease in λ_x from G6W1* ($\lambda^+ = 918$, $\lambda_x^+ \approx 2700$) to G6W2* ($\lambda^+ = 612$, $\lambda_x^+ \approx 1800$) results in a reduced effectiveness of the wavy wall at the same wave slope, i.e. the same equivalent forcing amplitude A_{SSL}^+. This trend contrasts with the drag-reduction trend of the SSL, which features an optimum around $\lambda_x^+ \approx 1250$. Therefore, there exists some unfavourable mechanism limiting the drag reduction achievable by the wavy wall. Such considerations will be discussed further in section 6.2.5.

5.4.3 Influence of the spanwise wavelength

The influence of the spanwise wavelength was studied by fixing the streamwise wavelength to that of the most promising simulation G6W1A2, i.e. $\lambda_x^+ \approx 2700$, and changing the angle of the wave. It was shown in chapter 4 that larger angles could be interesting, so the angle was increased up to $\theta = 80°$

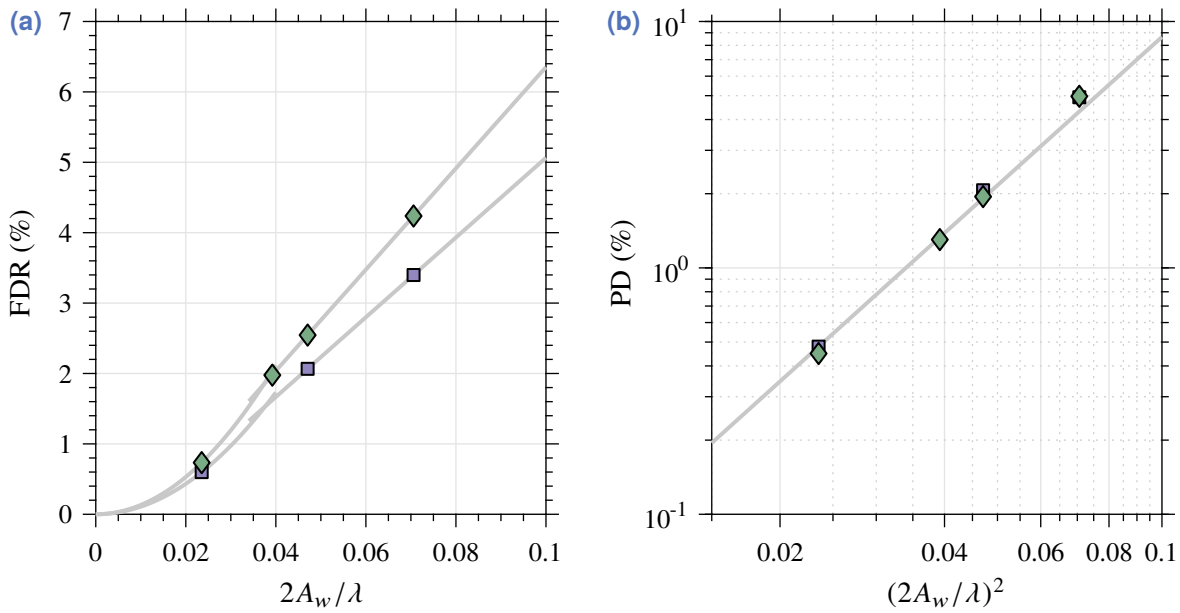


Figure 5.13: Levels of friction-drag reduction (FDR) and pressure-drag increase (PD) relative to the baseline. **(a)** Levels of friction-drag reduction for simulations G6W*A*. ♦ correspond to G6W1A* ($\lambda^+ = 918$), and ■ to G6W2A* ($\lambda^+ = 612$). Continuous lines represent quadratic and linear behaviours. The quadratic curve is interpolated from the value at $2A_w/\lambda = 0.024$ with zero values for the FDR and its derivative at $A_w/\lambda = 0$. The linear curve is interpolated from the two largest wave slopes. **(b)** Levels of pressure drag for simulations G6W*A*. Symbols: same as **(a)**, line: quadratic behaviour.

in the set of simulations G8W1A*. The relevant simulations are gathered in table 5.5, and the relative variations of the contributions to the drag are presented in figure 5.14 to figure 5.16. The error bars shown represent the time-averaging uncertainty of the total-drag reduction calculated using the method described in section 2.7.

Figure 5.14 shows that the friction-reduction curves at $\theta = 70°$ and $\theta = 75°$ almost collapse when scaled with the streamwise wave slope A_w/λ_x, whereas the $\theta = 80°$ case displays a different behaviour. As all simulations feature the same streamwise wavelength λ_x, the present results suggest that the

Table 5.5: Flow configurations extracted from table 5.2, all for $\lambda_x^+ \approx 2700$, and symbols used in figures 5.14 to 5.16.

θ	λ^+	λ_x^+	A_w^+	Simulations	Symbol	Baseline
70°	918	2684	{11,18,22,32}	G6W1A*	♢	G6P1
75°	695	2685	{11,22,32}	G8W1A*	●	G10P1
75°	685	2685	22	G10W1A3	×	G10P1
80°	468	2695	{11,22,32}	G9W1A*	▼	G10P1

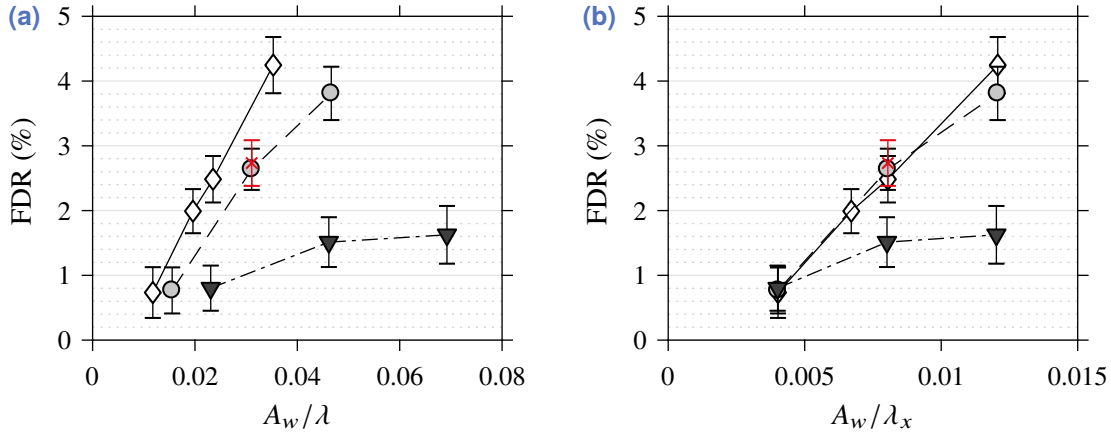


Figure 5.14: Reduction in skin-friction drag relative to the baseline drag level versus wave slope (left) or projected slope (right). Symbols are defined in table 5.5, error bars quantify the 90% confidence interval for the time-averaging error of the total-drag-reduction rate, calculated from the standard deviation of equation (2.56).

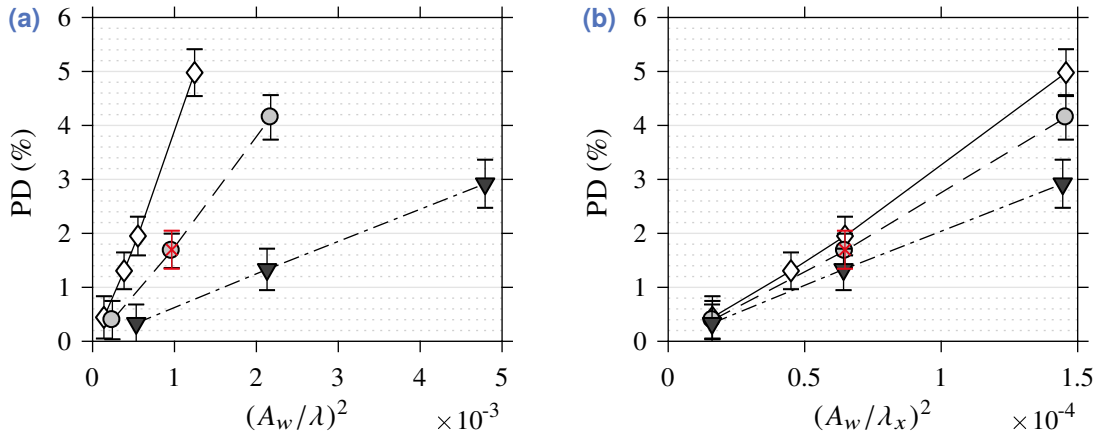


Figure 5.15: Pressure-drag penalty relative to the baseline drag level. Same legend as figure 5.14.

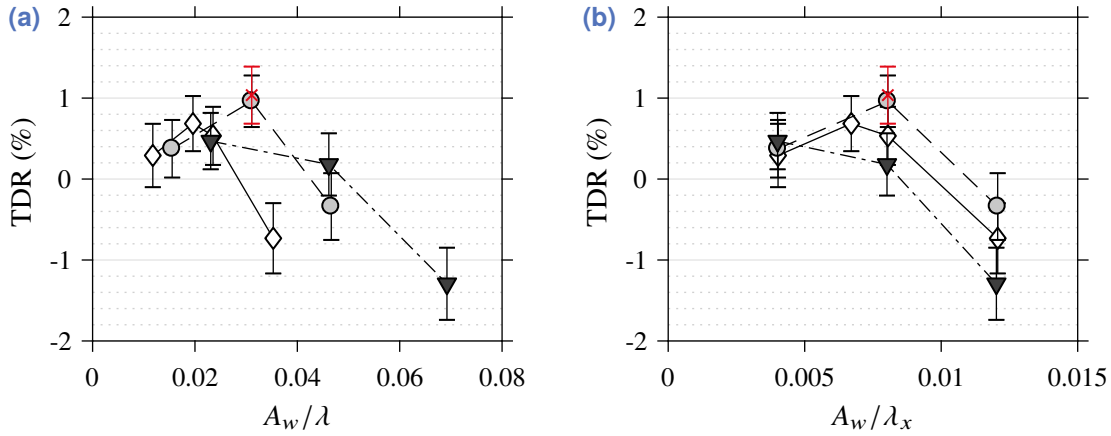


Figure 5.16: Net drag reduction relative to the baseline drag level. Same legend as figure 5.14.

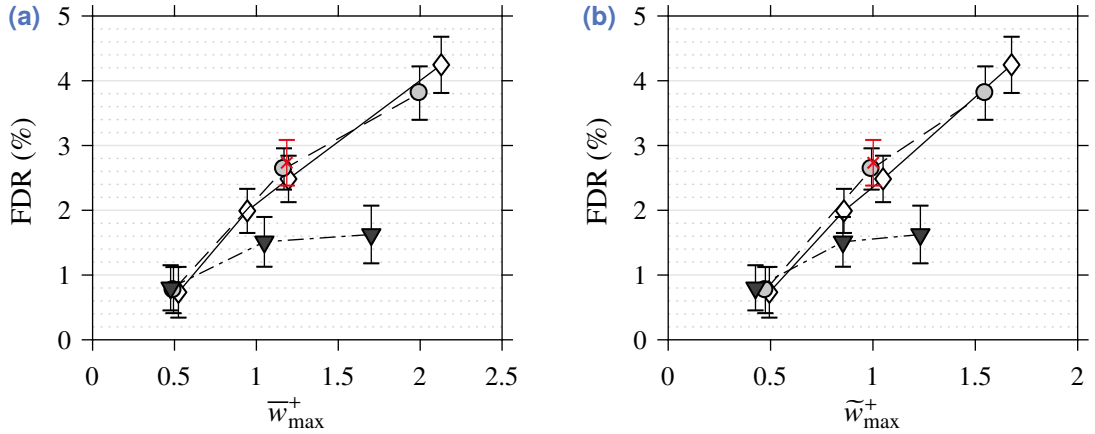


Figure 5.17: Reduction in skin-friction drag relative to the baseline drag level versus maximum spanwise velocity $\overline{w}^+_{max}$ (left) or maximum phase-varying velocity $\widetilde{w}^+_{max}$ (right), expressed in actual wall units. Symbols are defined in table 5.5, error bars quantify the 90% confidence interval for the time-averaging error of the total-drag-reduction rate, calculated from the standard deviation of equation (2.56).

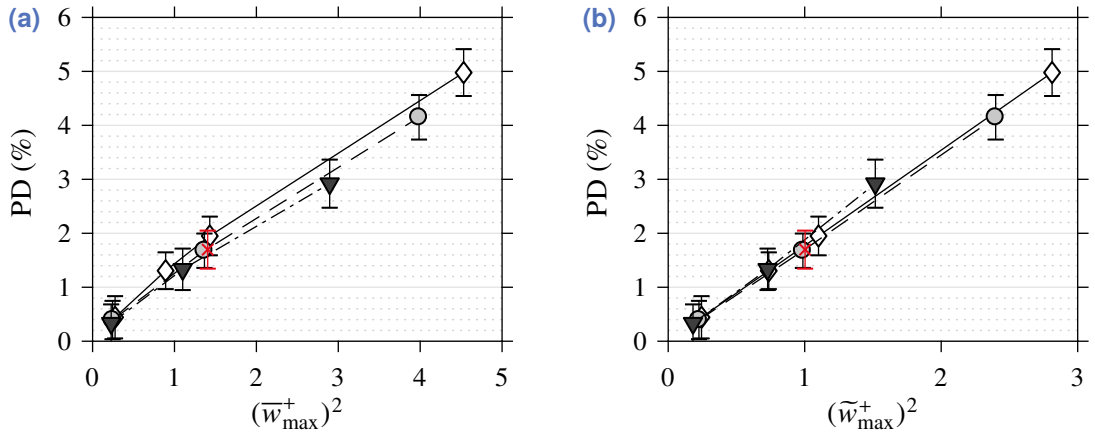


Figure 5.18: Pressure-drag penalty relative to the baseline drag level. Same legend as figure 5.17.

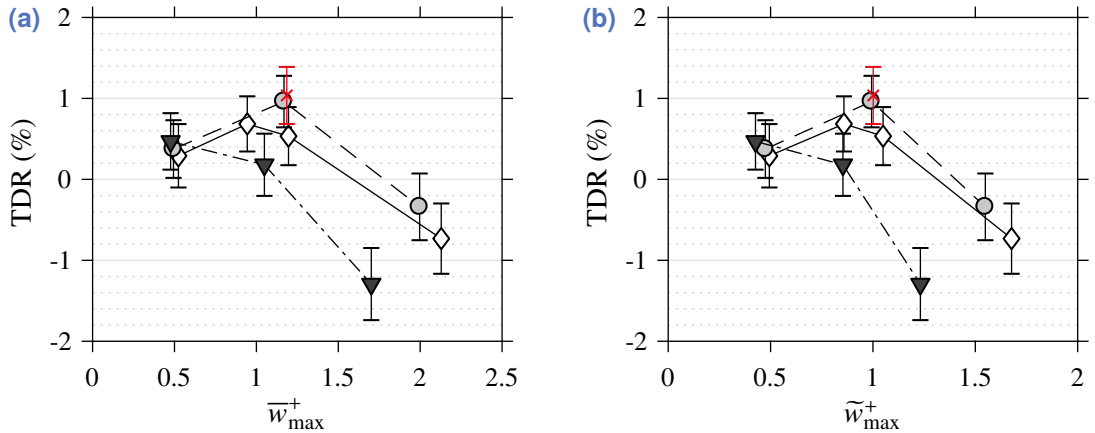


Figure 5.19: Net drag reduction relative to the baseline drag level. Same legend as figure 5.17.

spanwise wavelength has a material effect on the skin-friction-reduction level. For the shortest spanwise wavelength, at $\theta = 80°$, the friction reduction stops increasing above A_w/λ_x greater than about 0.01.

Similar to the behaviour discussed in section 5.4.2, the pressure drag follows a quadratic variation with wave slope, as shown in figure 5.15. Also, for the same streamwise wave slope, larger values of θ exhibit lower pressure drag, which is consistent with the observations of section 4.3.3.

The net change in drag, arising from the opposing actions of the skin-friction reduction and the pressure drag, is quantified in figure 5.16. For small wave slopes, the friction reduction slightly surpasses the pressure-drag increase, leading to small amounts of drag reduction. The most effective configuration at reducing the total drag is that at $\theta = 75°$, yielding a net drag reduction of about 1%. The very slight improvement from the configuration at $\theta = 70°$ arises from a combination of a lower pressure-drag level, a benefit of the greater angle, and a small improvement of the friction reduction. Although the decrease in the pressure-drag penalty with increasing angle is clear, as evidenced in figure 5.15, the improvement of the friction reduction is relatively small and may be the consequence of other sources of error.

The analogy made with the SSL in section 4.3.3 supposes that for similar streamwise wavelength and forcing amplitude, the friction reduction rates would be the same. Because of a lack of data from SSL simulations corresponding to the configurations considered, a different measure of the transverse-shear-strain intensity was considered, namely the maximum of the spanwise velocity. This choice differs from the minimisation of the L^2-norm employed in section 4.3.3, but presents the advantages of being more physically intuitive and not relying on any assumption on the SSL's shear-strain profiles. Thus, figures 5.17 to 5.19 show the same relative variations in drag, but as a function of the maximum spanwise velocity rather than the wave slope.

In each case, both the total spanwise velocity and the phase-varying spanwise velocity are considered in order to gauge the effect of the secondary motion described in section 5.3.2. The results back the assumption, made in chapter 4, that the phase variations are more relevant, since the curves collapse better. Moreover, figure 5.17b provides a plausible explanation to the lower effectiveness of the configurations at $\theta = 80°$ observed in figure 5.14b: when the maximum phase-varying spanwise velocity is used, the friction-reduction rate becomes closer to that of the other two angles considered, which shows that for such a high angle, where the grooves are nearly aligned with the main flow direction, the amplitude of the spanwise motion remains weak and hence has a milder effect on the friction drag. Finally, figure 5.18b shows that the pressure drag correlates with the square of the maximum phase-varying

spanwise velocity, the curves becoming independent of the angle of the grooves.

5.5 Turbulence characteristics

5.5.1 Overview

Further investigations of the flow properties of the configuration G6W1A2 ($A_w^+ = 18$, $\theta = 70°$ and $\lambda^+ = 918$) were carried out in order to understand how the presence of the wavy wall affects the near-wall turbulence in a case where the overall drag was lower than that of the baseline. Results of the same wavelength and angle but larger height will also be included in part of the analysis in order to shed light on the effect of increasing the wave slope, even though the configuration G6W1A4 ($A_w^+ = 32$, $\theta = 70°$ and $\lambda^+ = 918$) presents an increased drag level.

In order to provide a quantitative view of the the changes induced by the wavy wall, various aspects of the flow physics are analysed. A secondary aim of this analysis is to provide information that may be used to compare the friction-reduction mechanisms to other flow-control methods and help understand how the friction drag is reduced.

The first section is concerned with the changes in the statistical distribution of the velocity fluctuations, in order to gain insight on how the turbulent fluctuations are preferentially damped or enhanced, both in an integrated sense and at specific locations along the wave. Second, the impact on the state of anisotropy is shown with the aim of establishing a relationship between the changes in anisotropic state and friction. Third, the phase-integrated contributions to the transport of turbulence energy are compared with emphasis on the production and dissipation terms. Whilst this section focuses on the wavy wall and the effect of the wave slope, further analysis on how the energy budgets compare to those of a Stokes layer will be given in chapter 6.

5.5.2 PDFs of the velocity fluctuations

The consequences of the presence of the wavy boundary on the turbulent fluctuations were studied in more depth for the configuration G6W1A2 ($A_w^+ = 18$, $\theta = 70°$ and $\lambda^+ = 918$) by analysing the joint PDFs of the velocity fluctuations at a constant distance from the wall that corresponds to a wall-normal location of around $y^+ \approx 14$ for the baseline. In the wavy-wall case, it was shown in figure 5.5 that the wall friction varies substantially along the wave, so that the wall-normal location at which the data are taken is not constant in wall units. Figures 5.20 to 5.23 show joint u_i'–u_j' PDFs at the wall-distance

$y^+ \approx 14$ where streamwise turbulent fluctuations are especially high.

One consequence of the wavy wall, shown in figure 5.20, is the contraction of the phase-integrated PDFs with respect to the streamwise-velocity fluctuations. Although the difference between the use of the local friction velocity and the phase-integrated one is barely noticeable, the contours of the PDFs are slightly closer to those of the baseline when local scaling is used.

In contrast, figures 5.21 to 5.23 bring to light larger effects on the PDFs at particular phase locations along the wave. Both local and global scalings are shown for completeness at all phase locations, but they only differ by a constant scaling factor. It can be observed in figure 5.21 that the peaks of the joint u'–v' PDFs are shifted towards negative streamwise-velocity fluctuations relative to the baseline, in particular in the region where the flow is decelerated, i.e. between $x/\lambda = 0.25$ and $x/\lambda = 0.75$. In these regions, the correlation between the streamwise and wall-normal fluctuations is also strengthened.

Figure 5.22(e,f) show that the spanwise fluctuations are attenuated at $x/\lambda = 0.5$ and figure 5.22f indicates that strong negative streamwise fluctuations are less affected, whereas the positive fluctuations display larger tails.

At $x/\lambda = 0$, positive wall-normal fluctuations correlate with negative spanwise fluctuations, as shown in figure 5.23(a,b), whereas further along the slope, at $x/\lambda = 0.5$, the correlation reverses sign and becomes more symmetric. This phenomenon may be interpreted as a direct consequence of the angle of the wave: for $\theta = 70°$, the negative spanwise-velocity fluctuations coincide in sign with the local spanwise motion (cf. figure 5.3c), and this motion going against the wall induces a vertical motion by following the surface tangent, thereby explaining the correlation between negative spanwise fluctuations and positive vertical fluctuations. However, positive spanwise fluctuations correspond to the fluid moving farther from the wall towards the trough and does not enhance such a correlation.

At $x/\lambda = 0.5$, the spanwise motion is positive and is accentuated by the streaming motion. At this location, positive spanwise fluctuations move the fluid against the wall inducing an upward motion and conversely negative spanwise fluctuations induce a downward motion, consistently with the correlation observed in figure 5.23(e,f).

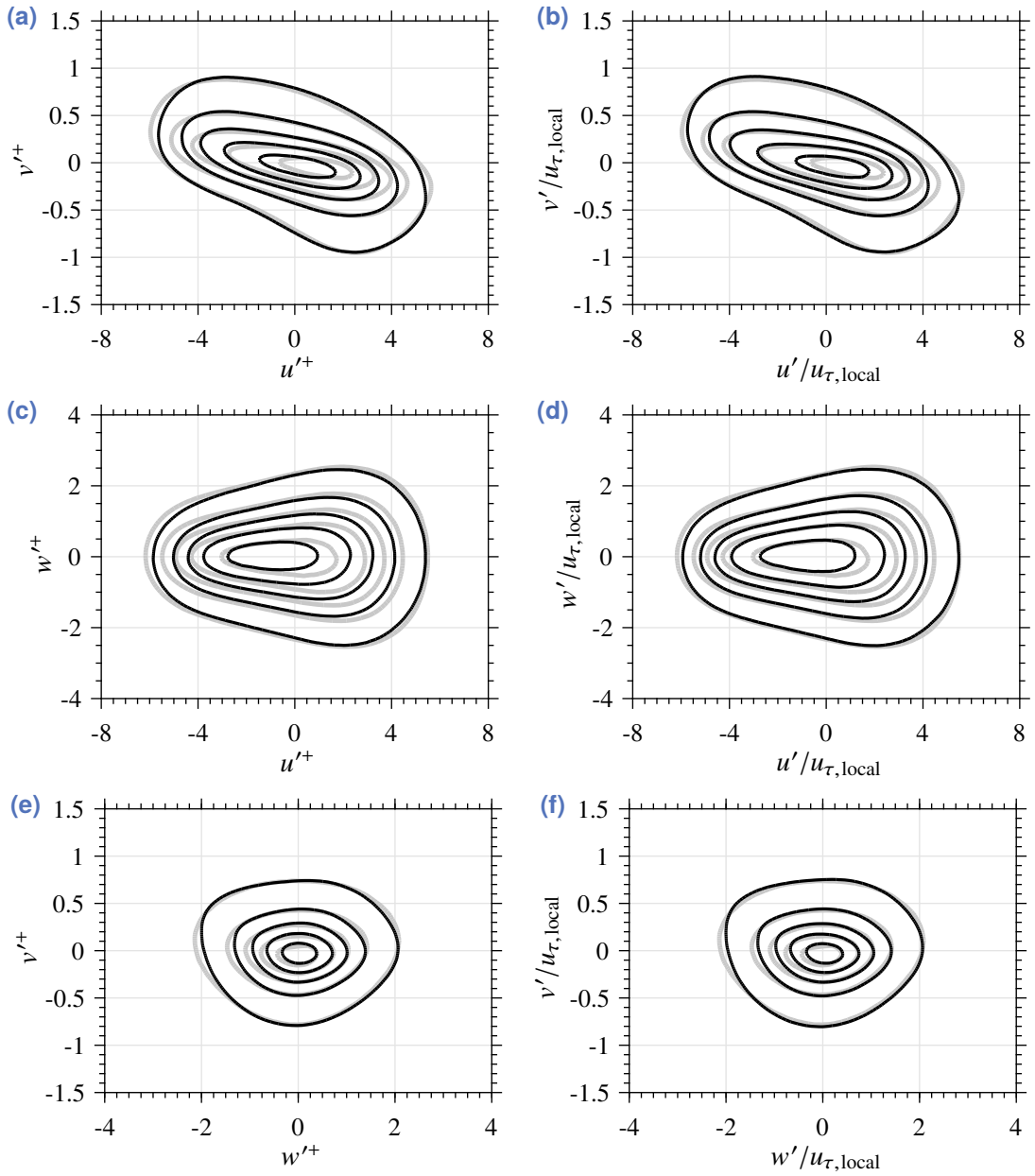


Figure 5.20: Joint PDFs at $y^+ \approx 14$ of the velocity fluctuations for G6W1A2 (black contours) and the baseline (grey contours). Left: fluctuations normalised by the mean friction velocity, right: fluctuations normalised by the local friction velocity. **(a,b)** joint u'–v' PDFs, **(c,d)** joint u'–w' PDFs, **(e,f)** joint w'–v' PDFs. Contours show the isolines of 10%, 30%, 50%, 70% and 90% of the maximum level.

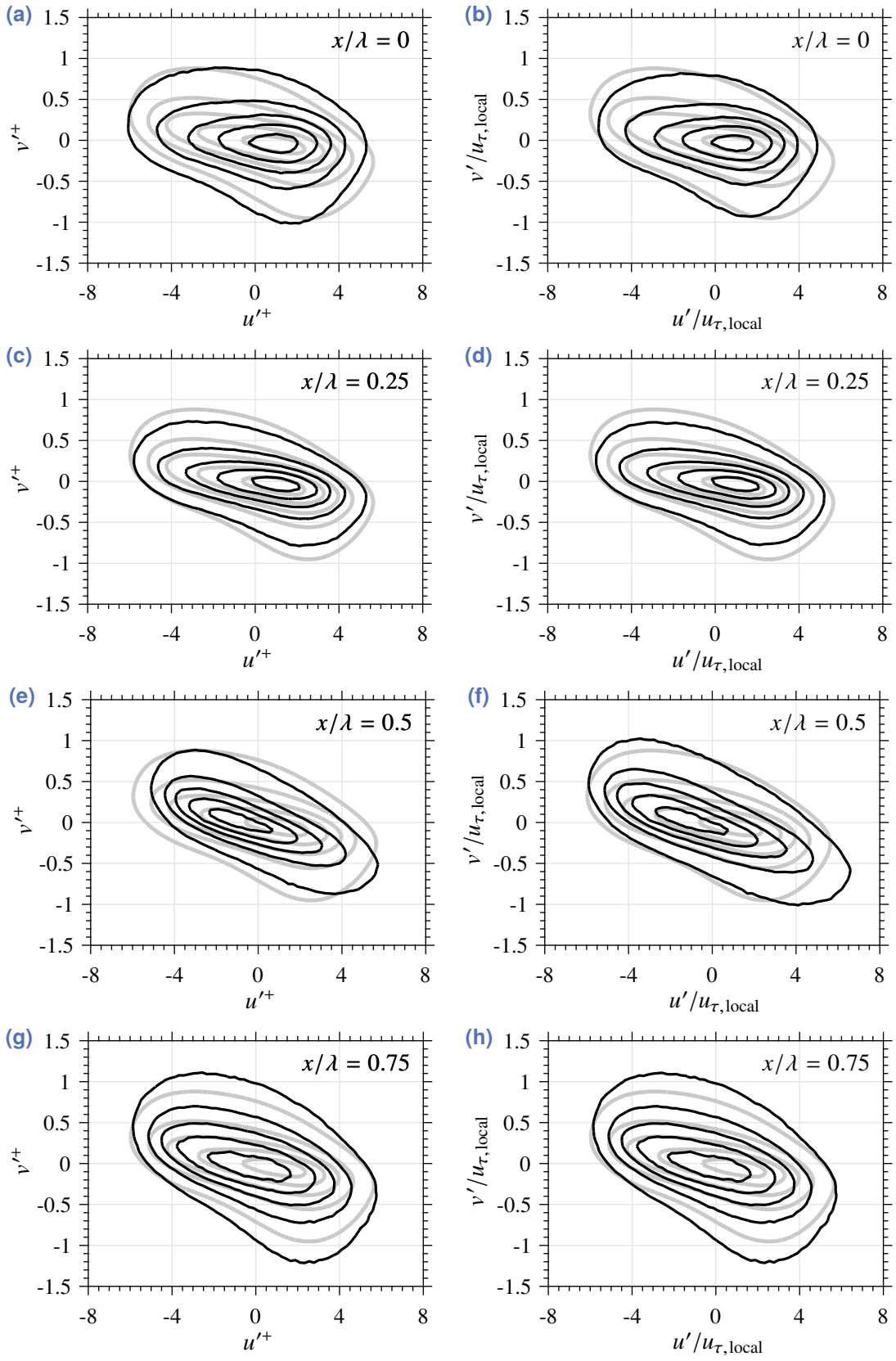


Figure 5.21: Joint u'–v' PDFs at fixed phase locations. Same legend as figure 5.20.

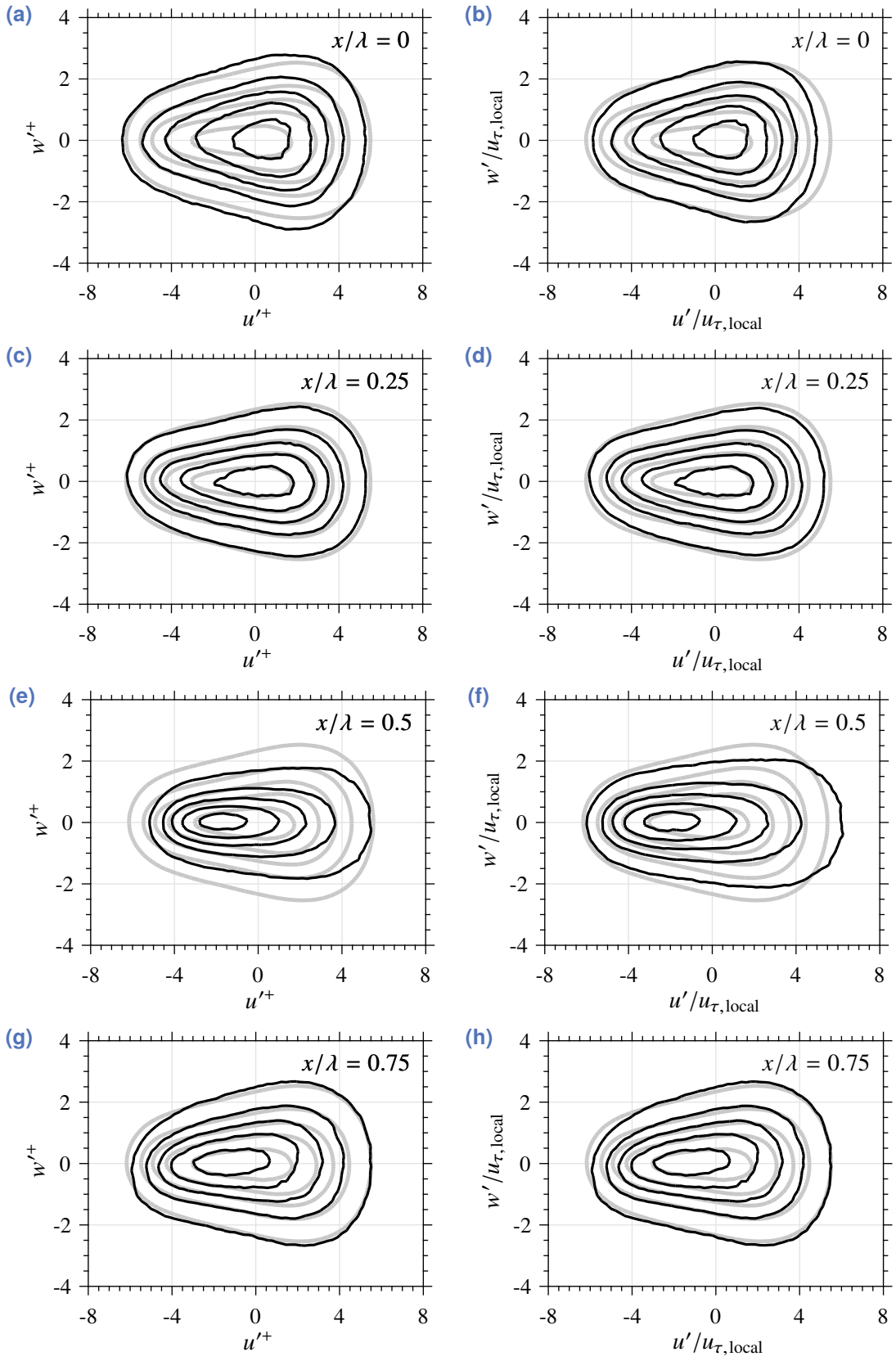


Figure 5.22: Joint v'–w' PDFs at fixed phase locations. Same legend as figure 5.20.

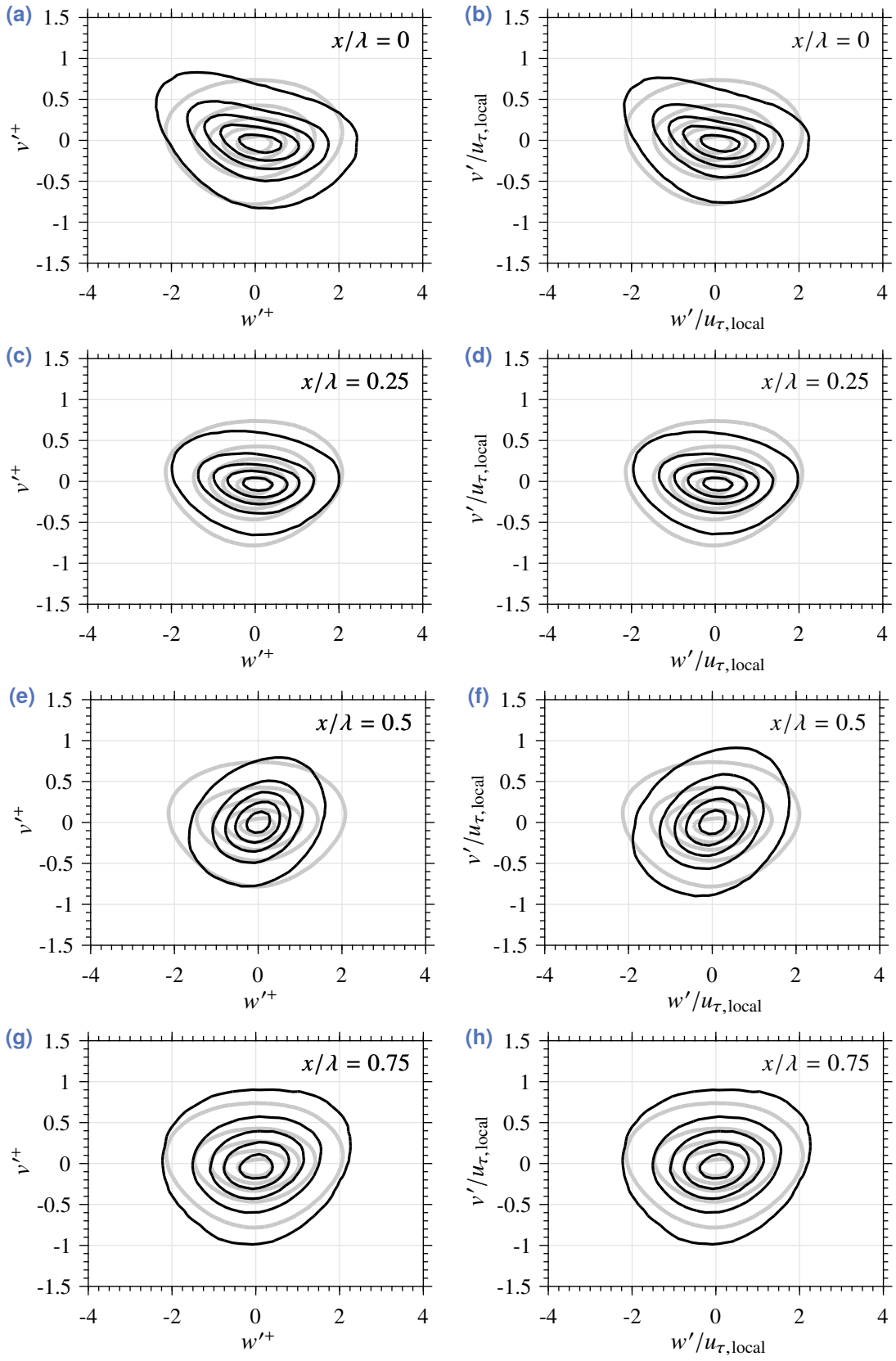


Figure 5.23: Joint w'–v' PDFs at fixed phase locations. Same legend as figure 5.20.

5.5.3 Anisotropy of the turbulence field

The anisotropic state of the turbulence field is studied by using the traceless anisotropy tensor (Lumley and Newman, 1977)

$$b_{ij} = \frac{\overline{u_i' u_j'}}{\overline{u_k' u_k'}} - \frac{1}{3}\delta_{ij} \tag{5.1}$$

to calculate the second and third invariants defined, respectively, as:

$$\mathrm{II} = -\frac{b_{ij} b_{ij}}{2}, \tag{5.2}$$

$$\mathrm{III} = \frac{b_{ij} b_{jk} b_{ki}}{3}. \tag{5.3}$$

The state of the anisotropy structure is shown in figure 5.24 by plotting the phase-integrated anisotropy invariant map—referred to as 'Lumley's triangle'—along a vertical line going from the wall (upper side of the triangle) to the centre of the channel (closest to the isotropic state at $(0,0)$). The plane-channel results were found to compare favourably with the results found in the literature (Mansour et al., 1988; Pope, 2000). Lumley and Newman (1977) showed that physical states are bounded by one two-component and two 'axisymmetric' states, the three of which form a triangular domain. Any realisable states must lie within this triangular region. The latter bounds are plotted in grey solid lines on figure 5.24 and figure 5.25.

The turbulence in the plane channel evolves from being two-component ('pancake'-like) at the wall towards the one-component state with one dominant eigenvalue close to the buffer layer where the elongated streaks are most strongly formed, before reaching a 'cigar'-like axisymmetric state on the way back to isotropy. This results in a peak in the Lumley map around $y^+ \approx 9$. For a wall oscillating at a close-to-optimal period of $T^+ = 100$, Touber and Leschziner (2012) showed that the effect of the forcing consisted of a weakening of the peak, in a similar way to that observed for the wavy wall in figure 5.24. This behaviour is at odds to the observations of Jovanović et al. (2006) and Frohnapfel et al. (2007) for polymers and riblets, suggesting that the friction-reducing mechanism differs from that pertaining to wall oscillations, or to the present case. Moreover, as the slope of the wavy wall is increased, this effect is amplified and the weakening of the one-component-state peak is enhanced.

Yet, the relation between the local change in friction and the behaviour of the anisotropy state relative to the one-component state is contrary to that expected from the above analysis. Figure 5.25 shows that the state of anisotropy varies significantly along the wave, with a strong weakening of the peak at

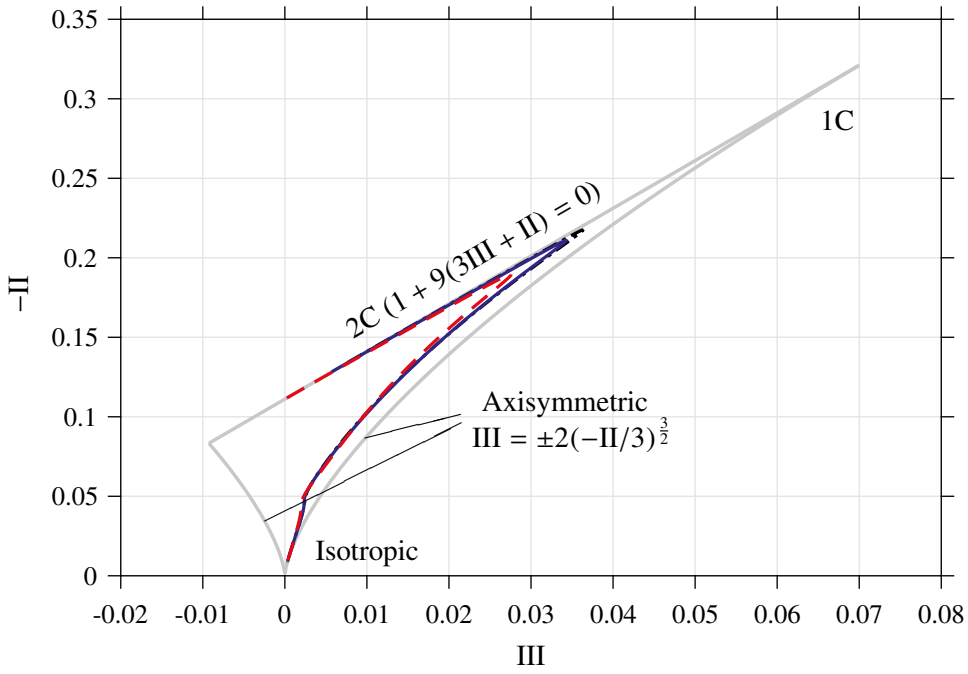


Figure 5.24: Lumley triangle for the baseline G6P1 (black dash-dotted lines), G6W1A2 (blue solid line) and G6W1A4 (red dashed line).

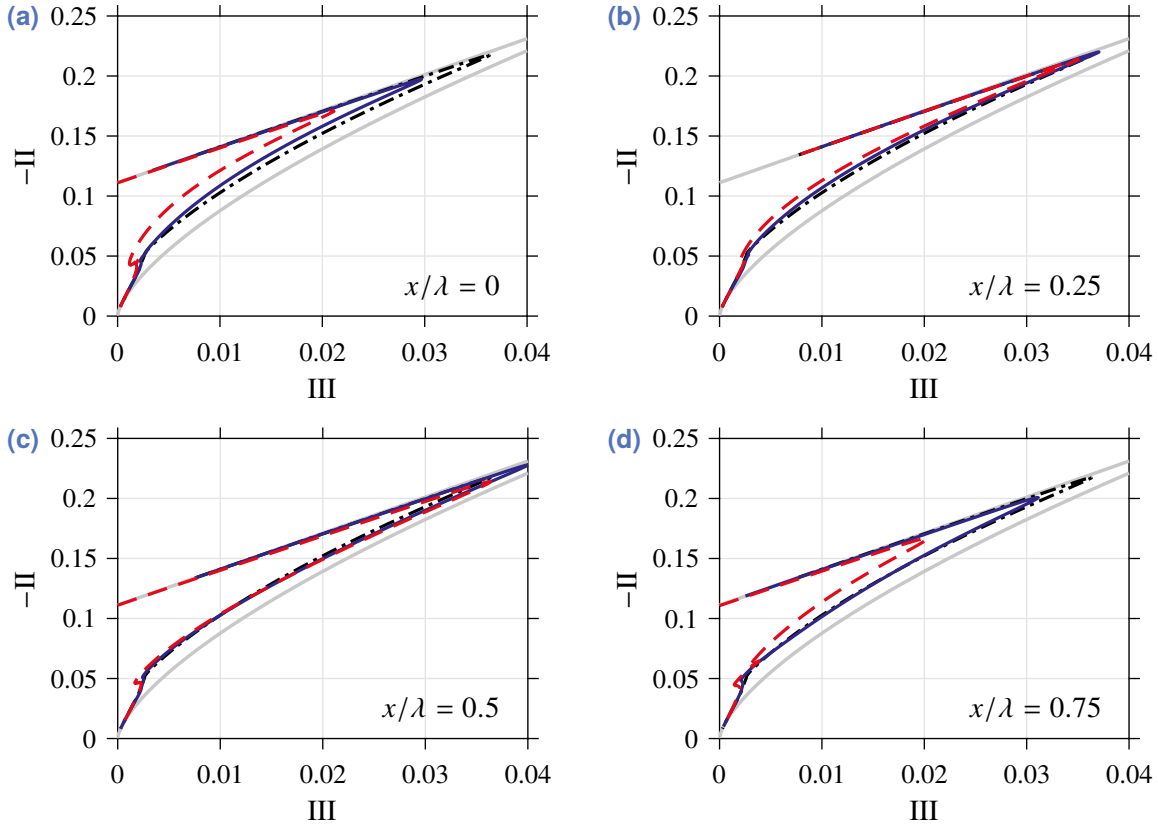


Figure 5.25: Lumley triangle at various phase locations. Same legend as figure 5.24.

the trough ($x/\lambda = 0.75$) and on the up-slope ($x/\lambda = 0$), i.e. where the friction is increased, whereas it undergoes a weak sharpening of the peak above the beginning of the down-slope up to about $x/\lambda = 0.5$, where the friction reduction is close its maximum.

5.5.4 Energy budgets

For an incompressible flow, the contributions to the transport of the turbulence energy are as follows:

$$\text{Production:} \quad \mathcal{P}_k = -\overline{u_i' u_j'} \frac{\partial \overline{u}_i}{x_j}, \tag{5.4a}$$

$$\text{Dissipation:} \quad \epsilon_k = \nu \overline{\frac{\partial u_i'}{\partial x_j} \frac{\partial u_i'}{\partial x_j}}, \tag{5.4b}$$

$$\text{Pressure diffusion:} \quad \Pi_k = -\frac{\partial \overline{p' u_i'}}{\partial x_i}, \tag{5.4c}$$

$$\text{Turbulent diffusion:} \quad T_k = -\frac{1}{2} \frac{\partial \overline{u_i' u_j' u_j'}}{\partial x_j}, \tag{5.4d}$$

$$\text{Viscous diffusion:} \quad D_k = \frac{\nu}{2} \frac{\partial^2 \overline{u_i' u_i'}}{\partial x_j \partial x_j}. \tag{5.4e}$$

With the above notation, the balance for the turbulence energy budgets becomes

$$\frac{\bar{D}k}{Dt} = \mathcal{P}_k - \epsilon_k + \Pi_k + T_k + D_k. \tag{5.5}$$

The phase-integrated budgets corresponding to the terms present in equation (5.5) are shown in figure 5.26 for simulations G6W1A2, G6W1A4 and the baseline G6P1. All the budget terms are calculated directly from the DNS data as in section 3.3.1, so that the balance in equation (5.5) is only approximately satisfied. A reduction in turbulence production and dissipation is observed above the wavy wall—relative to the baseline—inside the viscous sublayer and the buffer layer, but from the end of the buffer layer up to the log-law region, the turbulence production and dissipation then exceed the baseline value.

As would be expected from a universal behaviour of the flow properties expressed in wall units, the dissipation in the wavy cases matches the baseline value at the wall when scaled in wall units, as shown in figure 5.27. However, when scaled in outer units, the absolute value of the dissipation and turbulent diffusion is reduced at the wall. Figure 5.27 shows that the reduction in production is confined to the

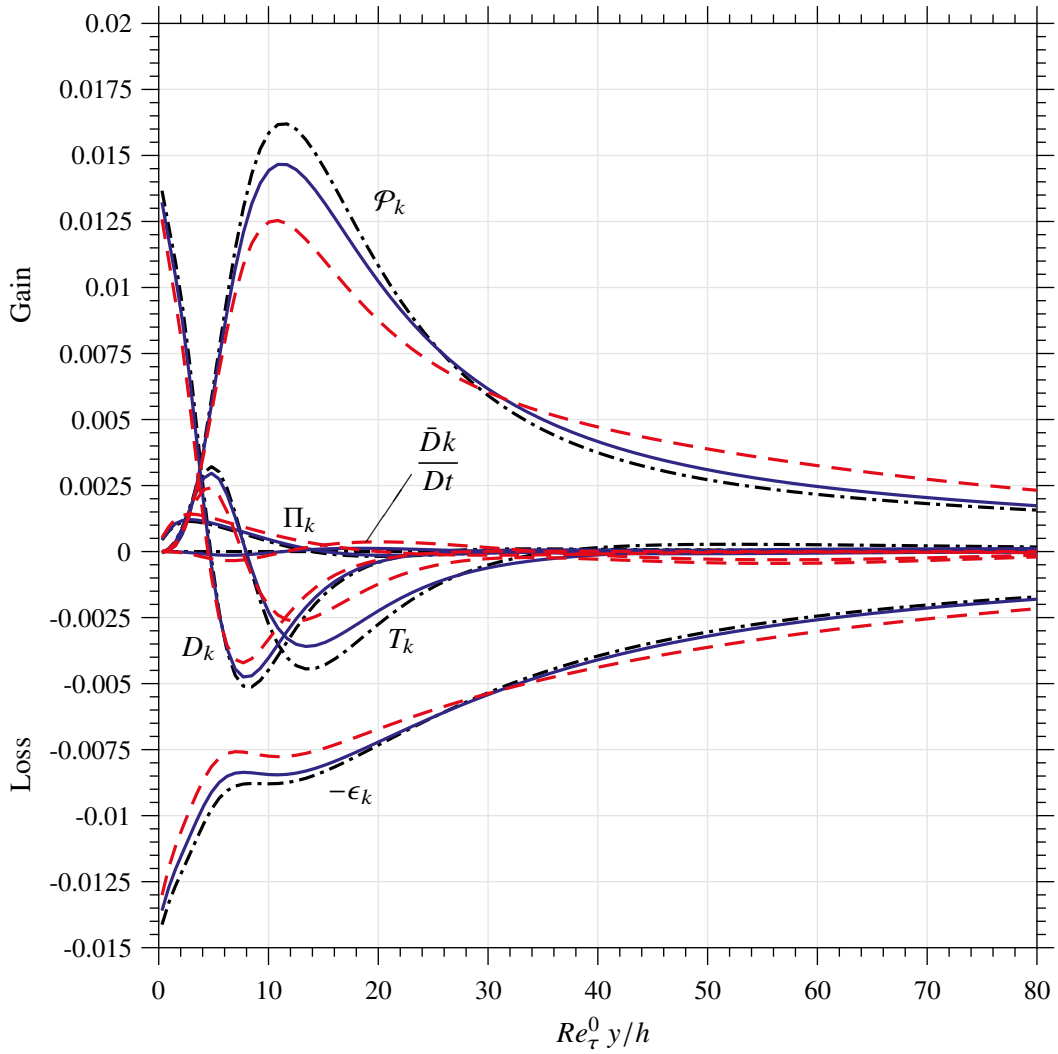


Figure 5.26: Phase-integrated contributions to the turbulence-energy budgets in outer units as a function of the wall-normal coordinate multiplied by the *baseline* friction Reynolds number Re_τ^0. The terms present in equation (5.4) are shown for the baseline G6P1 (black dash-dotted lines), G6W1A2 (blue solid line) and G6W1A4 (red dashed line).

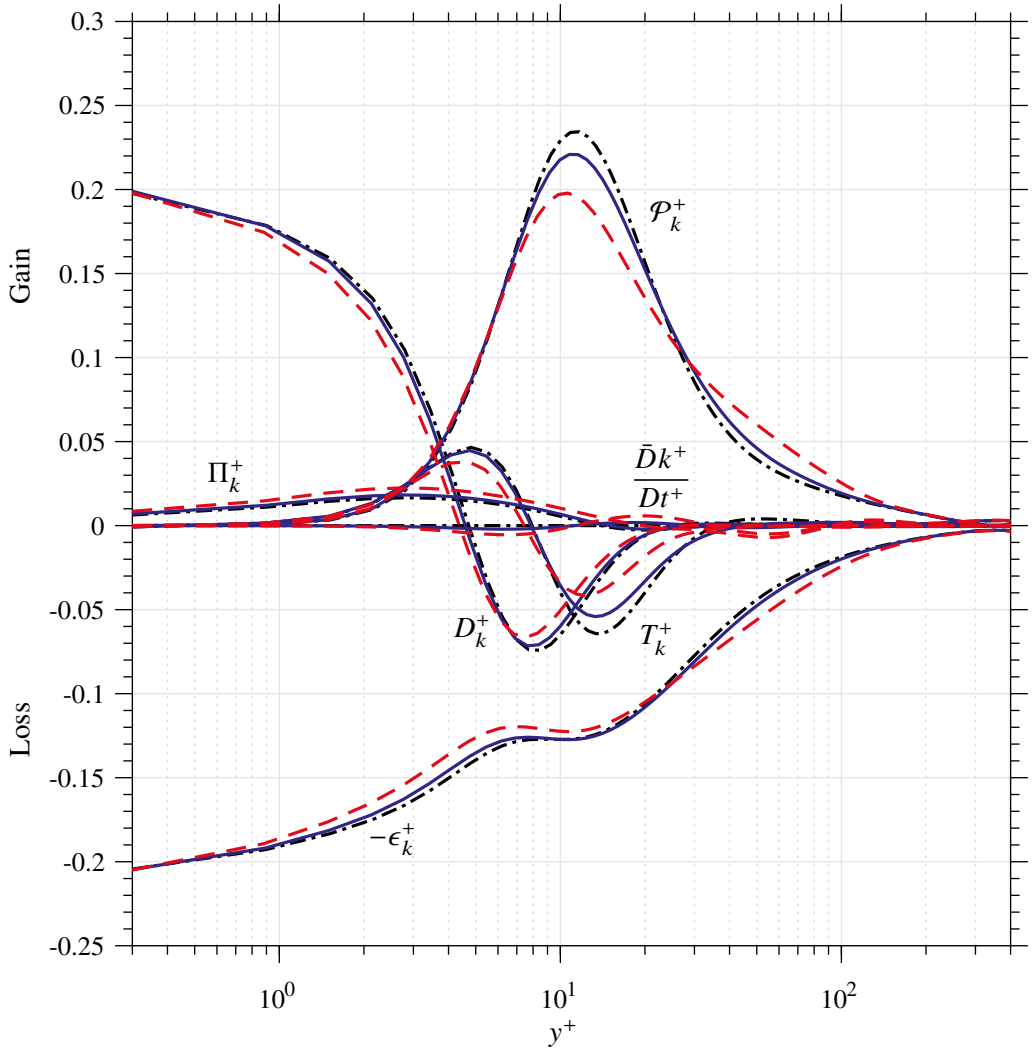


Figure 5.27: Phase-integrated contributions to the turbulence-energy budgets in wall units, calculated with the actual friction velocity. The terms present in equation (5.4) are shown for the baseline G6P1 (black dash-dotted lines), G6W1A2 (blue solid line) and G6W1A4 (red dashed line).

buffer layer, and that the dissipation, expressed in wall units, is significantly reduced in the viscous sublayer.

These effects go hand-in-hand with a reduction in the absolute value of the viscous and turbulent diffusion terms, but in contrast, the pressure diffusion term is strengthened. Moreover, unlike for the plane channel, the wavy wall induces some transport of the turbulence energy $\bar{D}k/Dt$, which is linked to the negative pressure diffusion between $y^+ = 40$ and $y^+ = 100$.

5.6 Conclusions

A set of fully developed wavy-channel-flow simulations was performed for a range of parameters and grid resolutions. The results were shown to be insensitive to the type of confinement imposed on the channel by flattening one of the two walls and comparing the resulting drag. It was shown that the oblique wavy wall locally deviates the flow in the vicinity of the wall, thereby inducing a streaming motion, the amplitude of which increases quadratically with the slope of the wave.

A modest net drag reduction was predicted for a few shallow configurations. A thorough grid-refinement study indicated an asymptotic level of 0.6% drag reduction for the configuration $A_w^+ = 18$, $\theta = 70°$ and $\lambda^+ = 918$, and introduced as a measure of the refinement level the projected spanwise spacing $\Delta\check{z}$, for cases where the main flow direction is at an angle to the mesh. The use of this measure enabled to closely match the results obtained for two independent sets of simulations with varying flow-to-mesh angles but similar resolution, provided that the baseline-drag level was taken from a simulation consisting of exactly the same numerical domain as the wavy simulation.

The drag reduction arises as a delicate balance between the friction reduction and the pressure-drag increase. For a fixed wavelength and angle, the drag reduction is made possible by the fact that the friction reduction increases more rapidly than the pressure drag as the wave height is increased. However, for lager wave slopes, the friction reduction becomes linear whereas the pressure-drag increase remains quadratic, which explains the existence of an optimal wave height minimising the overall drag.

For a constant streamwise wavelength $\lambda_x^+ \approx 2700$ but varying angle of the wave, it was shown that, as the flow becomes more aligned with the grooves, the resulting pressure drag decreases. Moreover, there is a strong drop in friction-reduction effectiveness between $\theta = 75°$ and $\theta = 80°$, which was partly explained as a consequence of a reduced capacity to generate a spanwise motion.

A significant weakening of the streamwise fluctuations was observed in the buffer layer, which results

in a contraction of the joint u'–v' PDFs, and in a turbulent state that is, on average, more isotropic than the plane channel around the wall-normal location $y^+ \approx 9$. Accordingly, the turbulence production and dissipation are on average depressed in the buffer layer, an effect that is opposed by the increased level above $y^+ \approx 30$.

Chapter 6

Wavy walls and Stokes layers

Contents

6.1 General observations 162
6.1.1 Transverse shear strain 162
6.1.2 Near-wall streaks 164
6.1.3 Streamwise velocity and Reynolds stresses 165
6.2 Focus on simulation G6W1A2 167
6.2.1 Transverse shear strain 167
6.2.2 Friction reduction 167
6.2.3 Streamwise velocity and Reynolds stress 168
6.2.4 Turbulence-energy budgets 169
6.2.5 Detrimental effects of the wavy wall 172
6.2.6 Effect of the streamwise forcing 175
6.3 Reynolds-number effect 176
6.4 Conclusions 180

The present approach of using a skewed wavy wall is based on the assumption that similar longitudinal patterns of the transverse shear strain, whether created by the SSL or the wavy wall, will lead to the same effects on turbulence and hence lead to some turbulent-drag reduction. In the case of a temporal Stokes layer, Touber and Leschziner (2012) showed that the wall oscillations led to a bimodal partial decay, reformation and reorientation of the streaks, a behaviour dictated by the unsteady Stokes strain in the buffer layer. If this mechanism is indeed intimately linked to the friction-drag reduction, the relevant forcing quantity is the resulting shear strain, rather than the forcing velocity itself. It is this key element that may allow for a passive surface, with no slip at the solid wall, to emulate the actuation by in-plane wall oscillations, through the action of a transverse pressure gradient that generates an

equivalent shear-strain field. *But to what extent is this emulation truthful?* The purpose of this chapter is to elucidate the similarities and differences between the SSL and the wavy wall, and to attempt to provide an answer to whether the friction-reducing mechanisms are similar.

6.1 General observations

6.1.1 Transverse shear strain

In contrast to the Stokes layer, the wavy wall also induces a wall-normal forcing that contributes to the shear strain via $\partial\overline{v}/\partial z$, but this additional effect was observed to be small compared to $\partial\overline{w}/\partial y$, especially in the near-wall region where the shear is maximum, as shown in figure 6.1. It follows that there is no significant effect of the wall-normal velocity on the spanwise forcing, justifying a direct comparison of $\partial\overline{w}/\partial y$ between wavy-wall and Stokes-layer configurations.

A slight difference between the SSL simulations presented in this chapter and those of Viotti et al. (2009a), has been introduced deliberately, in order to maximise the correspondence between the SSL and the wavy–wavy channel configuration. This difference is that the wall forcing on the upper wall is shifted by half a period relative to the lower wall. However, this change should not result in significant differences, since the thickness of the Stokes layer is much smaller than the channel half-height.

The reference SSL considered here is for a forcing amplitude of $A^+_{\mathrm{SSL}} = 2$ (based on the unactuated friction velocity) and a wavelength close to the optimum at this forcing amplitude, $\lambda^+_x \approx 1250$, subject to

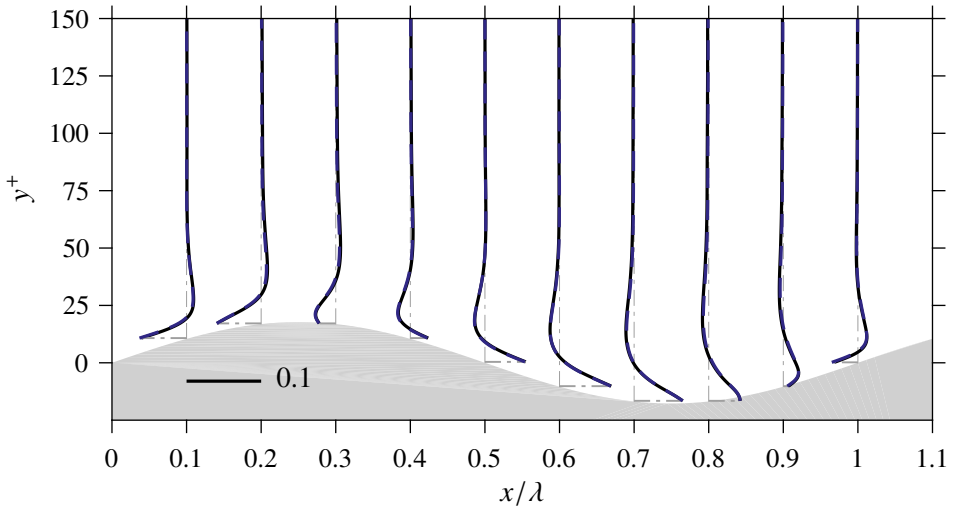


Figure 6.1: Total shear strain $(\partial\overline{w}^+/\partial y^+ + \partial\overline{v}^+/\partial z^+)/2$ (black line) and contribution of $(\partial\overline{w}^+/\partial y^+)/2$ (blue dashed line) for G6W1A2.

the assumption that the Reynolds-number change from $Re_\tau = 200$ in Viotti et al. (2009a), to the present value of $Re_\tau \approx 360$ does not have a significant impact on the optimal wavelength. The simulation was run on a domain $L_x^+ \approx 2500$, $L_z^+ \approx 1100$, with a grid resolution $\Delta x^+ = 9.8$, $\Delta z^+ = 5.8$, and $0.7 < \Delta y^+ < 7.3$. Such a resolution may not be sufficient for an accurate comparison of the drag levels, but is acceptable for the comparison of the shear-strain profiles, as shown in section 5.4.1.

The transverse shear-strain profiles, extracted from some of the simulations given in table 5.2, are compared to those of the reference SSL flow in figure 6.2. The strain profiles demonstrate that the wavy wall emulates reasonably well the shear layer of the SSL. This observation leads to the expectation that the reduction in turbulent skin friction achieved by the wavy wall would be similar, and that it arises from the same physical mechanism as in the SSL. In addition, the amplitude of the phase-wise variations in the shear-strain—and hence the corresponding SSL forcing amplitude A_{SSL}^+—appears to be mostly dictated by the streamwise wave slope A_w/λ_x, as suggested by rescaling the amplitude of the transverse shear strain by this ratio, so as to compensate for the different forcing amplitude. This implies that, for A_w and λ kept constant (same wave shape), increasing θ results in a decrease in the forcing amplitude, at least for angles in the range $\theta \in [50°, 70°]$.

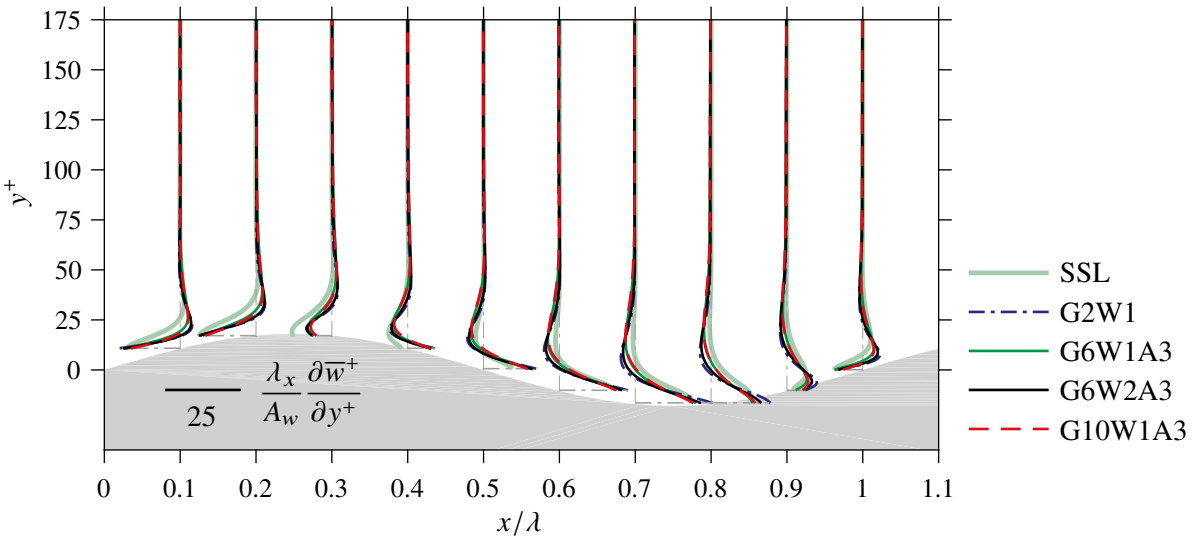


Figure 6.2: Comparison of $\partial\overline{w}^+/\partial y^+$ scaled by the streamwise-projected wave slope A_w/λ_x for various flow configurations. The SSL flow is for a wavelength of $\lambda_x^+ \approx 1250$ and forcing amplitude $A_{\mathrm{SSL}}^+ = 2$ based on the unactuated friction velocity. The value of $\partial\overline{w}^+/\partial y^+$ is based on the actual friction velocity, and the scaling factor A_w/λ_x for the SSL case is based on the parameters of G2W1. In all cases, the profiles were shifted in the wall-normal direction in order to match the wave height of G2W1.

6.1.2 Near-wall streaks

As previously mentioned, it is not the velocity but the shear strain that is important with respect to the emulation of the Stokes layer, and which dictates the orientation of the near-wall streaks. In Touber and Leschziner (2012), for a temporal Stokes layer, this orientation was observed to vary in time, with strong reduction in turbulence during the reorientation phase. For the wavy wall, the phase-modulation of the shear strain occurs in space, and also results in a reorientation following the shear-strain field, as well as in a weakening of the streaks, as shown in figure 6.3 at a constant distance from the wall around $y^+ \approx 10$. However, the effect is understandably far less pronounced than observed in Touber

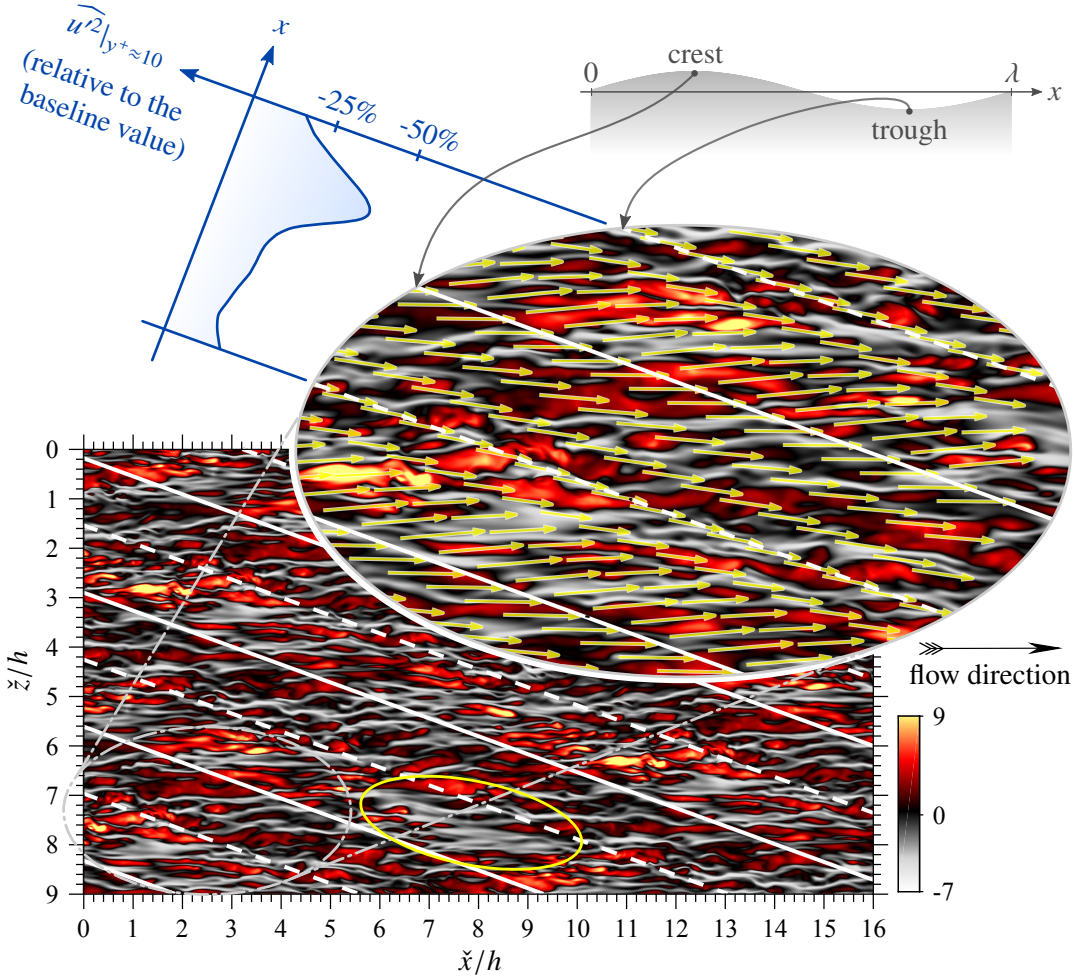


Figure 6.3: Turbulent fluctuations of the streamwise velocity u'^+ for G6W1A4 ($A_w^+ = 32$, $\theta = 70°$, $\lambda^+ = 918$), normalised by the local mean friction velocity at the particular phase location $\sqrt{\nu(\partial\overline{u}/\partial y)|_w}$ in a wavy horizontal slice located at constant y/h, around $y^+ \approx 10$. Solid thick white lines: location of the crests, dashed white lines: location of the troughs, yellow arrows: mean shear-strain field, yellow circle: region of strong streak weakening. The periodic boundary conditions have been exploited to increase the visualisation area.

and Leschziner (2012) for the forcing amplitude is much smaller in the present case.

6.1.3 Streamwise velocity and Reynolds stresses

As is observed with Stokes layers and, more generally, with most control strategies yielding turbulent-drag reduction, an upward shift in the log-law appears relative to the uncontrolled flow when actual scaling is used (i.e. with the modified friction velocity). This shift is shown in figure 6.4a for some key simulations. The corresponding flow configurations are characterised by two height-to-wavelength ratios and two wavelengths. Although there is a noticeable difference between the two profiles for the two wavelengths, it is observed that similar wave slopes yield approximately similar shifts, the configurations at $\lambda^+ = 918$ featuring a slightly greater shift implying a higher level of skin-friction reduction (cf. section 5.4.2). As the wave slope is linked to the forcing amplitude, the higher this ratio is, the higher the friction-drag reduction is. This close resemblance of the log shift at a given wave slope, but different wavelength, indicates a limited sensitivity of the friction-drag reduction for the range of wavelengths tested, especially at such a small forcing amplitude.

As far as the Reynolds stresses are concerned, shown in figure 6.4b, there is a substantial decline in the peak of the streamwise normal stresses—evidence of the weakening of the streaks. Although the wavy wall generates non-zero $\overline{u'w'}$- and $\overline{v'w'}$-shear-stresses, they are not shown in figure 6.4b since they are almost negligible relative to the other stresses. The behaviour of the Reynolds stresses is also similar for a given height-to-wavelength ratio, apart from a detrimental increase in the streamwise normal stresses for the shorter wavelength $\lambda^+ = 612$, starting within the buffer layer around $y^+ \approx 20$ and persisting up to $y^+ \approx 80$. However, unlike the wall-actuated Stokes layers studied in Agostini et al. (2014), Touber and Leschziner (2012) and Viotti et al. (2009a), which all entail a larger forcing amplitude, the decline in the streamwise stress only persists in the present configuration up to $y^+ \approx 35$, beyond which it exceeds the baseline value. Similarly, the shear stress is depressed up to about the same wall-normal location, beyond which it also exceeds the baseline level.

A more detailed account on how the streamwise-velocity and Reynolds-stress profiles compare to the actuated Stokes layer will be given in section 6.2.3 for the configuration G6W1A2.

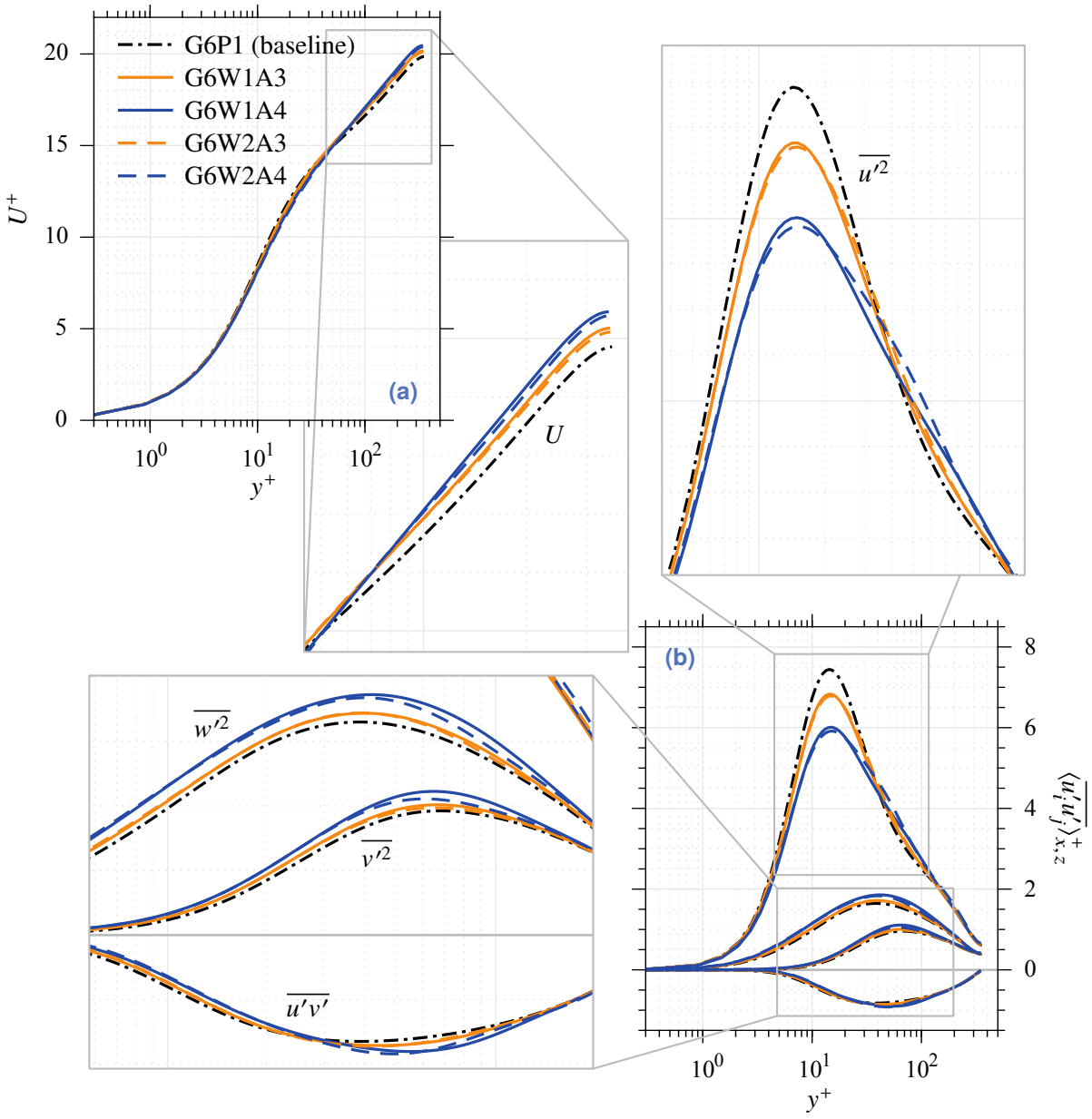


Figure 6.4: Comparison of **(a)** the mean streamwise velocity $U^+ = \langle \overline{u} \rangle_{x,z}/u_\tau$ and **(b)** Reynolds stresses $\langle \overline{u_i'u_j'} \rangle_{x,z}/u_\tau^2$ for wavy walls with wave slopes of $2A_w/\lambda \in \{0.05, 0.07\}$ (corresponding to labels *A3 and *A4) and wavelengths of $\lambda^+ \in \{612, 918\}$ (corresponding to labels *W2* and *W1*), and the baseline plane channel (G6P1) (scaled using the actual friction velocity).

6.2 Focus on simulation G6W1A2

The similarity between the SSL and the wavy wall, in terms of the friction-reducing transverse strain, is given further weight by a supplementary simulation of the wall-actuated case at the conditions $Re_\tau \approx 360$, $A^+_{\mathrm{SSL}} \approx 1.25$, and $\lambda^+_x \approx 2700$, approximately corresponding to the flow configuration that yields one of the highest drag-reduction levels, namely G6W1A2 ($A^+_w = 18$, $\theta = 70°$, $\lambda^+ = 918$). The mesh resolution used for the SSL simulation and the corresponding baseline flow was $\Delta x^+ = 4$, $\Delta y^+ \in [0.6, 4.5]$, $\Delta z^+ = 2$, and the domain size was $L_x = 7.5h$ by $L_z = 3.2h$.

6.2.1 Transverse shear strain

The proximity of this additional SSL simulation to the wavy-wall parameters, with respect to the forcing amplitude and wavelength, lends itself for a direct comparison of the transverse shear strain without any scaling factor, as shown in figure 6.5. Although the agreement is evidently imperfect, there exist strong similarities between the mean transverse shear-strain profiles in the wall-actuated and the wavy-wall scenarios.

The transverse shear strain is weaker than that of the SSL in the region corresponding to the windward side of the wave, and the shear layer penetrates above the buffer layer, with a significant negative strain above the trough region. It should be noted that the Stokes layer penetrates deeply in the buffer layer, a behaviour linked to reduced effectiveness in the case of temporal Stokes layers (Agostini et al., 2015). However, in the regions where the absolute value of the slope is greater, the wavy-wall transverse shear strain is higher than that of the SSL in the viscous sublayer, but is weaker in the lower portion of the buffer layer. These differences may compensate, in the various contributions to the global change in friction, for the penetration of the shear-strain layer away from the wall.

6.2.2 Friction reduction

The drag-reduction level measured for the SSL simulation is $1.9 \pm 0.3\%$, which compares favourably with the friction-reduction level in case G6W1A2 of $2.0 \pm 0.2\%$ reported in table 5.2. However, it should be understood that significant differences exist—as already brought to light for the transverse shear strain in section 6.2.1, in terms of the detailed physics—between the wall-actuated flow and the wavy-channel flow, and it is important to point out that the present comparison is limited to the particular flow configuration considered. In other flow configurations, the equivalence shown in figure 6.2 may not

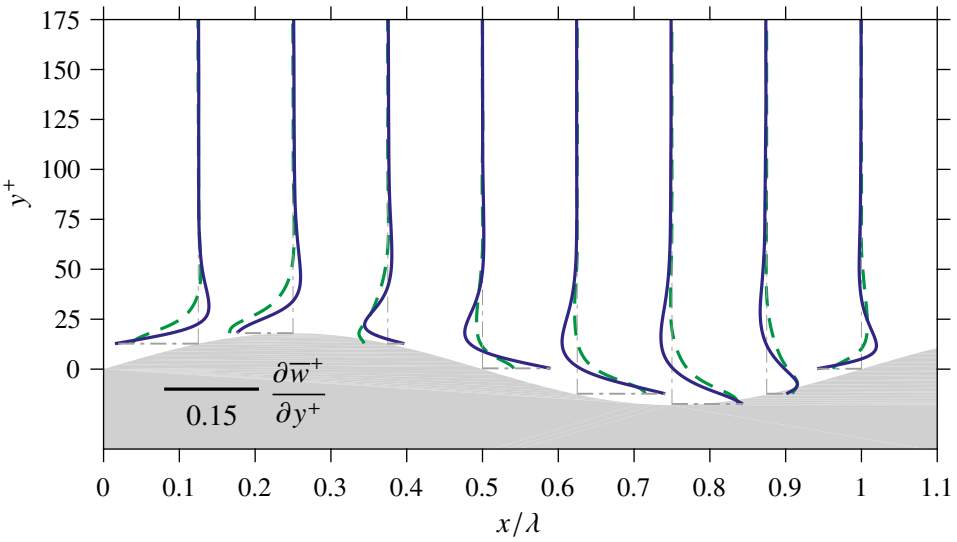


Figure 6.5: Comparison of the transverse strain non-dimensionalised by the actual friction velocity, for the SSL (green dashed lines) and the wavy-wall flow configuration G6W1A2 ($A_w^+ = 18$, $\theta = 70°$ and $\lambda_x^+ = 2684$; blue solid lines). The SSL flow is for a wavelength of $\lambda_x^+ = 2679$ and forcing amplitude $A_{\mathrm{SSL}}^+ = 1.23$ based on the unactuated friction velocity.

be as close, and other additional effects may be enhanced. More importantly, the simulations presented in section 5.4.3 showed that the spanwise wavelength was indeed influential.

6.2.3 Streamwise velocity and Reynolds stress

In addition to the results presented in section 6.1.3, the streamwise-velocity profiles and Reynolds stresses are compared for the baseline flow, the wavy-wall simulation G6W1A2 and the corresponding SSL simulation in figure 6.6.

The close correspondence of the friction-reduction levels between the wavy-wall and the SSL cases, reported in section 6.2.2, is corroborated by a similar shift of the log-law when actual scaling is used, as shown in figure 6.6a.

For the small wave slope of the configuration G6W1A2, the changes to the phase-integrated Reynolds stresses, shown in figure 6.6b, are relatively minor in the directions not aligned with the flow. It is observed that the reduction in the streamwise-energy peak is stronger in the wavy-wall case than in the SSL. However, the increase of the streamwise energy above the buffer layer, previously observed in section 6.1.3, albeit barely noticeable in figure 6.6b because of the small wave slope, is nevertheless present and differs from the behaviour of the SSL.

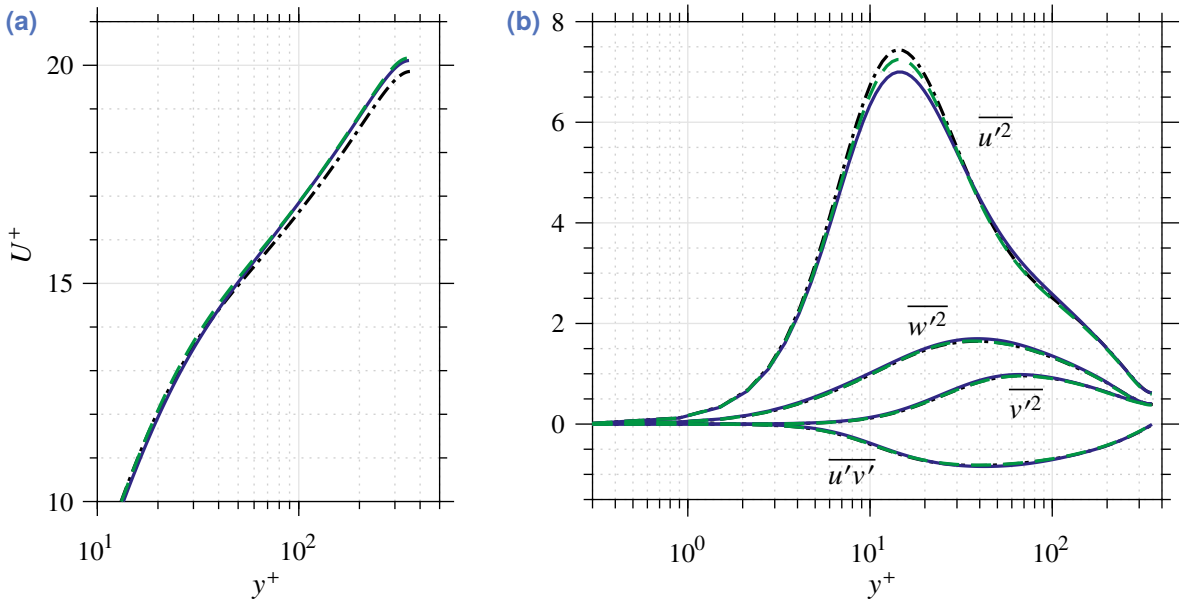


Figure 6.6: Black dash-dotted line: baseline flow G6P1; green dashed line: SSL; blue solid line: wavy wall G6W1A2. Wall units are calculated with the actual friction velocity. **(a)** Log-law region of the streamwise velocity profile, **(b)** phase-integrated Reynolds stresses.

6.2.4 Turbulence-energy budgets

It was shown in the above section 6.2.3 that the principal difference in the phase-integrated profiles between the wavy wall and the SSL is a stronger reduction of the streamwise-energy peak in the wavy-wall case. This difference is further examined by analysing the changes in the turbulence-energy budgets, shown in outer scaling in figure 6.7 and inner scaling in figure 6.8.

Regardless of the scaling employed, the stronger reduction of the streamwise energy is associated with a stronger decrease in turbulence production, which is compensated by an increase in the turbulent diffusion. Conversely, the increased streamwise energy above the buffer layer arises from the increase in turbulence production in that region.

When scaled in outer units, the budget contributions shown in figure 6.7 indicate that the dissipation is reduced at the wall and that this reduction is stronger in the wavy-wall case than for the SSL. However, when scaled in wall units, they seem to indicate an increase in dissipation in the buffer layer. It is also interesting to note that the change in the turbulence dissipation, integrated over the entire volume, is lower than the baseline level in outer units, but is larger than the baseline level in wall units. Although these results were found to be consistent whether the dissipation was evaluated directly from the velocity field or indirectly from the total balance, attention is drawn to the fact that the differences are small, so that concerns about statistical convergence and grid convergence may apply.

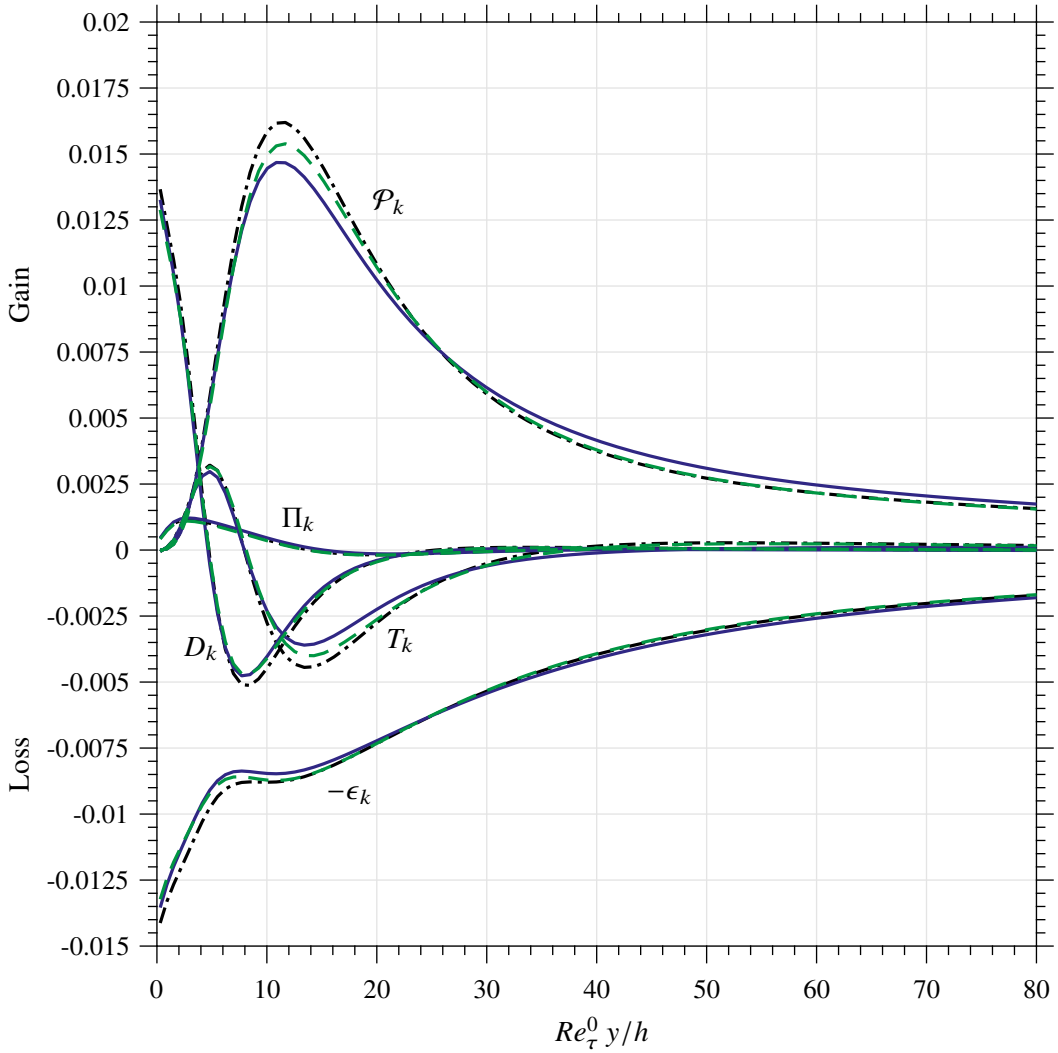


Figure 6.7: Phase-integrated contributions to the turbulence-energy budgets in outer units as a function of the wall-normal coordinate multiplied by the *baseline* friction Reynolds number Re_τ^0. The terms present in equation (3.20) are shown for the baseline G6P1 (black dash-dotted lines), G6W1A2 (blue solid line) and G6W1A4 (red dashed line).

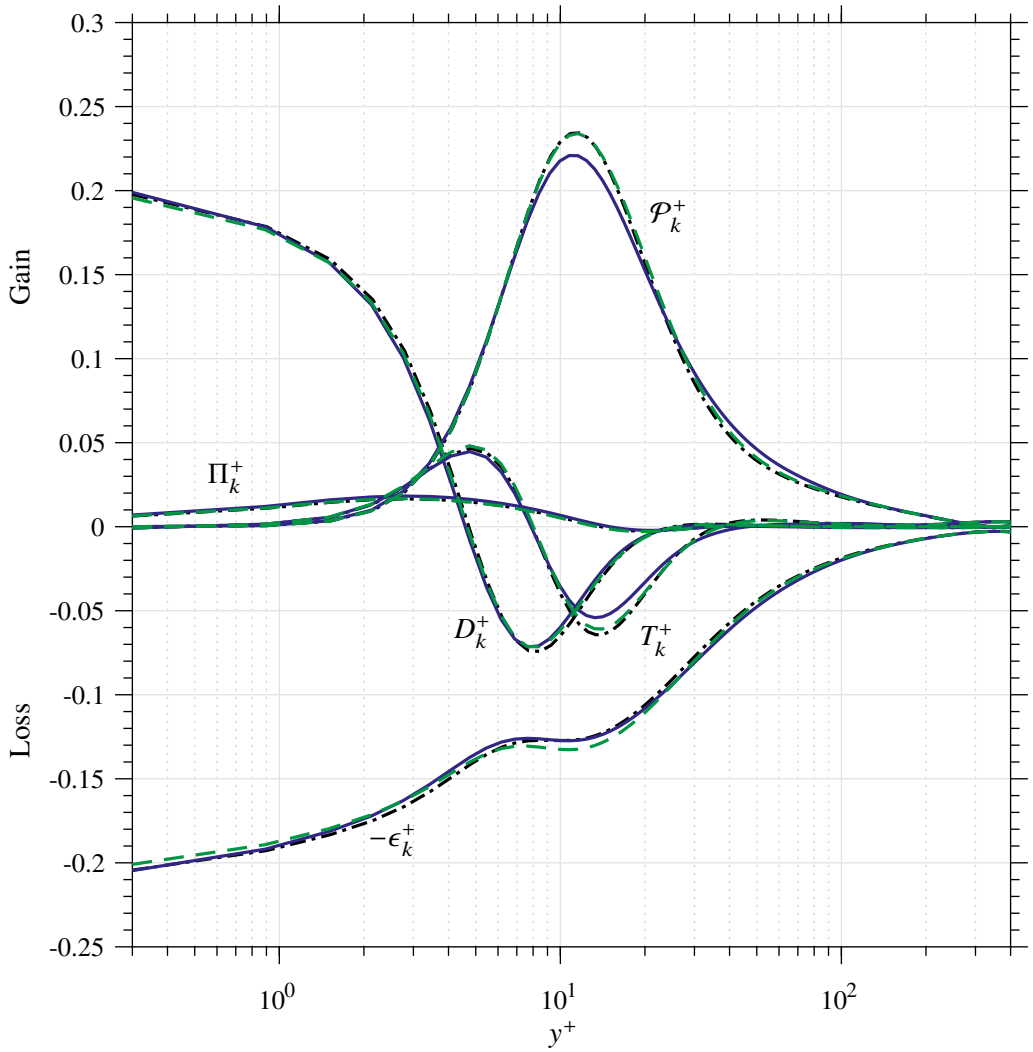


Figure 6.8: Phase-integrated contributions to the turbulence-energy budgets in wall units, calculated with the actual friction velocity. The terms present in equation (3.20) are shown for the baseline flow G6P1 (black dash-dotted lines), the SSL flow (green dashed lines) and the wavy configuration G6W1A2 (blue solid line).

An additional observation is that, apart from the differences in dissipation, all the other budget contributions of the SSL are very close to the baseline when expressed in wall units. In particular, as shown in figure 6.8, the turbulence production is virtually indistinguishable from the baseline. This may suggest that the action of the SSL—for this particular actuation scenario—lies essentially in the friction reduction, which results in a change in dissipation but causes little alteration onto the other budget contributions which seem to merely rescale to the actuated friction.

6.2.5 Detrimental effects of the wavy wall

Despite the similarity between the transverse shear strain of wavy walls and Stokes layers highlighted in sections 6.1.1 and 6.2.1, the friction-reduction effectiveness of the wavy wall was shown to vary significantly depending on the angle of the wave in section 5.4.3. For example, the friction reduction in G6W1A4 ($A_w^+ = 32$, $\lambda_x^+ = 2684$ and $\theta = 70°$) was observed to be greater than twice as much as that of *G9W1A4* ($A_w^+ = 32$, $\lambda_x^+ = 2685$ and $\theta = 80°$) despite having exactly the same streamwise wave slope and same streamwise wavelength. In order to understand the lower performance, two main mechanisms are considered as possible causes for the degradation. However, the two mechanisms presented should not be seen as being activated or deactivated depending on the flow configuration. Rather, these were observed in all cases but with varying degrees of intensity. Consequently, they are illustrated only for the particular flow configuration G6W1A2.

First, beyond the observations made in section 6.1.3, an important difference is that the friction is increased on the windward side of the wave, as shown in figure 6.9. The overall skin-friction reduction arises as a balance between the depressed friction on the leeward side of the wave and the enhanced friction on the windward side, whereas in the SSL case, the friction is decreased at all phases. This variation is associated with the magnitude of the phase-varying streamwise velocity $\widetilde{u}$, which is greater than $\widetilde{w}$, whereas the former is almost negligible in the SSL (in optimum actuation conditions). This phase variation of the mean longitudinal velocity was already identified in Chernyshenko (2013) as the main source of degradation of the performance of the wavy wall relative to that of the SSL.

Second, an additional mechanism, specific to the wavy wall, was revealed by the numerical calculations. As shown in figure 6.10a, there exists a zone of intense production of turbulence energy $\Pi_k = -\overline{u_i' u_k'}\, \partial \overline{u}_i / \partial x_k$ above the leeward side of the wave, reflecting a deeper penetration of the disturbance that arises from the wavy wall into the boundary layer. As shown in figure 6.10b, the increase in production relative to the baseline is quickly followed, in phase, by an increase in energy dissipation

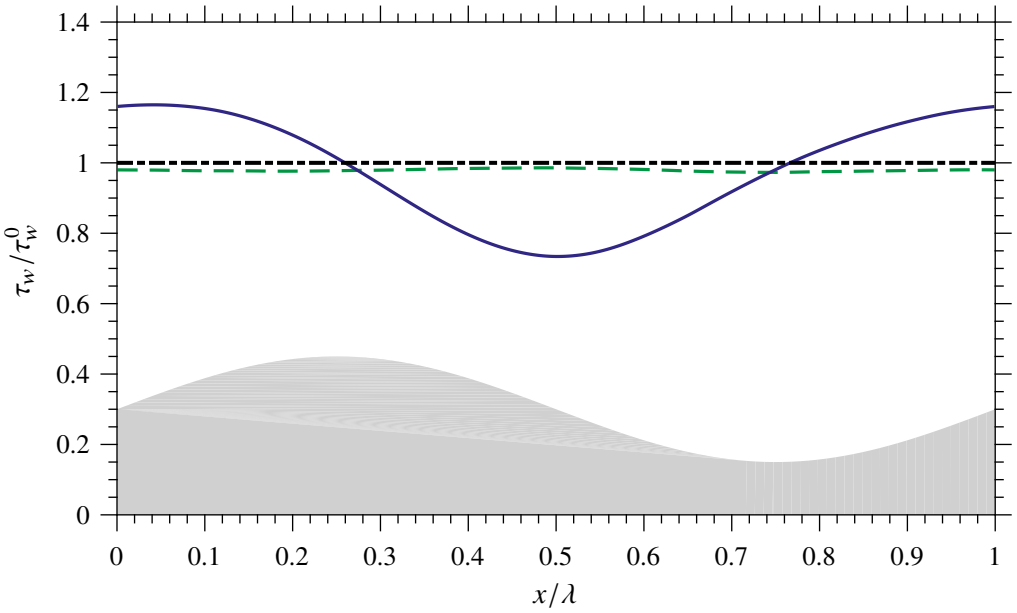


Figure 6.9: Phase-wise variation of the turbulent skin friction. Black dash-dotted line: plane channel G6P1, green dashed line: SSL ($\lambda_x^+ \approx 2700$, $A_{\mathrm{SSL}}^+ = 1.2$), solid line: G6W1A2, i.e. for $\lambda^+ = 918$, $\theta = 70°$, and $A_w^+ = 18$. The grey area shows the corresponding phase location on the wavy wall.

$\epsilon_k = \nu\,\overline{\partial u_i'/\partial x_k\;\partial u_i'/\partial x_k}$, at about the same wall-normal location. This phenomenon strengthens as the wave amplitude increases, and is stronger for G6W2* than for G6W1* at similar wave slopes. The location of the dissipation maximum slightly downstream of the production peak is reminiscent of the observation in a Kolmogorov flow by Goto and Vassilicos (2016) of the existence of a temporal lag, at low wave numbers, between the production and dissipation of kinetic energy in decaying turbulence. In the wavy-wall scenario, a temporal lag arises in the statistics as a spatial shift via the local convection velocity.

The difference between the streamwise Reynolds-stress levels for the wavy walls and the baseline case is shown in figure 6.11 for G6W2A2. This brings to light two different regions showing distinct physical features. One region is close to the wall, where a material weakening of the streaks takes place, as indicated in section 6.1.2, and another is further away above the trough, featuring enhanced streamwise turbulence intensity. The latter increase is stronger than the reduction above the crest, thus leading to a net increase in the mean streamwise turbulence intensity above $y^+ \approx 35$, relative to the baseline (cf. figure 6.4b).

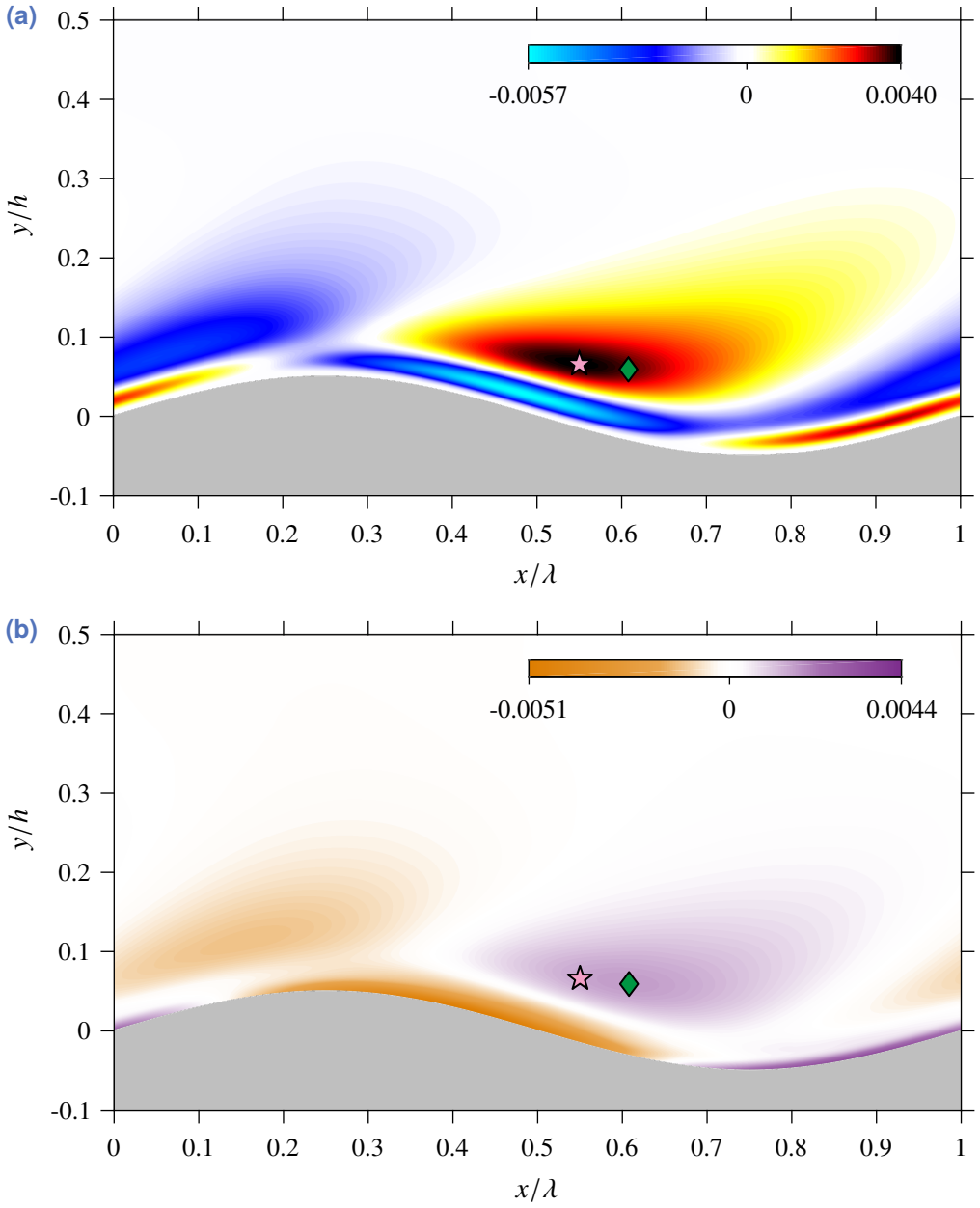


Figure 6.10: Change in the production $\widehat{\Pi}_k$ and dissipation $\widehat{\epsilon}_k$ from the baseline for G6W1A2 ($A_w^+ = 18$, $\theta = 70°$, $\lambda^+ = 918$). **(a)** production difference **(b)** dissipation difference, ★ peak in production difference, ♦ peak in dissipation difference.

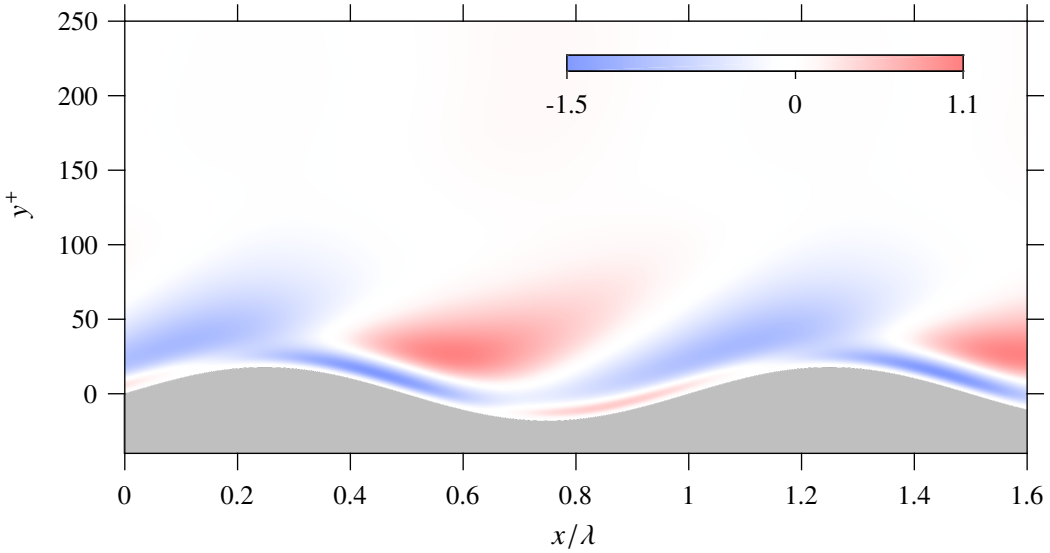


Figure 6.11: Change in the streamwise Reynolds-stress component with respect to the baseline. Contours of $\widehat{u'^2}/u_{\tau,0}^2$ for G6W1A2 ($A_w^+ = 18$, $\theta = 70°$, $\lambda^+ = 918$).

6.2.6 Effect of the streamwise forcing

It was shown in figure 5.3 that the spanwise motion is accompanied by a significant streamwise phase-varying motion. Although it was shown—both for laminar (Jovanović and Bamieh, 2005) and turbulent cases (Luchini et al., 2006)—that channel flows are much more sensitive to wall-normal and spanwise perturbations than they are to streamwise forcing, so that only the transverse motion is expected to matter for the friction reduction, Sigal (1971) observed a resemblance in the shear-stress distribution between the flow past a wavy wall with the waves perpendicular to the main flow direction and the solution of the Stokes problem (synonymously referred to as the Rayleigh problem in Sigal's thesis). As a consequence, there is merit to quantifying the effect of the streamwise forcing without transverse motion in order to isolate the effect of the wave skewness.

The consequences of the streamwise forcing were examined by performing a simulation with the same streamwise wavelength as the configuration G6W1A2, but with the crests and troughs perpendicular to the flow, i.e. for $\theta = 0$. The resulting simulation was labelled G11W1 in table 5.2. The friction reduction in the non-skewed case G11W1 is insignificant, which supports the assertion that the friction reduction arises principally as an effect of the spanwise motion.

Next, the shear strain fields of the perpendicular and oblique cases are compared. The longitudinal and transverse shear strains are shown for both wavy walls in figure 6.12. Figure 6.12a shows that the profiles pertaining to the perpendicular wavy wall are fairly symmetrical. Figure 6.12b shows that the

streamwise forcing in the oblique case is similar to the perpendicular geometry, apart from a skewing of the profiles that generates a stronger asymmetry. The latter is associated with a reduction in the streamwise shear strain close to the wall—in other words, the friction reduction, and an increase away from the wall where the strain level is larger.

Another route to quantifying the effect of the streamwise forcing is to investigate the impact on the streamwise fluctuations. It was shown previously in section 6.2.5 that an influential feature, interpreted as detrimental to the drag reduction, was the existence of a region where all the turbulent properties are enhanced above the leeward side of the wave. Figure 6.13 shows that the change in the streamwise energy is significantly affected by the spanwise forcing in the oblique case. Interestingly, the maximum streamwise energy for the perpendicular wave (figure 6.13a) is greater than that of the oblique wall (figure 6.13b) and is located much closer to the wall, penetrating into the buffer layer. Thus, the skewness of the wave appears to push the zone of increased turbulence energy away from the wall, where it is less affected by the turbulence and hence weaker than that of the perpendicular wave. Moreover, in stark contrast to the perpendicular case, where there is a minute reduction in the streamwise energy on the leeward side confined within the viscous sublayer, there is a continuous layer where it is reduced close to the wall in the oblique case, and this reduction in streamwise energy is largest inside the buffer layer.

6.3 Reynolds-number effect

An interesting question is to what extent the flow properties are sensitive to the Reynolds number, whilst the shape of the wall is kept constant in wall units. This has been investigated by reference to the flow configurations listed in table 6.1, the maximum friction Reynolds number being 1000.

Table 6.1: Flow configurations for friction Reynolds numbers ranging from 180 to 1000.

Simulation label	Re_τ	A_w^+	θ	λ^+
G1W1bis	180	20	70°	918
G6W1A2	360	18	70°	918
G5W1	1000	20	70°	900

Although net-drag-reduction levels of about 1–2% were observed for the three Reynolds numbers tested, the value is not quantifiable with any greater degree of precision, because it is extremely sensitive to various numerical issues, as demonstrated in section 5.4.1 through a grid-convergence study at $Re_\tau = 360$. However, it was also shown that the relative error of first- and second-order statistics is far

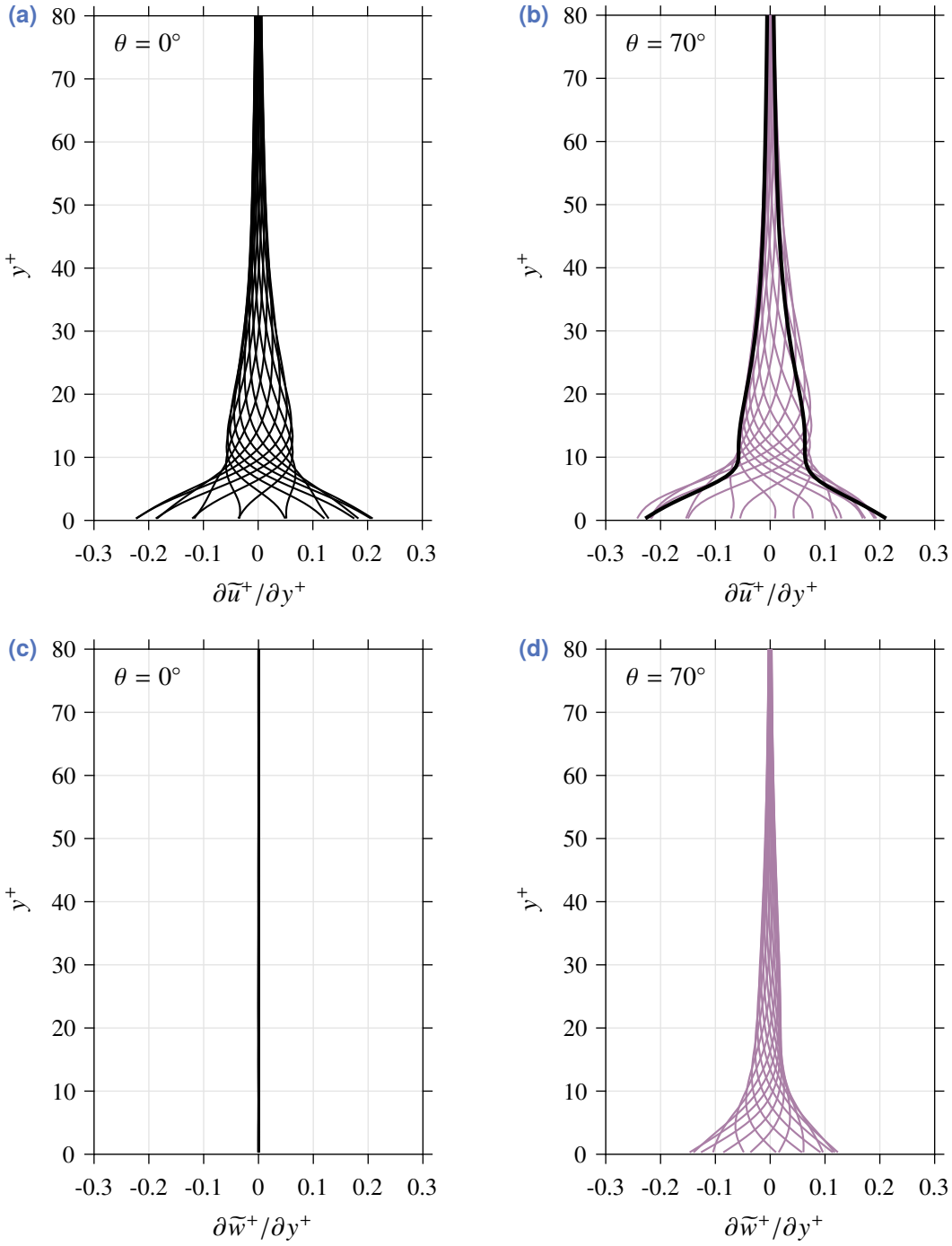


Figure 6.12: Profiles of the phase-varying longitudinal and transverse shear strains in actual wall units. **(a,c)** Perpendicular wavy wall G11W1 ($A_w^+ = 18$, $\theta = 0°$, $\lambda^+ = 2700$), **(b,d)** oblique wavy wall G6W1A2 ($A_w^+ = 18$, $\theta = 70°$, $\lambda^+ = 918$). The thick black lines in **(b)** indicate the envelope (i.e. phase extrema) of the profiles shown in **(a)**.

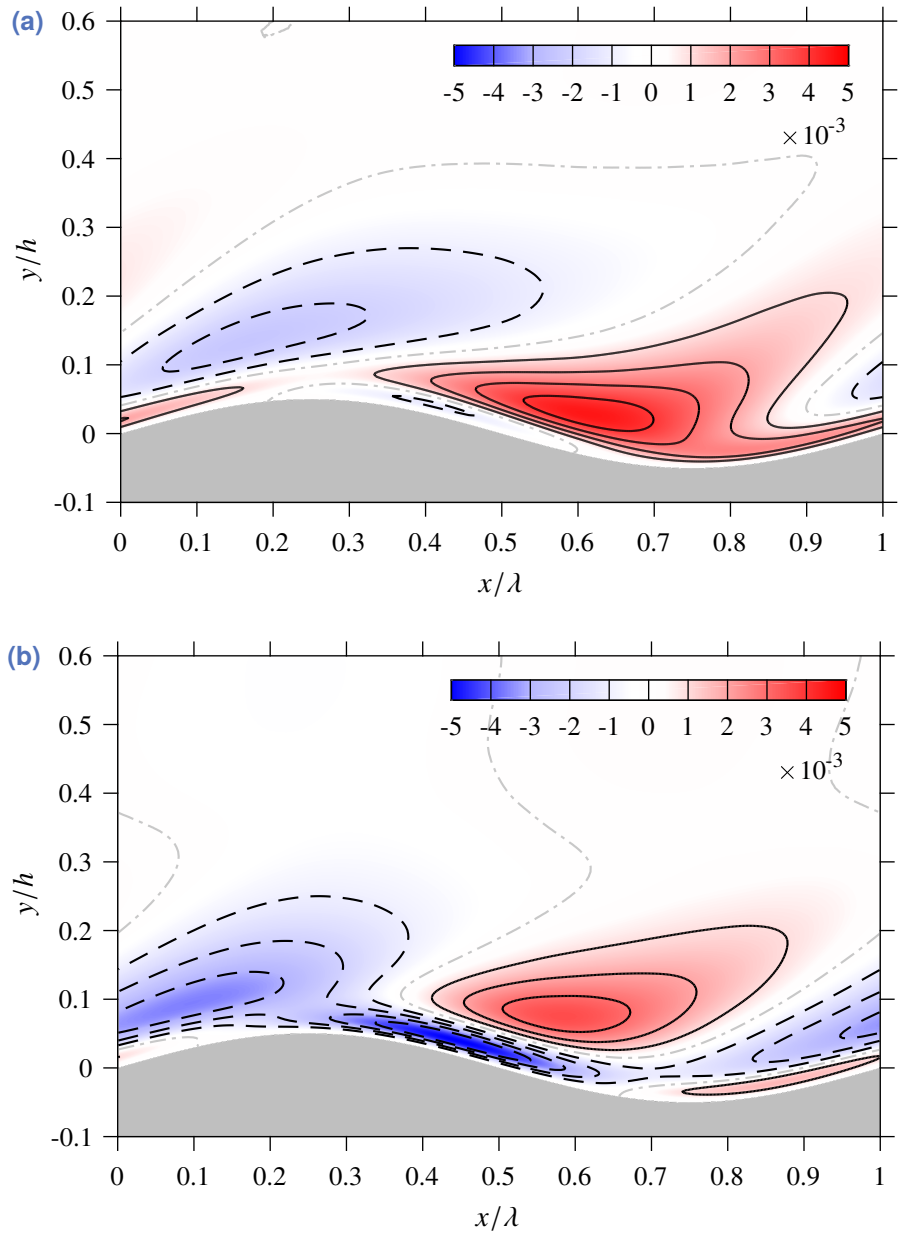


Figure 6.13: Change in the streamwise energy relative to the baseline value $\widehat{u'^2}/U_b^2$. Positive contours are shown with continuous black lines, negative contours with dashed black lines, and zero contour with grey dot-dashed line. **(a)** Perpendicular wavy wall G11W1 ($A_w^+ = 18$, $\theta = 0°$, $\lambda^+ = 2700$), **(b)** oblique wavy wall G6W1A2 ($A_w^+ = 18$, $\theta = 70°$, $\lambda^+ = 918$).

less sensitive to the grid spacing and could therefore be compared with much greater confidence.

The phase-integrated streamwise-velocity and Reynolds-stress profiles are shown in figure 6.14. Figure 6.14a indicates, more clearly than for lower Reynolds-number values, that there is an upward shift in the log law, associated with the friction reduction. In contrast, figure 6.4a shows, for $Re_\tau \approx 360$, a change in slope. However, this needs to be considered against the background of the very short log-law portion combined with the fact that the large wave height, $A_w^+ \approx 20$–30, provokes significant phase-varying streamwise-velocity perturbations that extend well into the log-law region, thus likely to cause deviations from the usual undisturbed channel-flow log-law.

Despite the wavy geometry in wall units not being exactly the same across the three flows in table 6.1, and the mesh being somewhat coarser for the $Re_\tau = 1000$ case, the shear-strain profiles, scaled in wall units, are almost identical as demonstrated in figure 6.15. At $Re_\tau = 180$, a wave height of $A_w^+ = 20$ represents a ratio A_w/h of about 11%, which is significant, while it decreases to 2% for $Re_\tau = 1000$. Consequently, the wave height A_w is small enough relative to the channel height, so that, even at the lowest Reynolds number where the ratio A_w/h is maximum, the distance between the walls remains sufficient to avoid an interference between the two solid boundaries, adding support to the findings reported in section 5.3.3.

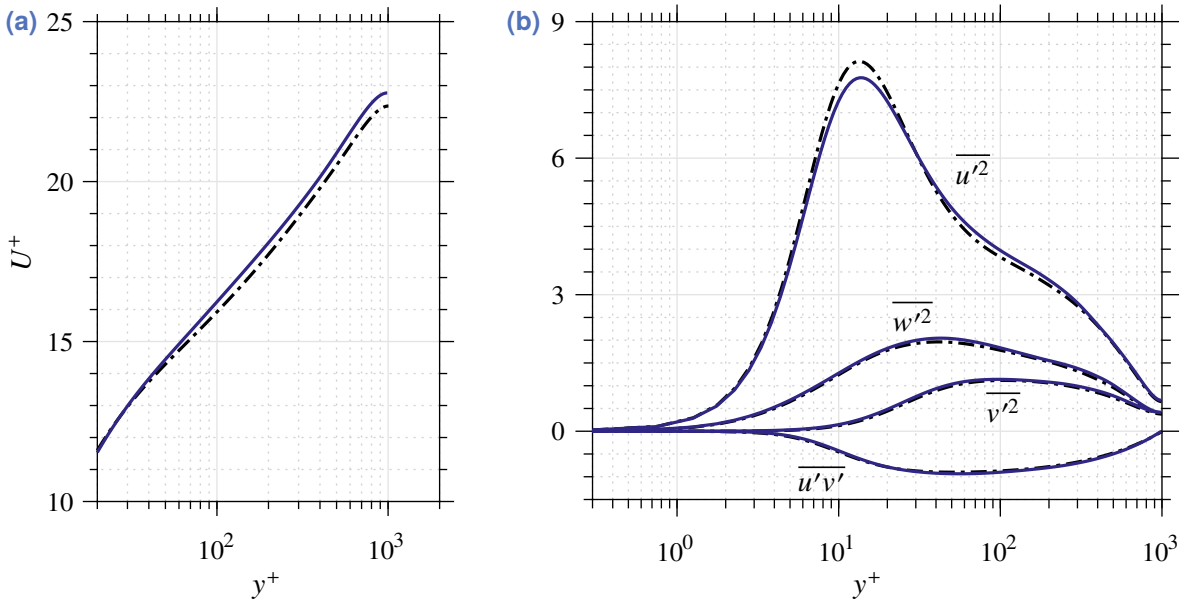


Figure 6.14: Comparison of the streamwise velocity profiles and Reynolds stresses with the baseline at $Re_\tau \approx 1000$ for the flow configuration G5W1 ($A_w^+ = 20$, $\theta = 70°$, $\lambda^+ = 900$), the blue solid lines correspond to the wavy case, and the dash-dotted line to the baseline simulation G5P1. **(a)** Log-law region of the streamwise velocity profile, **(b)** phase-integrated Reynolds stresses.

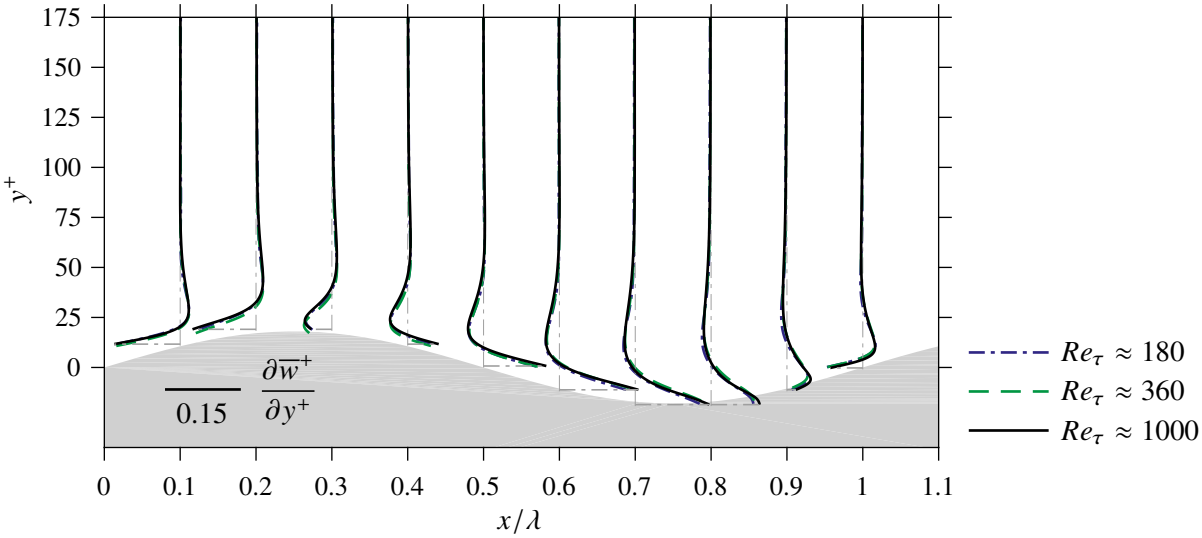


Figure 6.15: Comparison of the shear strain $\partial\overline{w}^+/\partial y^+$ for the same configuration at various Reynolds numbers. $A_w^+ \approx 20$, $\lambda^+ \approx 900$, $\theta = 70°$ (cf. table 6.1).

6.4 Conclusions

The relationship between Stokes layers and wavy walls was investigated in detail for a subset of the simulations presented in chapter 5. It was shown that the transverse shear strain above the wavy wall was comparable to that resulting from the impartment of steady, spatially modulated wall motions like those giving rise to a SSL. Moreover, the amplitude of the transverse shear strain generated by the presence of the wavy wall was shown to approximately scale with the streamwise wave slope A_w/λ_x.

The effect of the shear-strain field on the streaky structures was brought to light close to the wall where the turbulence energy is weakened. Next, the streamwise-velocity and Reynolds-stress profiles were analysed for various wavelengths and wave slopes at $\theta = 70°$. In the wavy-wall case, the streamwise fluctuations are strongly reduced on average in the buffer layer whereas there is an increase in the vertical and transverse normal stresses.

For the flow configuration G6W1A2, an additional simulation was performed for a SSL with the same streamwise wavelength and a forcing amplitude of $A_{SSL}^+ \approx 1.25$, chosen to approximately match the amplitude of the transverse shear strain between the two cases. Strong similarities were brought to light between the statistics of the two flows, in particular in the friction-reduction rate. However, significant differences also exist, such as the large variations of the statistics along the wave. It was shown that the longitudinal shear strain of G6W1A2 was close to that of a perpendicular wall with same streamwise wavelength and slope, a case for which there is no mean spanwise motion. Since only

the skewed wall exhibited a significant friction reduction, this observation supports the assertion that the friction reduction occurs in the oblique wavy wall mostly as a consequence of the spanwise motion.

The generation of a significant phase variation of the mean longitudinal velocity was augmented by the identification of a new mechanism consisting of the intense localised production of turbulence energy above the leeward side of the wave, followed by an increase in dissipation.

Finally, the profiles of the transverse shear strain were shown to be Reynolds-number invariant when the wave geometry is scaled in wall units for friction Reynolds numbers ranging from 180 to about 1000.

Chapter 7

Conclusions and outlook

The present research was concerned with the study of oblique wavy surfaces as a means of reducing the turbulent drag.

In the first phase, two semi-empirical models were proposed, resting on the assumption that the weakening of turbulence by the wavy wall and by in-plane wall oscillations were equivalent for similar induced spanwise motions. These models were used in order to identify a region of the parameter space most likely to yield drag reduction. The existence of an analogy between wavy walls and Stokes layers was assumed and the properties of the wavy-channel flow were predicted by means of a linear solution to the RANS equations with a constant eddy-viscosity profile. In view of the prohibitive cost of running many highly resolved DNSs of such flows, the main motivation for these models was to narrow down the range of parameters in preparation for the DNS exploration.

The first semi-empirical model considered that the transverse shear-strain would reduce the turbulent dissipation but increase the laminar dissipation arising from the mean-velocity gradient. The main observations were that for short wavelengths the additional laminar dissipation was larger than for shorter ones, so that larger wavelengths could be beneficial, and that the ratio between the laminar energy dissipation in the longitudinal and transverse directions relative to that solely in the transverse direction was minimal for angles between $\theta = 55°$ and $\theta = 75°$, given a fixed streamwise wavelength.

The second semi-empirical model assumed that the level of friction reduction could be linked to the specific shape of the transverse shear-strain field, counteracted by the opposing effect of the pressure drag. It was observed from the linear estimation of the pressure drag that larger wave angles θ resulted in lower pressure-drag levels. In order to compare the wavy wall to the Stokes layer, an equivalent wave height (α_{eq}) was derived as that minimising the difference in transverse shear strain between a

wavy wall of height α_{eq} and a SSL of forcing amplitude A_{SSL}, with the transverse shear-strain field evaluated from the linear model for the wavy wall and from the laminar Airy solution for the SSL. The results indicated that this equivalent height was significant even for small forcing amplitudes, and that the difference in the shear-strain profiles relative to the SSL for a wave of height α_{eq} was decreasing as the wavelength was increased—i.e., the emulation of the transverse shear strain was more faithful for large wavelengths.

In the second phase, a range of parameter combinations were simulated with high-resolution DNS. The first part of the computational research was dedicated to the modification and extensive validation and verification of the simulation software. Manufactured-solution fields were generated for a plane channel and a wavy channel to verify the correspondence between the formal spatial accuracy of the numerical scheme and the observed order of convergence towards the analytical manufactured solution as the mesh was refined. In addition, a broad range of turbulent-flow simulations were investigated and validated against reference data. Overall, it was shown that the results obtained from the post-processing routine were quantitatively consistent with previous simulations and experiments available in the literature.

The core part of the computational research dealt with the accurate simulation of wavy-channel flows for a wide range of flow configurations. The total drag was decomposed into frictional and pressure contributions, and each was separately analysed. As the amplitude of the wave was increased, the friction drag initially reduced faster than the pressure drag increased. This yielded a reduction in the overall drag level for small wave slopes. However, for larger wave slopes, the quadratic increase in pressure drag eventually surpassed the friction reduction, which resulted in an overall drag increase.

It was shown that the computational requirements of such simulations were exceptionally stringent relative to usual discretisation standards for near-wall flows. The flow configuration corresponding to a wave of amplitude $A_w^+ = 18$, wavelength $\lambda^+ = 918$ and angle $\theta = 70^\circ$ was put under scrutiny and simulations of this particular configuration were performed with various mesh resolutions, domain sizes, and flow-to-mesh angles. The results indicated a total-drag reduction of about 0.6% relative to a smooth surface for this flow configuration.

The comparison of the spanwise shear-strain profiles for various wavelengths, wave slopes and angles revealed that the profiles were broadly similar when scaled by the streamwise wave slope A_w/λ_x. It was observed, on average along the wave, that the streamwise normal Reynolds stress was depressed in the buffer layer whereas the transverse and vertical stresses increased, and this effect was accentuated as the

wave slope was increased. However, in the configurations studied, the decline in the streamwise normal stress only persisted up to $y^+ \approx 35$ (for the phase-integrated profile). Above that vertical distance, the baseline level was exceeded, both for the streamwise Reynolds stress and for the Reynolds shear stress. Similarly, the production and dissipation of the turbulence energy were shown to be depressed in the buffer layer but enhanced above $y^+ \approx 30$. This weakening also transpired in the contraction of the PDFs of the turbulent fluctuations at $y^+ \approx 14$. An interesting feature of the joint w'–v' PDF that was brought to light was the presence of a correlation between negative spanwise fluctuations and positive vertical fluctuations at $x/\lambda = 0$, as a result of the wave being skewed relative to the main flow direction.

Given a streamwise wavelength of about 2700 wall units, the effect of the spanwise wavelength (or the angle of the wave) was investigated for various wave slopes. The results indicated that, consistently with the linear analysis, the pressure drag decreased upon increasing the angle θ, and exposed a significant dependence of the friction reduction on the spanwise wavelength which was to some degree associated with a weaker spanwise motion at large angles when the crests and troughs became almost aligned with the main flow direction. It was observed that, for a given streamwise wave slope, little change in the friction-drag reduction rate occurred from $\theta = 70°$ to $\theta = 75°$, whereas a sharp decline of the friction reduction was observed at $\theta = 80°$.

One aspect of the simulation work was to draw quantitative and qualitative links between wavy-channel flows and spatial Stokes layers so as to determine to what degree the mechanisms leading to the reduction in friction drag could be claimed to be similar. Although the level of friction reduction for the above-mentioned flow configuration was shown to correspond to that of a Stokes layer of same streamwise wavelength and amplitude $A^+_{\mathrm{SSL}} \approx 1.25$, significant differences were identified between the two flows. Unlike for the SSL where the streamwise mean velocity and Reynolds stresses were almost phase invariant, the wavy wall featured large phase-wise variations for these quantities. As a consequence, an additional mechanism by which the performance of the wavy wall was altered appeared to consist of the formation of a region of increased turbulence production above the leeward side of the wave. This increase in production resulted in an increase in the streamwise energy, which was shown to be also present for a non-skewed wavy wall at an angle of $\theta = 0°$.

From a fundamental perspective, an interesting discovery was the strong similarity between this flow and a spatial Stokes layer of same streamwise forcing wavelength. Although the large phase variations of the wall friction in the wavy-wall scenario mark a clear difference relative to Stokes layers, the results indicate that the mechanism by which the friction is reduced is essentially similar. Since the spanwise

motion was shown to remain Reynolds-number independent when the dimensions of the wave were scaled in wall units (for friction Reynolds numbers ranging from 180 to 1000), this makes it reasonable to expect that observations for Stokes layers, such as those on the Reynolds-number dependence of the friction-drag-reduction rate, may also apply to the wavy wall.

Although the reductions in drag observed in the present research are insufficient for practical applications, there might exist ways by which the performance of the wavy wall could be improved. Some improvements may be sought by introducing a more complex wave-form with higher harmonics instead of a purely sinusoidal shape. This addition could potentially provide a more sustained weakening of the near-wall turbulence and hence improve the friction-reduction level. Alternatively, it may mitigate the pressure drag, which would allow for larger wave slopes. The advantage of attempting to act on the pressure drag is that this quantity is often more accurately predicted by low-fidelity models. For this purpose, a model similar to that presented in chapter 4 could be extended to the non-linear problem in order to optimise the wall geometry. Finally, another route for improvement would be to combine the effect of the wavy wall with other drag-reducing devices such as e.g. riblets or polymers.

Bibliography

Abrams, J. and Hanratty, T. J. (1984). Turbulent flow over small amplitude solid waves. Technical Report 4, The Office of Naval Research.

Abrams, J. and Hanratty, T. J. (1985). Relaxation effects observed for turbulent flow over a wavy surface. *Journal of Fluid Mechanics*, 151:443–455.

Agostini, L., Touber, E., and Leschziner, M. A. (2014). Spanwise oscillatory wall motion in channel flow: drag-reduction mechanisms inferred from DNS-predicted phase-wise property variations at $Re_\tau = 1000$. *Journal of Fluid Mechanics*, 743:606–635.

Agostini, L., Touber, E., and Leschziner, M. A. (2015). The turbulence vorticity as a window to the physics of friction-drag reduction by oscillatory wall motion. *International Journal of Heat and Fluid Flow*, 51:3–15.

Auteri, F., Baron, A., Belan, M., Campanardi, G., and Quadrio, M. (2010). Experimental assessment of drag reduction by traveling waves in a turbulent pipe flow. *Physics of Fluids*, 22(115103).

Balasubramanian, R. (1980). Analytical and design techniques for drag reduction studies on wavy surfaces. Contractor Report 3225, NASA.

Balasubramanian, R. and Orszag, S. A. (1981). Numerical studies of laminar and turbulent drag reduction. Technical Report 3498, NASA.

Bannier, A. (2016). *Contrôle de la traînée de frottement d'une couche limite turbulente au moyen de revêtements rainurés de type riblets*. Mécanique des fluides [physics.class-ph], Université Pierre et Marie Curie, Paris VI.

Baron, A. and Quadrio, M. (1996). Turbulent drag reduction by spanwise wall oscillations. *Applied Scientific Research*, 55:311–326.

Bechert, D. W. and Bartenwerfer, M. (1989). The viscous flow on surfaces with longitudinal ribs. *Journal of Fluid Mechanics*, 206:105–129.

Bechert, D. W., Bruse, M., Hage, W., van der Hoeven, J. G. T., and Hoppe, G. (1997). Experiments on drag-reducing surfaces and their optimization with an adjustable geometry. *Journal of Fluid Mechanics*, 338:59–87.

Bechert, D. W., Hoppe, G., and Reif, W.-E. (1985). On the drag reduction of the shark skin. In *23rd Aerospace Sciences Meeting*, number AIAA-85-0546 in AIAA Shear Flow Control Conference.

Bechert, D. W., Hoppe, G., van der Hoeven, J. G. T., and Makris, R. (1992). The Berlin oil channel for drag reduction research. *Experiments in Fluids*, 12:251–260.

Benschop, H. O. G. and Breugem, W.-P. (2017). Drag reduction by herringbone riblet texture in direct numerical simulations of turbulent channel flow. *Journal of Turbulence*, 18(8):717–759.

Bernard, R. S. and Kapitza, H. (1992). How to discretize the pressure gradient for curvilinear MAC grids. *Journal of Computational Physics*, pages 288–298.

Bewley, T. R. (2009). A fundamental limit on the balance of power in a transpiration-controlled channel flow. *Journal of Fluid Mechanics*, 632:443–446.

Bird, J., Santer, M., and Morrison, J. F. (2015a). In-plane forcing of a turbulent boundary layer, through the actuation of a compliant structure. In *European Drag Reduction and Flow Control Meeting, Cambridge, UK*. ERCOFTAC.

Bird, J. W., Santer, M., and Morrison, J. F. (2015b). Adaptive Kagome lattices for near wall turbulence suppression. In *23rd AIAA/AHS Adaptive Structures Conference*, number AIAA 2015-0270.

Blesbois, O., Chernyshenko, S. I., Touber, E., and Leschziner, M. A. (2013). Pattern prediction by linear analysis of turbulent flow with drag reduction by wall oscillation. *Journal of Fluid Mechanics*, 724:607–641.

Boomsma, A. and Sotiropoulos, F. (2016). Direct numerical simulation of sharkskin denticles in turbulent channel flow. *Physics of Fluids*, 28(035106).

Brachet, M. E., Meiron, D. I., Orszag, S. A., Nickel, B. G., Morf, R. H., and Frisch, U. (1983). Small-scale structure of the Taylor–Green vortex. *Journal of Fluid Mechanics*, 130:411–452.

Brown, D. L., Cortez, R., and Minion, M. L. (2001). Accurate projection methods for the incompressible Navier–Stokes equations. *Journal of Computational Physics*, 168:464–499.

Buckles, J., Hanratty, T. J., and Adrian, R. J. (1984). Turbulent flow over large-amplitude wavy surfaces. *Journal of Fluid Mechanics*, 140:27–44.

Bull, J. R. and Jameson, A. (2015). Simulation of the Taylor–Green vortex using high-order flux reconstruction schemes. *AIAA Journal*, 53(9).

Bushnell, D. M. and Moore, K. J. (1991). Drag reduction in nature. *Annual Review of Fluid Mechanics*, 23:65–79.

Calhoun, R. J. and Street, R. L. (2001). Turbulent flow over a wavy surface: Neutral case. *Journal of Geophysical Research*, 106(C5):9277–9293.

Cary, A. M. J., Weinstein, L. M., and Bushnell, D. M. (1980). Drag reduction characteristics of small amplitude rigid surface waves. In *Viscous flow drag reduction*, volume 72, pages 144–167. AIAA.

Chen, H., Rao, F., Shang, X., Zhang, D., and Hagiwara, I. (2014). Flow over bio-inspired 3d herringbone wall riblets. *Experiments in Fluids*, 55(1698).

Chernyshenko, S. I. (2013). Drag reduction by a solid wall emulating spanwise oscillations. Part 1. *ArXiv e-prints*, [physics.flu-dyn](arXiv:1304.4638).

Chernyshenko, S. I. and Baig, M. F. (2005). The mechanism of streak formation in near-wall turbulence. *Journal of Fluid Mechanics*, 544:99–131.

Cherukat, P., Na, Y., Hanratty, T. J., and McLaughlin, J. B. (1998). Direct numerical simulation of a fully developed turbulent flow over a wavy wall. *Theoretical Computational Fluid Dynamics*, 11:109–134.

Choi, H., Moin, P., and Kim, J. (1993). Direct numerical simulation of turbulent flow over riblets. *Journal of Fluid Mechanics*, 255:503–539.

Choi, H., Moin, P., and Kim, J. (1994). Active turbulence control for drag reduction in wall-bounded flows. *Journal of Fluid Mechanics*, 262:75–110.

Choi, K.-S. and Clayton, B. R. (2001). The mechanism of turbulent drag reduction with wall oscillation. *International Journal of Heat and Fluid Flow*, 22:1–9.

Choi, K.-S., DeBisschop, J.-R., and Clayton, B. R. (1998). Turbulent boundary-layer control by means of spanwise-wall oscillation. *AIAA Journal*, 336(7):1157–1163.

Chorin, A. J. (1969). On the convergence of discrete approximations to the Navier–Stokes equations. *Mathematics of Computation*, 23(106):341–353.

Chung, Y. M. and Talha, T. (2011). Effectiveness of active flow control for turbulent skin friction drag reduction. *Physics of Fluids*, 23(025102).

Cimarelli, A., Frohnapfel, B., Hasegawa, Y., Angelis, E. D., and Quadrio, M. (2013). Prediction of turbulence control for arbitrary periodic spanwise wall movement. *Physics of Fluids*, 25(075102).

De Angelis, V., Lombardi, P., and Banerjee, S. (1997). Direct numerical simulation of turbulent flow over a wavy wall. *Physics of Fluids*, 9(8):2429–2442.

Denison, M., Wilkinson, S. P., and Balakumar, P. (2015). On the effect of rigid swept surface waves on turbulent drag. In *45th AIAA Fluid Dynamics Conference*, number 2015-3221 in AIAA AVIATION Forum.

Duque-Daza, C. A., Baig, M. F., Lockerby, D. A., Chernyshenko, S. I., and Davies, C. (2012). Modelling turbulent skin-friction control using linearized Navier–Stokes equations. *Journal of Fluid Mechanics*, 702:403–414.

Ferziger, J. H. (1987). Simulation of incompressible turbulent flows. *Journal of Computational Physics*, 69:1–48.

Fishpool, G. M. and Leschziner, M. A. (2009). Stability bounds for explicit fractional-step schemes for the Navier–Stokes equations at high Reynolds number. *Computer & Fluids*, 38:1289–1298.

Frederick, K. A. and Hanratty, T. J. (1988). Velocity measurements for a turbulent nonseparated flow over solid waves. *Experiments in Fluids*, 6:477–486.

Frohnapfel, B., Lammers, P., Jovanović, J., and Durst, F. (2007). Interpretation of the mechanism associated with turbulent drag reduction in terms of anisotropy invariants. *Journal of Fluid Mechanics*, 577:457–466.

Fujii, H., Sakurai, K., Nakano, T., and Hagiwara, Y. (2011). Turbulence structure, friction drag and pressure drag due to turbulent flow over angled wavy surfaces. In *Fifth International Symposium on Turbulence and Shear Flow Phenomena*.

Gad-el Hak, M. (2000). *Flow Control: passive, active, and reactive flow management*. Cambridge University Press.

Gad-el-Hak, M. (2002). Compliant coatings for drag reduction. *Progress in Aerospace Sciences*, 38:77–99.

García-Mayoral, R. and Jiménez, J. (2011a). Drag reduction by riblets. *Philosophical Transactions of the Royal Society A*, 369:1412–1427.

García-Mayoral, R. and Jiménez, J. (2011b). Hydrodynamic stability and breakdown of the viscous regime over riblets. *Journal of Fluid Mechanics*, 678:317–347.

García-Mayoral, R. and Jiménez, J. (2012). Scaling of turbulent structures in riblet channels up to $Re_\tau \approx 550$. *Physics of Fluids*, 24(105101).

Gatti, D., Güttler, A., Frohnapfel, B., and Tropea, C. (2015). Experimental assessment of spanwise-oscillating dielectric electroactive surfaces for turbulent drag reduction in an air channel flow. *Experiments in Fluids*, 56(5):1–15.

Gatti, D. and Quadrio, M. (2013). Performance losses of drag-reducing spanwise forcing at moderate values of the Reynolds number. *Physics of Fluids*, 25(125109).

Gatti, D. and Quadrio, M. (2016). Reynolds-number dependence of turbulent skin-friction drag reduction induced by spanwise forcing. *Journal of Fluid Mechanics*, 802:553–582.

Ghebali, S., Chernyshenko, S. I., and Leschziner, M. (2017a). Can large-scale oblique undulations on a solid wall reduce the turbulent drag? *Physics of Fluids*, 29(105102).

Ghebali, S., Chernyshenko, S. I., and Leschziner, M. (2017b). Turbulent drag reduction by wavy wall. In *10th International Symposium on Turbulence and Shear Flow Phenomena (TSFP10)*, number 10B-1.

Ghebali, S., Chernyshenko, S. I., and Leschziner, M. (2017c). Turbulent skin-friction reduction by wavy surfaces. *ArXiv e-prints*, [physics.flu-dyn](arXiv:1705.01989).

Goto, S. and Vassilicos, J. C. (2016). Local equilibrium hypothesis and Taylor's dissipation law. *Fluid Dynamics Research*, 48(021402).

Gouder, K. (2011). *Turbulent friction drag reduction using electroactive polymer surfaces*. PhD thesis, Imperial College London.

Gray, J. (1936). Studies in animal locomotion VI. The propulsive powers of the dolphin. *Journal of Experimental Biology*, 13:192–199.

Greywall, M. S. (1991). Computation of three-dimensional flows using two stream functions. Technical Report 91-27, National Institute for Aviation Research.

Henn, D. S. and Sykes, R. I. (1999). Large-eddy simulation of flow over wavy surfaces. *Journal of Fluid Mechanics*, 383:75–112.

Hirsch, C. (2007). *Numerical Computation of Internal and External Flows: Fundamentals of Computational Fluid Dynamics*. Elsevier, second edition.

Hoyas, S. and Jiménez, J. (2008). Reynolds number effects on the Reynolds-stress budgets in turbulent channels. *Physics of Fluids*, 20(101511).

Hudson, J. D., Dykhno, L., and Hanratty, T. J. (1996). Turbulence production in flow over a wavy wall. *Experiments in Fluids*, 20:257–265.

Hurst, E., Yang, Q., and Chung, Y. M. (2014). The effect of Reynolds number on turbulent drag reduction by streamwise travelling waves. *Journal of Fluid Mechanics*, 759:28–55.

Jacobs, C. T., Jammy, S. P., and Sandham, N. D. (2017). OpenSBLI: A framework for the automated derivation and parallel execution of finite difference solvers on a range of computer architectures. *Journal of Computational Science*, 18:12–23.

Jovanović, J., Pashtrapanska, M., Frohnapfel, B., Durst, F., Koskinen, J., and Koskinen, K. (2006). On the mechanism responsible for turbulent drag reduction by dilute addition of high polymers: theory, experiments, simulations, and predictions. *Journal of Fluids Engineering*, 128(1):118–130.

Jovanović, M. R. and Bamieh, B. (2005). Componentwise energy amplification in channel flows. *Journal of Fluid Mechanics*, 534:145–183.

Jung, W. J., Mangiavacchi, N., and Akhavan, R. (1992). Suppression of turbulence in wall-bounded flows by high-frequency spanwise oscillations. *Physics of Fluids*, 4(8):1605–1607.

Kim, J. (2011). Physics and control of wall turbulence for drag reduction. *Philosophical Transactions of the Royal Society A*, 369:1396–1411.

Kim, J. and Moin, P. (1985). Application of a fractional-step method to incompressible Navier–Stokes equations. *Journal of Computational Physics*, 59:308–323.

Knotek, S. and Jícha, M. (2014). Modeling of shear stress and pressure acting on small-amplitude wavy surface in channels with turbulent flow. *Applied Mathematical Modelling*, 38:3929–3944.

Koh, S. R., Meysonnat, P., Statnikov, V., Meinke, M., and Schröder, W. (2015). Dependence of turbulent wall-shear stress on the amplitude of spanwise transverse surface waves. *Computers & Fluids*, 119:261–275.

Kolmogorov, D. K., Shen, W. Z., Sørensen, N. N., and Sørensen, J. N. (2015). Fully consistent SIMPLE-like algorithms on collocated grids. *Numerical Heat Transfer, Part B*, 67:101–123.

Kramer, F., Gruüneberger, R., Thiele, F., and Wassen, E. (2010). Wavy riblets for turbulent drag reduction. In *5th Flow control Conference*, AIAA 2010-4583.

Kühnen, J., Song, B., Scarselli, D., Budanur, N. B., Riedl, M., Willis, A. P., Avila, M., and Hof, B. (2018). Destabilizing turbulence in pipe flow. *Nature Physics*, 14:386–390.

Lardat, R. and Leschziner, M. A. (1998). A Navier–Stokes solver for LES on parallel computers. Technical report, Department of Mechanical Engineering, UMIST.

Lardeau, S. and Leschziner, M. A. (2013). The streamwise drag-reduction response of a boundary layer subjected to a sudden imposition of transverse oscillatory wall motion. *Physics of Fluids*, 25(075109).

Lee, C. and Kim, J. (1997). Application of neural networks to turbulence control for drag reduction. *Physics of Fluids*, 9(1740).

Lekoudis, S. G. and Sengupta, T. K. (1986). Two-dimensional turbulent boundary layers over rigid and moving swept wavy surfaces. *Physics of Fluids*, 29(4):964–970.

Lentink, D. and de Kat, R. (2014). Gliding swifts attain laminar flow over rough wings. *PLOS ONE*, 9(6).

Lien, F. S. and Leschziner, M. A. (1993). Multigrid acceleration for recirculating laminar and turbulent flows computed with a non-orthogonal, collocated finite-volume scheme. *Computational Methods in Applied Mechanics and Engineering*, 118:351–371.

Lin, J. C., Walsh, M. J., Watson, R. D., and Balasubramanian, R. (1983). Turbulent drag characteristic of small amplitude rigid surface waves. In *AIAA 21st Aerospace Sciences Meeting*, number AIAA-83-0228.

Luchini, P. (1996). Reducing the turbulent skin friction. *Computational Methods in Applied Sciences*, pages 466–470.

Luchini, P. (2016). Immersed-boundary simulations of turbulent flow past a sinusoidally undulated river bottom. *European Journal of Mechanics B/Fluids*, 55:340–347.

Luchini, P., Quadrio, M., and Zuccher, S. (2006). The phase-locked mean impulse response of a turbulent channel flow. *Physics of Fluids*, 18(121702).

Lumley, J. L. and Blossey, P. (1998). Control of turbulence. *Annual Review of Fluid Mechanics*, 30:311–27.

Lumley, J. L. and Newman, G. R. (1977). The return to isotropy of homogeneous turbulence. *Journal of Fluid Mechanics*, 82:161–178.

Maaß, C. and Schumann, U. (1996). Direct numerical simulation of separated turbulent flow over a wavy boundary. In Hirschel, E., editor, *Flow Simulation with High-Performance Computers II*, volume 48 of *Notes on Numerical Fluid Mechanics (NNFM)*, pages 227–241. Vieweg+Teubner Verlag.

Mamori, H. (2012). *Numerical analysis of drag reduction in channel flow by traveling wave-like blowing and suction*. PhD thesis, Keio University.

Mansour, N. N., Kim, J., and Moin, P. (1988). Reynolds-stress and dissipation-rate budgets in a turbulent channel flow. *Journal of Fluid Mechanics*, 194:15–44.

McLean, J. D., George-Falvy, D. N., and Sullivan, P. P. (1987). Flight-test of turbulent skin-friction reduction by riblets. In *Turbulent drag reduction by passive means*, pages 408–424. Royal Aeronautical Society.

McLean, J. W. (1983). Computation of turbulent flow over a moving wavy boundary. *Physics of Fluids*, 26(8):2065–2073.

Meneghello, G. (2013). *Stability and receptivity of the swept-wing attachment-line boundary layer: a multigrid numerical approach*. PhD thesis, LadHyX – École Polytechnique.

Moarref, R. and Jovanović, M. R. (2012). Model-based design of tranverse wall oscillations for turbulent drag reduction. *Journal of Fluid Mechanics*, 707:205–240.

Moser, R. D., Kim, J., and Mansour, N. N. (1999). Direct numerical simulation of turbulent channel flow up to $Re_\tau = 590$. *Physics of Fluids*, 11(4):943–945.

Nakanishi, R., Mamori, H., and Fukagata, K. (2012). Relaminarization of turbulent channel flow using traveling wave-like wall deformation. *International Journal of Heat and Fluid Flow*, 35:152–159.

Napoli, E., Armenio, V., and De Marchis, M. (2008). The effect of the slope of irregularly distributed roughness elements on turbulent wall-bounded flows. *Journal of Fluid Mechanics*, 613:385–394.

Nikitin, N. V. (2000). On the mechanism of turbulence suppression by spanwise surface oscillations. *Fluid Dynamics*, 35(2).

Oliver, T. A., Malaya, N., Ulerich, R., and Moser, R. D. (2014). Estimating uncertainties in statistics computed from direct numerical simulation. *Physics of Fluids*, 26(035101).

Orszag, S. A. (1986). Boundary conditions for incompressible flows. *Journal of Scientific Computing*, 1(1):75–111.

Peaceman, D. W. and H. H. Rachford, J. (1955). The numerical solution of parabolic and elliptic differential equations. *Journal of the Society for Industrial and Applied Mathematics*, 3(1):28–41.

Peet, Y. and Sagaut, P. (2009). Theoretical prediction of turbulent skin friction on geometrically complex surfaces. *Physics of Fluids*, 21(105105).

Peet, Y., Sagaut, P., and Charron, Y. (2008). Turbulent drag reduction using sinusoidal riblets with triangular cross-section. In *38th AIAA Fluid Dynamics Conference and Exhibit*, number AIAA-2008-3745.

Pope, S. B. (2000). *Turbulent flows*. Cambridge University Press.

Quadrio, M. (2011). Drag reduction in turbulent boundary layers by in-plane wall motion. *Philosophical Transactions of the Royal Society A*, 369(1940):1428–1442.

Quadrio, M., Frohnapfel, B., and Hasegawa, Y. (2016). Does the choice of the forcing term affect flow statistics in DNS of turbulent channel flow? *European Journal of Mechanics B/Fluids*, 55(2):286–293.

Quadrio, M. and Ricco, P. (2004). Critical assessment of turbulent drag reduction through spanwise wall oscillations. *Journal of Fluid Mechanics*, 521:251–271.

Quadrio, M. and Ricco, P. (2010). The laminar generalized Stokes layer and turbulent drag reduction. *Journal of Fluid Mechanics*, 667:135–157.

Quadrio, M., Ricco, P., and Viotti, C. (2009). Streamwise-travelling waves of spanwise wall velocity for turbulent drag reduction. *Journal of Fluid Mechanics*, 627:161–178.

Reynolds, W. C. and Tiederman, W. G. (1967). Stability of turbulent channel flow, with application to Malkus's theory. *Journal of Fluid Mechanics*, 27(2):253–272.

Rhie, C. M. and Chow, W. L. (1983). Numerical study of the turbulent flow past an airfoil with trailing edge separation. *AIAA Journal*, 21(11):1525–1532.

Ricco, P. and Wu, S. (2004). On the effects of lateral wall oscillations on a turbulent boundary layer. *Experimental Thermal and Fluid Science*, 29(1):41–52.

Roache, P. J. (1997). Quantification of uncertainty in computational fluid dynamics. *Annual Review of Fluid Mechanics*, 29(1):123–160.

Roache, P. J. (1998). *Verification and validation in computational science and engineering*. Hermosa Publishers.

Roache, P. J. (2002). Code verification by the method of manufactured solutions. *ASME journal of Fluids Engineering*, 124:4–10.

Roy, C. J., Nelson, C. C., Smith, T. M., and Ober, C. C. (2004). Verification of Euler/Navier–Stokes codes using the method of manufactured solutions. *International Journal for Numerical Methods in Fluids*, 44(6):599–620.

Russo, S. and Luchini, P. (2017). A fast algorithm for the estimation of statistical error in DNS (or experimental) time averages. *Journal of Computational Physics*, 347:328–340.

Salari, K. and Knupp, P. (2000). *Code verification by the method of manufactured solutions*. Sandia National Laboratories.

Sasamori, M., Mamori, H., Iwamoto, K., and Murata, A. (2014). Experimental study on drag-reduction effect due to sinusoidal riblets in turbulent channel flow. *Experiments in Fluids*, 55(1828).

Sengupta, T. K. and Lekoudis, S. G. (1984). Calculation of two-dimensional turbulent boundary layers over rigid and moving wavy surfaces. *AIAA Journal*, 23(4):530–536.

Shen, L., Zhang, X., Yue, D. K. P., and Triantafyllou, M. S. (2003). Turbulent flow over a flexible wall undergoing a streamwise travelling wave motion. *Journal of Fluid Mechanics*, 484:197–221.

Shen, W. Z., Michelsen, J. A., and Sørensen, J. N. (2001). Improved Rhie–Chow interpolation for unsteady flow computations. *AIAA Journal*, 39(12):2406–2409.

Shirokoff, D. and Rosales, R. R. (2011). An efficient method for the incompressible Navier–Stokes equations on irregular domains with no-slip boundary conditions, high order up to the boundary. *Journal of Computational Physics*, 230:8619–8646.

Sigal, A. (1971). *An experimental investigation of the turbulent boundary layer over a wavy wall*. PhD thesis, California Institute of Technology.

Skote, M. (2011). Turbulent boundary layer flow subject to streamwise oscillation of spanwise wall-velocity. *Physics of Fluids*, 23(081703).

Steinberg, S. and Roache, P. J. (1985). Symbolic manipulation and computational fluid dynamics. *Journal of Computational Physics*, 57:251–284.

Szodruch, J. (1991). Viscous drag reduction on transport aircraft. In *29th Aerospace Science Meeting*, number AIAA-91-0685.

Tay, C. M. J., Khoo, B. C., and Chew, Y. T. (2015). Mechanics of drag reduction by shallow dimples in channel flow. *Physics of Fluids*, 27(035109).

Taylor, G. I. and Green, A. E. (1937). Mechanism of the production of small eddies from large ones. *Proceedings of the Royal Society of London. Series A, Mathematical and Physical Sciences*, 158(895):499–521.

Temmerman, L. (2004). *Large Eddy Simulation of separating flows from curved surfaces*. PhD thesis, University of London.

Thorsness, C. B., Morrisroe, P. E., and Hanratty, T. J. (1978). A comparison of linear theory with measurements of the variation of shear stress along a solid wave. *Chemical Engineering Science*, 33:579–592.

Tomiyama, N. and Fukagata, K. (2013). Direct numerical simulation of drag reduction in a turbulent channel flow using spanwise traveling wave-like wall deformation. *Physics of Fluids*, 25(105115).

Touber, E. and Leschziner, M. A. (2012). Near-wall streak modification by spanwise oscillatory wall motion and drag-reduction mechanisms. *Journal of Fluid Mechanics*, 693:150–200.

Van Nesselrooij, M., Veldhuis, L. L. M., van Oudheusden, B. W., and Schrijer, F. F. J. (2016). Drag reduction by means of dimpled surfaces in turbulent boundary layers. *Experiments in Fluids*, 57(142).

Vermeire, B. C., Witherden, F. D., and Vincent, P. E. (2017). On the utility of GPU accelerated high-order methods for unsteady flow simulations: a comparison with industry-standard tools. *Journal of Computational Physics*, 334:497–521.

Viotti, C., Quadrio, M., and Luchini, P. (2009a). Streamwise oscillation of spanwise velocity at the wall of a channel for turbulent drag reduction. *Physics of Fluids*, 21(115109).

Viotti, C., Quadrio, M., and Luchini, P. (2009b). Streamwise oscillation of spanwise velocity at the wall of a channel for turbulent drag reduction. *ArXiv e-prints*, [physics.flu-dyn](arXiv:0911.0114v1).

Virk, P. S. (1975). Drag reduction fundamentals. *American Institute of Chemical Engineers*, 21(4):625–656.

Viswanath, P. R. (2002). Aircraft viscous drag reduction using riblets. *Progress in Aerospace Sciences*, 38:571–600.

Vodop'yanov, I. S., Nikitin, N. V., and Chernyshenko, S. I. (2013). Turbulent drag reduction by spanwise oscillations of a ribbed surface. *Fluid Dynamics*, 48(4):461–470.

Walsh, M. J. and Weinstein, L. M. (1979). Drag and heat-transfer characteristics of small longitudinally ribbed surfaces. *AIAA Journal*, 17(7):770–771.

Wang, Z., Yeo, K. S., and Khoo, B. C. (2006). DNS of low Reynolds number turbulent flows in dimpled channels. *Journal of Turbulence*, 7(37).

Wang, Z. J., Fidkowski, K., Abgrall, R., Bassi, F., Caraeni, D., Cary, A., Deconinck, H., Hartmann, R., Hillewaert, K., Huynh, H. T., Kroll, N., May, G., Persson, P.-O., van Leer, B., and Visbal, M. (2013). High-order CFD methods: current status and perspective. *International Journal for Numerical Methods in Fluids*, 72:811–845.

Warsi, Z. U. A. (1999). *Fluid Dynamics: Theoretical and Computational Approaches*. CRC Press, second edition edition.

Wen, L., Weaver, J. C., and Lauder, G. V. (2014). Biomimetic shark skin: design, fabrication and hydrodynamic function. *Journal of Experimental Biology*, 217:1656–1666.

Wilkinson, S. P., Anders, J. B., Lazos, B. S., and Bushnell, D. M. (1988). Turbulent drag reduction research at NASA Langley: progress and plans. *International Journal of Heat and Fluid Flow*, 9(3):266–277.

Yao, Y., Lu, C., Si, T., and Zhu, K. (2010). Experimental investigation on the drag reduction characteristics of traveling wavy wall at high Reynolds number in wind tunnel. *Journal of Hydrodynamics*, 22(5):719–724.

Yoon, H., El-Samni, O. A., Huynh, A., Chun, H. H., Kim, H. J., Pham, A. H., and Park, I. R. (2009). Effect of wave amplitude on turbulent flow in a wavy channel by direct numerical simulation. *Ocean Engineering*, 36:697–707.

Zare, A., Lieu, B. K., and Jovanović, M. R. (2012). Turbulent drag reduction by streamwise traveling waves. In *51st IEEE Conference on Decision and Control*, pages 3122–3126.

Zilker, D. P., Cook, G. W., and Hanratty, T. J. (1977). Influence of the amplitude of a solid wavy wall on a turbulent flow. Part 1. Non-separated flows. *Journal of Fluid Mechanics*, 82:29–51.